CORA Cork Open Research Archive
Cartlann Taighde Oscailte Chorcaí

Title	New design techniques and architectures for highly-reconfigurable and continuously-tunable RF filters using acoustic-wave and planar-microwave resonators
Authors	Nasser, Mohammed
Publication date	2025-12-31
Original Citation	Nasser, M. R. A. 2025. New design techniques and architectures for highly-reconfigurable and continuously-tunable RF filters using acoustic-wave and planar-microwave resonators. PhD Thesis, University College Cork.
Type of publication	Doctoral thesis
Rights	© 2025, Mohammed Nasser. - https://creativecommons.org/licenses/by-nc-nd/4.0/
Download date	2026-10-27 07:29:52
Item downloaded from	https://hdl.handle.net/10468/18780

UCC
University College Cork, Ireland
Coláiste na hOllscoile Corcaigh

Ollscoil na hÉireann, Corcaigh

National University of Ireland, Cork



New Design Techniques and Architectures for Highly-Reconfigurable and Continuously-Tunable RF Filters Using Acoustic-Wave and Planar-Microwave Resonators

Thesis presented by

Mohammed R. A. Nasser

B.Sc., The Islamic University of Gaza, 2017

M.Sc., Akdeniz University, 2020

[ORCID: 0000-0002-2512-3723]

for the degree of

Doctor of Philosophy

University College Cork

School of Engineering and Architecture

Electrical & Electronic Engineering Department

Head of School: Prof. Jorge Oliveira

Supervisor(s): Prof. Dimitra Psychogiou

Dr. Kevin McCarthy

2025

Table of Contents

TABLE OF CONTENTS ..... **II**
LIST OF FIGURES ..... **IV**
LIST OF TABLES ..... **XVII**
GLOSSARY OF TERMS ..... **XVIII**
DECLARATION ..... **XX**
ACKNOWLEDGEMENTS ..... **XXI**
ABSTRACT ..... **XXII**
CHAPTER 1: INTRODUCTION **1**
1.1 MOTIVATION AND BACKGROUND 1
1.2 ACOUSTIC WAVE RESONATOR (AWR)-BASED RF FILTERS 4
1.3 MULTI-FUNCTIONAL AWR-BASED FILTERS 9
1.3.1 Reconfigurable AWR-based filters *9*
1.3.2 Multi-band bandpass filters with reflectionless characteristics *20*
1.4 WIDELY TUNABLE BANDPASS FILTERS 25
1.5 THESIS OUTLINE 28
CHAPTER 2: AWR-BASED FILTERS WITH MULTI-CONFIGURABLE AND ANALOG TUNING CHARACTERISTICS **31**
2.1 INTRODUCTION 31
2.2 HIGHLY SELECTIVE AWLR-BASED BPFS WITH TUNABLE BW 32
2.2.1 Theoretical foundations *32*
2.2.2 Experimental validation *41*
2.3 AWR-BASED BPFS WITH MULTI-CONFIGURABLE AND CONTINUOUSLY TUNABLE TF CAPABILITIES 43
2.3.1 Theorical foundations *43*
2.3.2 Experimental validation *60*
2.4 MULTI-CONFIGURABLE AWLR-BASED BANDPASS-TO-BANDSTOP FILTERS WITH CONTINUOUSLY TUNABLE CHARACTERISTICS 70
2.4.1 Theoretical foundations *70*
2.4.2 Experimental validation *84*
2.5 COMPARISON WITH STATE-OF-THE-ART AWR FILTERS 96
2.6 SUMMARY 99
CHAPTER 3: MULTI-BAND AWLR-BASED BPFS WITH REFLECTIONLESS CHARACTERISTICS **100**
3.1 THEORETICAL FOUNDATIONS 101
3.1.1 Generalized multiband AWLR-Based filter concept using multi-resonant stages *101*
3.1.2 Reflective multi-band AWLR-based BPF *104*
3.1.3 Quasi-reflectionless multi-band AWLR-based BPFs *109*
3.2 EXPERIMENTAL VALIDATION 115
3.2.1 Reflective multi-band AWLR-based BPFs *115*
3.2.2 Quasi-reflectionless multi-band AWLRs *118*
3.2.3 Comparison with state-of-the-art multi-band AWR filters *120*
3.3 SUMMARY 121
CHAPTER 4: SWITCHLESS MULTI-OCTAVE TUNE-ALL BPF MANIFOLD **122**

4.1 THEORETICAL FOUNDATIONS 122
4.1.1 Concept of the RF switchless manifold 122
4.1.2 BPF manifold implementation 125
4.2 EXPERIMENTAL VALIDATION 131
4.3 SUMMARY 140

CHAPTER 5: CONCLUSION AND FUTURE WORK 141

5.1 CONCLUSION 141
5.2 LIST OF PUBLICATIONS 143
5.2.1 Publications emanated from this thesis 143
5.2.2 Other publications 144
5.3 FUTURE WORK 145

BIBLIOGRAPHY 148

List of Figures

Figure 1.1. Block diagram of: (a) conventional multi-band RF front-end receiver comprising multiple RF switched filter banks; (b) a highly-miniaturized RF front-end comprising of tunable RF components. 2

Figure 1.2. Typical structure of a one-port SAW resonator [21]. 5

Figure 1.3. BAW resonator structure [22]. 6

Figure 1.4. Relationship between electromechanical coupling and filter FBW for three types of filter configurations [23]. 7

Figure 1.5. Measured transmission characteristics (S_{21}) of SAW bandpass filters exhibiting spurs and amplitude fluctuations, based on devices with the following characteristics: a) 15°YX-LN/SiO_2/Si with h_{Cu} = 200 nm; b) 20°YX-LN/SiO_2/Si with h_{Cu} = 200 nm; c) 15°YX-LN/SiO_2/Si with h_{Cu} = 240 nm, and; d) 20°YX-LN/SiO_2/Si with h_{Cu} = 240 nm [24]. 8

Figure 1.6. Wideband BPF based on a hybrid film-bulk acoustic resonator, coupled-line, and transmission-line structure: (a) Photograph of the manufactured BPF; (b) Simulated and measured S-parameters [25]. 8

Figure 1.7. Conceptual illustration of a reconfigurable BPF with continuously tunable characteristics: (a) Bandpass response with an interfering signal distant from the passband; (b) Tuning the f_{cen} to avoid interference emerging on the right side of the passband; (c) Narrowing the BW to mitigate interference appearing on both sides of the passband. 9

Figure 1.8. Photograph of the 1.5 stage BST FBAR filters. (a) Transmission responses for the measured and simulated 1.5 stage BST FBAR filter in its ON and OFF states [37]. 10

Figure 1.9. BW-switchable ferroelectric BAW filters: (a) Photograph of the manufactured BST FBAR filter with three BW states; (b) RF measured transmission response [34]. 11

Figure 1.10. BST FBAR filter bank: (a) Photograph of a fabricated multiband 2.5-stage BST FBAR filter bank; (b) Transmission responses of the measured 2.5-stage triple-band filter bank when the filters are turned ON individually [38]. 11

Figure 1.11. Contour-mode resonators: (a) Optical photograph of the fabricated resonator; (b) Measured response demonstrating fine-tuning of the resonator through mass loading by actuating between 0 and 6 fingers on each side of the transducer [39]. 12

Figure 1.12. f_{cen} switchable three-pole SAW filter using VO_2 switches: (a) Photograph of the fabricated tunable three-pole filter with a close-up view of the monolithically integrated VO_2 switches; (b) Measured transmission response [44]..... 13

Figure 1.13. Measured S-parameter response of the five-pole switched dual-band filter when: (a) both channels are on; (b) both channels are off; (c) only high channel is on; and (d) only low channel is on [45]. 13

Figure 1.14. Two-state PCM-based BW-reconfigurable acoustic-wave filter: (a) Manufactured filter prototype; (b) Measured response of the filter integrated with VO_2 switches [46]. 14

Figure 1.15. AWLR-based BPF with continuously tunable BW: (a) Manufactured prototype; (b) Measured RF power transmission response for various tunable BW states [47]. 15

Figure 1.16. AWLR-based BSF with continuously tunable BW: (a) Manufactured prototype; (b) Measured transmission response showing continuously tunable stopband BW [48]. 16

Figure 1.17. Dual-band AWLR-based BSF with tunable BW: (a) Manufactured prototype; (b) Symmetric BW tuning of both stopbands; (c) Intrinsic RF switching of each band individually and simultaneously (all-pass response shown in red trace) [11]. .. 16

Figure 1.18. Dual-band BP-to-BS AWLR-based filter: (a) Manufactured prototype; (b) Measured transmission responses in BPF and BSF modes [49]. 17

Figure 1.19. AWLR-based BS-to-AP filter: (a) Manufactured prototype; (b) Measured BP-to-AS response [50]. 17

Figure 1.20. RF-switched single-to-multi-band reconfigurable AWLR-based BPF: (a) Manufactured prototype; (b) Measured single-band response with one channel activated [12]..... 17

Figure 1.21. AWLR-based BSF with equi-ripple absorptive stopband: (a) Manufactured prototype; (b) Measured response showing variable stopband IL [51]. 18

Figure 1.22. Absorptive microstrip BPF: (b) Manufactured prototype; (c) Measured results [57]. 21

Figure 1.23. Symmetrical quasi-absorptive microstrip BPF: (a) manufactured prototype; (b) simulated and measured RF response [58]. 21

Figure 1.24. AWR-based multiplexer: (a) Quadplexer circuit topology; (b) simulated and measured responses [58]. 22

Figure 1.25. Double-Ladder dual-band filter using BAW resonators: (a) Generic configuration; (b) Simulated example using measured BAW resonators [65]. 22

Figure 1.26. Symmetrical Quasi-Reflectionless SAW-Based BPFs: (a) manufactured two-stage prototype; (b) RF-measured/simulated S-parameters [66]..... 23

Figure 1.27. f_{cen}-tunable filters: (a) Manufactured interdigital BPF with measured tunable f_{cen} from 0.72 to 1.22 GHz (TR: 1.69:1) [17]; (b) Manufactured hairpin BPF with measured tunable f_{cen} from 1.5 to 1.9 GHz (TR: 1.26:1) [18]. 26

Figure 1.28. Reconfigurable BPF with both f_{cen} and BW tuning: (a) Manufactured prototype; (b) Measured f_{cen} tuning response; (c) Measured BW tuning response [70]. 27

Figure 1.29. RF-switched BPF manifold with tunable f_{cen}: (a) Manufactured protoype; (b) Measured $|S_{21}|$ 27

Figure 2.1. Quasi-elliptic AWLR-based BPF that exhibits N poles and $2N$ TZs: (a) Generalized circuit diagram and example TFs; (b) Circuit schematic and example response of a filter comprising one series-type and one parallel-type stages; (c) Circuit schematic and example response of a filter comprising two parallel-type stages [90]. 33

Figure 2.2. (a) Simulated power transmission $|S_{21}|$ of a SAW resonator (C_M = 1.85 fF, L_M = 16.32 μH, R_M = 11.3 Ω, C_0 = 2.18 pF, $\Delta\varphi$ = 9.38°, k_t^2 = 0.12%, f_s= 916.4 MHz) and a series-type AWLR multi-resonant stage; (b) Power transmission response $|S_{21}|$ of the series-type multi-resonant stage that exhibits one pole and two TZs. The TZs can be controlled by altering ω_r [90]. 34

Figure 2.3. Power transmission $|S_{21}|$ and reflection $|S_{11}|$ responses of the parallel-type AWLR multi-resonant stage: (a) TZs control around the pole by tuning ω_p; (b) BW control by altering (L_P/L_0) [90]. 37

Figure 2.4. (a) Circuit schematic of the quasi-elliptic four-pole/ eight-TZ AWLR BPF that comprises four multi-resonant AWLR stages; (b) Theoretical power transmission $|S_{21}|$ and reflection $|S_{11}|$ of the BPF and its constituent stages (Stage #1, Stage #2, Stage #3, and Stage #4) obtained with linear circuit simulations [90]. 38

Figure 2.5. Theoretical power transmission $|S_{21}|$ response of the four-stage quasi-elliptic BPF for alternative locations of TZs (by altering ω_{r1}, ω_{r2}, ω_{P1}, and ω_{P2}) demonstrating the reconfigurability of the TF in the out-of-band. 38

Figure 2.6. Theoretical power transmission $|S_{21}|$ response of the four-stage quasi-elliptic BPF for alternative levels of FBW by altering the inductance ratio L_P/L_0 and the impedance inverter values. For the case of: i) L_P/L_0=0.546, C_{pp1}= C_{pp2}=0.51 pF, C_{p1}=2.77 pF, C_{p2}=2.69 pF, C_{ex}=1.32 pF, L_{ex}=17 nH, C_{23}= 0.63 pF, L_{23}=33.2 nH, ii) L_P/L_0=0.39, C_{pp1}= C_{pp2}=0.89 pF, C_{p1}=2.02 pF, C_{p2}=2.08 pF, C_{ex}=1.94 pF, L_{ex}=14.5 nH, C_{23}= 0.66 pF, L_{23}=22.4 nH, ii) L_P/L_0=0.34, C_{pp1}= C_{pp2}=0.51 pF, C_{p1}=1.934 pF, C_{p2}=1.888 pF, C_{ex}=1.32 pF, L_{ex}=17.06 nH, C_{23}= 0.626 pF, L_{23}=29.9 nH. (The rest of the design parameters are: L_{p1}=Lp_2 = 7.6 nH, L_{r1} = L_{r2} =25 nH, C_{r1}= C_{r2}=2.15 pF) [90]. 39

Figure 2.7. Theoretical power transmission $|S_{21}|$ response of the four-stage four-pole/eight-TZ BPF as a function of Q_M and Q_{LE} [90]. 40

Figure 2.8. Theoretical power transmission $|S_{21}|$ response of the four-stage four-pole/eight-TZ BPF. Continuous BW tuning is obtained by varying the location of the TZs [90]. 40

Figure 2.9. Circuit schematic of the six-stage six-pole/twelve-TZ BPF alongside with its ideally-simulated S-parameters [90]. 41

Figure 2.10. Manufactured prototype of four-stage quasi-elliptic AWLR prototype [90]..... 42

Figure 2.11. RF-measured S-parameters of the four-stage quasi-elliptic AWLR BPF prototype with continuously tunable FBW. An EM-simulated state is also included for comparison purposes [90]. 42

Figure 2.12. Multi-resonant AWLR module with multi-configurable and continuously-tunable TF characteristics: (a) Block diagram; (b) BPF response shaped by one pole and two TZs, showcasing continuous tuning of the f_{cen} achieved by altering f_L; (c) Continuous BW control; (d) AP mode; (e) AS mode [91]. 44

Figure 2.13. Multi-configurable multi-branch AWLR stage with extended continuously tunable TF characteristics and generalized higher-order BPF TFs and showcases of conceptual responses: (a) Generalized block diagram of a multi-branch AWLR stage with k AWLR modules; (b) Switching between the AWLR modules through $Z_{E1\text{-}k}$ and $R_{1\text{-}k}$ to facilitate discrete f_{cen} tuning; (c) Extended continuous f_{cen} tuning by tuning R_L and module switching; (d) Generalized higher order BPF block diagram; (e) Conceptual BPF response shaped by N poles and $2N$ TZs [91]. ... 45

Figure 2.14. (a) Simulated $|S_{21}|$ of a SAW resonator (f_{s1}= 1000 MHz, L_{M1}= 25.72 μH, $C_{M1}=1/(L_{M1}\bullet 4\pi^2 f_{s1}^2)$, C_{01}= 1.09 pF, k_t^2= 0.12%, $Q_{M1}=\infty$) and a multi-resonant AWLR f_{s1} stage that comprises one R_{H1} and one impedance inverter Z_{E1} and exhibits one pole and two TZs; (b) S-parameters of a multi-resonant stage comprising one R_{H1}, one R_L and one Z_{E1} demonstrating that f_{cen} tuning is controlled by f_L; (c) Alternative FBWs obtained by altering the Z_{E1} values: i) BW= 1.44 MHz (Z_{E1}=70 Ω), ii) BW= 0.8 MHz (Z_{E1}= 50 Ω), iii) BW= 0.43 MHz (Z_{E1}=35 Ω) when: $f_L=f_1=f_{s1}$. In these examples, L_L=2 nH, L_1=2.6 nH [91]. 47

Figure 2.15. Simulated response of the multi-resonant AWLR stage for different operational modes: (a) TZs control around the transmission pole achieved by altering f_1 when Z_{E1}=70 Ω and $f_L=f_{s1}$; (b) AP mode achieved by setting $f_1=2.16f_{s1}$, Z_{E1}=100 Ω and $f_L=f_{s1}$; (c) AS mode obtained by setting f_1= $0.78f_{s1}$, Z_{E1}=10 Ω and $f_L=f_{s1}$. In these examples, L_L=2 nH, L_1=2.6 nH [91]. 48

Figure 2.16. Linear simulation of a multi-branch AWLR stage comprising two-AWLR modules ($AWLR_{\#1}$, $AWLR_{\#2}$): (a) Discrete f_{cen} tuning by intrinsic switching ON/OFF each

of the AWLR modules (AWLR$_{\#i}$s) achieved by altering f_1, f_2 and Z_{E1}, Z_{E2}. Case 1: AWLR$_{\#1}$ ON and AWLR$_{\#2}$ OFF: $f_1=f_s$, $f_2=2.16f_s$, $Z_{E1}=50\ \Omega$, $Z_{E2}=100\ \Omega$, Case 2: AWLR$_{\#1}$ OFF and AWLR$_{\#2}$ ON, $f_1=2.16f_s$, $f_2=f_s$, $Z_{E1}=100\ \Omega$, $Z_{E2}=50\ \Omega$ when $f_L=f_s$, where $f_s = (f_{s1} \bullet f_{s2})^{1/2}$; (b) Utilizing the intrinsic switch capability of AWLR$_{\#i}$s to extended the f_{cen} tuning and continuously tuning it by altering f_L. (The rest of design parameters are L_i=2.6 nH, L_L= 2 nH) [91]. 51

Figure 2.17. Frequency-tunable quasi-elliptic BPF using two-stage/three-branch AWLR modules (i.e., AWLR$_{\#1}$, AWLR$_{\#2}$, AWLR$_{\#3}$): (a) Circuit schematic; (b) Simulated S-parameters obtained through linear circuit simulation with AWLR$_{\#2}$ intrinsically switched ON and AWLR$_{\#1}$, AWLR$_{\#3}$ intrinsically switched OFF: $f_1=f_3=2.16f_s$, $f_2=f_s$, $Z_{E1}=Z_{E3}=100\ \Omega$, $Z_{E2}=55\ \Omega$, $f_L=f_s$, demonstrating a two-pole/four-TZ AWLR BPF (N=2, k=3 in Figure 2.13). (The remaining design parameters are: L_i= 2.6 nH, L_L= 2 nH, $Z_{ex}=33\ \Omega$, $Z_{1,2}=20\ \Omega$) [91]..... 52

Figure 2.18. Frequency-tunable quasi-elliptic BPF using two-stage/three-branch AWLRs (Figure 2.17(a)): (a) Intrinsic switching-OFF alteration between AWLR$_{\#i}$s achieved by varying f_is, and Z_{Ei}s when $f_L=f_s$; The cases shown are: i) Case 1 (red traces): f_{cen}=999.6 MHz, when AWLR$_{\#1}$ ON and AWLR$_{\#2}$ and AWLR$_{\#3}$ OFF obtained by setting $f_1=f_s$, and $f_2=f_3=2.16f_s$, and $Z_{E1}=55\ \Omega$, and $Z_{E2}=Z_{E3}=100\ \Omega$, ii) Case 2 (black traces): f_{cen}=1000.7 MHz, when AWLR$_{\#2}$ is ON and AWLR$_{\#1}$ and AWLR$_{\#3}$ are OFF obtained by setting $f_2=f_s$, and $f_1=f_3=2.16f_s$, and $Z_{E2}=55\ \Omega$, and $Z_{E1}=Z_{E3}=100\ \Omega$, iii) Case 3 (blue traces), f_{cen}=1001.7 MHz, correspond to the case where AWLR$_{\#3}$ ON and AWLR$_{\#1}$ and AWLR$_{\#2}$ OFF obtained by setting $f_3=f_s$, and $f_1=f_2=2.16f_s$, and $Z_{E3}=55\ \Omega$, and $Z_{E1}=Z_{E2}=100\ \Omega$; (b) Continuous f_{cen} tuning achieved by varying f_L and extended by intrinsically switching ON/OFF AWLR$_{\#i}$s [91]..... 53

Figure 2.19. Simulated S-parameters obtained through linear circuit simulations of the two-stage/ three-branch AWLR based BPF in Figure 2.17(a) demonstrating: (a) Alternative FBWs when AWLR$_{\#2}$ is intrinsically switched ON and AWLR$_{\#1}$, AWLR$_{\#3}$ are intrinsically switched OFF, achieved by altering the Z_{E2} values resulting in: i) BW= 1.99 MHz ($Z_{E2}=35\ \Omega$); ii) BW= 1.1 MHz ($Z_{E2}=50\ \Omega$); iii) BW= 0.55 MHz ($Z_{E2}=70\ \Omega$); (b) AP mode obtained by setting $f_1=f_2=f_3=2.16f_s$, $Z_{E1}=Z_{E2}=Z_{E3}=100\ \Omega$ and $f_L=f_s$; (c) AS mode by setting $f_1=f_2=f_3=0.78f_s$, $Z_{E1}=Z_{E2}=Z_{E3}=15\ \Omega$ and $f_L=f_s$ [91]..... 54

Figure 2.20. A more realistic BVD model of the AWRs, incorporating R_{si} to represent the RF electrical losses in a realistic resonator..... 55

Figure 2.21. Simulated S-parameters of the two-pole/four-TZ, three-branch, AWLR based BPF in Figure 2.17(a) when AWLR$_{\#2}$ is intrinsically switched ON and AWLR$_{\#1}$, and

AWLR$_{\#3}$ are intrinsically switched OFF. They are obtained by setting $f_2 = f_s$, and $f_1 = f_3 = 2.16f_s$, $Z_{E2} = 50\ \Omega$, $Z_{E1} = Z_{E3} = 100\ \Omega$, and $f_L = f_s$. The finite Q-factor effect is demonstrated when: i) R_i is represented by an LC resonator (black curves), and ii) R_i is represented by an inductor (blue curves) [91]. 56

Figure 2.22. Simulated S-parameters of the two-pole/four-TZ three-branch AWLR-based BPF in Figure 2.17(a) when AWLR$_{\#2}$ is intrinsically switched ON and AWLR$_{\#1}$, AWLR$_{\#3}$ are intrinsically switched OFF. They are obtained by setting $f_2 = f_s$, and $f_1 = f_3 = 2.16f_s$, $Z_{E2} = 40\ \Omega$, $Z_{E1} = Z_{E3} = 100\ \Omega$, and $f_L = f_s$, demonstrating f_{cen} tuning by varying f_L for: (a) lossless ($Q_{Mi} = 9500$, $Q_{LE} = \infty$, and $R_{si} = 0\ \Omega$); (b) lossy ($Q_{Mi} = 9500$, $Q_{si} = 8080$ [$R_{si} = 3\ \Omega$], and $Q_{LE} = 100$) [91]..... 57

Figure 2.23. Simulated S-parameters of the two-pole/four-TZ, three-branch, AWLR based BPF in Figure 2.17(a) when AWLR$_{\#2}$ is intrinsically switched ON and AWLR$_{\#1}$, and AWLR$_{\#3}$ are intrinsically switched OFF. They are obtained by setting $f_2 = f_s$, and $f_1 = f_3 = 2.16f_s$, $Z_{E2} = 40\ \Omega$, $Z_{E1} = Z_{E3} = 100\ \Omega$, and $f_L = f_s$. The TF demonstrates f_{cen} tuning by varying f_L for various lossy cases: i) $Q_{si} = 8080$, $Q_{LE} = 250$ and; ii) $Q_{si} = 8080$, and $Q_{LE} = 100$ [91]. 58

Figure 2.24. Simulated S-parameters of the two-pole/four-TZ, three-branch, AWLR stage based BPF (Figure 2.17(a)) illustrating the influence of FBW on the frequency TR. This analysis is carried out with AWLR$_{\#2}$ intrinsically switched ON and AWLR$_{\#1}$, and AWLR$_{\#3}$ OFF for: i) Case 1 (BW=1.55 MHz) obtained by setting: $f_2 = f_s$, $f_1 = f_3 = 2.16f_s$, $Z_{E2} = 60\ \Omega$, $Z_{E1} = Z_{E3} = 100\ \Omega$, ii) Case 2 (BW=1.07 MHz) obtained by setting: $f_2 = f_s$, $f_1 = f_3 = 2.16f_s$, $Z_{E2} = 50\ \Omega$, $Z_{E1} = Z_{E3} = 100\ \Omega$ [91]. 59

Figure 2.25. Simulated S-parameters of the two-pole/four-TZ, three-branch, AWLR stage based BPF (depicted in Figure 2.17(a)) demonstrating the impact of altering the (AWR)s' k_t^2 on both the in-band IL and the out-of-band IS, while maintaining a fixed FBW for the BPF. This analysis is conducted with AWLR$_{\#2}$ intrinsically switched ON and AWLR$_{\#1}$, AWLR$_{\#3}$ intrinsically switched OFF: obtained by setting $f_2 = f_s$, and $f_1 = f_3 = 2.16f_s$, $Z_{E2} = 20\ \Omega$, $Z_{E1} = Z_{E3} = 100\ \Omega$, and $f_L = f_s$ [91].60

Figure 2.26. Manufactured prototype and block diagram of the two-stage/two-branch AWLR prototype (each AWLR consist of two AWLR-modules: AWLR$_{\#1}$ and AWLR$_{\#2}$) along with the utilized SMD components [91]. 62

Figure 2.27. RF-measured S-parameters of the two-stage/ two-branch AWLR BPF prototype showcasing continuous f_{cen} tuning in the following configurations: i) AWLR$_{\#1}$ switched ON and AWLR$_{\#2}$ switched OFF; ii) AWLR$_{\#2}$ switched ON and AWLR$_{\#1}$ switched OFF. EM simulated states are also provided [91]. 62

Figure 2.28. RF-measured S-parameters of the two-stage/two-branch AWLR BPF prototype showcasing continuously tunable FBW: (a) AWLR$_{\#1}$ intrinsically switched ON

and AWLR$_{\#2}$ intrinsically switched OFF; (b) AWLR$_{\#1}$ intrinsically switched OFF and AWLR$_{\#2}$ intrinsically switched ON [91]. 63

Figure 2.29. RF-measured S-parameters of the two-stage/two-branch AWLR BPF prototype exhibiting an: (a) AS mode; (b) AP mode. EM simulated states are also provided [91]. 64

Figure 2.30. Manufactured prototype and block diagram of the three-stage/two-branch AWLR prototype (each AWLR stage consists of two AWLR-modules: AWLR$_{\#1}$ and AWLR$_{\#2}$) along with the utilized SMD components [91]. 66

Figure 2.31. RF-measured S-parameters of the three-stage/two-branch AWLR BPF prototype showcasing continuous f_{cen} tuning in the following configurations: i) AWLR$_{\#1}$ intrinsically switched ON and AWLR$_{\#2}$ intrinsically switched OFF (an EM simulated state is also provided); ii) AWLR$_{\#1}$ intrinsically switched OFF and AWLR$_{\#2}$ is intrinsically switched ON [91]. 66

Figure 2.32. RF-measured S-parameters of the three-stage/two-branch AWLR BPF prototype showcasing continuously tunable FBW: (a) AWLR$_{\#1}$ intrinsically switched ON and AWLR$_{\#2}$ intrinsically switched OFF (an EM simulated state is also included); (b) AWLR$_{\#1}$ intrinsically switched OFF and AWLR$_{\#2}$ intrinsically switched ON [91]. 67

Figure 2.33. RF-measured S-parameters of the three-stage/two-branch AWLR BPF prototype illustrating the: (a) AS mode; (b) AP mode [91]. 68

Figure 2.34. RF-measured S-parameters of the three-stage/two-branch AWLR BPF prototype showing f_{cen} tuning when AWLR$_{\#1}$ is OFF and AWLR$_{\#2}$ is ON in the following cases: (a) BW=0.58 MHz (FBW=0.48k_t^2); (b) BW=0.9 MHz (FBW=0.73k_t^2). EM simulated states are also included [91]. 69

Figure 2.35. BP-to-BS multi-resonant AWLR stage with multi-configurable and continuously-tunable TF characteristics: (a) CRD model; (b) BPF response shaped by one pole and two TZs, showcasing continuous tuning of the f_{cen} achieved by altering M_{LL}; (c) BPF response exhibiting continuous BW control by altering $M_{EE,}$ and M_{11}; (d) BS response shaped by one TZ and two RZs, demonstrating continuous tuning of the f_{cen} achieved by altering M_{EE}; (e) BS response featuring continuous BW control by altering $M_{EE,}$ $M_{11,}$and $M_{LL,}$; (f) AP mode; (g) AS mode [92]. 71

Figure 2.36. Generalized N^{th} order filters using N multi-configurable BP-to-BS AWLR stages with continuously tunable TF: (a) Generalized CRD (R_H: high-Q resonating node; R_E, R_1, and R_L: low-Q resonating nodes; white circles: source and load; grey circles: non-resonating nodes); (b) Generalized circuit block diagram using N AWLR stages and N+1 impedance inverters; (b) Illustration of the generalized BP mode TF exhibiting N poles and 2N TZs close to its passband; (c) Illustration

of the generalized BS mode TF exhibiting N TZ and 2N RZs close to the stopband [92]. 72

Figure 2.37. Proposed multi-functional AWLR stage CRD and circuit models with corresponding CM-based synthesized and circuit-simulated responses: (a) CRD and detailed circuit models; (b) BP response with one pole and two TZs obtained by setting the resonant frequencies of the low-Q resonant nodes to f_E= 0.753f_s, f_1 = 0.822f_s, and f_L = 0.904f_s; (c) BS response with one TZ and two RZs obtained by setting: f_E= 1.076f_s, f_1 = 1.705f_s, and f_L = 0.671f_s. AWR parameters: k_t^2= 0.12%, BW= 1 MHz at f_{cen}= 916.4 MHz (i.e., FBW= 0.109%), C_M= 1.895 fF, L_M= 15.92 uH, R_M= 11.3 Ohm, C_0= 2.17 pF. Low-Q resonator parameters: L_E= 20 nH, L_1= 4.2 nH, and L_L= 4 nH. The static coupling coefficients of the CRD model are N_N= 1, N_E= 23.9, N_H= 0.71, N_1= 19, N_L= 17.2, M_{NN}= 0, and M_{HH}= 0, with variable coefficients are listed in Table 2.1 [92]..... 76

Figure 2.38. CM-based synthesized and circuit-simulated responses of the multi-resonant AWLR stage shown in Figure 2.37(a) showcasing: (a) AP response obtained by setting: f_E= 1.47f_s, f_1= 0.74f_s, f_L = 1.25f_s; (b) AS response obtained by setting: f_E= 0.55f_s, f_1= 1.505f_s, f_L = 0.388f_s. The coupling coefficients are listed in Table 2.1 [92]. 77

Figure 2.39. Synthesized S-parameters of the multi-resonant AWLR stage when operating in its BP mode showcasing: (a) Continuous f_{cen} tuning by altering the self-coupling coefficient of the low-Q resonant node R_L (M_{LL}); (b) Continuous BW tuning by altering the self-coupling coefficient of the low-Q resonant nodes R_E and R_1 (M_{EE} and M_{11}) [92]. 78

Figure 2.40. Synthesized response of the multi-resonant AWLR stage when operating in its BS mode showcasing: (a) Continuous f_{cen} tuning obtained by altering the self-coupling coefficient of the low-Q resonant node R_E (M_{EE}), and by adjusting the self-coupling coefficient of the low-Q resonant nodes R_L and R_1 (M_{LL} and M_{11}) in order to maintain the BW; (b) Continuous BW tuning obtained by altering the self-coupling coefficient of the low-Q resonant nodes R_E, R_1 and R_L (M_{EE}, M_{11} and M_{LL}) [92]..... 79

Figure 2.41. CRD and synthesized S-parameter response of a two-stage AWLR-based filter: (a) CRD model; (b) BP mode showing two transmission poles and four TZs; (c) BS mode exhibiting two TZs and four RZs. The static coupling coefficients are $K_{S,1}$= 1, $K_{2,L}$= -1, $K_{1,2}$= 1.11, N_N= 1, N_E= 23.9, N_H= 0.71, N_1= 19, N_L= 17.2, M_{NN}=M_{HH}= 0 [92]. 81

Figure 2.42. Synthesized S-parameter response of the two-stage AWLR-based filter in Figure 2.41(a) showcasing: (a) AP mode; (b) AS mode [92]..... 82

Figure 2.43. Synthesized S-parameter response of the two-stage AWLR-based filter in Figure 2.41(a) when configured in BP mode showcasing: (a) a BP response with continuous f_{cen} tuning obtained by altering the self-coupling coefficient of the low-Q resonant node R_L (M_{LL}); (b) a BP response with BW tuning obtained by altering the self-coupling coefficient of the low-Q resonant nodes R_E and R_1 (M_{EE} and M_{11}) [92]. 83

Figure 2.44. Synthesized S-parameter response of the two-stage AWLR-based filter in Figure 2.41 (a) when operating in its BS mode showcasing: (a) Continuous f_{cen} tuning obtained by altering the self-coupling coefficient of the low-Q resonant node R_E (M_{EE}), and by adjusting the self-coupling coefficient of the low-Q resonant nodes R_L and R_1 (M_{LL} and M_{11}) in order to maintain the BW; (b) Continuous BW tuning obtained by altering the self-coupling coefficient of the low-Q resonant nodes R_E, R_1 and R_L (M_{EE}, M_{11} and M_{LL}) [92]. 84

Figure 2.45. Circuit block diagram and photograph of the manufactured two-stage BP-to-BS AWLR filter along with the utilized SMD components [92]..... 86

Figure 2.46. RF-measured S-parameters of the manufactured two-stage AWLR filter prototype in Figure 2.45 demonstrating its: (a) BP response exhibiting continuous f_{cen} tuning; (b) BP response exhibiting continuous BW tuning [92]..... 87

Figure 2.47. RF-measured S-parameters of the manufactured two-stage filter prototype in Figure 2.45, showcasing its BS response with tunable f_{cen} when: (a) BW= 0.96 MHz (i.e., FBW= $0.87k_t^2$), EM/circuit co-simulated states also included (b) BW= 1.42 MHz (i.e., FBW= $1.3k_t^2$) [92]..... 88

Figure 2.48. RF-measured S-parameters of the manufactured two-stage filter prototype in Figure 2.45, illustrating its BS response with tunable BW when: (a) f_{cen}=916.14 MHz; (b) f_{cen}=916.5 MHz; (c) f_{cen}=916.9 MHz; EM/circuit co-simulated states also included [92]. 89

Figure 2.49. RF-measured S-parameters of the manufactured two-stage filter prototype in Figure 2.45 showcasing: (a) AP mode; (b) AS mode. EM/circuit co-simulated results are also included [92]. 90

Figure 2.50. Circuit block diagram and photograph of the manufactured three-stage filter, along with the utilized SMD components [92]. 91

Figure 2.51. RF-measured S-parameters of the manufactured three-stage prototype in Figure 2.50 illustrating its: (a) BP response exhibiting continuous f_{cen} tuning; (b) BP response exhibiting continuous BW tuning. EM/circuit co-simulated states are also included [92]. 92

Figure 2.52. RF-measured S-parameters of the manufactured three-stage prototype in Figure 2.50 depicting its: (a) BS response exhibiting continuous f_{cen} tuning; (b) BS response exhibiting continuous BW tuning [92]. 93

Figure 2.53. RF-measured S-parameters of the manufactured three-stage prototype in Figure 2.50 depicting its: (a) AP mode; (b) AS mode [92]. 94

Figure 3.1. Multi-band quasi-elliptic AWLR-based BPFs using multi-resonant AWLR stages with reflective response characteristics: (a) Generalized circuit schematic of the reflective multi-band AWLR-based BPF comprising N in-series cascaded bandpass-type multi-resonant stages (black circles) (R_1, … ,R_N) and N-1 impedance inverters (black rectangles). Each multi-resonant stage comprises one LE inductor and K in-parallel cascaded AWRs, each with a different series resonant frequency, f_{sK},where f_{sK} is the f_{cen} of the K^{th} passband; (b) Conceptual S-parameters of the reflective multi-band AWLR-based BPF that exhibits K bands shaped by K•(N) poles and a total of N•(K+1) TZs [94]. 102

Figure 3.2. Multi-band quasi-elliptic AWLR-based BPFs using multi-resonant AWLR stages with quasi-reflectionless response characteristics: (a) Generalized circuit schematic of the quasi-reflectionless AWLR multi-band BPF. The quasi-reflectionless response is obtained by connecting two resistively-terminated bandstop-type multi-resonant AWLR stages (R_C) at the RF input/output ports of the multi-band AWLR BPF in Figure 3.1(a). Each R_C stage comprises one LE inductor (L_1) that is connected in-parallel to K AWRs. These are connected in series to a LE capacitor, C_E, and are loaded with a LE inductor, L_L; (b) Conceptual S-parameters of the quasi-reflectionless multi-band AWLR-based BPFs [94]. 103

Figure 3.3. Dual-band BPF shaped by two multi-resonant stages and that exhibits a four-pole/six-TZ TF: (a) Circuit schematic; (b) Simulated S-parameters using linear circuit simulations (Z_{ex}=86 Ω, Z_{12}=37 Ω, f_{01}=0.988f_s, f_{02}=1.0138f_s, f_{s1} is the series resonant frequency of the commercially available SAW resonator with L_{M1}=22.47 µH, C_{M1}=1.056 fF, and C_{01}=1.142 pF, f_{s2} is the series resonant frequency of the commercially available SAW resonator with L_{M2}=19.42 µH, C_{M2}=1.206 fF, and C_{02}=1.272 pF, both SAW resonators have a k_t^2=0.12%, and f_s=(f_{s1}·f_{s2})$^{1/2}$) [94]. 105

Figure 3.4. Simulated S-parameters of the two-stage dual-band BPF in Figure 3.3(a) for alternative FBWs obtained by altering the Z_{ex} and Z_{12} impedance values. In these examples, f_{01}=0.988f_s and f_{02}=1.0138f_s [94]. 105

Figure 3.5. Simulated S-parameters of the two-stage dual-band BPF showing TZs tuning. . 107

Figure 3.6. Simulated S-parameters of the two-stage dual-band BPF in Figure 3.3(a): (a) FBW enhancement by increasing the number of SAW resonators in the multi-resonant AWLR stage for each f_{sj} without needing to alter the impedance inverters; (b) Independent FBW control by increasing the SAW resonators in the multi-resonant AWLR stage that correspond to a specific f_{sj} without needing to alter the impedance inverters. In these examples, the impedance inverters are set to Z_{ex}=62.7 Ω and Z_{12}=86.25 Ω [94]. 108

Figure 3.7. Simulated S-parameters for a two-stage, triple-band, BPF by incorporating in the multi-resonant AWLR stages (R_i) three distinct AWRs with series resonant frequencies f_{s1}, f_{s2}, f_{s3} that correspond to the f_{cen}s of band 1, 2, and 3 respectively [94]. 109

Figure 3.8. Simulated power transmission ($|S_{21}|=|S_{12}|$) and reflection ($|S_{11}|=|S_{22}|$) responses of the BS-type, multi-resonant, AWLR stage illustrating FBW control by altering L_1, C_E, and L_L [94]. 110

Figure 3.9. Simulated power transmission ($|S_{21}|=|S_{12}|$) and reflection ($|S_{11}|=|S_{22}|$) responses of the: (a) BP-type multi-resonant AWLR stage and its complementary BS-type multi-resonant AWLR stage; (b) and the quasi-reflectionless dual-band stage. Simulated S-parameters using linear circuit simulations (f_{01}=0.988f_s, f_{02}=1.0138f_s, L_1=6.94 nH, C_E= 1.01 pF, L_L=26.6 nH) [94]..... 111

Figure 3.10. Two-stage, dual-band, quasi-reflectionless, AWLR-based BPF shaped by two multi-resonant AWLR stages and two resistively-terminated multi-resonant AWLR stages with complementary TF. It exhibits a four-pole/six-TZ TF: (a) Circuit schematic; (b) Simulated S-parameters using linear circuit simulations (Z_{12}=56.5 Ω, f_{01}=0.988f_s, f_{02}=1.0138f_s, f_1=1.24f_s, C_E= 1.91 pF, L_L=12.14 nH) [94]. 113

Figure 3.11. Three-stage triple-band, quasi-reflectionless BPF shaped by three multi-resonant AWLR stages and two resistively-terminated BS-type multi-resonant AWLR stages. It exhibits a nine-pole/twelve-TZ TF: (a) Circuit schematic; (b) Simulated S-parameters using linear circuit simulations (Z_{12}=50 Ω, Z_{12}=52 Ω, f_{01}=0.988f_s, f_{02}=1.0138f_s, f_1=1.24f_s, C_E= 1.91 pF, L_L=12.14 nH) [94]. 114

Figure 3.12. Second-order dual-band AWLRs BPF: (a) Filter layout; (b) Photograph of the manufactured prototype; (b) RF-measured power transmission ($|S_{21}|=|S_{12}|$) and reflection ($|S_{11}|=|S_{22}|$) response of the manufactured prototype alongside its corresponding EM-simulated response using: i) single-mode (black trace), ii) multi-mode (blue trace) SAW BVD models [94]. 116

Figure 3.13. Second-order triple-band AWLRs BPF: (a) Filter layout; (b) Photograph of the manufactured prototype; (c) RF-measured power transmission ($|S_{21}|=|S_{12}|$) and

reflection ($|S_{11}|=|S_{22}|$) response of the manufactured prototype alongside its corresponding EM-simulated response [94]. 117

Figure 3.14. Symmetric, quasi-reflectionless, second-order, dual-band AWLR BPF: (a) Filter layout; (b) Photograph of the manufactured prototype; (c) RF-measured power transmission and reflection response [94]. 119

Figure 4.1. RF-switchless two-BPF manifold using a high-pass/low-pass diplexer junction: (a) Block diagram; (b) Conceptual power transmission response exhibiting a tune-all TF with: i) a single-band mode featuring ultra-wide and continuous f_{cen} and BW tuning (either $BPF_{\#1}$ and $BPF_{\#2}$ is ON); ii) a dual-band mode with independently-tuned bands in terms of f_{cen} and BW (both $BPF_{\#1}$ and $BPF_{\#2}$ are ON), and iii) an AS mode (both $BPF_{\#1}$ and $BPF_{\#2}$ are intrinsically-switched OFF) [96]..... 123

Figure 4.2. Low-pass/high-pass diplexer in back-to-back configuration: (a) Case 1: LPFs: directly connected (via short thru line), HPFs: open. (b) Case 2: HPFs: directly connected, LPFs: open; (c) Circuit simulations: LPF: L_1=3.04 nH, C_2=1.44 pF, L_3=1.79 nH, HPF: C_4=0.52 pF, L_5=1.1 nH, C_6=0.88 pF [96]. 124

Figure 4.3. (a) Five-pole/two-TZ BPF comprising four varactor-loaded coupled resonators and one multi-resonant cell; (b) CRD; (c) f_{cen} tuning, circuit-simulated response in black with f_{cen}= 3 GHz, FBW= 44% obtained for Z_{oe}= 180 Ω, Z_{oo}= Z_{oe}/2 Ω, θ_0= 62°, Z_1= 117 Ω, θ_1= 87.8°, C_{z1}= 0.2 pF, Z_2= 123 Ω, θ_2= 41.6°, C_{P1}=C_{P2}=C_{Z1}=C_{Z2}= 0.2 pF; (d) BW tuning [96]. 127

Figure 4.4. DC block effect on: (a) Q_{total}. (b) $C_{varactor}$ and C_{total}. 129

Figure 4.5. Experimental evaluation of the effect of the DC block on the unloaded Q-factor (Q_U) and TR of the varactor-loaded resonator: (a) Photograph of the manufactured resonator. The utilized SMDs and resonator's characteristics are as follows: Varactor: MACOM MAVR-000120-14110G; DC blocks: GJM0335 and GRM0335 Murata series; Resonator characteristic: impedance Z=109 Ω, electrical length: 55°at 4 GHz, substrate: RO5880 with a height of 1.575 mm; (b) Relationship between applied DC voltage and extracted Q_U; (c) Relationship between applied DC voltage and f_{cen} TR [96]. 130

Figure 4.6. Measured and EM simulated back-to-back diplexers: (a) Case 1: LPFs: connected and HPFs: open; (b) Case 2: LPFs: open and HPFs: connected. (c) RF measured response for Case 1 and Case 2 [96]. 132

Figure 4.7. Manufactured prototype of the switchless two-BPF manifold and its RF-measured S-parameters: (a) Prototype; (b) $BPF_{\#1}$ ON exhibiting continuous f_{cen} tuning and $BPF_{\#2}$ intrinsically-switched OFF; (c) $BPF_{\#2}$ ON exhibiting continuous f_{cen} tuning with $BPF_{\#1}$ intrinsically-switched OFF [96]. 134

Figure 4.8. RF performance summary of the measured f_{cen} tuning states presented in Figure 4.7 in terms of BW and minimum IL (min-IL): (a) $BPF_{\#1}$ f_{cen} tuning performance when $BPF_{\#2}$ is switched OFF (Figure 4.7(a)); (b) $BPF_{\#2}$ f_{cen} tuning performance when $BPF_{\#1}$ is switched OFF (Figure 4.7(b)) [96]. 135

Figure 4.9. RF-measured S-parameters: (a) Continuous BW tuning of $BPF_{\#1}$ at f_{cen}= 2.2 and 3 GHz, when $BPF_{\#2}$ is OFF; (b) Continuous BW tuning of $BPF_{\#2}$ at f_{cen}= 4.9 and 6.2 GHz, when $BPF_{\#1}$ is OFF [96]. 136

Figure 4.10. RF-measured S-parameters: (c) Dual-band responses when $BPF_{\#1}$ and $BPF_{\#2}$ are ON; (d) AS response: $BPF_{\#1}$ and $BPF_{\#2}$ are OFF [96]. 137

Figure 4.11. RF-measured IIP3 for various tuning states [96]. 138

Figure 4.12. RF-measured S-parameters showing the: i) the maximum f_{cen} of $BPF_{\#1}$ when $BPF_{\#2}$ is OFF and ii) the minimum f_{cen} of $BPF_{\#2}$ when $BPF_{\#1}$ is OFF [96]. 138

Figure 5.1. Schematic and layout of the hybrid BPF design integrating IPD, acoustic, and substrate technologies [120]. 146

List of Tables

Table 1.1. State-of-the-art reconfigurable AWR-based filters. 19
Table 2.1. Normalized coupling coefficients of the synthesized examples in Figure 2.37, Figure 2.38, Figure 2.41, and Figure 2.42, and associated with the CRDs in Figure 2.37, and Figure 2.41. 73
Table 2.2. Normalized coupling coefficients of the synthesized examples in Figure 2.39, and Figure 2.43, and related to continuous f_{cen} and BW tuning in the BP mode. 73
Table 2.3. Normalized coupling coefficients of the synthesized examples in Figure 2.39, and Figure 2.44, and related to continuous f_{cen} and BW tuning in the BS mode. 73
Table 2.4. Performance summary of the measured two-, and three-stage prototypes..... 95
Table 2.5. Comparison with state-of-the-art reconfigurable AWR-based filters. 98
Table 3.1. Comparison with state-of-the-art AWR-based multi-band BPFs..... 120
Table 4.1. Performance summary for various tuning states when either $BPF_{\#1}$ or $BPF_{\#2}$ is ON, based on the measured data in Figure 4.7(a), (b). 137
Table 4.2. Comparison with state-of-the-art tunable manifolds. 139

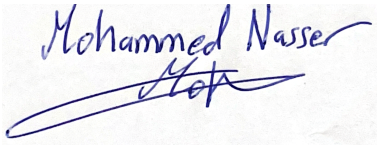
Glossary of Terms

5G	Fifth-generation
6G	Sixth-generation
ADS	Advanced Design System
AP	All-pass
AS	All-stop
AWLR	Acoustic-wave lumped-element resonator e
AWR	Acoustic-wave-resonator
BAW	Bulk acoustic wave
BP	Bandpass
BPF	Bandpass filter
BS	Bandstop
BSF	Bandstop filter
AlN	Aluminum nitride
BW	3-dB Bandwidth
BVD	Butterworth-Van Dyke
CMR	contour-mode resonators
CR	Cognitive radios
EM	electromagnetic
FBAR	Thin-film bulk acoustic resonator
FBW	Fractional bandwidth
f_{cen}	centre frequency
FoM	Figure of Merit
FR1	Frequency range 1

FR2	Frequency range 2
GaAs	Gallium arsenide
HFSS	High-frequency structure simulator
HPF	High-pass filter
IL	Insertion loss
IS	Isolation
IPD	Integrated passive devices
k_t^2	The electromechanical coupling coefficient of AWR
LE	Lumped-element
LPF	Low-pass filter
LTCC	Low-temperature co-fired ceramics
MEMS	Micro-electromechanical systems
MMIC	Monolithic microwave integrated circuits
Q	Quality factor
Q_{eff}	Effective quality factor
Q_{Total}	Total quality factor
RF	Radio frequency
SAW	Surface acoustic wave
ScAIN	Scandium aluminum nitride
SDRs	Software-defined radios
SH	Shear-horizontal
SOI	Silicon-on-insulator
TF	Transfer function
TR	Tuning range
TZ	Transmission zero
VO_2	Vanadium dioxide
Wi-Fi	Wireless Fidelity

Declaration

This is to certify that the work I am submitting is my own and has not been submitted for another degree, either at University College Cork or elsewhere. All external references and sources are clearly acknowledged and identified within the contents. I have read and understood the regulations of University College Cork concerning plagiarism and intellectual property.

Signed:  Date: June 26th, 2025

Acknowledgements

First and foremost, I would like to express my deepest appreciation to my supervisors, Prof. Dimitra Psychogiou and Dr. Kevin G. McCarthy, for their exceptional guidance, mentorship, and encouragement throughout this research journey. Their expertise and insights were invaluable in shaping the direction and quality of my work.

I am profoundly grateful to University College Cork and Tyndall National Institute for providing the resources and supportive environment that made this research possible. To my peers and fellow researchers, thank you for sharing this journey with me and for making the challenging moments bearable.

This work is dedicated to honouring the memory of my beloved father, Riad, whose wisdom and love continue to inspire me every day. It is also dedicated to the cherished memories of my beloved brother Mehyar and nephew Baraa, my uncle Sameh, my aunties Karima, Na'imaa and Radwa's, and their families, who we tragically lost in the war. Their lives were a testament to resilience and love, and their memories have been a source of strength and purpose throughout this journey.

To my family, thank you for your unwavering love, prayers, and belief in me. To my mother, Itaf, your strength and support have been the foundation of all my achievements. To my siblings, thank you for standing by me and encouraging me.

Finally, I would like to acknowledge the financial support provided by Research Ireland, which has been the primary source of funding for this work. Additional support was also received from Indiana Microelectronics, without which this research would not have been possible.

Abstract

The rapid growth of wireless networks, for example, the fifth and sixth generation (5G/6G) of wireless is increasingly calling for highly-versatile radio frequency (RF) front-ends capable of sensing the electromagnetic spectrum and dynamically adapting to changing spectral conditions and user needs. To facilitate their deployment, ultra compact and highly-reconfigurable RF filters need to be incorporated in their RF transceivers to facilitate detection of low-power RF signals amid high-power, dynamically-allocated interferers and adaptive band selection. Acoustic-wave-resonator (AWR)-based filtering technologies have been the main filtering technology for mobile RF transceivers due to their ultracompact size and their inherent high unloaded quality factor (Q) ≈ 2,000-10,000. However, they are limited by static transfer functions (TFs) and very narrow fractional bandwidths (FBWs) <0.5% that are approximately equal to 0.4–0.8k_t^2 (k_t^2 is the electromechanical coupling coefficient). Microwave planar-based RF filters such as those based on microstrip, stripline and coplanar waveguide (CPW) resonator technologies exhibit wider FBWs (2-10%) and can tune their TFs in terms of frequency, bandwidth (BW), and number of bands. However, they suffer from low Q (≈50-100) and despite being tunable their tuning range is limited to 1.5:1 and to frequencies up to L-band.

This thesis is centered around new design techniques, tuning concepts and integration approaches for continuously-tunable RF filters using AWRs and highly-miniaturized planar microwave resonators. Specifically, it introduces new classes of: i) quasi-elliptic acoustic-wave lumped-element resonator (AWLR)-based RF filters with continuously tunable frequency and BW, and multi-configurable tunable modes of operation (i.e., adapted between multiple bandpass, bandstop, all-pass and all-stop operational modes) while having enhanced FBWs (i.e.,>0.4–0.8k_t^2) as needed for effective spectrum management in multi-standard communications; ii) reflective and quasi-reflectionless multi-band AWR-based bandpass filters (BPFs) to facilitate multi-band operability and minimize RF signal reflections, improving the signal-to-noise ratio (SNR), and iii) widely-tunable tune-all planar-based BPFs with ultra-wide centre frequency (f_{cen}) and BW tunability of almost two octaves within the most crowded part of the Frequency Range 1 (FR1) spectrum using a new-type of a switchless manifold two-filter approach.

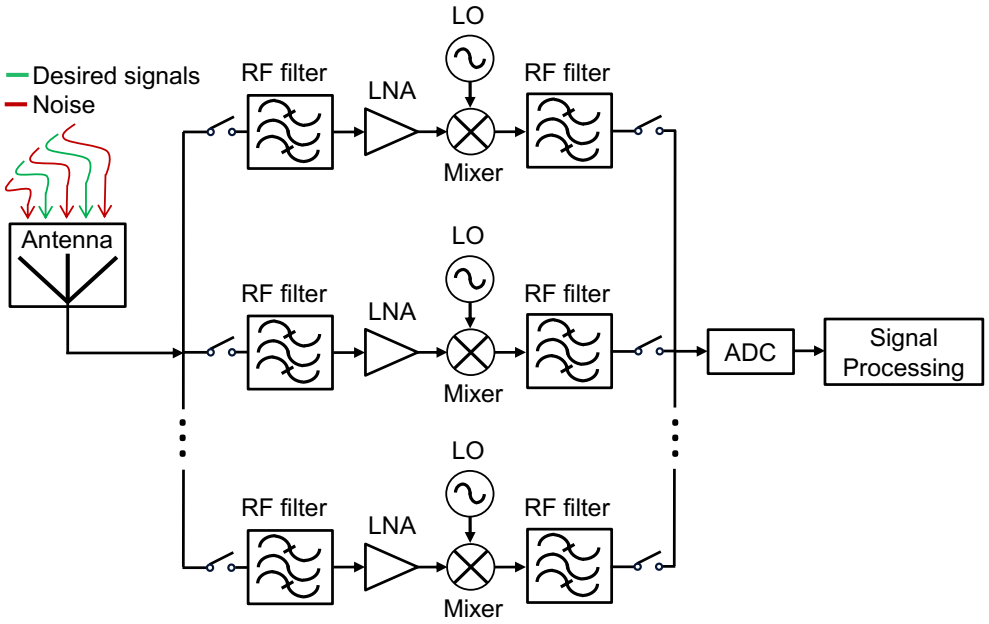
Chapter 1: Introduction

1.1 Motivation and Background

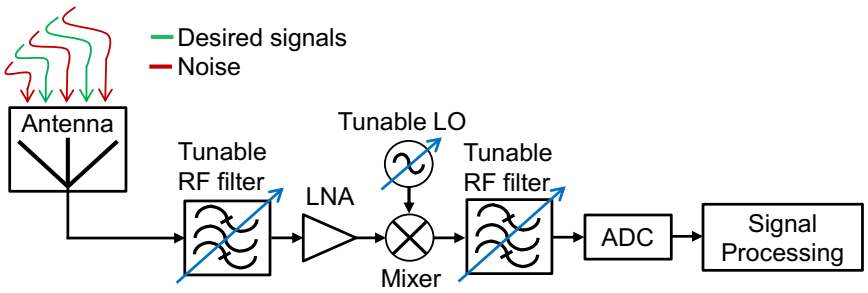
Modern wireless communication systems need to support a large number of services and standards, posing significant challenges in the implementation of radio frequency (RF) hardware and contributing to the scarcity of available frequency bands within the electromagnetic (EM) spectrum [1]. Current smartphones need to support multiple communication standards—ranging from 2G to 5G—while simultaneously supporting other applications such as Wireless Fidelity (Wi-Fi), Bluetooth, and geo-localization. The number of RF filters required in their RF front-ends is directly proportional to the number of services and applications that they need to support with current 5G smartphones, relying on about 100 off-chip RF-switched filter banks, making their integration with other chip-based RF components very challenging [2]. This complexity will further increase in 6G as devices must support more bands, wider bandwidths, and new functions such as integrated sensing, making current RF front-end architectures untenable and requiring highly reconfigurable, compact, and more efficiently integrated off-chip RF components.

The increasing complexity of RF systems, combined with the limited availability of the RF spectrum, is driving the need for spectrum-efficient communications that optimise the utilisation of frequency bands while reducing hardware complexity. Technologies such as software-defined radios (SDRs) and cognitive radios (CRs) have emerged as promising solutions for enhancing spectrum utilisation [3], [4], [5], [6], [7], [8]. SDRs integrate high-frequency RF hardware with low-frequency programmable digital software, enabling dynamic access to the RF spectrum through the adjustment of frequency, bandwidth (BW), and modulation schemes. By down-converting signals to frequencies that can be processed by digital circuits, SDRs can effectively improve RF spectrum utilization and simultaneously reduce system complexity, size, and cost [9]. Moreover, this approach contributes to sustainability by mitigating the environmental impacts associated with frequent hardware replacements, which are often driven by the need to adopt new hardware that meets updated standards and specifications [10]. However, the demand of modern wireless applications requires SDRs capable of receiving high-frequency signals across diverse modulation schemes and frequency bands. As digital circuitry alone is

insufficient to manage all necessary RF functions, there is a growing need for advanced, frequency-agile analog RF components that can perform signal conditioning at microwave and millimetre-wave frequencies. A key challenge in current RF front-end design is the reliance on static, application-specific components–particularly RF filters–which are not easily reconfigurable across different standards or frequency bands. Traditional approaches that require adding discrete filters for each new service results in increased system complexity, size, cost, and the rate of hardware replacement—negatively impacting both scalability and sustainability [9], [10].



(a)



(b)

Figure 1.1. Block diagram of: (a) conventional multi-band RF front-end receiver comprising multiple RF switched filter banks; (b) a highly-miniaturized RF front-end comprising of tunable RF components.

To address these challenges, the development of versatile and agile RF front-ends capable of operating across multiple bands and standards is crucial for future

communication systems, as illustrated in Figure 1.1. Ideally, conventional RF-switched front-end architectures would be replaced by a single, frequency-agile receiver chain; however, in practice, modern devices typically require multiple reconfigurable chains to support simultaneous operation across different services and MIMO modes. Even so, replacing large banks of fixed filters and dedicated receive paths with a small number of tunable, wide-coverage chains significantly facilitates real-time adaptation to the RF environment, ensuring optimal performance as users transition between frequency bands while simultaneously reducing the size and complexity of RF transceivers. The deployment of such systems necessitates the integration of ultra-compact, highly reconfigurable RF filters into the transceivers to facilitate the detection of low-power signals amid high-power, dynamically allocated interferers, thereby enabling adaptive band selection [11], [12], [13].

Presently, acoustic-wave-resonators (AWRs), such as surface acoustic wave (SAW) and bulk acoustic wave (BAW) resonators, are favoured for mobile RF transceivers due to their exceptional Qs (Q approximating 2,000-10,000), compact dimensions (measured in millimetres), and low cost (<$0.50 per unit) [14], [15], [16]. However, they are constrained by static TF characteristics and a narrow fractional bandwidth (FBW) < 0.5%, approximately equal to 0.4-0.8k_t^2 (where k_t^2 is the electromechanical coupling coefficient). In contrast, microwave planar-based RF filters, such as those based on microstrip, stripline, and coplanar waveguide (CPW) resonator technologies, exhibit wider FBWs (2-10%) and tunable TFs in terms of frequency, BW, and number of bands. Nevertheless, these filters suffer from lower Q (approximately 50-100), resulting in in-band high insertion loss (IL) (typically 3-9 dB), and despite being tunable, their tuning range (TR) is limited to 1.5:1 [17], [18], [19], and [20].

This thesis focuses on innovative design techniques, tuning concepts, and integration strategies for continuously tunable RF filters using AWRs and highly miniaturized planar microwave resonators. Specifically, it presents: i) new classes of quasi-elliptic acoustic-wave lumped-element resonator (AWLR)-based RF filters with continuously tunable centre frequency (f_{cen}) and BW, as well as multi-configurable transfer functions (TFs) (e.g., bandpass, bandstop, all-pass, and all-stop modes), while offering enhanced FBWs that are greater than 0.4k_t^2 to 0.8k_t^2 for effective spectrum management in multi-standard communication systems; ii) reflective and quasi-

reflectionless multi-band AWR-based bandpass filters (BPFs) that support multi-band operation, minimize RF signal reflections, and improve signal-to-noise ratio (SNR), while achieving miniaturization by consolidating multiple frequency bands into a single component, thereby reducing the need for discrete filters and saving PCB space; iii) widely tunable planar-based BPF manifolds featuring ultra-wide tunability—spanning nearly two octaves within the most congested portion of the Frequency Range 1 (FR1) spectrum—using a novel switchless two-filter approach, enabling real-time channel detection, interference mitigation, and dynamic RF spectrum management for enhanced spectral efficiency.

The following sections provide a comprehensive overview of state-of-the-art filtering concepts relevant to this thesis. The discussion is organized into the following key areas: i) AWR-based filters, including multi-functional implementations such as multi-reconfigurable and multi-band AWR-based filters with reflectionless characteristics; and ii) widely tunable planar adaptive BPFs.

1.2 Acoustic Wave Resonator (AWR)-Based RF Filters

Acoustic wave devices have been the primary choice for filtering for the RF front ends of modern mobile transceivers. This preference stems from their exceptionally high *Q*-factors, compact size, and low cost. The two main subgroups of filters that have found their way into high volume production are based on SAW and BAW technologies [15][16].

SAW filtering technologies have been widely adopted since the advent of mobile phones. A typical structure of a SAW resonator is illustrated in Figure 1.2. It is based on interdigital transducers (IDTs), which are periodic arrays of metal fingers deposited on a piezoelectric substrate. Conventional piezoelectric substrates include quartz, lithium tantalate ($LiTaO_3$), or lithium niobate ($LiNbO_3$). An RF signal initiates an acoustic wave that travels horizontally across the substrate, perpendicular to the IDT fingers. SAW resonators consist of input/output IDT electrodes and gratings that reflect acoustic waves from both sides, thereby minimising energy loss and enhancing the *Q*-factor. The IDT finger width and spacing are typically equal to a quarter wavelength ($\lambda/4$), resulting in an interdigital electrode and grating period of half a wavelength ($\lambda/2$). SAW resonators are extensively used in 4G, Wi-Fi, and bluetooth

front-ends, duplexers, and receiver filters at frequencies typically below 2.5 GHz. They exhibit low IL, excellent out-of-band rejection, and a broad BW while having a very small footprint.

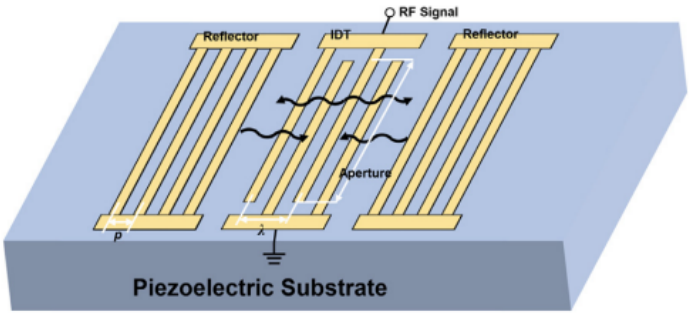


Figure 1.2. Typical structure of a one-port SAW resonator [21].

SAW technology's low fabrication cost is attributed to wafer-level processing, which involves a single deposition and patterning of IDT metal electrodes. This approach enables the production of filters for diverse frequency bands on a single wafer or chip. The precise adjustment of the spacing between the IDT fingers allows for the tuning of the frequency, making SAW technology highly adaptable to various applications. However, SAW resonators face limitations at higher frequencies, including a reduction in *Q*-factor and the shrinkage of electrode dimensions to the sub-micron scale, which increases manufacturing complexity. Additionally, as the IDT finger width and spacing approach sub-micron levels, SAW devices become more susceptible to temperature variations, electrostatic discharge, and reduced power handling capability.

BAW filtering technologies address many of the limitations of SAW including operation at frequencies higher than 2 GHz. In a BAW device, the acoustic wave propagates perpendicular to the substrate. As illustrated in Figure 1.3, a thin film piezoelectric layer is deposited between the top and bottom metal electrodes. The thickness extension (TE) resonance frequency, the primary acoustic mode for BAW devices, is determined by the thickness of the piezoelectric layer (which is equivalent to $\lambda/2$) and the mass of the electrodes.

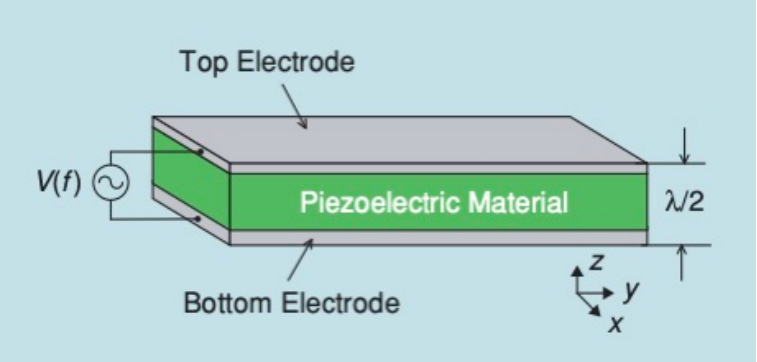


Figure 1.3. BAW resonator structure [22].

Unlike SAW devices, BAW devices confine mechanical energy between the electrodes, resulting in superior performance in the GHz frequency range. Power handling in BAW devices is defined by the maximum temperature that the material comprising the resonator can withstand, enabling it to handle higher power compared to SAW technology. The most significant advantage of BAW technology is the ability to achieve frequencies up to 6 GHz without substantial manufacturing challenges. However, BAW technology faces certain limitations. It incurs higher manufacturing costs compared to SAW technology due to the complex manufacturing process and additional processing steps required for depositing and patterning the piezoelectric layers. Additionally, BAW technologies encounter difficulties in accommodating resonators and filters with distinct frequency bands on a single wafer, as the resonance frequency is predominantly determined by the uniform thickness of the deposited piezoelectric layer across the wafer.

Despite the advantages of SAW and BAW filter technologies, their response is often constrained by static TF characteristics and relatively narrow FBWs, typically within the range of 0.4–0.8k_t^2 as shown in Figure 1.4 [23]. Furthermore, most of the SAW/BAW implementations are restricted to bandpass type TFs. Recent research efforts are exploring methods to overcome these limitations. One approach entails the utilisation of scandium-doped aluminium nitride (AlScN), which can augment k_t^2 to nearly 25%, thereby facilitating wider BWs. Another promising approach exploits shear-horizontal (SH) modes on lithium niobate substrates to achieve broader FBWs [26], [24], [27], [28], as demonstrated in Figure 1.5. However, these improvements frequently entail trade-offs, such as diminished Q-factors (ranging from 173 to 500), in-band amplitude fluctuations (such as ripples and spurs), as shown in Figure 1.5, and

compromised temperature stability [28], [29], [30], and [31]. Furthermore, hybrid implementations that co-integrate AWRs with microstrip transmission lines, lumped-element (LE) inductors/capacitors, or other transmission-line-based elements have demonstrated wider passbands (with FBWs > 0.4–0.8k_t^2), as illustrated in Figure 1.6. However, their in-band IL is significantly influenced by the relatively low to moderate Q-factors of the microwave elements, typically ranging from 50 to 200. Additionally, their physical dimensions are constrained by the inherently large dimensions of the microstrip elements, and they exhibit only static response [25], [32], [33], [34], [35], [36].

In conclusion, while AWR technologies—encompassing both SAW and BAW resonators, as well as their emerging variants—continue to deliver excellent performance for fixed-band RF filters, current implementations offer limited potential for meeting the goals of this research. Although recent advances have demonstrated wider FBWs through material engineering, modal optimisation, or hybrid integration, these enhancements are typically accompanied by significant trade-offs in Q-factor, IL, temperature stability, and spurious-free dynamic behaviour. Moreover, the TF characteristics of existing AWR-based filters remain fundamentally static, preventing real-time adaptability. Consequently, despite their maturity and widespread commercial adoption, state-of-the-art AWR solutions do not yet provide the reconfigurability, or spectral agility required for next-generation agile RF front-ends.

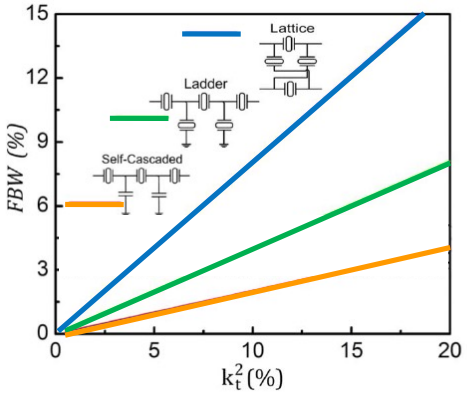


Figure 1.4. Relationship between electromechanical coupling and filter FBW for three types of filter configurations [23].

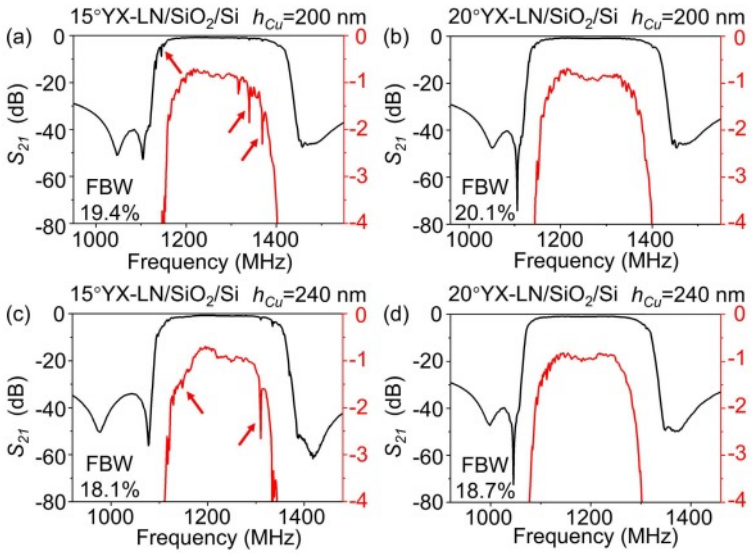
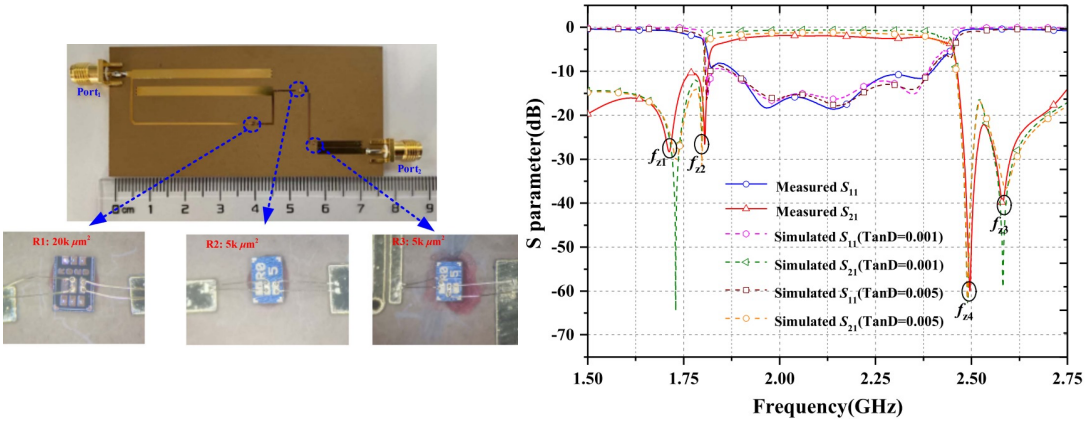


Figure 1.5. Measured transmission characteristics (S_{21}) of SAW bandpass filters exhibiting spurs and amplitude fluctuations, based on devices with the following characteristics: a) 15°YX-LN/SiO_2/Si with h_{Cu} = 200 nm; b) 20°YX-LN/SiO_2/Si with h_{Cu} = 200 nm; c) 15°YX-LN/SiO_2/Si with h_{Cu} = 240 nm, and; d) 20°YX-LN/SiO_2/Si with h_{Cu} = 240 nm [24].



(a) (b)

Figure 1.6. Wideband BPF based on a hybrid film-bulk acoustic resonator, coupled-line, and transmission-line structure: (a) Photograph of the manufactured BPF; (b) Simulated and measured S-parameters [25].

1.3 Multi-Functional AWR-Based Filters

Conventional acoustic filters are limited by their static frequency and BW characteristics. These limitations become more pronounced with the growing adoption of carrier aggregation—where multiple frequency bands must be used simultaneously to achieve higher data rates—and the continuous introduction of new operating bands across modern wireless standards. A potential solution to these challenges is the use of multi-configurable acoustic filters. Their flexibility allows them to operate across multiple frequency bands and are particularly valuable in crowded RF spectral environments, where interference can severely degrade the desired signal quality. As illustrated in Figure 1.1(b), a reconfigurable RF front-end receiver can dynamically respond to changing signal conditions. The reconfigurable filter plays a critical role by adapting its frequency response to pass the desired signal while suppressing interference. A conceptual illustration of a reconfigurable BPF response is demonstrated in Figure 1.7. Specifically, Fig. 1.7(a) shows a BPF response that covers a wide frequency band and suppresses distant interfering signals, Fig. 1.7(b) illustrates f_{cen} tuning to avoid nearby interference, and Fig. 1.7(c) depicts BW narrowing to mitigate interference on both sides of the desired signal, preserving signal integrity.

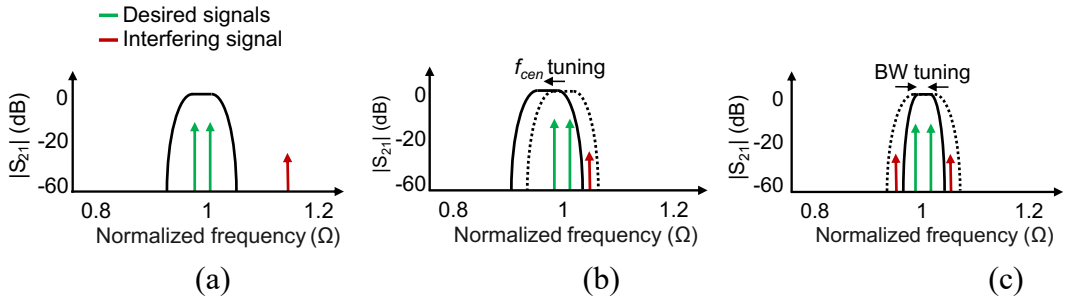
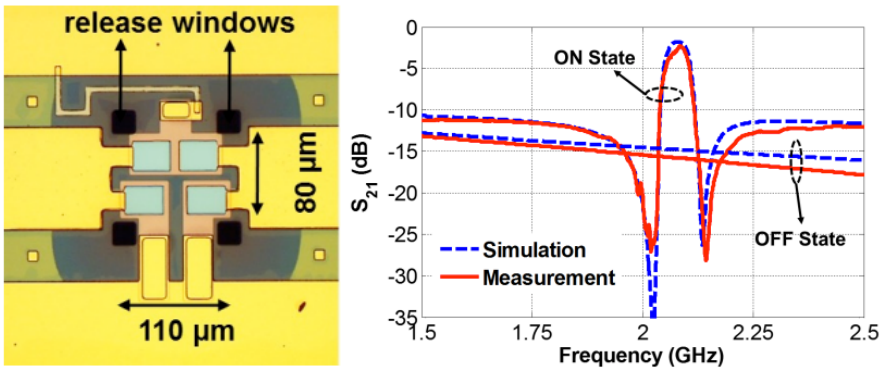


Figure 1.7. Conceptual illustration of a reconfigurable BPF with continuously tunable characteristics: (a) Bandpass response with an interfering signal distant from the passband; (b) Tuning the f_{cen} to avoid interference emerging on the right side of the passband; (c) Narrowing the BW to mitigate interference appearing on both sides of the passband.

1.3.1 Reconfigurable AWR-based filters

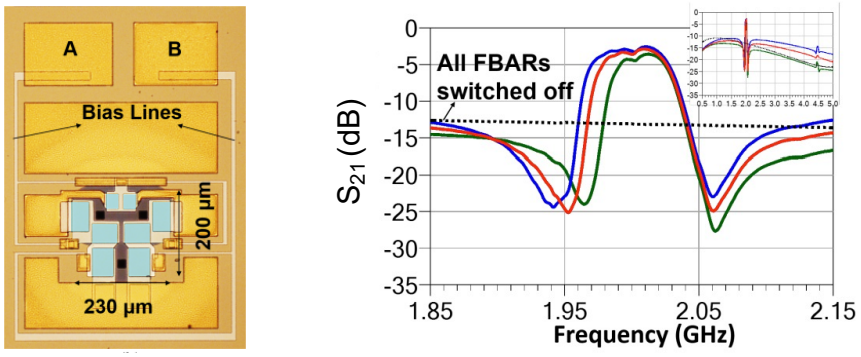
Recent studies have explored the development of reconfigurable AWR-based filters. For example, several research efforts have focused on intrinsically switched

ferroelectric thin-film bulk acoustic resonators (FBARs) [37],[34], [39], [40], [38], and [41]. The reconfigurable filter examples discussed in [37], and [42] are based on ferroelectric barium strontium titanate (BST) FBARs, which intrinsically switch their response, as illustrated in Figure 1.8. In another example, presented in [34], the BPF supports BW reconfiguration with three different FBW states of 3%, 2.5%, and 2%, as shown in Figure 1.9, and also enables an OFF state with 13 dB isolation (IS). Additionally, [38] presents a triple-band switchable filter bank operating at 1.85, 1.96, and 2.04 GHz, with IL around 10 dB and OFF-state IS exceeding 27 dB, as depicted in Figure 1.10. This design cascades three RF switched bandpass filters. In these approaches, reconfiguration is achieved by varying the direct current (DC) bias applied to the ferroelectric substrate within the FBARs, enabling resonance control. However, these filters typically suffer from high IL (up to 10 dB) and rely on a relatively complex fabrication process, as they require multiple resonators operating at different frequencies. Furthermore, they require high DC biasing voltages (70-125 V) and are only suitable for discrete tuning.



(a) (b)

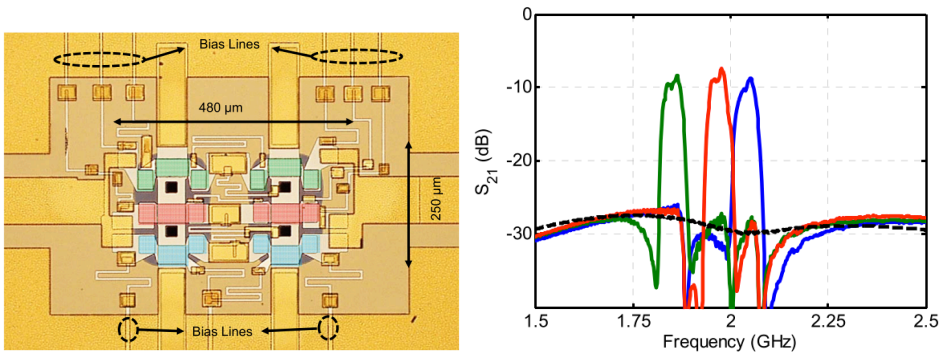
Figure 1.8. Photograph of the 1.5 stage BST FBAR filters. (a) Transmission responses for the measured and simulated 1.5 stage BST FBAR filter in its ON and OFF states [37].



(a) (b)

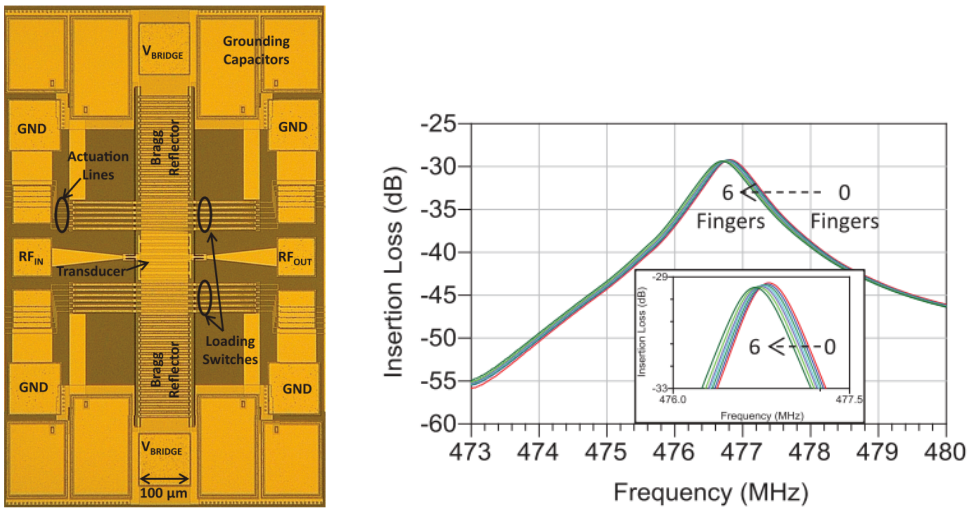
Figure 1.9. BW-switchable ferroelectric BAW filters: (a) Photograph of the manufactured BST FBAR filter with three BW states; (b) RF measured transmission response [34].

Aluminum nitride (AlN) contour-mode resonators (CMRs) have emerged as promising components for reconfigurable acoustic filters [39], [43]. These devices integrate micro-electromechanical systems (MEMS) switching technology to modulate the coupling between electrodes and the piezoelectric material, enabling switchable and tunable resonator responses. As illustrated in Figure 1.11, the resonator exhibits a f_{cen} of 476.815 MHz. By mass-loading the resonator through actuating the fingers, the f_{cen} shifts to 476.688 MHz, demonstrating discrete tuning of the resonator's operational frequency. This approach enables discrete tuning of the resonator's operational frequency and suffers from high IL~30 dB and limited TR. Furthermore, [43] demonstrates the use of intrinsically-switchable AlGaN/GaN resonators to achieve f_{cen} tuning. Nevertheless, these resonators have a very high IL of about 60 dB.



(a) (b)

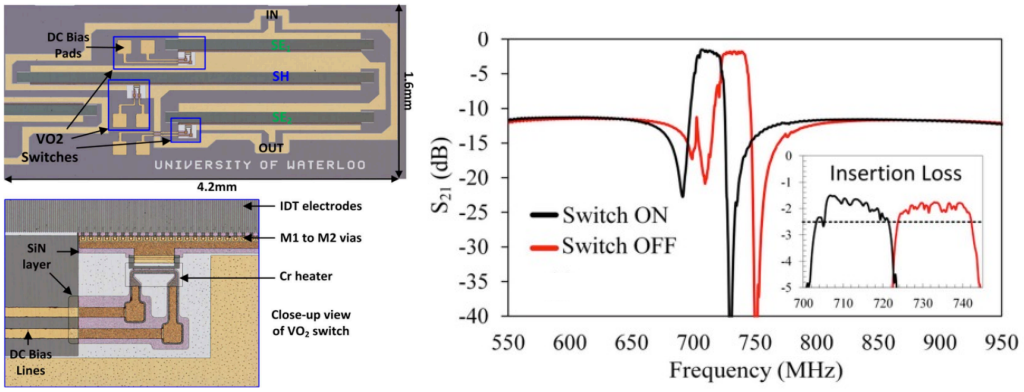
Figure 1.10. BST FBAR filter bank: (a) Photograph of a fabricated multiband 2.5-stage BST FBAR filter bank; (b) Transmission responses of the measured 2.5-stage triple-band filter bank when the filters are turned ON individually [38].



(a) (b)

Figure 1.11. Contour-mode resonators: (a) Optical photograph of the fabricated resonator; (b) Measured response demonstrating fine-tuning of the resonator through mass loading by actuating between 0 and 6 fingers on each side of the transducer [39].

Another research approch has focused on developing reconfigurable SAW resonators and tunable filters using vanadium dioxide (VO_2) switches. Specifically, the concept in [44] demonstrates a SAW resonator with monolithically integrated VO_2 switches, achieving frequency tuning from 700 to 720 MHz while maintaining a Q above 350, as depicted in Figure 1.12. This concept only allows for two discrete f_{cen} tuning. In [45], the VO_2 switches are used to develop switchable dual-band SAW filters through both hybrid and monolithic integration, resulting in a filter bank capable of switching its passbands ON and OFF, enabling single-band, dual-band, or OFF-state responses, as illustrated in Figure 1.13. In [46], the phase-change behaviour of VO_2—transitioning between insulating and conductive states—is exploited to dynamically reconfigure the SAW filter BW. This approach enables varying the k_t^2, which allows the reconfiguration across different BW states, as illustrated by the two-state BW reconfigurable filter in Figure 1.14, where the FBW changed from 4.0% to 4.5%. Nevertheless, the presented reconfigurable SAW resonator-based BPFs using VO_2 switches support only discrete reconfigurability and they are limited by narrow FBW between 0.4- $0.8k_t^2$ as in every conventional AWR-based BPF and suffer in-band response fluctuations. Moreover, implementation requires complex manufacturing techniques.



(a) (b)

Figure 1.12. f_{cen} switchable three-pole SAW filter using VO_2 switches: (a) Photograph of the fabricated tunable three-pole filter with a close-up view of the monolithically integrated VO_2 switches; (b) Measured transmission response [44].

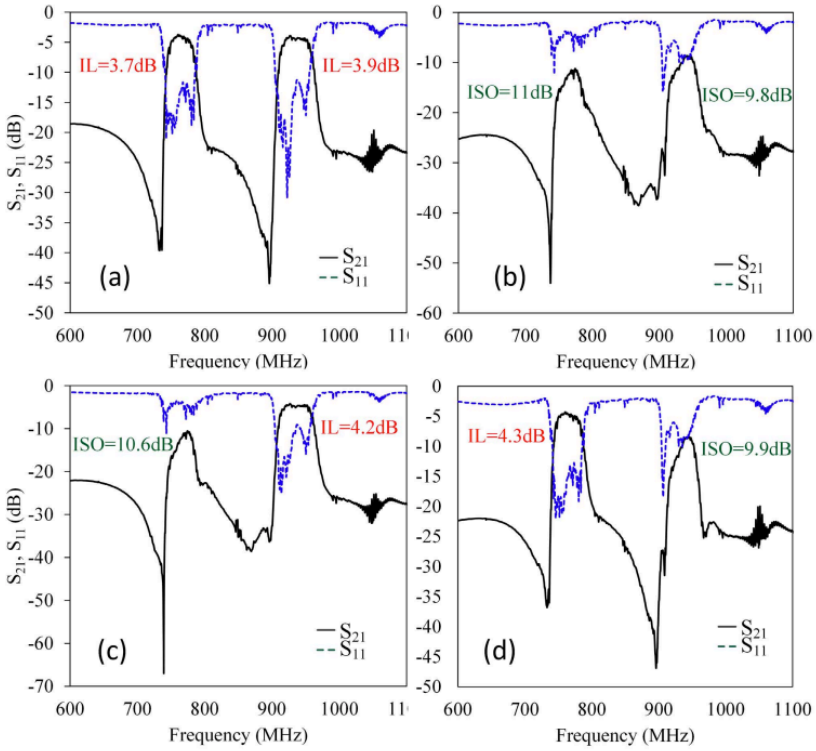
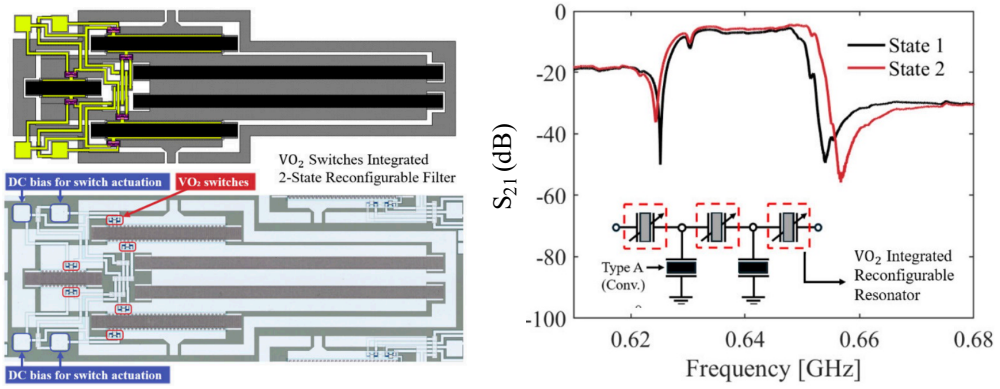


Figure 1.13. Measured S-parameter response of the five-pole switched dual-band filter when: (a) both channels are on; (b) both channels are off; (c) only high channel is on; and (d) only low channel is on [45].



(a) (b)

Figure 1.14. Two-state PCM-based BW-reconfigurable acoustic-wave filter: (a) Manufactured filter prototype; (b) Measured response of the filter integrated with VO_2 switches [46].

In an alternative approach, AWRs are integrated with LEs in hybrid AWLR-based filter configurations. These configurations offer high-Q passbands and enhanced functionality in terms of response reconfigurability, overcoming the limitations of conventional acoustic wave filters. AWLR-based filters enable the realisation of BPFs with FBWs larger than the 0.4-0.8k_t^2 limit of conventional AWR-based BPFs. Furthermore, they utilise AWRs with identical characteristics. Notably, this approach also facilitates the realisation of bandstop responses, which are generally not feasible in traditional AWR-based filters. Representative examples have been demonstrated, including: i) BPFs with continuously tunable BW and out-of-band IS, as demonstrated in [52]. This concept has been extended to support dual-band responses with tunable BW [47], as illustrated in Figure 1.15. The presented filter example achieves tunable BWs between 0.16 and 0.49 MHz (0.5-1.5k_t^2) representing an FBW enhancement of 1.8–3.8× over conventional AWR-based designs, with IL ranging from 3.3 to 1.2 dB and Qs exceeding 3,500. ii) BSFs with continuously tunable BW, as demonstrated in Figure 1.16, [48] The prototype achieves a tunable FBW range of 0.55–2.2k_t^2 with stopband attenuation between 25 and 40 dB and Q-factors above 8,000. This concept was further developed in [11] to support enhanced functionality, where a dual-band BSF with tunable BW and an all-pass (AP) response was demonstrated. As shown in Figure 1.17, the demonstrated prototype exhibits two stopbands centred at 418 MHz and 434 MHz with tunable FBWs between 0.6 and 1.9k_t^2, as well as an AP state. iii) RF filters with reconfigurable TFs. For instance, the reconfiguration of the bandpass-

to-sandstop (BP-to-BS) filter response is presented in [49] and illustrated in Figure 1.18, where RF switches reconfigure the response between dual-band bandpass (BP) and bandstop (BS) modes (418 MHz and 434 MHz, with FBW > k_t^2). Additional configurations include BS-to-AP [11], as shown in Figure 1.17(c), and BP-to-AS as demonstrated in Figure 1.19, [50]. The latter employs a BST FBAR-based AWLR resonator, providing a BP response at 2.1 GHz that can be reconfigured to an AS response by biasing off the BST FBAR. A single-to-multi-band filter in Figure 1.20, [12], achieves single-, dual-, and triple-band responses by integrating multiple parallel filtering channels using PIN diodes. The filter's size scales proportionally to the number of passbands. Finally, an absorptive BSF with tunable IS is demonstrated in [51] and shown in Figure 1.21, enabling variable stopband IS between 17 and 65 dB.

Despite these advancements, the majority of AWLR-based filters with BW tuning still rely on mechanical tuning mechanisms (e.g., trimmer capacitors or inductors). Furthermore, current reconfigurable AWLR-based filters lack continuous tunability of centre frequencies and are limited in their functionality, as each of the presented filters allows for a limited reconfiguration level.

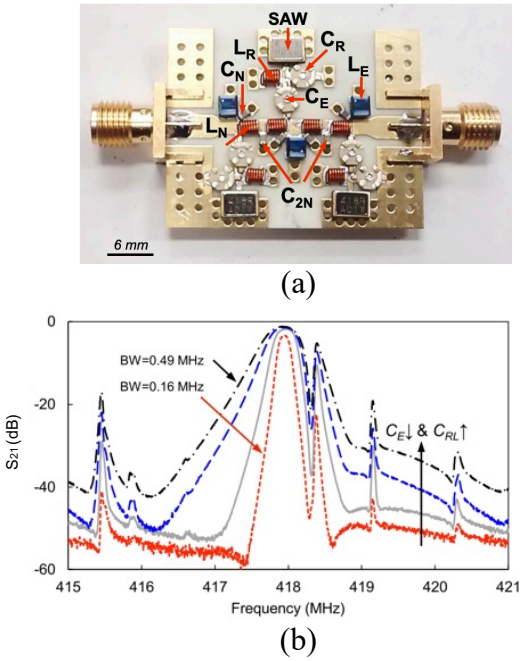
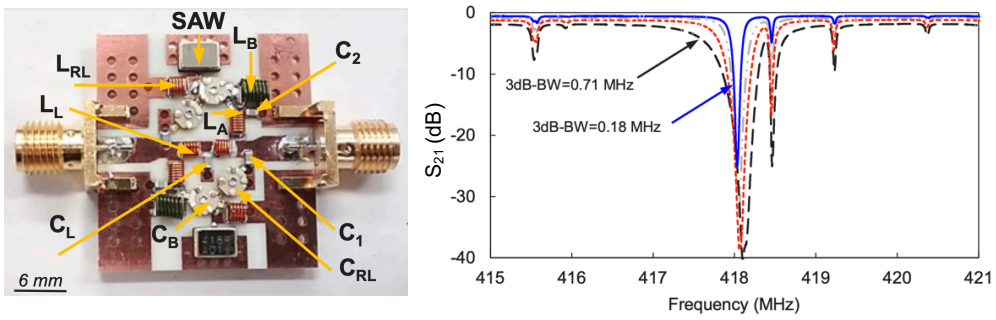


Figure 1.15. AWLR-based BPF with continuously tunable BW: (a) Manufactured prototype; (b) Measured RF power transmission response for various tunable BW states [47].



(a) (b)

Figure 1.16. AWLR-based BSF with continuously tunable BW: (a) Manufactured prototype; (b) Measured transmission response showing continuously tunable stopband BW [48].

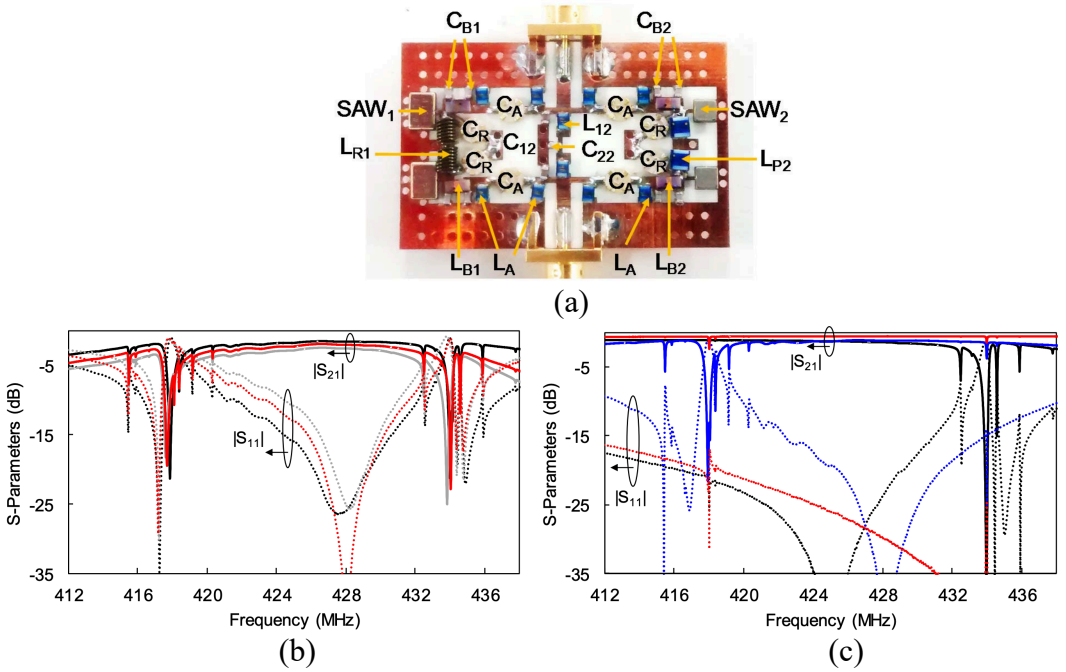
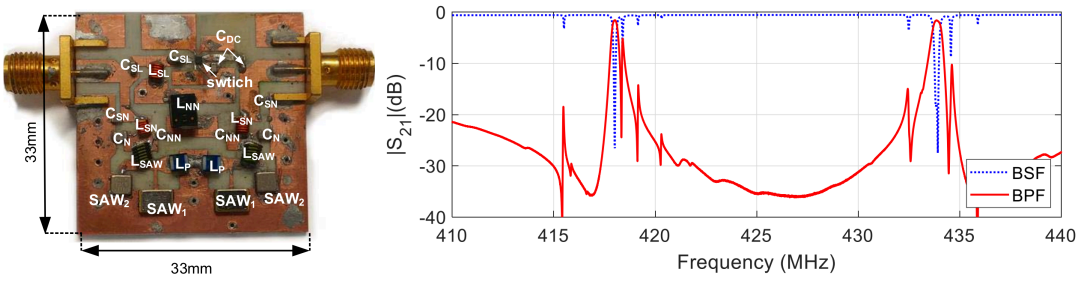
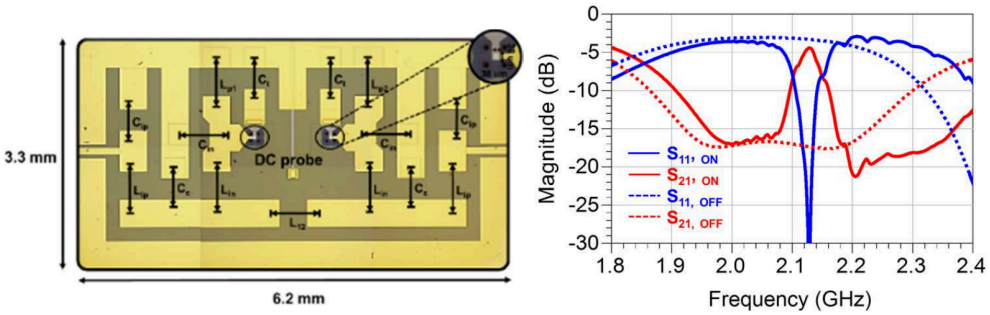


Figure 1.17. Dual-band AWLR-based BSF with tunable BW: (a) Manufactured prototype; (b) Symmetric BW tuning of both stopbands; (c) Intrinsic RF switching of each band individually and simultaneously (all-pass response shown in red trace) [11].



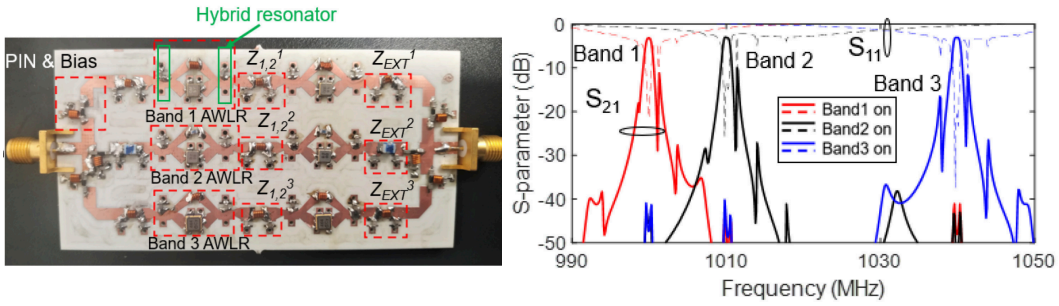
(a) (b)

Figure 1.18. Dual-band BP-to-BS AWLR-based filter: (a) Manufactured prototype; (b) Measured transmission responses in BPF and BSF modes [49].



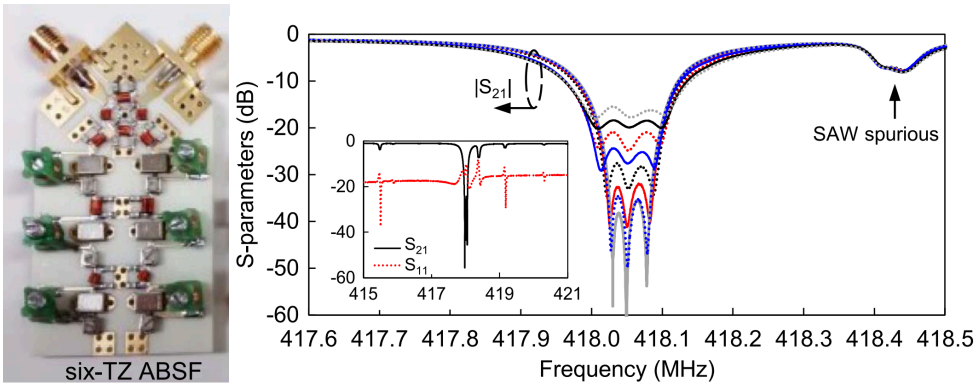
(a) (b)

Figure 1.19. AWLR-based BS-to-AP filter: (a) Manufactured prototype; (b) Measured BP-to-AS response [50].



(a) (b)

Figure 1.20. RF-switched single-to-multi-band reconfigurable AWLR-based BPF: (a) Manufactured prototype; (b) Measured single-band response with one channel activated [12].



(a) (b)

Figure 1.21. AWLR-based BSF with equi-ripple absorptive stopband: (a) Manufactured prototype; (b) Measured response showing variable stopband IL [51].

Table 1.1 presents a concise summary of the state-of-the-art AWR-based reconfigurable filters. The filters described in [37], [41], [34], [42], and [38] are based on BST FBAR technology and support ON/OFF switching by varying the applied DC bias. However, they require high DC voltages (70–125 V) and require a relatively complex manufacturing process. These filters only exhibit discrete reconfiguration states. Specifically, [37], [41], and [42] enable BP-to-AS reconfiguration, [34] supports two switchable BW states, while [38] provides switchable operating bands. These approaches lack the ability to continuously tune the filtering response. The resonator concepts in [39] and [43] also enable BP-to-AS reconfiguration but suffer from high IL of approximately 30 dB. Approaches in [44], [45], and [46] utilize VO_2 switches for discrete reconfiguration. [44] presents a switchable BPF with two f_{cen} states; [45] demonstrates a dual-band BPF with switchable bands; and [46] and [53] showcase BPFs with switchable BWs. These designs primarily support discrete tuning and require complex manufacturing processes.

Table 1.1. State-of-the-art reconfigurable AWR-based filters.

Ref.	Resonator Technology	Rec. modes	Reconfiguration method	FBW (xk_t^2)
[37]	π- network / BST FBAR	BP / AS	Switchable BST FBAR	< 0.8
[41]	π- network / BST FBAR	BP / AS	Switchable BST FBAR	0.43
[34]	Ladder / FBAR	BP (S. BW) / AS	Switchable BST FBAR	0.33-0.50
[42]	Ladde-lattice FBAR	BP/AS	Switchable BST FBAR	0.50
[38]	Ladder/ BST FBAR	BP (S. bands)	Switchable BST FBAR	< 0.8
[39]	AIN Resonator	BP / AS	MEMS switches	N/ A
[43]	AIGaN Resonator	BP / AS	MEMS switches	N/ A
[44]	VO_2 Switched SAW/ Ladder	S. f_{cen}	VO_2 switches	N/ A
[45]	VO_2 Switched SAW/ Ladder	BP (S. bands)	VO_2 switches	N/ A
[46]	VO_2 Switched SAW/ Ladder	BP (S. BW)	VO_2 switches	<0.8
[53]	SAW/ ladder	BP (S. BW)	PCM VO_2 switches	N/A
[52]	AWLR/SAW	BP (M. Tun. BW)	M. Tun.	0.50-1.50
[47]	AWLR/ SAW	BP (M. Tun. BW & IS) / AP	M. Tun.	0.93-1.68
[48]	AWLR/ SAW	BS (M. Tun. BW)	M. Tun.	0.55-2.2
[11]	AWLR/SAW	BS (M. Tun. BW)	M. Tun.	0.27-1.9
[49]	AWLR/ SAW	BP/ BS	RF switches	1.03/ 1.26
[50]	AWLR/FBAR	BP / AS	Switchable BST FBAR	0.333
[50]	AWLR/FBAR	BS / AP	Switchable BST FBAR	0.31
[54]	AWLR/SAW	BS (M. Tun. IS) / AP	Varactor	2.7-3.3
[51]	AWLR/SAW	BS (M. Tun. IS)	M. Tun.	0.34
[12]	AWLR/SAW	BP (S. bands)	BIN diodes	0.8- 0.9

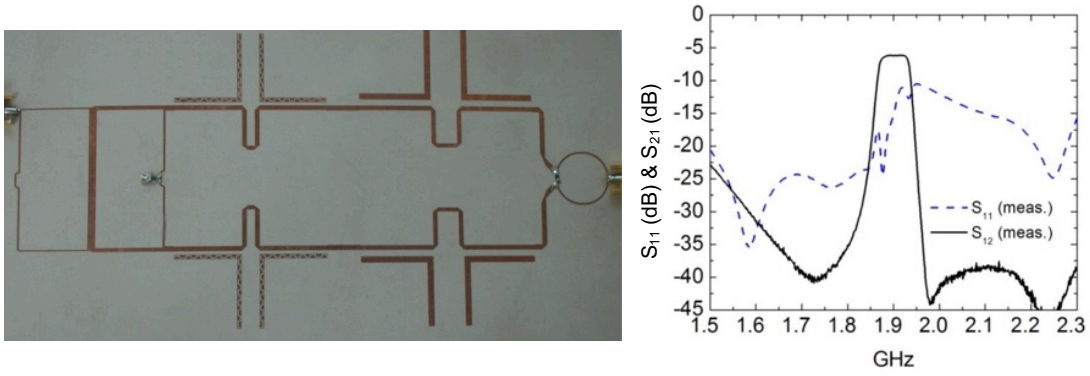
(T.W.: This work, C. E. Tun.: Continuous electronically tunable, M. Tun.: Manual tuning, S.: Switchable, BP: Bandpass, BS: Bandstop, AS: All-stop, AP: All-pass, IS: Isolation)

In contrast, AWLR-based filters in [52] and [47] demonstrate continuously tunable BW for BPFs, while [48] and [11] present BSFs with tunable BW. However, all of these rely on mechanical tuning methods. The concept in [49] employs RF switches to achieve BP-to-BS reconfiguration. Meanwhile, [50] leverages the intrinsic switching behaviour of BST FBARs to realize BP-to-AS and BS-to-AP reconfigurations, but without continuous tuning capabilities. References [54] and [51] enable BSF responses with continuously tunable IS using varactor diodes and mechanical trimmers, respectively. The design in [12] supports switchable band responses via in-parallel cascaded filter branches using PIN diodes. Despite these

advancements, none of the reported works demonstrate BPFs with continuously tunable BW using electronic tuning (e.g., varactor diodes), and none provide AWR-based filters with continuously tunable f_{cen}. Most implementations are limited in terms of reconfiguration states. In light of these limitations, Chapter 2: of this thesis introduces novel AWLR-based filter concepts with enhanced functionality, both theoretically and experimentally. Specifically, it demonstrates: i) A new class of highly-selective quasi-elliptic BPFs, realized by cascading multi-resonant AWLR stages. These filters offer enhanced FBW (>0.4–0.8k_t^2) and continuous BW tuning via electronically reconfigurable varactors. ii) A unique class of multi-configurable and continuously tunable AWLR-based quasi-elliptic filters that demonstrate: 1) continuous f_{cen} tuning, 2) continuous BW tuning with enhanced FBW by modifying the impedance inverters and 3) AP and AS mode reconfigurability. iii) An advanced multi-resonant, multi-configurable quasi-elliptic AWLR-based filter exhibiting: 1) BP and BS responses with tunable f_{cen} and BW, 2) AP and AS mode reconfigurability with high IS levels and 3) enhanced FBW (>0.4– 0.8k_t^2).

1.3.2 Multi-band bandpass filters with reflectionless characteristics

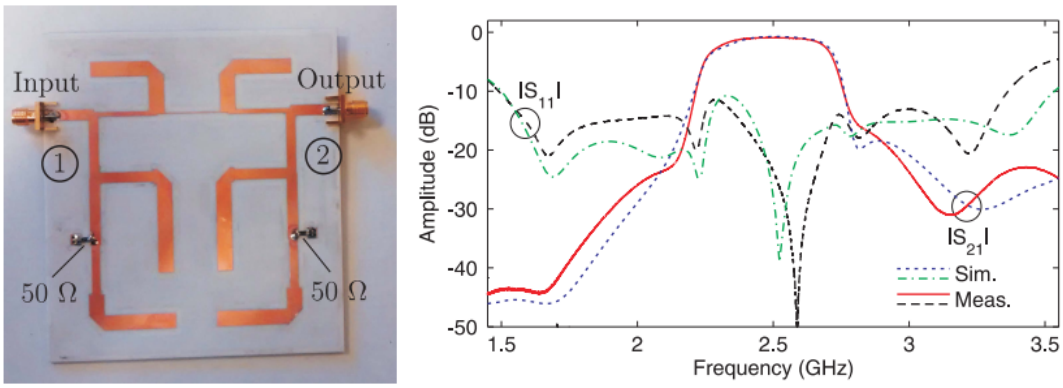
Multi-band transceivers, capable of operating across various frequency bands and supporting diverse waveforms and signalling schemes, are increasingly being researched. These transceivers aim to minimize cost, reduce power consumption, and maximize integration by reusing hardware across different standards [9], [55]. At the same time, there is growing interest in reflectionless or absorptive high-frequency filters to enhance the operational robustness of RF front-end chains. Unlike conventional reflective-type filters, which reflect unwanted signals back to the source, these filters dissipate non-transmitted input-signal energy within their own structure, particularly in the stopband regions. This significantly mitigates detrimental signal reflections that could otherwise impair the performance of adjacent active stages [56]. To enhance the operational characteristics of multi-band transceivers, compact, low IL (i.e., high-Q), and reflectionless multi-band RF filters are essential. Their integration can reduce the need for bulky filter banks, improve the SNR, and enable scalability for future applications.



(a) (b)

Figure 1.22. Absorptive microstrip BPF: (b) Manufactured prototype; (c) Measured results [57].

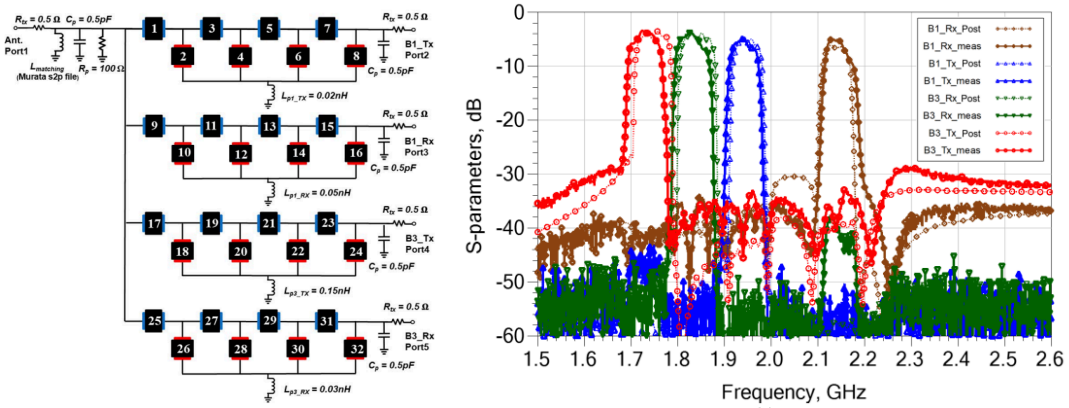
Alternative designs of absorptive or reflectionless BPFs have been reported. Notable examples include the input quasi-reflectionless BPFs described in [57] and [59], each with certain drawbacks. For example, the design in in Figure 1.22, [57] relies on power-distribution circuits such as directional couplers, which increase circuit size. The approach in [59] requires a higher number of components to achieve high selectivity. Input quasi-reflectionless filters based on a complementary-diplexer approach have also been demonstrated using both LE and microstrip technologies [60]. Complementary-diplexer-architecture-based reflectionless BPFs [56], [58] achieve input and symmetric quasi-reflectionless responses. The design in [58], shown in Figure 1.23, includes a main bandpass section along with nearly complementary BS sections at the input and output ports, terminated with resistors that dissipate non-transmitted input signal energy, enabling quasi-absorptive functionality.



(a) (b)

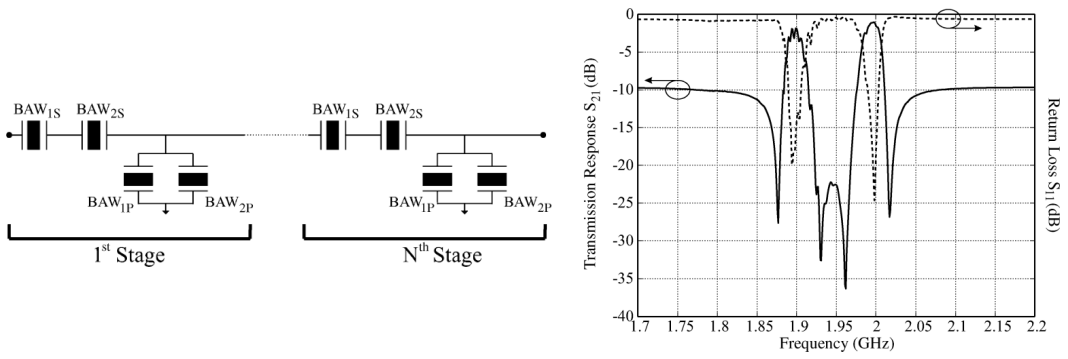
Figure 1.23. Symmetrical quasi-absorptive microstrip BPF: (a) manufactured prototype; (b) simulated and measured RF response [58].

The BPFs presented in [61] and [62] introduce low-reflection single- and multi-passband filters using shunt lossy stubs to absorb stopband energy rather than reflect it back to the source. Balanced-circuit-based BPFs [63] are implemented by combining two identical BPFs with quadrature hybrids, which route reflected signals to resistively terminated ports for absorption. Symmetric reflectionless filters based on even/odd-mode subcircuit compensation have also been proposed [64]. Nevertheless, none of these designs fully meet the stringent requirements for compactness, low IL, and high Q-factor demanded by modern wireless communication transceivers —requirements that acoustic filters are well-positioned to fulfill. Moreover, designs typically exhibit large physical footprints due to the use of low-Q resonators, with Q values ranging from 20 to 150, and most support only single-band responses.



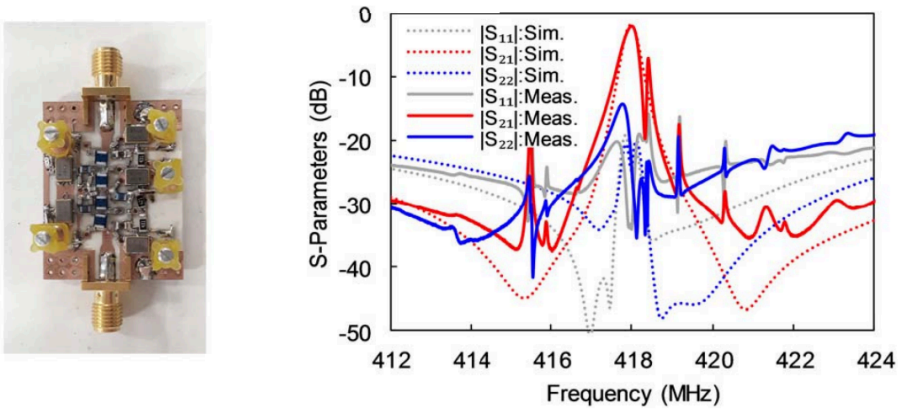
(a) (b)

Figure 1.24. AWR-based multiplexer: (a) Quadplexer circuit topology; (b) simulated and measured responses [58].



(a) (b)

Figure 1.25. Double-Ladder dual-band filter using BAW resonators: (a) Generic configuration; (b) Simulated example using measured BAW resonators [65].



(a) (b)

Figure 1.26. Symmetrical Quasi-Reflectionless SAW-Based BPFs: (a) manufactured two-stage prototype; (b) RF-measured/simulated S-parameters [66].

For high-Q and compact-size implementations, AWR-based filters are preferred. However, most AWR-based filters exhibit single-band TFs, which results in large filter banks when multi-band operation is required in RF transceivers [38], [67], as shown in Figure 1.10 and Figure 1.24. In an alternative approach a double-ladder dual-band filter topology based on BAW resonators, is reported in [65] and illustrated in Figure 1.25. This approach suffers from poor out-of-band rejection, typically around 10 dB. Furthermore, the AWR-based multi-band filters explored in [38], [67], and [65] reflect unwanted RF signal energy in their stopbands, which can cause instabilities in adjacent active stages. The AWLR-based filter concepts in [11], [47], [68] can realize dual-band BP and BS TFs, as shown in Figure 1.17 and Figure 1.18. Despite demonstrating high levels of TF versatility (e.g., bands tuned in terms of BW or are intrinsically switchable [49]), these implementations are based on: i) multi-resonant multi-stage configurations that require a large number of LE inverters, whose losses degrade in-band IL and out-of-band rejection; ii) multiple RF-switched BPF paths [12] whose size scales with the number of bands (see Figure 1.20); and iii) they exhibit reflective characteristics. In another approach, AWLR-based BPFs with quasi-reflectionless characteristics have been demonstrated in [66], [69]; However, these are limited to a single-band mode of operation as demonstrated in Figure 1.26. Furthermore, none of the aforementioned designs has successfully enabled a compact, multi-band response—i.e., using fewer LE components per AWLR stage—while achieving reflectionless characteristics.

Considering the aforementioned limitations, Chapter 3: introduces a unique class of AWLR-based multi-band BPFs that offer reflective and symmetrical quasi-reflectionless responses, compact physical size, improved out-of-band IS, and lower IL compared to previously reported AWLR BPFs [11], [47], [68], and [12].

1.4 Widely Tunable Bandpass Filters

Ultrawideband spectrum sensing is an essential requirement for mission critical communication systems where low power RF signals need to be identified within the presence of high power and dynamically allocated interferers. Widely tunable and highly-versatile RF filters have the potential to enhance the sensitivity of these systems [1]. Although significant research has focused on developing widely tunable filters, most of the existing electronically-tunable BPFs technologies that have been developed today exhibit limited functionality. They are primarily tunable in terms of f_{cen}, often within narrow ranges—for example, f_{cen} tuning ratios (TR) of only 1.2–1.5:1 were shown in [17], [18], [19], [71], [72] and such an example case is illustrated in Figure 1.27. Fully tunable filters that support both f_{cen} and BW reconfigurability have been demonstrated in [73], [74], [20], [75], [76], [77], [78], and [70], with an example shown in Figure 1.28. However, these filters still exhibit limited TRs, with f_{cen} and BW TR typically below < 2:1. Furthermore, their operational frequencies are generally restricted to 1–3 GHz [19], [79], [80], [81], [82], [83], [84], making them insufficient for covering the full 5G+ FR1 band (0.41–7.125 GHz).

The maximum TR of a BPF is limited by the capacitance ratio of the varactor technology and its relation to the total capacitance of the resonator. To overcome this limitation, manifolds comprising multiple RF-switched filters are recently being considered as for example the ones in [85], [86], [87]. An example of an RF-switched BPF manifold with an extended f_{cen} TR from 0.5 to 2.4 GHz (TR: 4.4:1) is shown in Figure 1.29. State-of-the-art BPF manifolds are typically based on lossy RF switches or PIN diodes that increase the RF front-end complexity and power consumption, introduce additional loss to each of the filtering channels (e.g., 1.8 dB for Silicon-on-insulator (SOI) switches [88]) and have limited TF adaptivity. For example, in [85], [86], [87], only f_{cen} tuning is achieved—through two or three RF-switched f_{cen}-tunable BPFs within the manifold—while BW tuning is not supported. These manifolds are fairly large in size, their BW can't be tuned, and their operational frequencies are limited to 2.4 GHz. Furthermore, these manifolds are restricted in operation to a single band at a time.

The research presented in this thesis—particularly in Chapter 4: —introduces, for the first time, a novel RF-switchless integration scheme for BPF manifolds. It utilizes two fully tunable BPFs—i.e., with multi-configurable TF parameters,

including f_{cen} tuning, BW tuning, and an intrinsic RF switch-off capability—interconnected with two low-pass/high-pass RF diplexer junctions. Moreover, the proposed BPF manifold, compared to the state-of-the-art, is the only RF-switchless manifold to date that covers the highest operational frequency (1.9 – 7.3 GHz) while exhibiting ultra-wide f_{cen} and BW tuning, and supporting the largest number of operating modes, namely single-band, dual-band, and AS modes of operation.

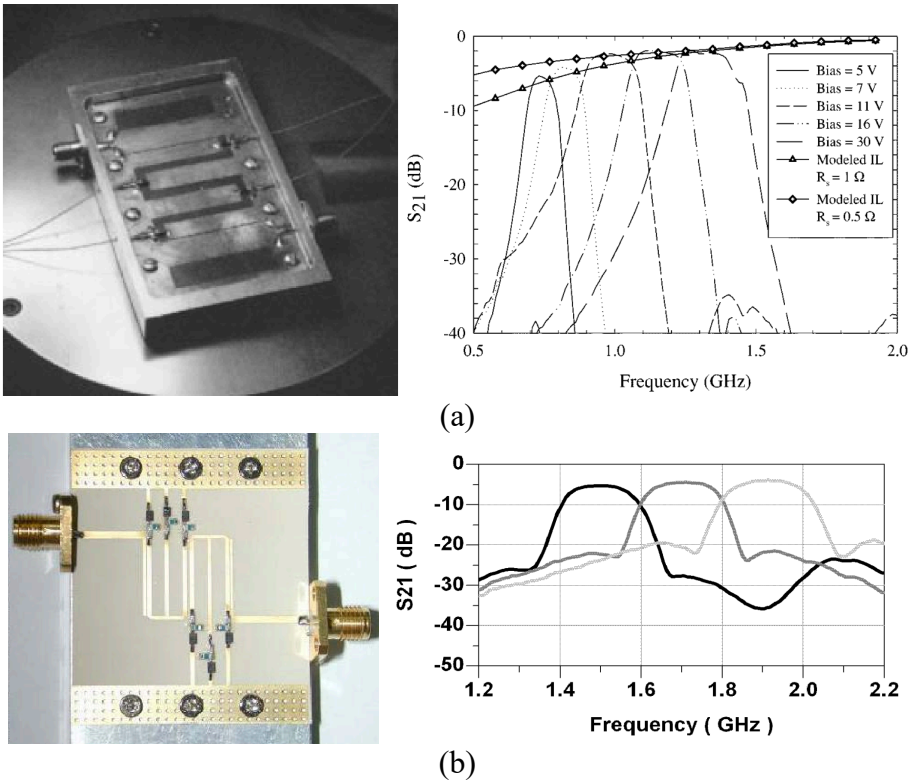
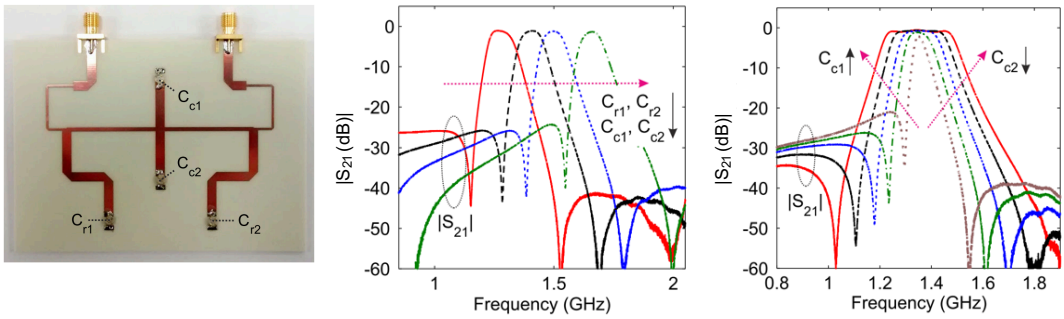
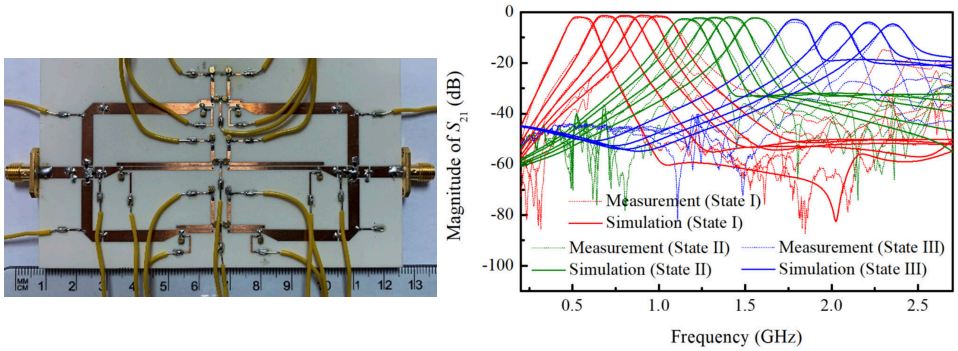


Figure 1.27. f_{cen}-tunable filters: (a) Manufactured interdigital BPF with measured tunable f_{cen} from 0.72 to 1.22 GHz (TR: 1.69:1) [17]; (b) Manufactured hairpin BPF with measured tunable f_{cen} from 1.5 to 1.9 GHz (TR: 1.26:1) [18].



(a) (b) (c)

Figure 1.28. Reconfigurable BPF with both f_{cen} and BW tuning: (a) Manufactured prototype; (b) Measured f_{cen} tuning response; (c) Measured BW tuning response [70].



(a) (b)

Figure 1.29. RF-switched BPF manifold with tunable f_{cen}: (a) Manufactured protoype; (b) Measured $|S_{21}|$.

1.5 Thesis Outline

Considering the previously discussed limitations in RF filter technologies for future spectrum-efficient communication systems, this thesis introduces innovative filter design concepts that enhance the performance and functionality of existing AWR-based reconfigurable and widely tunable RF filters. Specifically, it presents novel concepts for AWLR-based filters with multi-configurable and continuously tunable capabilities, including f_{cen} tuning, BW tuning, and other reconfigurable TF characteristics. Notably, this is the first time AWR-based filters with continuous f_{cen} tuning are introduced for both BPF and BSF modes. Moreover, the thesis introduces a new class of reflective and quasi-reflectionless multi-band quasi-elliptic AWR-based BPFs designed to reduce size, minimize the number of LEs and reduce out-of-band reflections, thereby enhancing both performance and integration in the RF front-end. Furthermore, the thesis demonstrates state-of-the-art widely tunable RF BPF concepts, particularly addressing the challenges associated with achieving ultra-wideband f_{cen} tuning. For the first time, a novel RF-switchless integration scheme for BPF manifolds is proposed. This manifold exhibits ultra-wide and highly versatile TF characteristics, supporting multiple modes of operation.

The rest of this thesis is structured as follows:

- Chapter 2 presents new types of AWR-based filter designs, featuring multi-configurable and continuously-tunable responses. First, a new class of AWR-based BPFs with continuously tunable FBW is introduced. These BPFs achieve highly selective quasi-elliptic TFs, with enhanced and tunable FBW. Second, novel architectures for multi-configurable and continuously tunable AWR-based BPFs are explored. A key advancement in this concept is the introduction of a novel tuning mechanism that enables continuous f_{cen} tuning of AWR-based BPFs for the first time. Additionally, the concept allows for continuous BW tuning and the ability to intrinsically switch the TF response to achieve AP and AS modes. The final contribution of this chapter is a novel and more advanced class of multi-configurable quasi-elliptic AWLR-based filters with continuously tunable characteristics. These filters can intrinsically switch between different operation modes, namely: i) BP, ii) BS, iii) AP,

and iv) AS responses. Additionally, they exhibit continuous tuning of both the f_{cen} and BW when operating in BP and BS modes. The theoretical foundations are demonstrated via coupling matrix models. The contributions of this chapter are presented in [89], [90], [91], and [92].

- Chapter 3 introduces a novel architecture for AWR-based multi-band BPFs featuring quasi-elliptic TFs. The proposed design enables the realization of highly selective multiple passbands with enhanced FBWs $> 0.4k_t^2 – 0.8k_t^2$, all within a compact form factor. It also supports reconfigurable reflective and quasi-reflective characteristics. The architecture is based on high-Q, multi-resonant AWLR bandpass stages interconnected in series via LE impedance inverters. Additionally, a method for achieving symmetric quasi-reflectionless characteristics is presented by integrating resistively terminated BS-type AWLR stages. This chapter outlines a comprehensive design methodology and presents a practical realization scheme for the proposed filter architecture. The contributions of this chapter are reported in [93] and [94].
- Chapter 4 introduces a novel, tune-all, manifold BPF concept with multi-octave f_{cen} and BW tuning capabilities. The manifold is based on two independently tunable BPFs uniquely integrated using two high-pass/low-pass RF diplexer-based filtering junctions. This diplexer-based integration enables the manifold to support both single-band and dual-band BPF responses with independently tunable characteristics—marking a significant advancement over conventional RF-switched manifolds, which are limited to single-band operation. To further optimize performance, a technique for minimizing IL is introduced, based on using varactors and high-Q static DC block capacitors. The proposed manifold exhibits ultra-wide and highly versatile TF characteristics, supporting three distinct modes of operation: i) single-band BPF, ii) dual-band BPF, and iii) all-reject mode. The manifold enables wide f_{cen} tunability across a broad portion of the FR1 frequency range. The contributions of this chapter are presented in [95] and [96].

- Chapter 5 summarizes the key contributions of this thesis and lays the groundwork for future developments in this field providing insight into future possibilities for highly versatile RF filters.

Chapter 2: AWR-Based Filters with Multi-Configurable and Analog Tuning Characteristics

2.1 Introduction

This chapter explores the development of AWR-based filter designs with multi-configurable and continuously tunable characteristics. Section 2.2 introduces a new class of highly selective quasi-elliptic AWLR-based BPF with electronically reconfigurable FBW. Section 2.3 presents AWLR-based BPFs that materialize continuously tunable f_{cen}. To the best of the authors' knowledge, this is the first time that continuous f_{cen} tuning capability in demonstrated AWR-based BPFs. These BPFs also support continuously tunable BW and multi-configurable operational modes, enabling intrinsic switching between BP, AP, and AS modes. Section 2.4 introduces a new class of quasi-elliptic AWLR-based BP-to-BS filters. These filters can intrinsically switch between BP and BS modes without the need for RF switches—unlike state-of-the-art designs that rely on physical RF switches [49], [97], [98]. The proposed architecture uniquely facilitates continuous tuning of both f_{cen} and BW across two distinct BP and BS modes. To the best of the authors' knowledge, this is the first demonstration of continuous f_{cen} tuning in AWR-based BS filters. This capability allows AWR-based BP and BS filters to dynamically adapt to varying RF environments—an essential feature for advanced RF transceivers to support dynamic signal acquisition and effective noise mitigation. Furthermore, the filters can reconfigure their TF into additional AP and AS modes, enhancing their overall versatility. These multi-configurable and continuously tunable capabilities are realized within the same filter volume. The content of this chapter has been published in [89], [90], [91], and [92].

2.2 Highly Selective AWLR-Based BPFs with Tunable BW

This section reports on a new class of quasi-elliptic AWLR-based BPFs with electronically-reconfigurable FBW. They are based on cascaded series- and parallel-type multi-resonant AWLR stages whose TF characteristics are tuned by electronically-reconfigurable varactors. As opposed to conventional AWR-based filters, they facilitate the realization of highly-selective quasi-elliptic TFs with enhanced (i.e., FBW> 0.4-0.8k_t^2) and continuously-tunable FBW while exhibiting high effective quality factor (Q_{eff}). Furthermore, these filtering architectures are based on identical AWRs as opposed to classical AWR-based implementation schemes using resonators with closely spaced frequencies with tight fabrication requirements.

2.2.1 Theoretical foundations

The generalized circuit diagram of the proposed multi-stage AWLR-based multi-configurable and continuously-tunable BPF concept is illustrated in Figure 2.1(a). It is based on the cascade of two series-type multi-resonant stages (coupled to the RF ports via impedance inverters (Z_{ex}))and N-2 parallel-type multi-resonant stages that are cascaded by N-3 impedance inverters ($Z_{2,i}$–$Z_{i,K}$). In this manner, highly-selective quasi-elliptic TFs with N poles, $2N$ transmission zero (TZs) can be obtained. By reconfiguring the resonant characteristics of the LE resonators in each stage, the TZs can be either placed symmetrically or asymmetrically around the passband [see Figure 2.1(a)] allowing, the ability to tailor the roll-off and out-of-band rejection. This is also shown in the conceptual examples of two different two-stage BPFs that are either comprised of one-series-type and one parallel-type stage or two parallel-type stages as illustrated in Figure 2.1(b), (c). The SAW resonators are represented by their Butterworth-Van Dyke (BVD) model. To better illustrate the operating principles of the multi-stage AWLR BPF concept various design examples of the multi-resonant stages and their use in high-order BPFs are considered next. The circuit details of the series-type multi-resonant AWLR stage are illustrated in Figure 2.2(a). One AWR (series resonant frequency: ω_s, parallel resonant frequency: ω_a) is cascaded in parallel with a series-type LE resonator (resonant frequency $\omega_r=1/(C_rL_r)^{1/2}$) that decouples ω_a from ω_s. In this manner, a quasi-elliptic response that has one-pole and two-TZ can be obtained [see Figure 2.2(a)]. The location of the pole and TZs can be specified using (2.1), and (2.2).

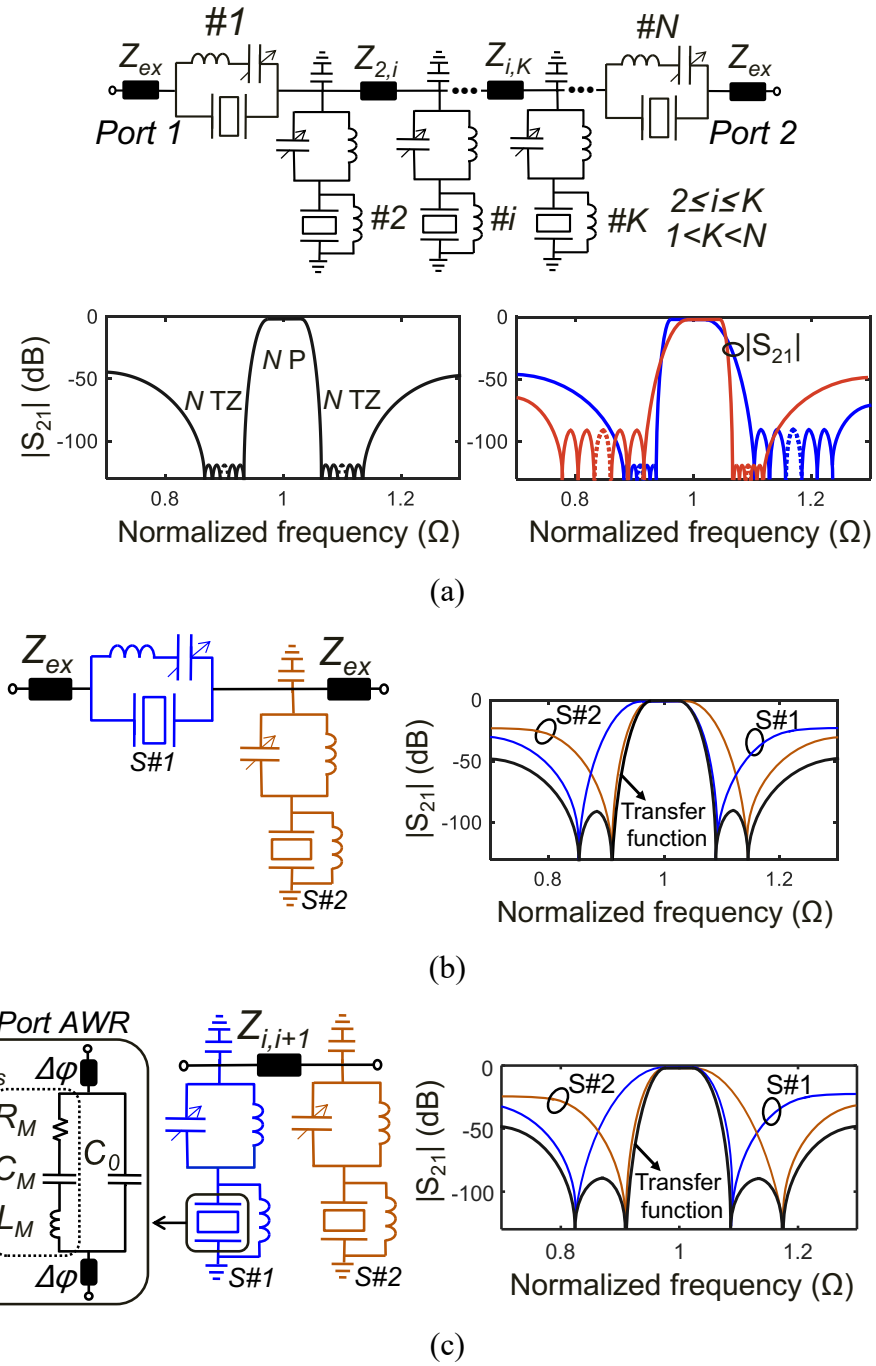
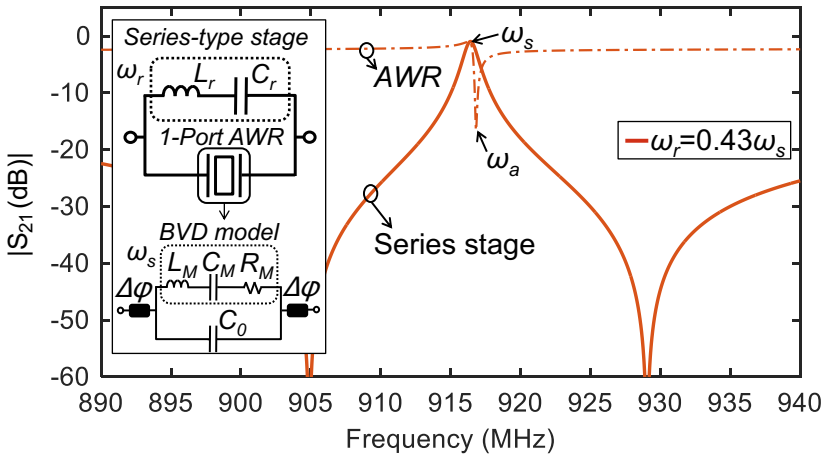
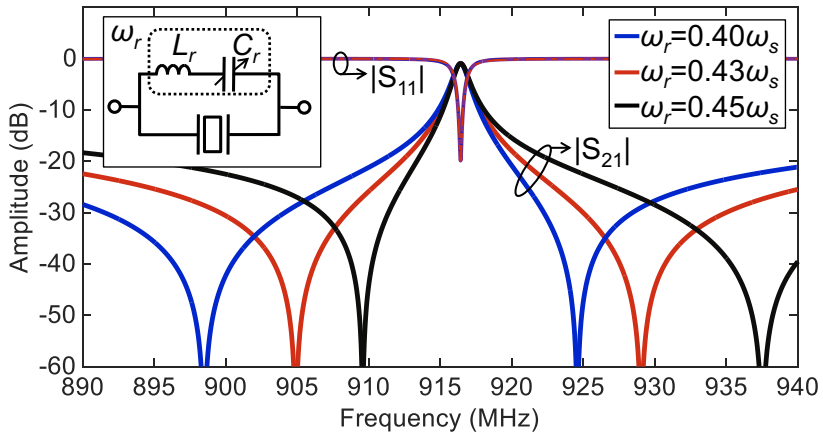


Figure 2.1. Quasi-elliptic AWLR-based BPF that exhibits N poles and $2N$ TZs: (a) Generalized circuit diagram and example TFs; (b) Circuit schematic and example response of a filter comprising one series-type and one parallel-type stages; (c) Circuit schematic and example response of a filter comprising two parallel-type stages [90].



(a)



(b)

Figure 2.2. (a) Simulated power transmission $|S_{21}|$ of a SAW resonator (C_M = 1.85 fF, L_M = 16.32 µH, R_M = 11.3 Ω, C_0 = 2.18 pF, $\Delta\varphi$ = 9.38°, k_t^2 = 0.12%, f_s= 916.4 MHz) and a series-type AWLR multi-resonant stage; (b) Power transmission response $|S_{21}|$ of the series-type multi-resonant stage that exhibits one pole and two TZs. The TZs can be controlled by altering ω_r [90].

It should be noted that the TZs can be reconfigured around the pole by altering ω_r that resonates at a frequency 0.45 times lower than ω_s as shown in Figure 2.2(b). The circuit schematic and the theoretical S-parameters of the parallel-type multi-resonant stage are depicted in Figure 2.3. It is made up of an AWR that is connected in parallel with an inductor L_0 and is cascaded in series with a parallel LE resonator (resonant frequency ω_p=$1/(C_p \cdot L_p)^{1/2}$). The LE resonator resonates at ω_p 1.2x higher than ω_s; and together with its neighbouring elements acts as an impedance inverter. In this manner, a quasi-elliptic response having one-pole and two TZs can be created [see Figure 2.3(a)] whose frequencies can be specified using (2.3), and (2.4). Moreover,

the resulting TZs can be tuned around the transmission pole by altering ω_p, as shown in Figure 2.3(a). The parallel-type multi-resonant stage can be designed for arbitrary FBW states by appropriately adjusting the inductance ratio (L_p/L_0) as illustrated in Figure 2.3(b).

Considering the operating principles of the multi-resonant stages, highly-selective TFs can be designed. Specifically, Figure 2.4, illustrates how a four-pole/eight-TZ quasi-elliptic TF with enhanced FBW can be obtained by cascading two series-type (stage #1, stage #4) and two-parallel type multi-resonant stages (stage #2, stage #3). Their poles and TZs can be specified using (2.1) to (2.4). In these equations, C_r denotes the capacitance of the series-type resonator, L_r denotes the inductance of the series-type resonator, while C_M and L_M represent the motional capacitance and inductance of the AWR resonator, and C_0 is the parasitic capacitance of the AWR, as shown in Figure 2.2(a). The cascading of the multi-resonant stages makes the placement of the poles and the TZs in the overall BPF governed by the individual multi-resonant stages. This allows flexibility in reconfiguring the response; for example, the TZs can be reconfigured to show different roll-off rates around the passband by controlling the resonance of the LE resonators of each constituent stage as demonstrated in Figure 2.5. Unlike the conventional ladder-type AWR based filter designs, the proposed configuration enables the design of passbands with arbitrary FBWs (>0.4-0.8k_t^2) as shown in Figure 2.6 where FBWs of 1-2.65k_t^2 are illustrated. They are achieved by adjusting L_p/L_0 along with C_{pp1}, C_{pp2}, Z_{23} and Z_{ex}. In these examples, inverters Z_{23} and Z_{ex} are replaced with their π-type LE equivalents using the following: $L= Z/\omega_{cen}$, $C= 1/(Z\cdot\omega_{cen})$ and $\omega_{cen}=2\pi\cdot f_{cen}$, where f_{cen} is the centre frequency and Z is the inverter impedance.

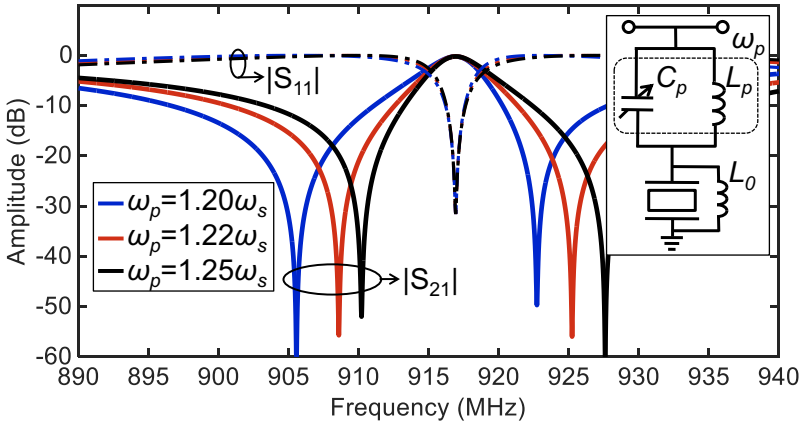
$$\omega_{Pole}^{Series} = \frac{1}{\sqrt{C_M L_M}} \tag{2.1}$$

$$\omega_{TZ1,2}^{Series} = \sqrt{\frac{(C_0+C_r)\omega_s^{-2}+(C_0+C_M)\omega_r^{-2} \pm \sqrt{\left((C_0+C_r)\omega_s^{-2}\right)^2+\left((C_M+C_0)\omega_r^{-2}\right)^2+\left(2C_rC_M-2C_0C_M-2C_0C_r-2C_0^{-2}\right)\omega_s^{-2}\omega_r^{-2}}}{2C_0\omega_r^{-2}\omega_s^{-2}}} \tag{2.2}$$

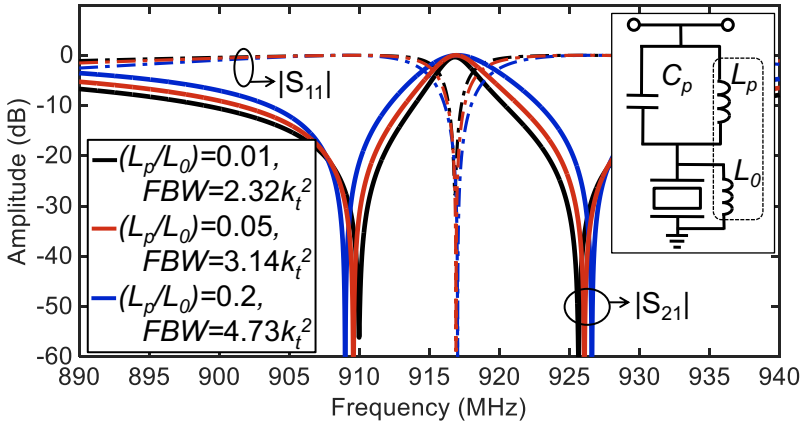
$$\omega_{Pole}^{Parallel} = \sqrt{\frac{C_M L_0+W_0^{-2}+\omega_s^{-2} \pm \sqrt{\omega_0^{-4}+\omega_s^{-4}+2C_M L_0(\omega_0^{-2}+\omega_s^{-2})-2\omega_0^{-2}\omega_s^{-2}+C_M^2 L_0^2}}{2\omega_0^{-2}\omega_s^{-2}}} \tag{2.3}$$

$$\omega_{TZ1,2}^{Parallel} = \sqrt{\frac{jL_P\left(\omega_0^{-2}+L_0C_M+\omega_s^{-2}\right)+jL_0\left(\omega_s^{-2}+\omega_P^{-2}\right) \pm \sqrt{X}}{2j\omega_s^{-2}\left(\omega_0^{-2}L_P+\omega_P^{-2}L_0\right)}} \tag{2.4}$$

$$X = -(L_P^2+L_0^2)\omega_s^{-4} - 2L_0L_P\left(\omega_s^{-4}-\omega_0^{-2}\omega_s^{-2}+\omega_0^{-2}\omega_p^{-2}-\omega_s^{-2}\omega_p^{-2}\right) - 2C_ML_0L_P^2(\omega_s^{-2}+\omega_0^{-2}) - 2C_ML_PL_0^2\left(\omega_s^{-2}+\omega_p^{-2}\right)$$
$$-L_P^2(\omega_0^{-4}-2\omega_0^{-2}\omega_s^{-2}+C_M^2L_0^2) - L_0^2(\omega_p^{-4}-2\omega_s^{-2}\omega_p^{-2}) \tag{2.5}$$



(a)



(b)

Figure 2.3. Power transmission $|S_{21}|$ and reflection $|S_{11}|$ responses of the parallel-type AWLR multi-resonant stage: (a) TZs control around the pole by tuning ω_p; (b) BW control by altering (L_P/L_0) [90].

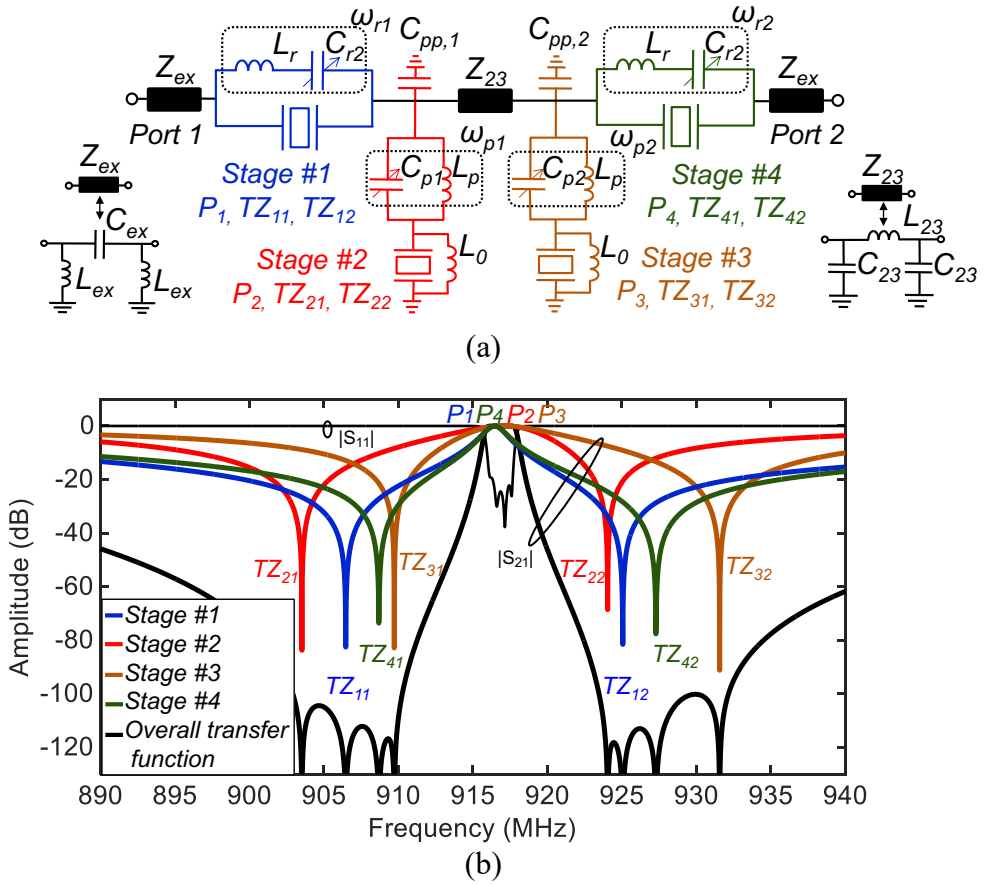


Figure 2.4. (a) Circuit schematic of the quasi-elliptic four-pole/ eight-TZ AWLR BPF that comprises four multi-resonant AWLR stages; (b) Theoretical power transmission $|S_{21}|$ and reflection $|S_{11}|$ of the BPF and its constituent stages (Stage #1, Stage #2, Stage #3, and Stage #4) obtained with linear circuit simulations [90].

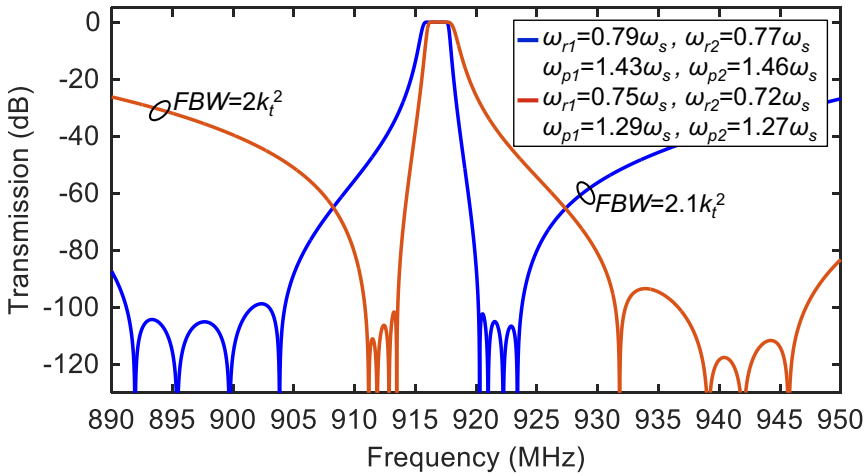


Figure 2.5. Theoretical power transmission $|S_{21}|$ response of the four-stage quasi-elliptic BPF for alternative locations of TZs (by altering ω_{r1}, ω_{r2}, ω_{P1}, and ω_{P2}) demonstrating the reconfigurability of the TF in the out-of-band.

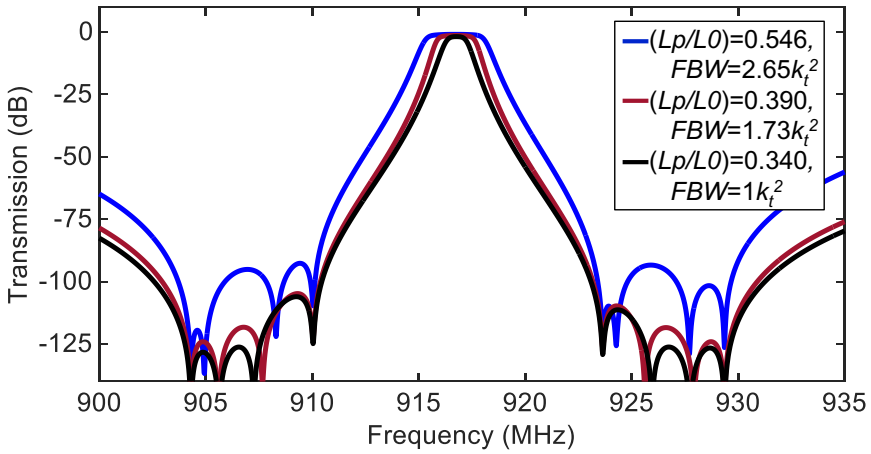


Figure 2.6. Theoretical power transmission $|S_{21}|$ response of the four-stage quasi-elliptic BPF for alternative levels of FBW by altering the inductance ratio L_P/L_0 and the impedance inverter values. For the case of: i) L_P/L_0=0.546, C_{pp1}= C_{pp2}=0.51 pF, C_{p1}=2.77 pF, C_{p2}=2.69 pF, C_{ex}=1.32 pF, L_{ex}=17 nH, C_{23}= 0.63 pF, L_{23}=33.2 nH, ii) L_P/L_0=0.39, C_{pp1}= C_{pp2}=0.89 pF, C_{p1}=2.02 pF, C_{p2}=2.08 pF, C_{ex}=1.94 pF, L_{ex}=14.5 nH, C_{23}= 0.66 pF, L_{23}=22.4 nH, ii) L_P/L_0=0.34, C_{pp1}= C_{pp2}=0.51 pF, C_{p1}=1.934 pF, C_{p2}=1.888 pF, C_{ex}=1.32 pF, L_{ex}=17.06 nH, C_{23}= 0.626 pF, L_{23}=29.9 nH. (The rest of the design parameters are: L_{p1}=Lp_2 = *7.6 nH,* L_{r1} = L_{r2} =25 nH, C_{r1}= C_{r2}=2.15 pF) [90].

To evaluate the performance of the filter in the presence of lossy elements, finite Q is considered for the TF example in Figure 2.7 where Q_M is the Q factor of the AWRs and Q_{LE} is the Q-factor of the auxiliary LEs (21 total). As shown, Q_{LE} has minimal effect on the in-band IL and the passband preserves the high-Q SAW resonator characteristics. On the other hand, low Q_{LE} primarily affects the out-of-band attenuation levels. However, even with Q_{LE} as low as 62.5, the attenuation levels are higher than 60 dB. The multi-stage AWLR-based BPF concept can be readily scaled to the realization of high order TFs. This is shown in Figure 2.9 for the case of a six-stage BPF design that is comprised of two series-type stages and four parallel-type stages and exhibits six-poles and twelve-TZs. The BW tuning concept for the devised multi-stage AWLR BPF concept is illustrated in Figure 2.8 for the example case of a four-pole/eight-TZ BPF. It is performed by altering the TZs around the passband. Specifically, by decreasing ω_{r1} and ω_{r2}, (achieved by lowering $C_{r1,2}$) the TZs associated with the series stages (located on the upper edge of passband) are brought closer to the f_{cen}. Likewise, by increasing ω_{p1} and ω_{p2} (achieved by lowering $C_{p1,2}$), the TZs of the parallel stages (located at the lower edge of passband) are brought closer to

f_{cen}. In this manner, the FBW can be tuned to narrower stages. As shown in Figure 2.8, when tuning the FBW to narrower states, the IS levels close to the passband decrease whereas the IS BW widens due to some of the TZs having moved to distant frequencies.

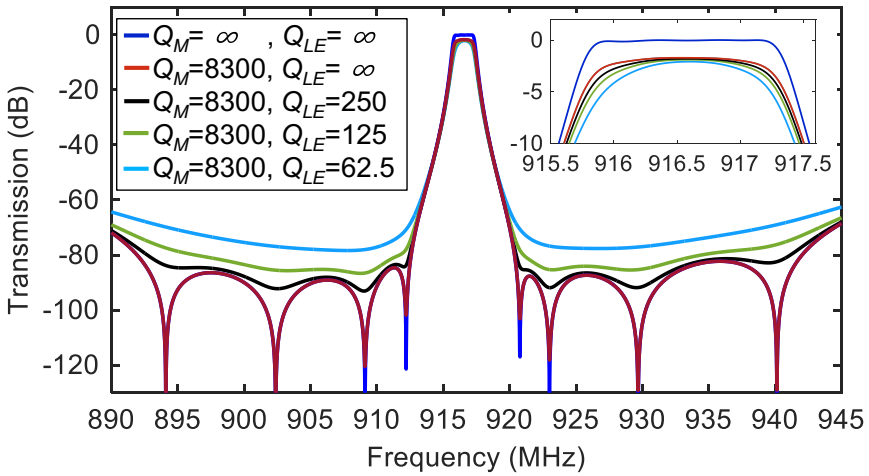


Figure 2.7. Theoretical power transmission $|S_{21}|$ response of the four-stage four-pole/eight-TZ BPF as a function of Q_M and Q_{LE} [90].

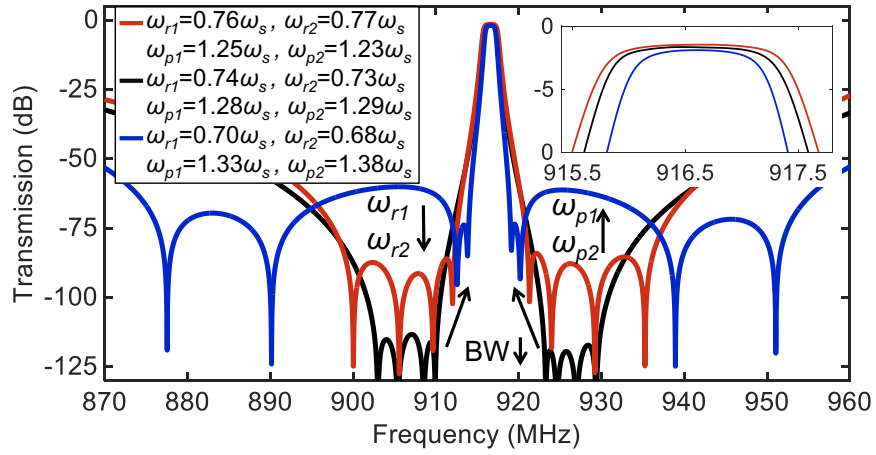


Figure 2.8. Theoretical power transmission $|S_{21}|$ response of the four-stage four-pole/eight-TZ BPF. Continuous BW tuning is obtained by varying the location of the TZs [90].

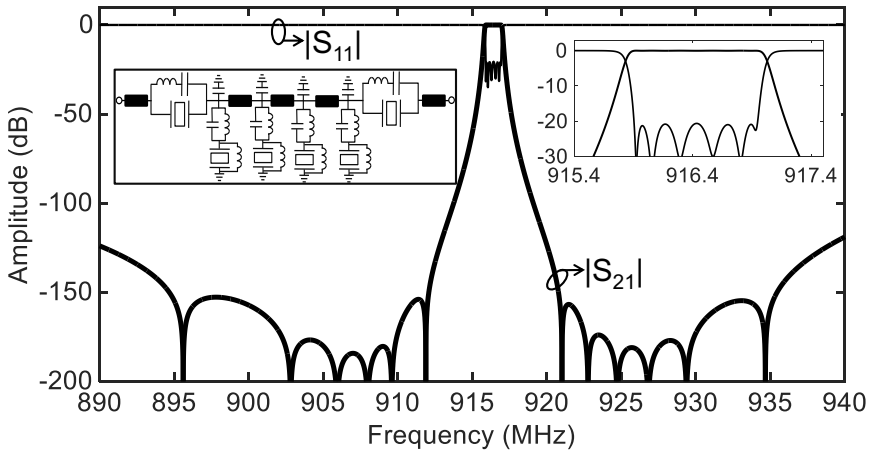


Figure 2.9. Circuit schematic of the six-stage six-pole/twelve-TZ BPF alongside with its ideally-simulated S-parameters [90].

2.2.2 Experimental validation

To validate the proposed AWLR-based quasi-elliptic BPF concept, a four-stage (N=4) BPF prototype exhibiting four-poles and eight-TZ has been designed, manufactured and tested. The prototype was implemented at 916.6 MHz using commercially-available SAW resonators from Murata Inc. and LE components from Coilcraft Inc. [99] and Johanshon [100]. RF tuning is performed using Skywork Varactors [101]. The design was performed on Roger 4003C substrate (dielectric thickness H = 0.813 mm, permittivity ε_r=3.55), using the software package Keysight Advanced Design System (ADS) and following the design guidelines in Section 2.3.1. RF characterization was performed by means of S-parameters using a Keysight N5244A network analyzer. Photograph of the manufactured four-stage AWLR BPF prototype is shown in Figure 2.10 alongside the details of the utilized surface mount devices (SMDs)-based components, the circuit diagram of this prototype is shown in Figure 2.4(a). In Figure 2.11, the measured RF response of the prototype is obtained by altering the DC biasing on the varactor diodes between 0 V and 30 V. It can be observed that continuous BW tuning is obtained between 0.63–1.32 MHz (i.e., FBW=0.573 - 1.32k_t^2) which corresponds to a TR of 2.31:1. For all tuning stages, the minimum IL was measured between 2.2 and 3.9 dB (effective Q (Q_{eff}) = 6,000- 7,700) and the out-of-band IS levels were between 27 and 55 dB. An EM simulated state is also provided and appears to be in a good agreement successfully verifying the proposed filter concept.

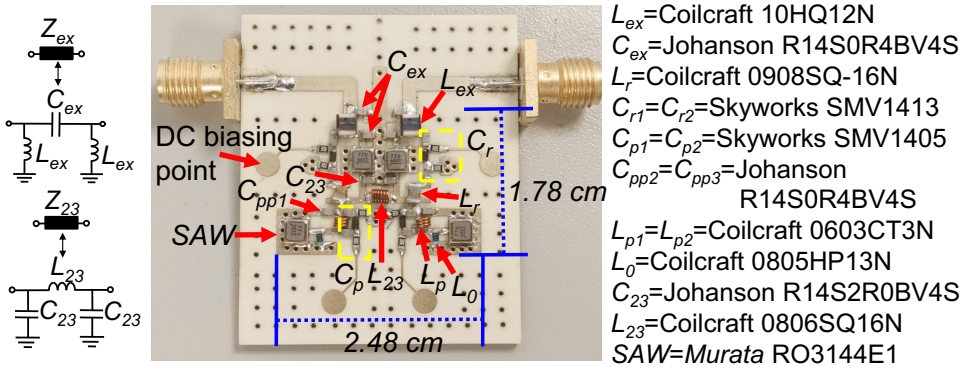


Figure 2.10. Manufactured prototype of four-stage quasi-elliptic AWLR prototype [90].

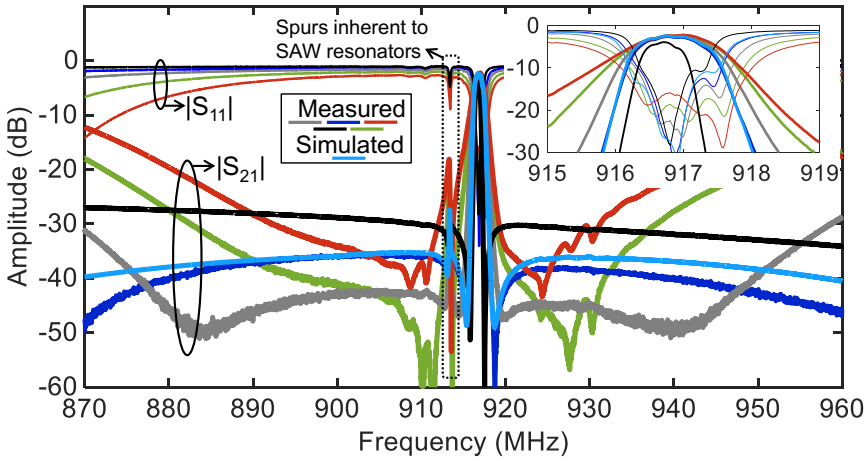


Figure 2.11. RF-measured S-parameters of the four-stage quasi-elliptic AWLR BPF prototype with continuously tunable FBW. An EM-simulated state is also included for comparison purposes [90].

2.3 AWR-Based BPFs With Multi-configurable and Continuously Tunable TF Capabilities

This section presents the potential to materialize f_{cen} tunable quasi-elliptic AWR based-BPFs using a new class of tunable multi-branch multi-resonant AWLR stage. The proposed AWLR concept enables multi-configurability within the TF of the filter leading to multiple independently-tunable and unique TF characteristics. They include: i) continuous f_{cen}-tunability, ii) continuous BW tuning, iii) an AP mode of operation, and iv) an AS mode of operation. Furthermore, these filtering architectures are designed in a simple manner, utilizing AWLRs with identical characteristics—unlike traditional AWR-based filter topologies such as ladder or lattice structures, which require multiple AWRs with customized characteristics. This adds complexity to the design, as custom AWRs are time-consuming to develop and involve complex manufacturing processes.

2.3.1 Theorical foundations

2.3.1.1 Generalized concept

The block diagram and conceptual TF of the devised multi-resonant-AWLR concept with multi-configurable and continuously-tunable TF capabilities are visualized in Figure 2.12. It allows for: i) continuous f_{cen}-tunability [Figure 2.12(b)], ii) continuous FBW tuning [Figure 2.12(c)], iii) an AP mode of operation [Figure 2.12(c)], and iv) an AS mode of operation [Figure 2.12(d)]. The multi-resonant AWLR module consists of one high-Q resonator module (R_{Hi}) that comprises a high-Q one-port-type AWR (C_{Mi}, L_{Mi}, R_{Mi} are the motional capacitance, inductance and resistance, while C_{0i} is the parasitic capacitance) and a low-Q LE resonator (R_i: L_i, C_i) that resonates at the series resonant frequency of the AWR f_{si} which coincides with the f_{cen} of the passband. The R_{Hi} and R_i are cascaded in-parallel with a low-Q LE resonator (R_L: L_L, C_L) through an impedance inverter Z_{Ei} and exhibits one pole and two TZs. By reconfiguring the resonant characteristics of R_L and R_i, and altering the impedance of Z_{Ei}, multiple-reconfiguration can be obtained, as shown in Figure 2.12(b-e). Specifically: i) continuous f_{cen} tuning is obtained by altering the resonant frequency of R_L, ii) continuous BW tuning is implemented by varying Z_{Ei}, iii) the AP mode and the AS mode are facilitated by reconfiguring Z_{Ei} and the resonant frequency of R_i.

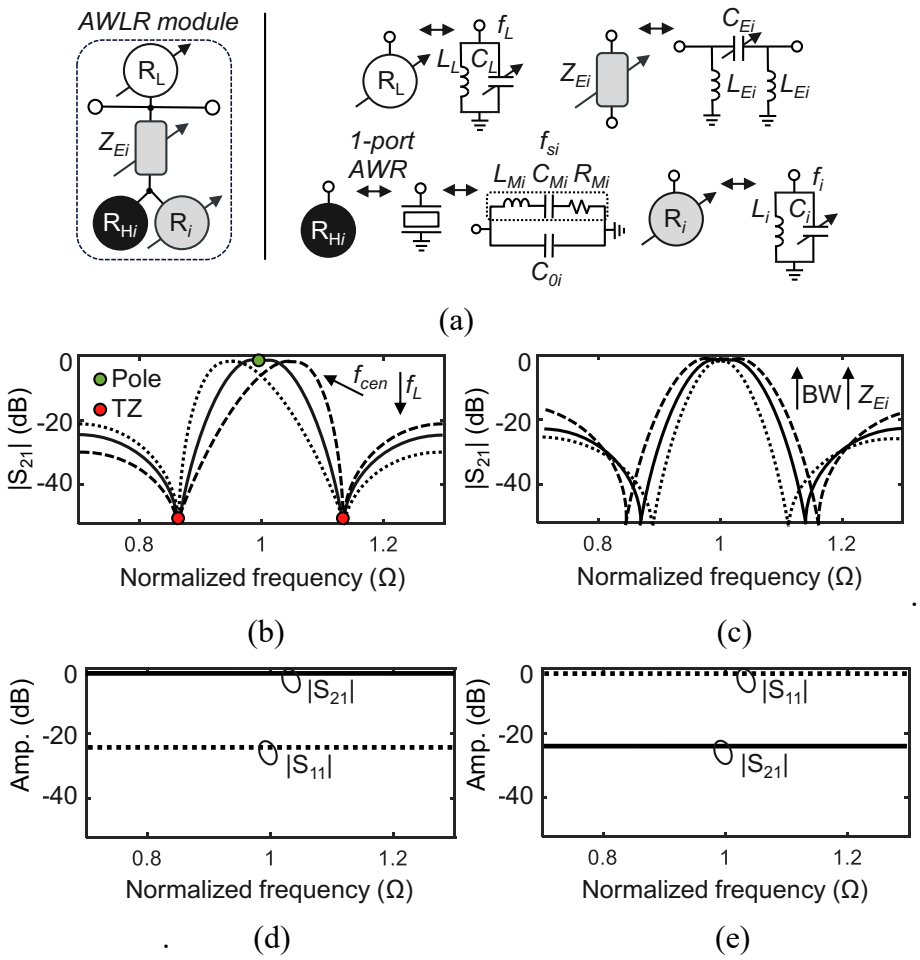


Figure 2.12. Multi-resonant AWLR module with multi-configurable and continuously-tunable TF characteristics: (a) Block diagram; (b) BPF response shaped by one pole and two TZs, showcasing continuous tuning of the f_{cen} achieved by altering f_L; (c) Continuous BW control; (d) AP mode; (e) AS mode [91].

Benefiting from the ability to intrinsically-switch ON and OFF the AWLR module by altering Z_{Ei} *and* f_i, multiple (i.e., *k)* AWLR modules can be interconnected in parallel within a multi-branch AWLR stage, as shown in the generalized multi-branch AWLR stage in Figure 2.13(a). This interconnection of AWLR modules is used to increase the f_{cen} TR in a progressive manner by sliding the passband of the multi-branch AWLR stage between the passbands of each AWLR module [Figure 2.13(b)]. This is achieved by altering f_i*s*, Z_{Ei}*s,* and by tuning the resonant frequency of R_L to continuously tune f_{cen} [Figure 2.13(c)]. For high order TFs, *N* multi-branch AWLR stages need to be cascaded with *N*+1 impedance inverters (*N*-1 inter-stage inverters $Z_{1,2}$-$Z_{N\text{-}1,N}$ and two external couplings inverters Z_{ex} as shown in Figure 2.13(d) to obtain a tunable quasi-elliptic-type BPF TF that comprises *N* poles and 2*N* TZs as

shown in Figure 2.13(e). To better illustrate the operating and tuning principles of the multi-stage AWLR BPFs concept, various design examples are discussed next.

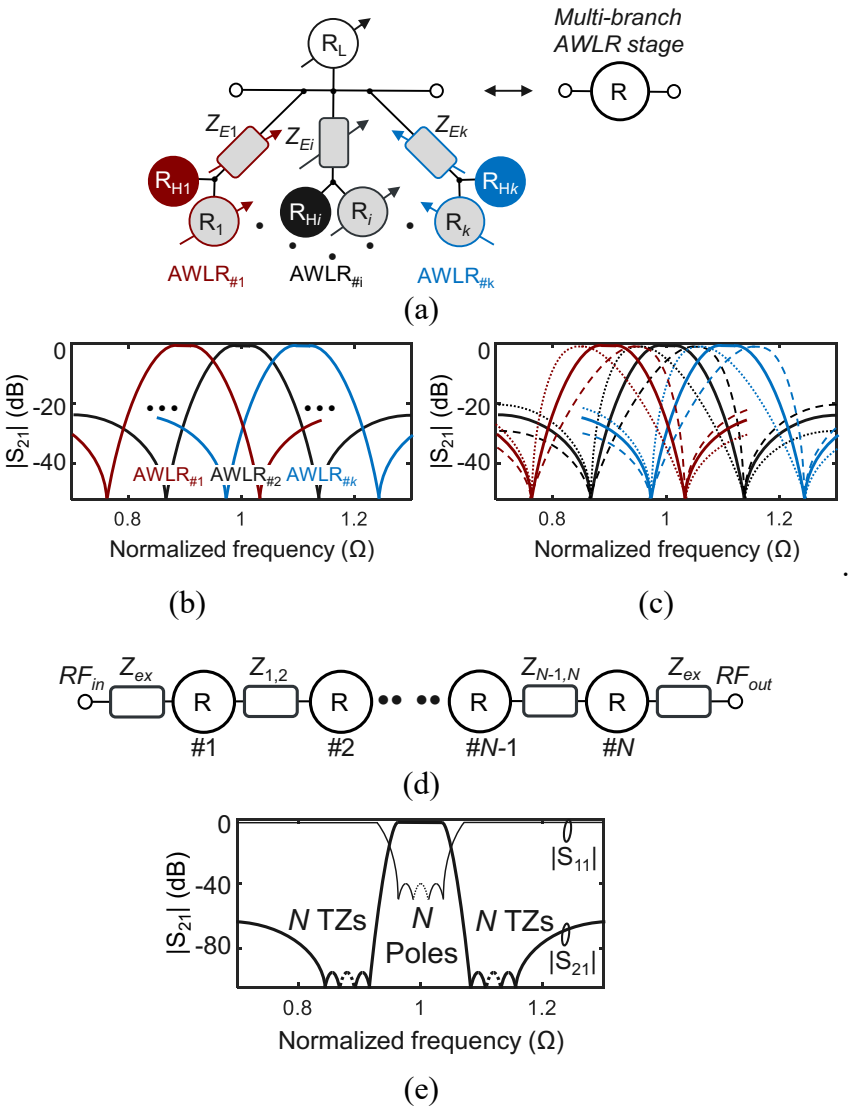


Figure 2.13. Multi-configurable multi-branch AWLR stage with extended continuously tunable TF characteristics and generalized higher-order BPF TFs and showcases of conceptual responses: (a) Generalized block diagram of a multi-branch AWLR stage with k AWLR modules; (b) Switching between the AWLR modules through $Z_{E1\text{-}k}$ and $R_{1\text{-}k}$ to facilitate discrete f_{cen} tuning; (c) Extended continuous f_{cen} tuning by tuning R_L and module switching; (d) Generalized higher order BPF block diagram; (e) Conceptual BPF response shaped by N poles and $2N$ TZs [91].

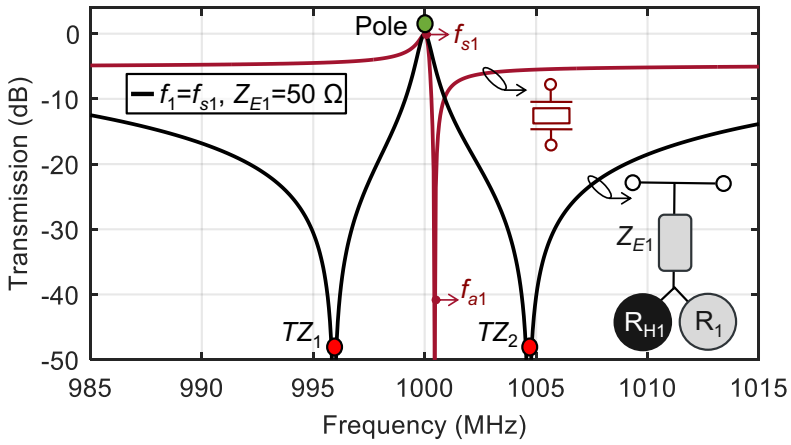
2.3.1.2 Multi-resonant-AWLR stage

The design and tuning principles of the multi-resonant AWLR stage are discussed here, which will be used to create higher-order TFs, as exemplified in later examples presented in Figure 2.17 to Figure 2.19.

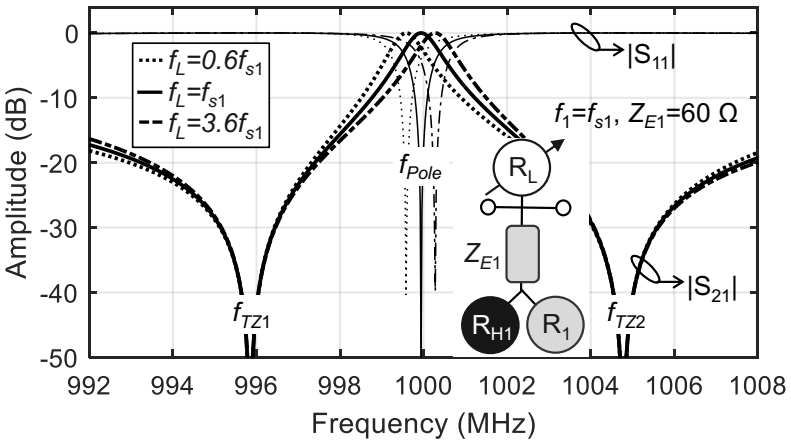
i) Single branch AWLR stage: The details of a single branch AWLR stage are shown in Figure 2.12 and Figure 2.14. It consists of one one-port type AWR–shaped by two tightly-coupled resonances, namely the series resonance: $f_{si}=1/2\pi(C_{Mi}\bullet L_{Mi})^{1/2}$ and the anti-resonance $f_{ai}=1/2\pi(L_{Mi}\bullet C_{Mi}\bullet C_{0i}/(C_{Mi}+C_{0i}))^{1/2}$ (see Figure 2.14(a))– that is connected in parallel with R_i. In this manner, the two resonances get decoupled and inverted through Z_{Ei} and the overall TF of the AWLR is shaped by one pole and two TZs as shown in Figure 2.14(a) (a) for a passband centered at 1 GHz. Whereas the pole of the overall TF appears at f_{si}, the location of the TZs depends on the resonant frequency $f_i=1/2\pi((C_i+C_{0i})\bullet L_i)^{1/2}$ of R_i. Specifically, when C_{0i}, C_i, L_i resonate at $f_i=1/2\pi((C_i+C_{0i})\bullet L_i)^{1/2}$ which coincides with f_{si}, the TZs are symmetrically-located around the transmission pole (as also discussed in for a simpler version of an AWLR in [47]).

ii) Tuning f_{cen}: By loading the two-resonator configuration in Figure 2.14(a) with an additional LE resonator R_L (as shown in Figure 2.12(a)) that resonates at $f_L=1/2\pi(C_L\bullet L_L)^{1/2}$, the f_{cen} of the passband can be tuned by altering f_L as illustrated in Figure 2.14(b). Specifically, when $f_L < f_{s1,}$ R_L loads Z_{E1} capacitively and moves the passband to lower frequencies. On the other hand, when $f_L > f_{s1,}$ R_L loads Z_{E1} inductively and moves the passband to higher frequencies. As such, by altering f_L between 0.6-3.6$f_{s1,}$ the f_{cen} of the passband can be continuously tuned between 999.6 MHz and 1000.3 MHz. In this case, the location of the pole and TZs can be specified using (2.6), and (2.7).

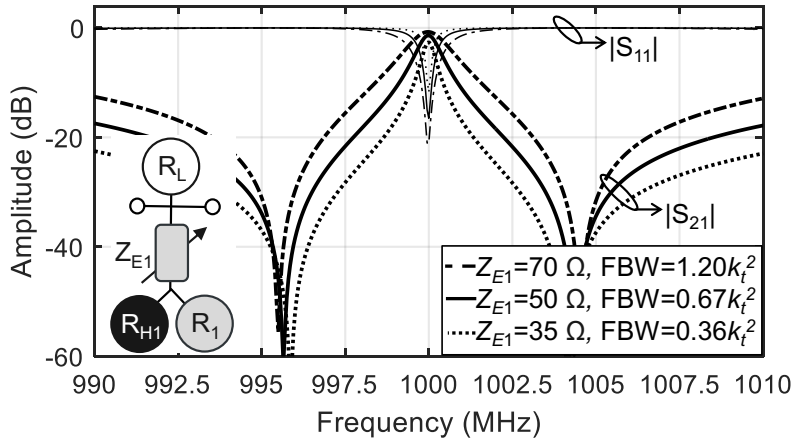
iii) Tuning FBW and reconfiguring TZs: FBW tunability can be obtained in a continuous manner by altering the impedance of Z_{E1}. For example, as shown in Figure 2.14(c) by varying Z_{E1} from 35- 70 Ω, the FBW can be tuned between 0.36-1.2k_t^2. As noticed, it can be made wider than the 0.4- 0.8k_t^2 limit of conventional AWR-based BPFs based on ladder and lattice configurations [23]. Moreover, the TZs can be tuned to be symmetrically or asymmetrically allocated around the pole by altering f_1, as illustrated in Figure 2.15(a).



(a)



(b)



(c)

Figure 2.14. (a) Simulated $|S_{21}|$ of a SAW resonator (f_{s1}= 1000 MHz, L_{M1}= 25.72 µH, $C_{M1}=1/(L_{M1}\bullet 4\pi^2 f_{s1}^2)$, C_{01}= 1.09 pF, k_t^2= 0.12%, $Q_{M1}=\infty$) and a multi-resonant AWLR f_{s1} stage that comprises one R_{H1} and one impedance inverter Z_{E1} and exhibits one pole and two TZs; (b) S-parameters of a multi-resonant stage comprising one R_{H1}, one R_L and one Z_{E1} demonstrating that f_{cen} tuning is controlled by f_L; (c) Alternative FBWs obtained by altering the Z_{E1} values: i) BW= 1.44 MHz (Z_{E1}=70 Ω), ii) BW= 0.8 MHz (Z_{E1}= 50 Ω), iii) BW= 0.43 MHz (Z_{E1}=35 Ω) when: $f_L=f_1=f_{s1}$. In these examples, L_L=2 nH, L_1=2.6 nH [91].

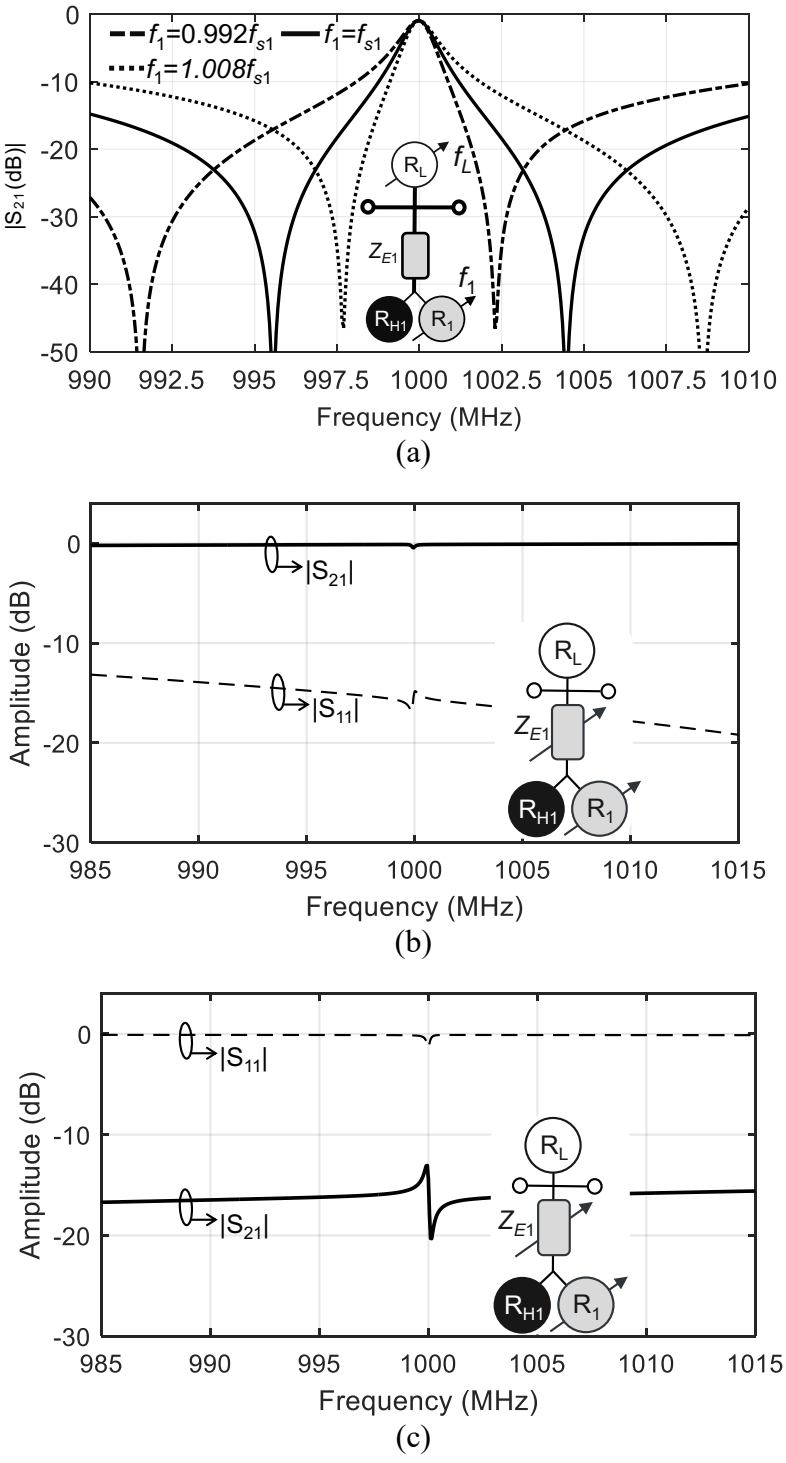


Figure 2.15. Simulated response of the multi-resonant AWLR stage for different operational modes: (a) TZs control around the transmission pole achieved by altering f_1 when Z_{E1}=70 Ω and f_L= f_{s1}; (b) AP mode achieved by setting f_1=2.16f_{s1}, Z_{E1}=100 Ω and f_L=f_{s1}; (c) AS mode obtained by setting f_1= 0.78f_{s1}, Z_{E1}=10 Ω and f_L=f_{s1}. In these examples, L_L=2 nH, L_1=2.6 nH [91].

$$f_{pole} = \frac{1}{2\pi}\sqrt{\frac{\sqrt{L_i L_L \omega_i^2 (L_i L_L \omega_L^4 \omega_i^2 \omega_{si}^4 + 4\omega_L^4 - 2\omega_L^2 \omega_{si}^2) + 1} + L_L L_i \omega_L^2 \omega_i^2 \omega_{si}^2 - 1}{2 L_L L_i \omega_L^2 \omega_i^2}} \quad (2.6)$$

$$f_{TZ1,2} = \frac{1}{4\pi}\sqrt{\sqrt{2}(\omega_i^2 \pm \sqrt{(C_{Mi} L_i \omega_i^2 \omega_{si}^2 + (\omega_i - \omega_{si})^2)(C_{Mi} L_i \omega_i^2 \omega_{si}^2 + (\omega_i + \omega_{si})^2)} + \omega_{si}^2 + C_{Mi} L_i \omega_i^2 \omega_{si}^2)} \quad (2.7)$$

iv) Reconfigurable AP and AS modes: The multi-resonant AWLR stage also allows for two additional reconfigurable TF states, namely an AP and an AS response that can be obtained by readily reconfiguring the resonant frequency of R_1 and the impedance of Z_{E1}. Specifically, an AP response can be created by setting $f_1 = 2.16 f_{s1}$ and $Z_{E1} = 100\ \Omega$ as shown in Figure 2.15(b). Likewise, the AS mode of operation can be materialized by setting $f_1 = 0.78 f_{s1}$ and $Z_{E1} = 10\ \Omega$ as illustrated in Figure 2.15(c); in both cases f_L is fixed at f_{s1}. The loading resonator R_L enables continuous f_{cen} tuning, while the switching ON/OFF is achieved by altering R_1 and Z_{E1}. It should be noted that the maximum f_{cen} TR of the AWLR is limited by the maximum TR of R_L which is bounded by the available capacitance ratio of semiconductor varactors.

v) Increasing f_{cen} TR: By leveraging the switch ON/OFF capability of the AWLR module, a multi-branch AWLR architecture can be considered to increase the f_{cen} TR as shown in Figure 2.13. A specific example of a two-branch configuration is provided in Figure 2.16(a) to best explain the tuning enhancement principles. In this case, AWLR modules $AWLR_{\#1}$ and $AWLR_{\#2}$ (i.e., k=2 in Figure 2.13(a)) are used. They are based on two commercially available AWRs with the following characteristics: (for i=1 and 2: L_{Mi}=*25.72* μH, C_{0i}=1.09 pF, Q_{Mi}=9,500, f_{s1}= 999.6 MHz, and f_{s2}= 1000.7 MHz). By reconfiguring Z_{E1}, Z_{E2}, f_1 and f_2, the passband of the multi-branch AWLR can be altered between the passbands of $AWLR_{\#1}$ (i.e., $f_{cen}=f_{s1}$=999.6 MHz) and $AWLR_{\#2}$ (i.e., $f_{cen}= f_{s2}$=1000.7 MHz) as shown in Figure 2.16(a). The red traces correspond to the case when $AWLR_{\#1}$ is switched ON and when $AWLR_{\#2}$ is intrinsically switched OFF whereas the black traces correspond to the case where $AWLR_{\#1}$ is intrinsically switched OFF and when $AWLR_{\#2}$ is switched ON. To achieve continuous f_{cen} tuning between f_{s1} and f_{s2}, the resonant frequency f_L needs to be tuned while altering the Z_{Ei} and f_i of each $AWLR_{\#i}$ as shown in Figure 2.16(b). Specifically, by intrinsically-switching ON and OFF $AWLR_{\#1}$, $AWLR_{\#2}$ and by altering f_L from 0.8 to 3.6f_s, f_{cen} can be tuned between 998.55 MHz and 1000.6 MHz which is 2x larger than in the case of the single-branch configuration in Figure 2.14(b).

It should be noted that for continuously-tunable TF, the f_{si}s of the AWR need to be appropriately selected so that there is an overlap between the passbands of each AWLR. R_i and R_L are implemented by tunable LE resonators using commercially available varactors with a wide capacitance TR– higher capacitance tuning results in a broader tuning of the response, thereby enabling effective tuning of the AWLR characteristics.

When selecting the varactor model, a varactor that provides a wide capacitance TR alongside a good *Q*-factor needs to be used. For instance, the MACOM MA46H072 varactor demonstrates a total capacitance TR of C_T=1- 8 pF and possesses a *Q*-factor of 3,000 at 4V 50 MHz, according to the datasheet in [102]. The average capacitance is chosen ($\bar{C}_T$= 2.83 pF=C_L=C_i) as the initial reference for selecting the appropriate inductors. Utilizing the formula $f=1/2\pi(L\cdot C)^{1/2}$, the desired L_L inductance of R_L is calculated to be $L_L=1/((2\pi\cdot f_s)^2\cdot C_L)$, and the desired L_i inductance of R_i is calculated to be $L_i=1/((2\pi\cdot f_{si})^2\cdot C_i)$. Both f_i and f_L can be experimentally adjusted by varying the applied reverse-voltage on the corresponding varactor diode representing C_i and C_L. The impedance inverter Z_{Ei} is represented by its π-type first-order high-pass circuit equivalent, with inductance $L_{Ei}= Z_{Ei}/(2\pi\cdot f_{si})$ and capacitance $C_{Ei}= 1/(2\pi\cdot f_{si}\cdot Z_{Ei})$. Tuning of Z_{Ei} can be achieved by varying the applied reverse voltage on the corresponding varactor diode representing C_{Ei}.

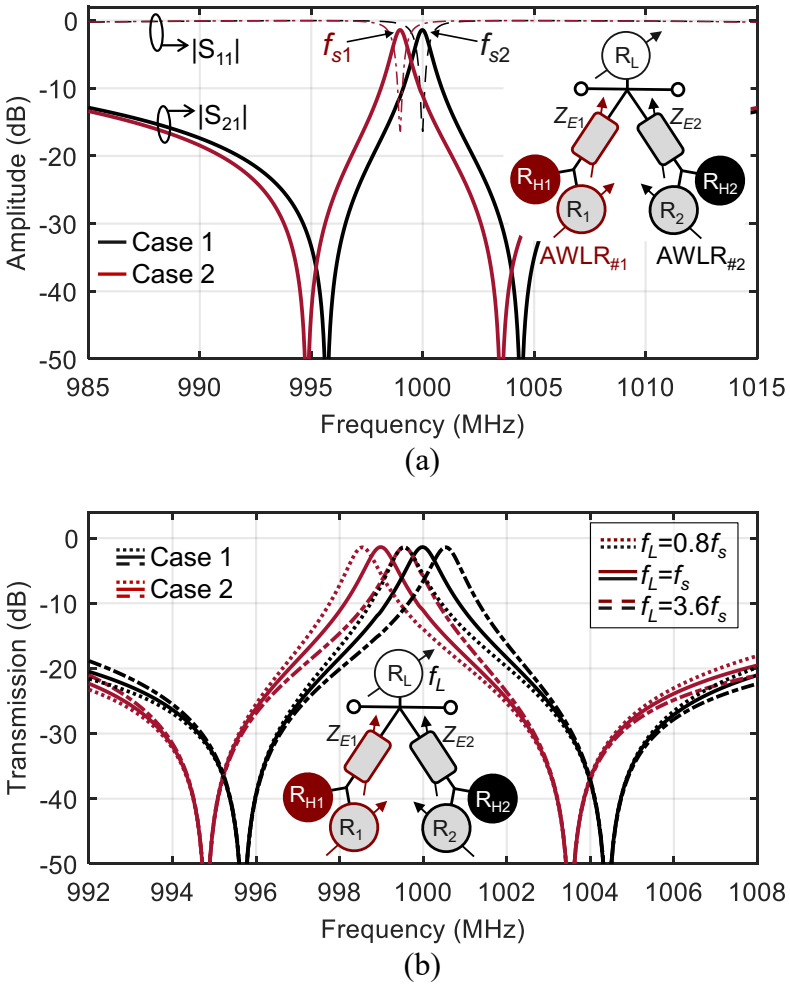


Figure 2.16. Linear simulation of a multi-branch AWLR stage comprising two-AWLR modules (AWLR$_{\#1}$, AWLR$_{\#2}$): (a) Discrete f_{cen} tuning by intrinsic switching ON/OFF each of the AWLR modules (AWLR$_{\#i}$s) achieved by altering $f_{1,}f_2$ and Z_{E1}, Z_{E2}. Case 1: AWLR$_{\#1}$ ON and AWLR$_{\#2}$ OFF: f_1=f_s, f_2=2.16f_s, Z_{E1}=50 Ω, Z_{E2}=100 Ω, Case 2: AWLR$_{\#1}$ OFF and AWLR$_{\#2}$ ON, f_1=2.16f_s, f_2=f_s, Z_{E1}=100 Ω, Z_{E2}=50 Ω when f_L=f_s, where $f_s = (f_{s1} \bullet f_{s2})^{1/2}$; (b) Utilizing the intrinsic switch capability of AWLR$_{\#i}$s to extended the f_{cen} tuning and continuously tuning it by altering f_L. (The rest of design parameters are L_i=2.6 nH, L_L= 2 nH) [91].

2.3.1.3 High-order multi-configurable TFs

N^{th}-order TFs can be realized by coupling N multi-resonant stages using N+1 impedance inverters (N-1 inter-stage inverters $Z_{1,2}$-$Z_{N\text{-}1,\ N}$ and two external coupling inverters Z_{ex}, as shown in Figure 2.13(d)). The block diagram of an example two-stage/three-branch BPF configuration (i.e., N=2, k=3) is provided in Figure 2.17(a). In this case, two three-branch AWLR stages are cascaded in series with $Z_{1,2}$ and are coupled to the RF ports using Z_{ex}. Each three-branch AWLR comprises three AWLR

modules namely AWLR$_{\#1}$, AWLR$_{\#2}$ and AWLR$_{\#3}$ that are shaped by AWRs with L_{Mi}=25.72 µH, C_{0i}=1.09 pF, Q_{Mi}=9,500 and f_{s1}=999.6 MHz, f_{s2}=1000.7 MHz and f_{s3}=1001.7 MHz. The overall BPF has a quasi-elliptic TF shaped by two-poles and four-TZ, as shown in Figure 2.17(b) for the case when AWLR$_{\#2}$ is ON and AWLR$_{\#1}$ and AWLR$_{\#3}$ are intrinsically switched OFF. Figure 2.18(a) illustrates the intrinsic switching ON alteration between AWLR$_{\#1}$, AWLR$_{\#2}$, and AWLR$_{\#3}$ that is achieved by varying f_1, f_2, f_3, and Z_{E1}, Z_{E2}, Z_{E3}. Figure 2.18(b) shows how continuous f_{cen} tuning between 999.15 and 1002.35 MHz can be achieved by varying f_L from 0.8 to 3.6f_s [where $f_s = (f_{s1}f_{s2}f_{s3})^{1/3}$] and by intrinsically switching ON/OFF AWLR$_{\#1}$, AWLR$_{\#2}$ and AWLR$_{\#3}$. In Figure 2.19(a), BW tuning between 0.55 and 1.99 MHz (i.e., FBW= 0.46–1.66k_t^2) is illustrated when AWLR$_{\#2}$ is ON and AWLR$_{\#1}$, AWLR$_{\#3}$ are OFF. These states are acquired by increasing Z_{E2} values from 35 to 70 Ω. Lastly, Figure 2.19(b), (c) shows how an AP mode and an AS mode of operation can be obtained by altering f_is and Z_{Ei}s respectively.

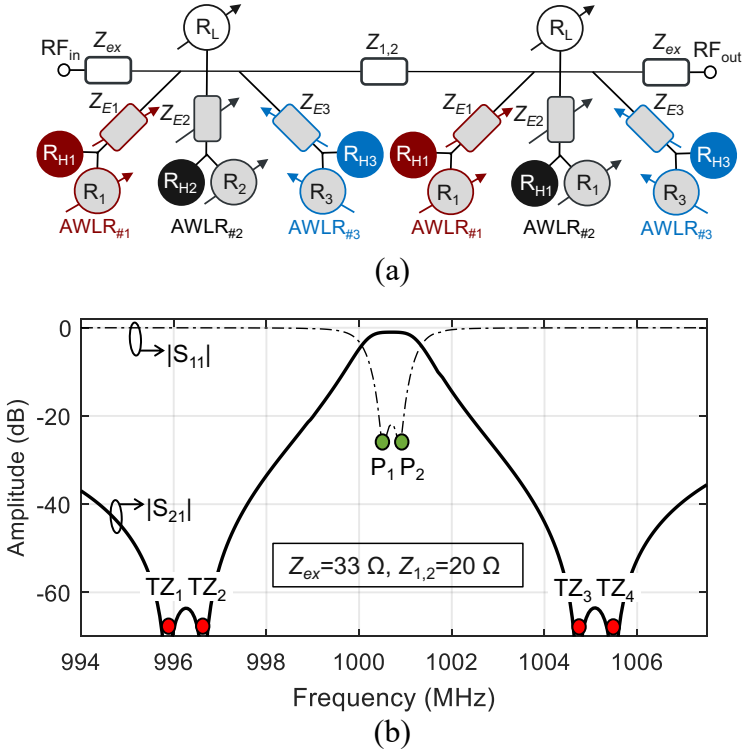
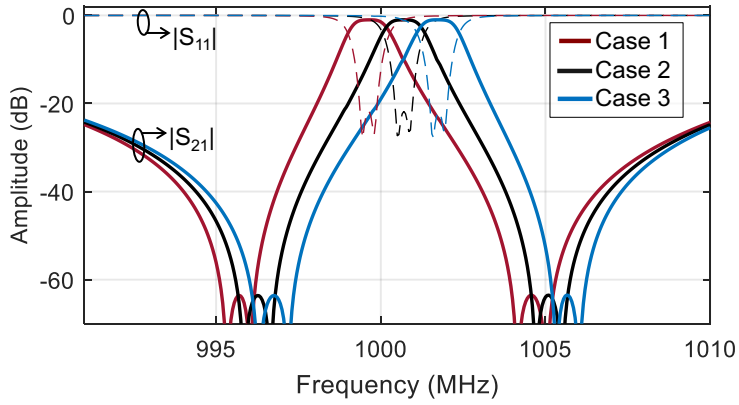
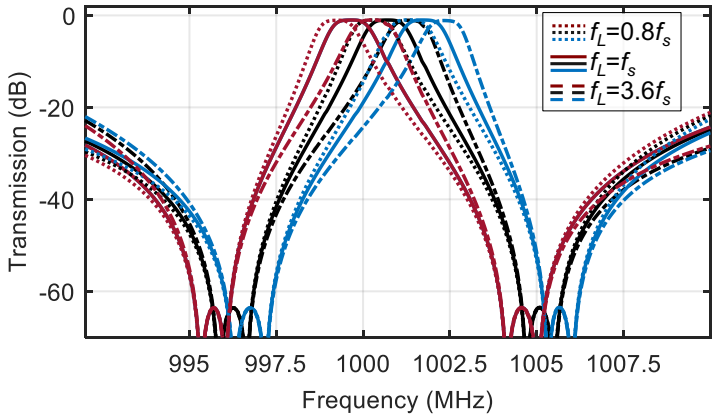


Figure 2.17. Frequency-tunable quasi-elliptic BPF using two-stage/three-branch AWLR modules (i.e., AWLR$_{\#1}$, AWLR$_{\#2}$, AWLR$_{\#3}$): (a) Circuit schematic; (b) Simulated S-parameters obtained through linear circuit simulation with AWLR$_{\#2}$ intrinsically switched ON and AWLR$_{\#1}$, AWLR$_{\#3}$ intrinsically switched OFF: f_1=f_3=2.16f_s, f_2=f_s, Z_{E1}=Z_{E3}=100 Ω, Z_{E2}=55 Ω, f_L=f_s, demonstrating a two-pole/four-TZ AWLR BPF (N=2, k=3 in Figure 2.13). (The remaining design parameters are: L_i= 2.6 nH, L_L= 2 nH, Z_{ex}=33 Ω, $Z_{1,2}$=20 Ω) [91].



(a)



(b)

Figure 2.18. Frequency-tunable quasi-elliptic BPF using two-stage/three-branch AWLRs (Figure 2.17(a)): (a) Intrinsic switching-OFF alteration between AWLR$_{\#i}$s achieved by varying f_is, and Z_{Ei}s when $f_L = f_s$; The cases shown are: i) Case 1 (red traces): f_{cen}=999.6 MHz, when AWLR$_{\#1}$ ON and AWLR$_{\#2}$ and AWLR$_{\#3}$ OFF obtained by setting $f_1 = f_s$, and $f_2 = f_3 = 2.16f_s$, and Z_{E1}= 55 Ω, and $Z_{E2} = Z_{E3}$= 100 Ω, ii) Case 2 (black traces): f_{cen}=1000.7 MHz, when AWLR$_{\#2}$ is ON and AWLR$_{\#1}$ and AWLR$_{\#3}$ are OFF obtained by setting $f_2 = f_s$, and $f_1 = f_3 = 2.16f_s$, and Z_{E2}= 55 Ω, and $Z_{E1} = Z_{E3}$= 100 Ω, iii) Case 3 (blue traces), f_{cen}=1001.7 MHz, correspond to the case where AWLR$_{\#3}$ ON and AWLR$_{\#1}$ and AWLR$_{\#2}$ OFF obtained by setting $f_3 = f_s$, and $f_1 = f_2 = 2.16f_s$, and Z_{E3}= 55 Ω, and $Z_{E1} = Z_{E2}$= 100 Ω; (b) Continuous f_{cen} tuning achieved by varying f_L and extended by intrinsically switching ON/OFF AWLR$_{\#i}$s [91].

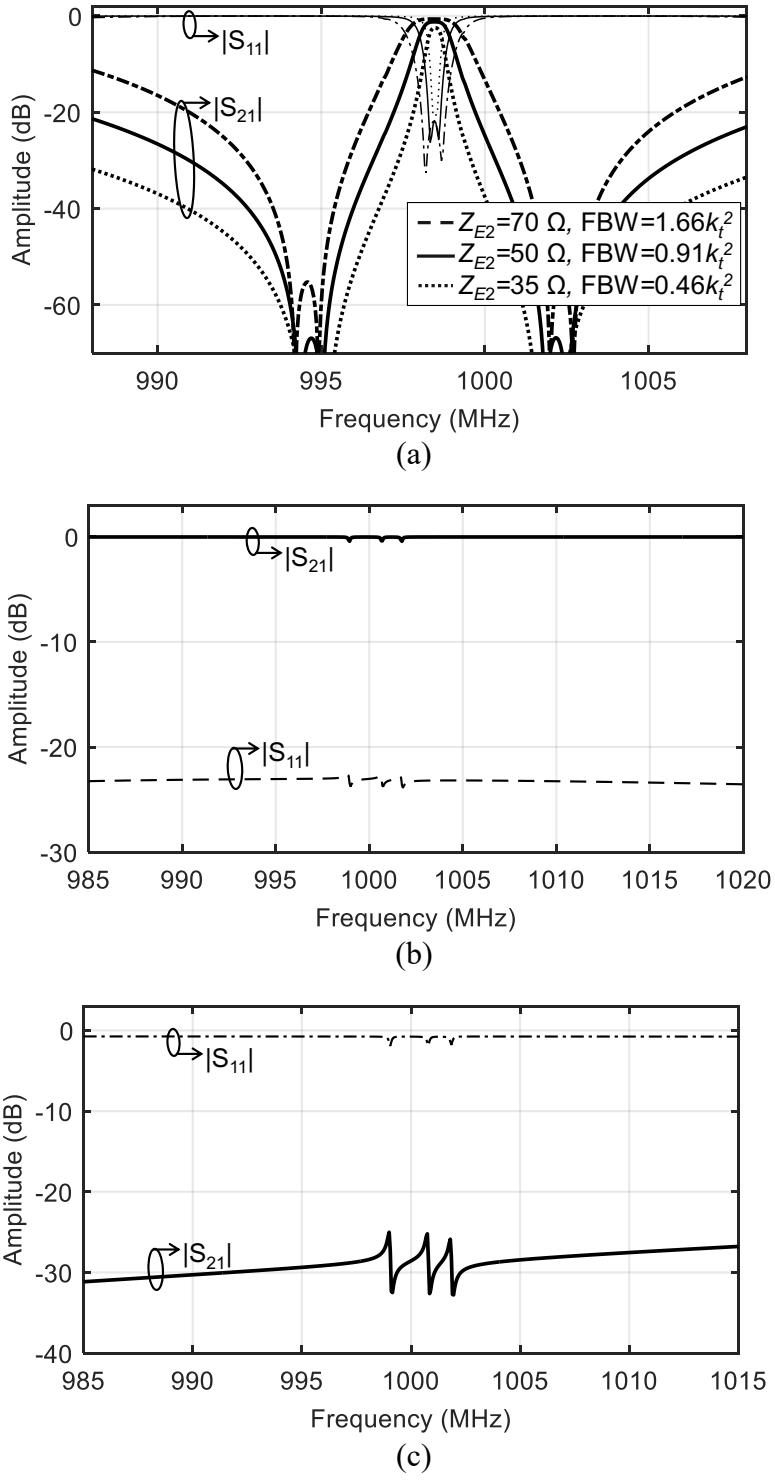


Figure 2.19. Simulated S-parameters obtained through linear circuit simulations of the two-stage/ three-branch AWLR based BPF in Figure 2.17(a) demonstrating: (a) Alternative FBWs when $AWLR_{\#2}$ is intrinsically switched ON and $AWLR_{\#1}$, $AWLR_{\#3}$ are intrinsically switched OFF, achieved by altering the Z_{E2} values resulting in: i) BW= 1.99 MHz (Z_{E2}= 35 Ω); ii) BW= 1.1 MHz (Z_{E2}= 50 Ω); iii) BW= 0.55 MHz (Z_{E2}= 70 Ω); (b) AP mode obtained by setting f_1= f_2= f_3=2.16f_s, Z_{E1}=Z_{E2}=Z_{E3}= 100 Ω and f_L=f_s; (c) AS mode by setting f_1=f_2=f_3=0.78f_s, Z_{E1}=Z_{E2}=Z_{E3}=15 Ω and f_L=f_s [91].

2.3.1.4 Finite *Q* effect on the filter's performance

To evaluate the RF performance of the two-pole/four-TZ, three-branch, AWLR-based BPF in a practical realization scenario, a more realistic AWR BVD model is considered for R_{Hi} [Figure 2.20]. Losses are incorporated in both the impedance inverters (implemented by their π-type first-order, high-pass, circuit equivalent) and the resonators R_i and R_L. Specifically, the effect of Q_{Mi} (unloaded *Q*-factor of the AWRs), Q_{si} (effective *Q*-factor of the AWRs incorporating RF electrical losses represented by R_{si} note that when R_{si}=0 Ω, Q_{si}=Q_{Mi}=9500, and when R_{si}=3 Ω, Q_{si}=8080), and Q_{LE} (*Q*-factor assigned to the LE resonators and LE inverters) are considered.

To illustrate the finite *Q* effect when R_i is i) a resonating node represented by an LC resonator (Case 1) and ii) a non-resonating node represented by an inductor (Case 2), the S-parameters of the two-pole/four-TZ, three-branch, AWLR-based BPF are plotted in Figure 2.21(b). It can be observed that when considering lossless LEs [Q_{LE}=∞], both Case 1 and Case 2 exhibit the same in-band characteristics. However, the TZs in Case 2 are further away from the passband. Lowering Q_{LE} makes Case 2 to have a wider FBW and TZs with higher attenuation when compared to Case 1. Case 1 and Case 2 exhibit almost the same IL levels when lowering Q_{LE}; however, Case 1 showcases a higher effective Q_{eff}s.

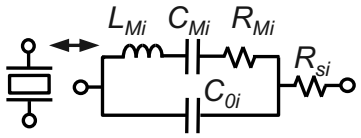


Figure 2.20. A more realistic BVD model of the AWRs, incorporating R_{si} to represent the RF electrical losses in a realistic resonator.

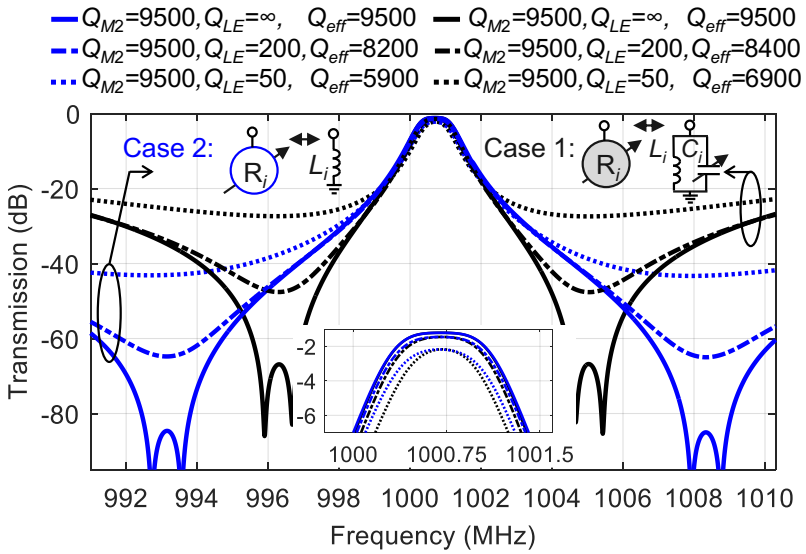
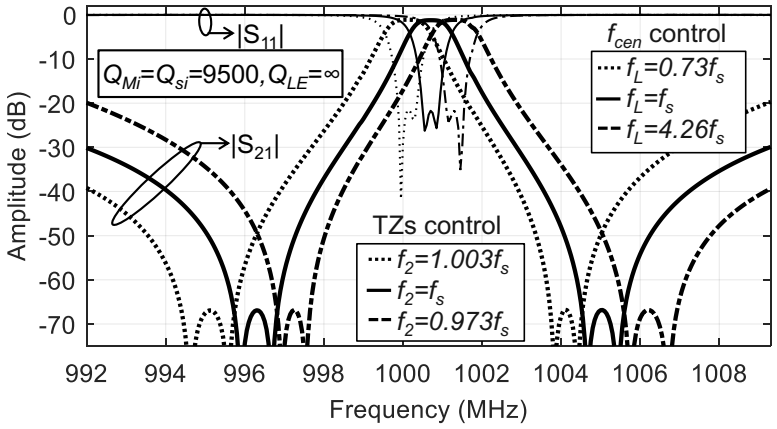
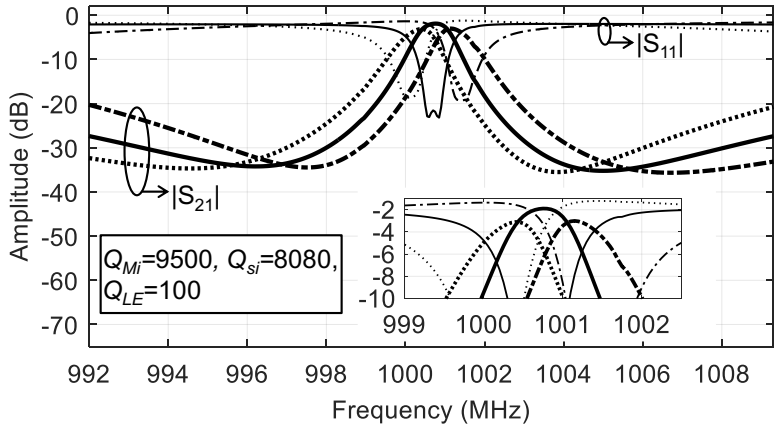


Figure 2.21. Simulated S-parameters of the two-pole/four-TZ, three-branch, AWLR based BPF in Figure 2.17(a) when AWLR$_{\#2}$ is intrinsically switched ON and AWLR$_{\#1}$, and AWLR$_{\#3}$ are intrinsically switched OFF. They are obtained by setting $f_2 = f_s$, and $f_1 = f_3 = 2.16f_s$, $Z_{E2} = 50\ \Omega$, $Z_{E1} = Z_{E3} = 100\ \Omega$, and $f_L = f_s$. The finite Q-factor effect is demonstrated when: i) R_i is represented by an LC resonator (black curves), and ii) R_i is represented by an inductor (blue curves) [91].

To demonstrate the Q_{LE} effect on the continuous f_{cen} tuning performance, two tuning scenarios are considered: i) lossless scenario in Figure 2.22(a) with $Q_{LE} = \infty$ and Q_{Mi}=Q_{si} = 9,500 for the AWRs. ii) lossy scenario in Figure 2.22(b) with Q_{LE} = 100 for all of the LE resonators and inverters, and Q_{Mi} = 9,500, Q_{si} = 8,080 for the AWRs. As shown, by altering f_L from 0.73 to 4.26f_s, in the lossless case, f_{cen} is continuously tunable from 1000.1 MHz to 1001.3 MHz. However, when loss is added, the f_{cen} TR narrows, ranging from 1000.32 to 1001.23 MHz. In the lossy scenario, tuning f_{cen} away from f_{si} results in degradation of the FBW at both edges of the passband, leading to a reduced TR for the f_{cen} compared to the lossless scenario [91]. To elaborate further on the finite Q_{LE} effect on the continuous f_{cen} tuning capability, two additional lossy f_{cen} tuning examples are considered in Figure 2.23: i) in the first lossy scenario, Q_{Mi} = 9,500, Q_{si} = 8,080, and Q_{LE} = 250, the BW is 0.96 MHz (i.e., FBW = 0.8k_t^2), and f_{cen} tunes from 1000.27 to 1001.29 MHz, TR:100.1 ii) in the second lossy scenario, Q_{Mi} = 9,500, Q_{si} = 8,080, and Q_{LE} = 100, the BW is 0.9 MHz (i.e., FBW = 0.76k_t^2), and f_{cen} tunes from 1000.33 to 1001.23 MHz, TR:100.89. With lower Q_{LE}, the FBW narrows, and the f_{cen} TR is reduced.



(a)



(b)

Figure 2.22. Simulated S-parameters of the two-pole/four-TZ three-branch AWLR-based BPF in Figure 2.17(a) when AWLR$_{\#2}$ is intrinsically switched ON and AWLR$_{\#1}$, AWLR$_{\#3}$ are intrinsically switched OFF. They are obtained by setting $f_2 = f_s$, and $f_1 = f_3 = 2.16f_s$, $Z_{E2} = 40\ \Omega$, $Z_{E1} = Z_{E3} = 100\ \Omega$, and $f_L = f_s$, demonstrating f_{cen} tuning by varying f_L for: (a) lossless ($Q_{Mi} = 9500$, $Q_{LE} = \infty$, and $R_{si} = 0\ \Omega$); (b) lossy ($Q_{Mi} = 9500$, $Q_{si} = 8080$ [$R_{si} = 3\ \Omega$], and $Q_{LE} = 100$) [91].

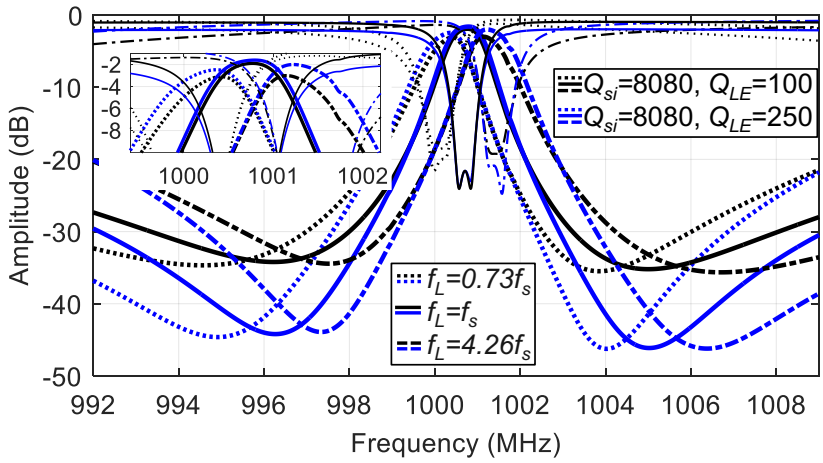


Figure 2.23. Simulated S-parameters of the two-pole/four-TZ, three-branch, AWLR based BPF in Figure 2.17(a) when AWLR$_{\#2}$ is intrinsically switched ON and AWLR$_{\#1}$, and AWLR$_{\#3}$ are intrinsically switched OFF. They are obtained by setting $f_2 = f_s$, and $f_1 = f_3 = 2.16f_s$, $Z_{E2} = 40\ \Omega$, $Z_{E1} = Z_{E3} = 100\ \Omega$, and $f_L = f_s$. The TF demonstrates f_{cen} tuning by varying f_L for various lossy cases: i) $Q_{si} = 8080$, $Q_{LE} = 250$ and; ii) $Q_{si} = 8080$, and $Q_{LE} = 100$ [91].

2.3.1.5 FBW effect on f_{cen} tuning

To evaluate the effect of the passband BW on the f_{cen} tuning performance, two different example cases are considered and are provided in Figure 2.24 for a BW of 1.07 MHz and 1.55 MHz (designed at 1000.7 MHz). It is observed that when the BW is set to 1.07 MHz (Case 2), the f_{cen} tunes from 1000.15 MHz to 1001.25 MHz, resulting in a f_{cen} TR of 100.11%:1. When the BW is increased to 1.55 MHz (Case 1), the f_{cen} tunes from 999.95 MHz to 1001.4 MHz, yielding a TR of 100.14%:1. Hence, it can be concluded that wider BW passbands can have wider f_{cen} TR. As an additional advantage to be highlighted, the FBW isn't limited by the k_t^2 limit as in conventional ladder, or lattice-based AWR BPFs [23].

2.3.1.6 FoM effect on TF performance

The performance of the AWRs is characterized by their k_t^2 and Q_{Mi}, through a Figure of Merit: (FoM)=k_t^2.Q_{Mi} which is constant as discussed in [103], [104]. Consequently, in conventional ladder/lattice AWR BPFs, increasing the k_t^2 with the purpose of increasing FBW, comes at the expense of Q_{Mi} and thus excess loss in the passband. On the contrary, in the case of the proposed multi-configurable AWLR BPF concept, enhanced FBW (i.e. > than the k_t^2 limit) and lower IL can be obtained for smaller k_t^2 as shown in the example cases in Figure 2.25 for the case of a two-pole/four-TZ, three-branch, AWLR-based BPF (Figure 2.17(a)). Specifically, the examples demonstrate the effect of altering AWRs' k_t^2 for a FoM=k_t^2.Q_{Mi}=10, while maintaining a fixed FBW for the BPF. As evidenced, an advantage the proposed architecture is to relax the AWR technology requirements for high k_t^2, in addition to facilitating f_{cen} tuning alongside multiple levels of TF reconfigurability.

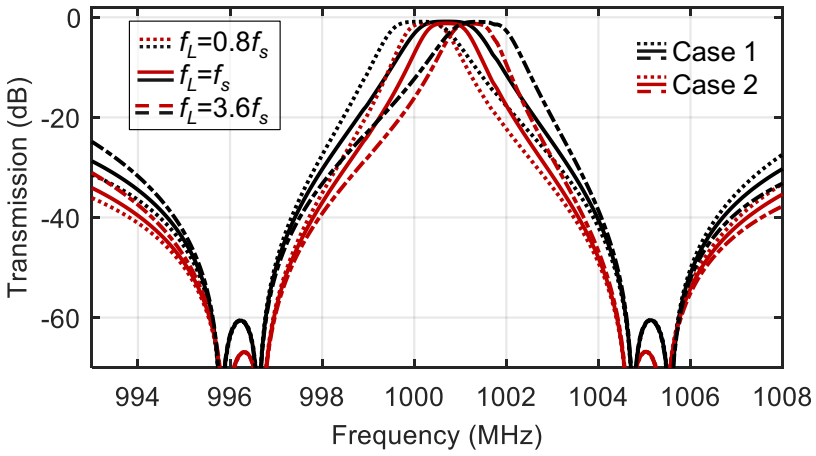


Figure 2.24. Simulated S-parameters of the two-pole/four-TZ, three-branch, AWLR stage based BPF (Figure 2.17(a)) illustrating the influence of FBW on the frequency TR. This analysis is carried out with AWLR$_{\#2}$ intrinsically switched ON and AWLR$_{\#1}$, and AWLR$_{\#3}$ OFF for: i) Case 1 (BW=1.55 MHz) obtained by setting: $f_2 = f_s$, $f_1 = f_3 = 2.16f_s$, Z_{E2}= 60 Ω, Z_{E1}= Z_{E3}= 100 Ω, ii) Case 2 (BW=1.07 MHz) obtained by setting: $f_2 = f_s$, $f_1 = f_3 = 2.16f_s$, Z_{E2} = 50 Ω, $Z_{E1} = Z_{E3}$ = 100 Ω [91].

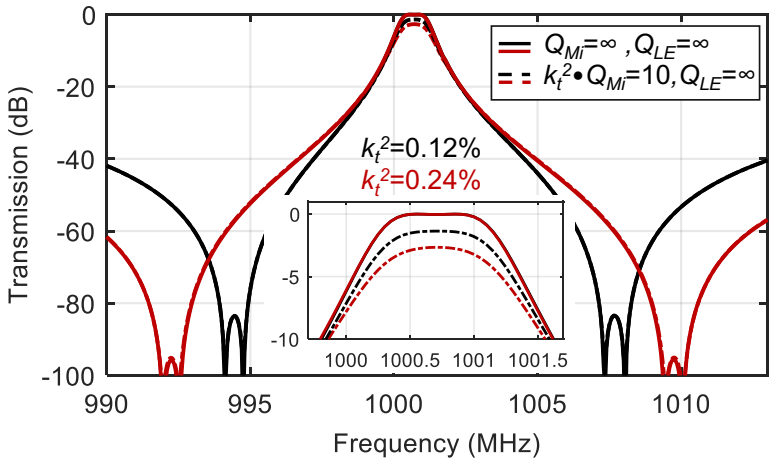


Figure 2.25. Simulated S-parameters of the two-pole/four-TZ, three-branch, AWLR stage based BPF (depicted in Figure 2.17(a)) demonstrating the impact of altering the (AWR)s' k_t^2 on both the in-band IL and the out-of-band IS, while maintaining a fixed FBW for the BPF. This analysis is conducted with $AWLR_{\#2}$ intrinsically switched ON and $AWLR_{\#1}$, $AWLR_{\#3}$ intrinsically switched OFF: obtained by setting $f_2 = f_s$, and $f_1 = f_3 = 2.16 f_s$, $Z_{E2} = 20\ \Omega$, $Z_{E1} = Z_{E3} = 100\ \Omega$, and $f_L = f_s$ [91].

2.3.2 Experimental validation

To experimentally validate the multi-configurable and continuously-tunable multi-branch AWLR-based BPF concept with continuously tunable f_{cen}, two filtering prototypes were designed, manufactured and characterized at L-band following the theoretical design examples presented in Section 2.3.1. The prototypes are based on two commercially available two terminal, one-port-type, SAW resonators from Tai-Saw Technology (TST) [105]: 1) TST TC0528A with series resonant frequency=999.87 MHz and Q_{M1}=Q_{s1}= 7640 and 2) TST TC0629A with series resonant frequency=1000.64 MHz and Q_{M2}=9300 and Q_{s2}= 7850 (Q_{si} is the effective Q factor of the SAW resonator when a series resistance R_s is present [106]) that are used in $AWLR_1$ and $AWLR_2$ of the multi-branch AWLR stages. The remaining low-Q resonators and impedance inverters (represented by their first-order high-pass π-type networks) were implemented using commercially available SMDs. Their element values are listed in Figure 2.26 and Figure 2.30. The prototypes were implemented on a Rogers 4003C substrate (dielectric constant ε_r = 3.55, thickness H = 0.813 mm, dielectric loss tangent tan (δ_D) = 0.0027, and 1 oz copper cladding).

2.3.2.1 Two-stage/two-branch AWLR-based BPF prototype

Figure 2.26 shows the circuit schematic and the photograph of the manufactured two-stage/two-branch AWLR BPF prototype, along with the details of the utilized SMD components. Figure 2.27. illustrates the RF-measured response that demonstrates continuous f_{cen} tuning between 999.74 and 1001.04 MHz (i.e., f_{cen} TR: 100.13%:1), which is has been obtained by intrinsically switching-ON and OFF $AWLR_{\#1}$ and $AWLR_{\#2}$. Specifically, when: i) $AWLR_{\#1}$ is ON and $AWLR_{\#2}$ is OFF, a TF with 3-dB BW of 0.72 MHz (i.e., FBW= $0.6k_t^2$) is created at 1000 MHz whose f_{cen} can be continuously tuned between 999.74 and 1000.29 MHz (TR:100.054%:1) with a minimum in-band IL between 5.1 and 4.1 dB (i.e., Q_{eff}=3,600-4,600) and when ii) $AWLR_{\#1}$ is OFF and $AWLR_{\#2}$ ON, a TF with 3-dB BW of 0.79 MHz (i.e., FBW= $0.66k_t^2$) is obtained at 1000.6 MHz and its f_{cen} can be tuned between 1000.44-1001.04 MHz with a minimum in-band IL of between 5.6 and 6.6 dB (i.e., Q_{eff}=3,000-3,600).

The RF-measured BW tuning capabilities of the two-stage BPF prototype are shown in Figure 2.28 for two different center frequencies. Specifically, Figure 2.28(a) corresponds to the case when: $AWLR_{\#1}$ is ON and $AWLR_{\#2}$ is OFF where the 3-dB BW tunes between 0.26 and 0.72 MHz (i.e., FBW= 0.22- $0.6k_t^2$, BW TR: 2.7:1) at 999.92 MHz with a minimum in-band IL ranges of 7.3 to 4.1 dB (i.e., Q_{eff}= 5900-4600). In Figure 2.28(b), $AWLR_{\#1}$ is OFF and $AWLR_{\#2}$ is ON and the 3-dB BW continuously tunes between 0.4 and 0.88 MHz (FBW= 0.34- $0.73k_t^2$, BW TR: 2.14:1) at 1000.7 MHz with minimum in-band IL between 4.3 and 6.44 dB (i.e., Q_{eff}= 5,500-3,600). The AS mode of operation is shown in Figure 2.29 (a). It exhibits a 27 dB IS over the measured frequency range. Lastly, Figure 2.29(b) illustrates the RF-measured response of the AP state with an average IL of 1.2 dB. The EM simulated states (obtained by co-simulations in Keysight ADS) are also added in these figures and demonstrate good agreement with the RF measurements. The f_{cen} TR of the filter can be augmented by adding additional branches in the multi-resonant AWLR which can be added on the same metallization layer or on additional layers that may be added using a multi-layer PCB stack-up.

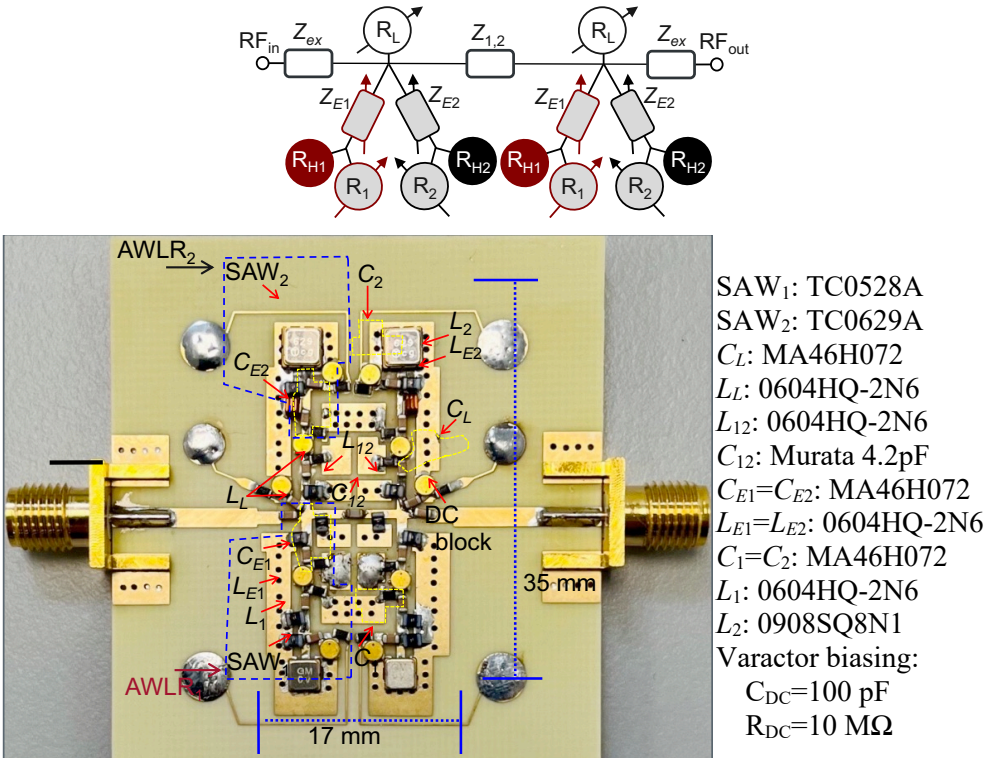


Figure 2.26. Manufactured prototype and block diagram of the two-stage/two-branch AWLR prototype (each AWLR consist of two AWLR-modules: AWLR$_{\#1}$ and AWLR$_{\#2}$) along with the utilized SMD components [91].

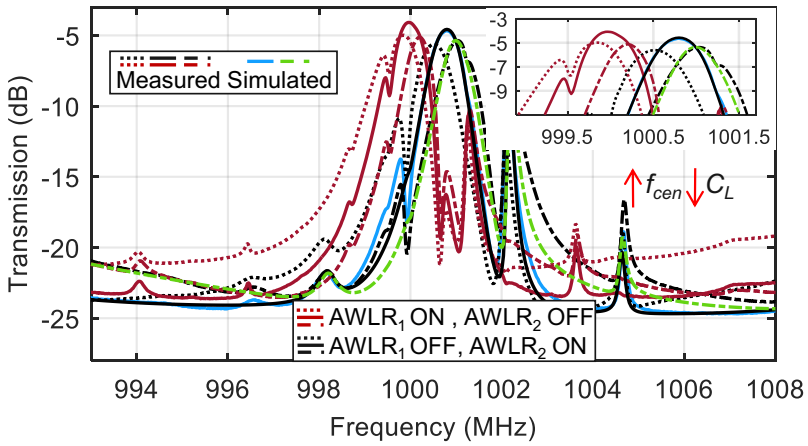
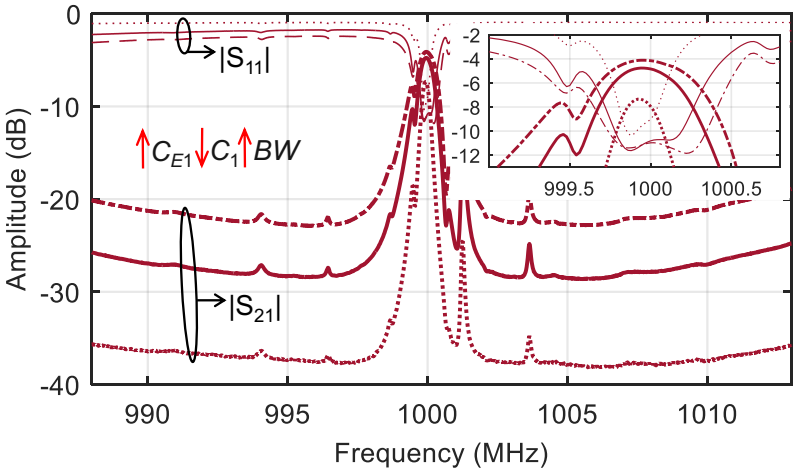
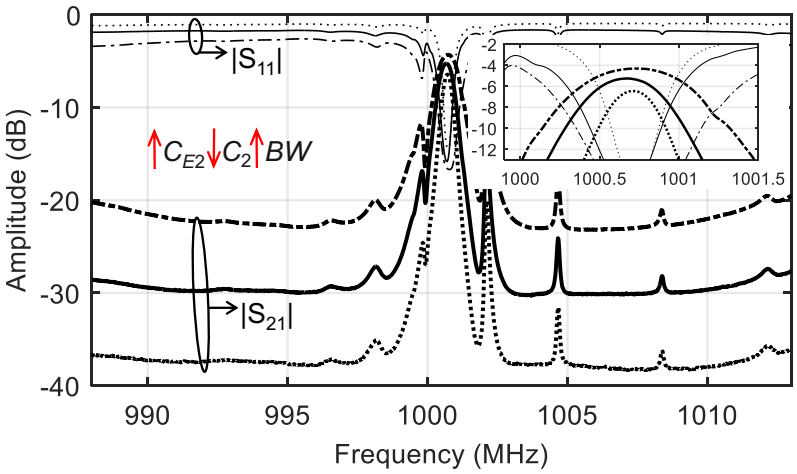


Figure 2.27. RF-measured S-parameters of the two-stage/ two-branch AWLR BPF prototype showcasing continuous f_{cen} tuning in the following configurations: i) AWLR$_{\#1}$ switched ON and AWLR$_{\#2}$ switched OFF; ii) AWLR$_{\#2}$ switched ON and AWLR$_{\#1}$ switched OFF. EM simulated states are also provided [91].



(a)



(b)

Figure 2.28. RF-measured S-parameters of the two-stage/two-branch AWLR BPF prototype showcasing continuously tunable FBW: (a) AWLR$_{\#1}$ intrinsically switched ON and AWLR$_{\#2}$ intrinsically switched OFF; (b) AWLR$_{\#1}$ intrinsically switched OFF and AWLR$_{\#2}$ intrinsically switched ON [91].

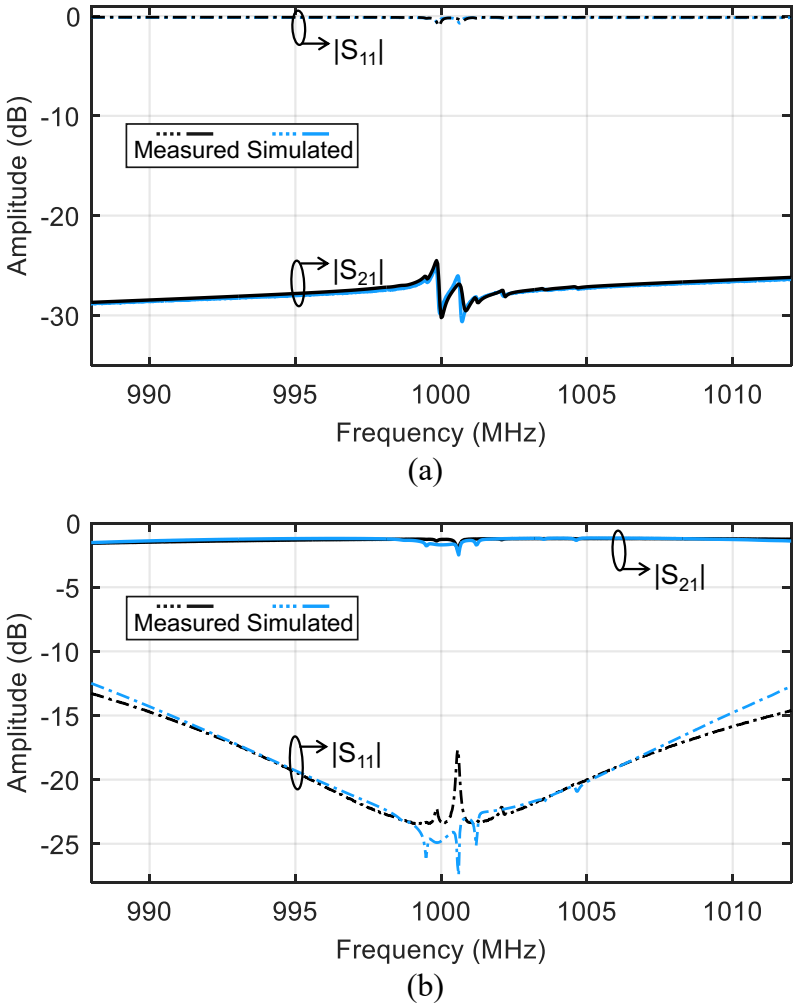


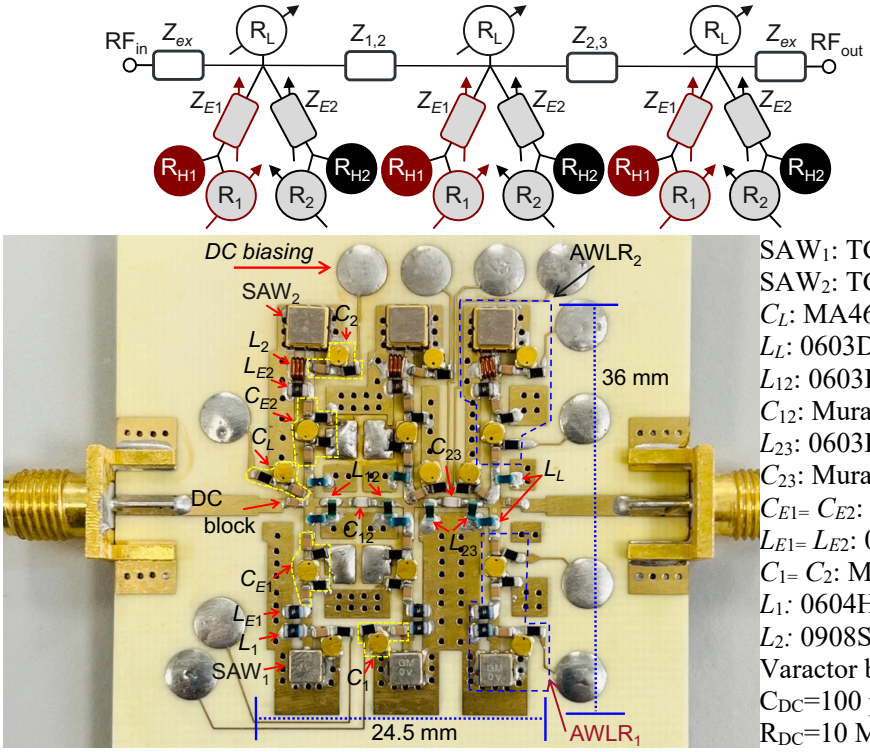
Figure 2.29. RF-measured S-parameters of the two-stage/two-branch AWLR BPF prototype exhibiting an: (a) AS mode; (b) AP mode. EM simulated states are also provided [91].

2.3.2.2 Three-stage/two-branch AWLR-based BPF

The block diagram and photograph of the manufactured three-stage/two-branch AWLR BPF prototype are presented Figure 2.30, along with the details of the utilized SMD components. Figure 2.31 illustrates the RF-measured response that demonstrates continuous f_{cen} tuning between 999.72 and 1000.95 MHz (i.e., TR of 100.12%:1), which has been obtained by intrinsically switching ON and OFF $AWLR_{\#1}$ and $AWLR_{\#2}$ respectively. Specifically, when: i) $AWLR_{\#1}$ is ON and $AWLR_{\#2}$ is OFF, a TF with 3-dB BW of 0.7 MHz (i.e., FBW= $0.57k_t^2$) is created at 999.92 MHz whose f_{cen} can be continuously tuned between 999.72 and 1000.2 MHz (TR of 100.05%:1) with a minimum in-band IL between 3.8 and 4.7 dB (i.e., Q_{eff}= 4,800-6,100) and when

ii) AWLR$_{\#1}$ is OFF and AWLR$_{\#2}$ is ON, a TF with 3-dB BW of 0.88 MHz (i.e., FBW= 0.73k_t^2) is obtained at 1000.66 MHz and its f_{cen} can be tuned between 1000.38 and 1000.95 MHz with a minimum in- band IL between 3.9 and 5.2 dB (i.e., Q_{eff}= 4,000-5,000).

The RF-measured BW tuning capabilities of the three-stage BPF prototype are shown in Figure 2.32 for two different center frequencies. Specifically, Figure 2.32(a) corresponds to the case when: AWLR1 is ON and AWLR$_{\#2}$ is OFF where the 3-dB BW tunes between 0.37 and 1.0 MHz (i.e., FBW= 0.31- 0.83k_t^2, BW TR: 2.67:1) at 999.92 MHz with a minimum in-band IL that ranges from 6.9 to 3.4 dB (i.e., Q_{eff}= 5,700- 6,400). In Figure 2.32(b), AWLR$_{\#1}$ is OFF and AWLR$_{\#2}$ is ON, and the 3-dB BW continuously tunes between 0.43 and 1.28 MHz (FBW= 0.36- 1.066k_t^2, BW TR: 2.97:1) at 1000.6 MHz with a minimum in-band IL between 6.17- 3.3 dB (i.e., Q_{eff}= 4,300- 6,100). The AS mode of operation is shown in Figure 2.33(a). It exhibits a 57 dB IS over the measured frequency range. Lastly, Figure 2.33(b) illustrates the RF-measured response of the AP state with an average IL of 1.2 dB. Figure 2.34, illustrates the f_{cen} tuning of the three-stage BPF prototype for the case where AWLR$_{\#2}$ is ON and AWLR$_{\#1}$ is OFF, at various FBW levels: i) for a BW=0.58 MHz (i.e., FBW=0.48 k_t^2), the f_{cen} TRs between 1000.48- 000.81 MHz, with a TR of 100.03:1; ii) For a BW=0.9 MHz (i.e., FBW=0.73 k_t^2) the f_{cen} TRs between 1000.38-1000.95 MHz, with a TR of 1000.06:1. The results agree well with the tuning principles explained in Section 2.3.1, where a higher f_{cen} TR is obtained for larger FBW. Overall, the EM simulated states in Figure 2.31, Figure 2.32, and Figure 2.34 show good agreement with the RF measurements, successfully validating the proposed AWLR-based BPF concept.



SAW_1: TC0528A
SAW_2: TC0629A
C_L: MA46H072
L_L: 0603DC3N9
L_{12}: 0603DC-4N3
C_{12}: Murata 3.3 pF
L_{23}: 0603DC-4N3
C_{23}: Murata 3.6 pF
C_{E1}= C_{E2}: MA46H072
L_{E1}= L_{E2}: 0604HQ-2N6
C_1= C_2: MA46H072
L_1: 0604HQ-2N6
L_2: 0908SQ8N1
Varactor biasing:
C_{DC}=100 pF
R_{DC}=10 MΩ

Figure 2.30. Manufactured prototype and block diagram of the three-stage/two-branch AWLR prototype (each AWLR stage consists of two AWLR-modules: $AWLR_{\#1}$ and $AWLR_{\#2}$) along with the utilized SMD components [91].

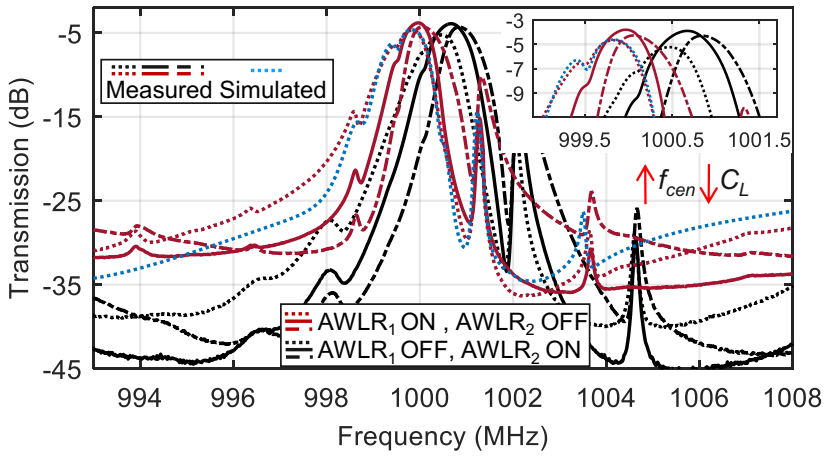


Figure 2.31. RF-measured S-parameters of the three-stage/two-branch AWLR BPF prototype showcasing continuous f_{cen} tuning in the following configurations: i) $AWLR_{\#1}$ intrinsically switched ON and $AWLR_{\#2}$ intrinsically switched OFF (an EM simulated state is also provided); ii) $AWLR_{\#1}$ intrinsically switched OFF and $AWLR_{\#2}$ is intrinsically switched ON [91].

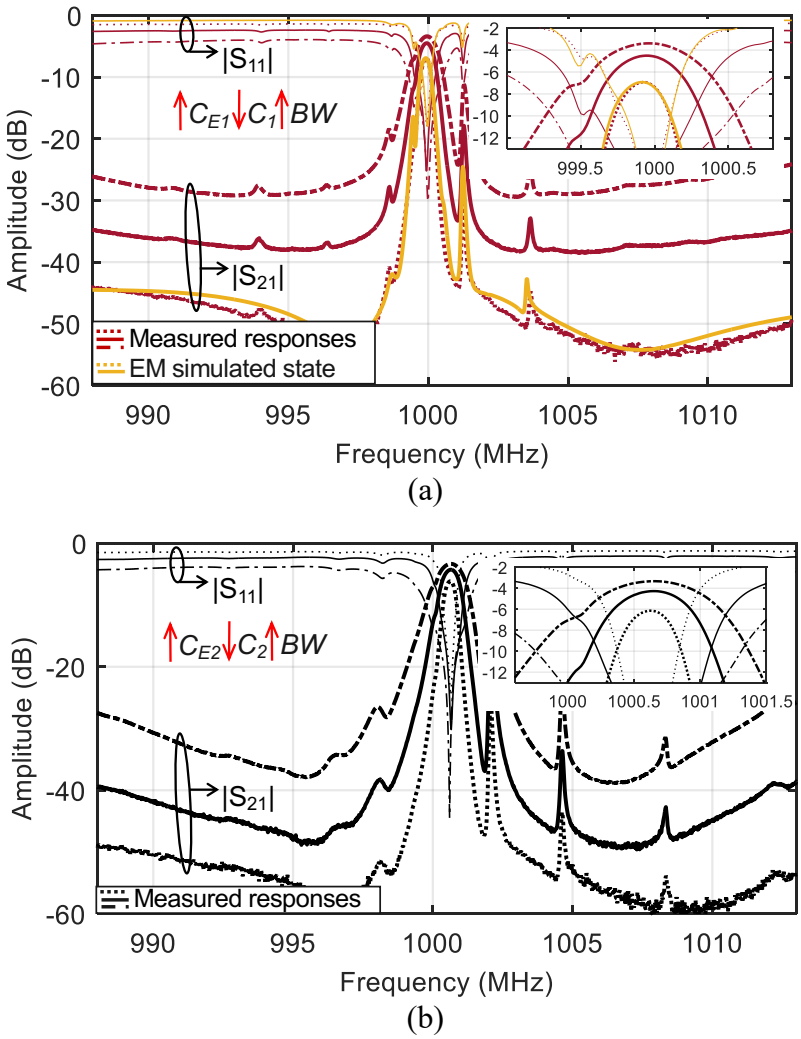


Figure 2.32. RF-measured S-parameters of the three-stage/two-branch AWLR BPF prototype showcasing continuously tunable FBW: (a) AWLR$_{\#1}$ intrinsically switched ON and AWLR$_{\#2}$ intrinsically switched OFF (an EM simulated state is also included); (b) AWLR$_{\#1}$ intrinsically switched OFF and AWLR$_{\#2}$ intrinsically switched ON [91].

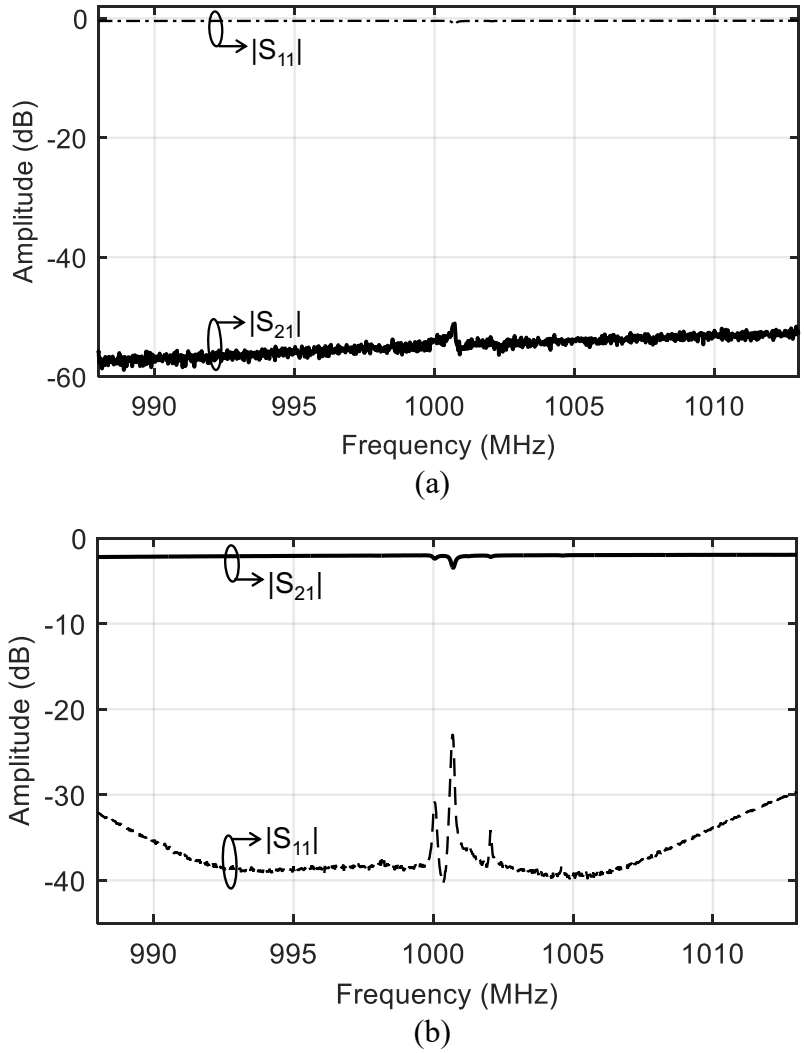


Figure 2.33. RF-measured S-parameters of the three-stage/two-branch AWLR BPF prototype illustrating the: (a) AS mode; (b) AP mode [91].

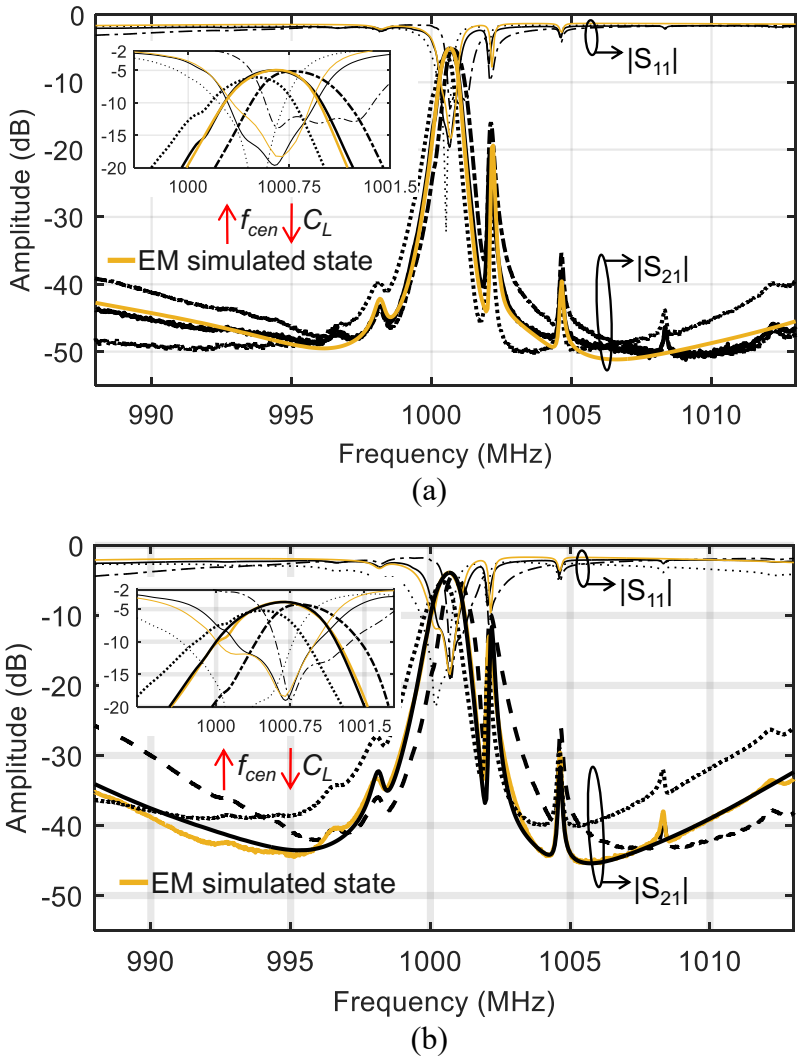


Figure 2.34. RF-measured S-parameters of the three-stage/two-branch AWLR BPF prototype showing f_{cen} tuning when AWLR$_{\#1}$ is OFF and AWLR$_{\#2}$ is ON in the following cases: (a) BW=0.58 MHz (FBW=0.48k_t^2); (b) BW=0.9 MHz (FBW=0.73k_t^2). EM simulated states are also included [91].

2.4 Multi-Configurable AWLR-Based Bandpass-to-Bandstop Filters With Continuously Tunable Characteristics

This section introduces a new class of quasi-elliptic AWLR-based BP-to-BS filters that can be reconfigured between two distinct BP and BS filtering modes without utilizing RF switches. The proposed architecture enables continuous tuning of f_{cen} and BW in both of its BP and BS modes. This is a unique contribution of this thesis, and particularly the f_{cen} tuning concept for AWR-based BSFs is presented in this work for the first time. Additionally, these filters support AP and AS operating modes, which can be obtained within the same RF filtering component.

2.4.1 Theoretical foundations

2.4.1.1 Generic concept

The coupling routing diagram (CRD) of the proposed multi-configurable AWLR stage with BP-to-BS, AP, and AS reconfigurability is shown in Figure 2.35. The CRD is of fundamental importance because it defines the resonator-coupling topology that governs the flow of energy through the filter. Consequently, it directly determines the pole–zero distribution, guides the coupling-matrix synthesis, and forms the essential link between the theoretical transfer-function (TF) response and its practical physical implementation. The CRD of the proposed concept in Figure 2.35 consists of four resonating nodes: one high-Q resonant node (R_H) and three tunable low-Q resonant nodes (R_1, R_E, and R_L). Additionally, four non-resonating nodes are incorporated to include impedance inverters. They, in turn, couple the resonating nodes and facilitate independent control of their impedances. Figure 2.35(b)-(g) illustrate the conceptual TF responses of the proposed multi-configurable AWLR stage. By adjusting the self-coupling coefficients of the low-Q resonating nodes (M_{11}, M_{EE}, and M_{LL}), the TF response can be configured for multiple operating modes, namely: i) a BP response shaped by one pole and two TZs that can be continuously tuned in terms of f_{cen} as shown in Figure 2.35(b)] and BW tuning as depicted in Figure 2.35(c); ii) a BS response shaped by one TZ and two reflection zeros (RZs) providing continuous f_{cen} tuning as demonstrated in Figure 2.35(d) and BW tuning as depicted in Figure 2.35(e);

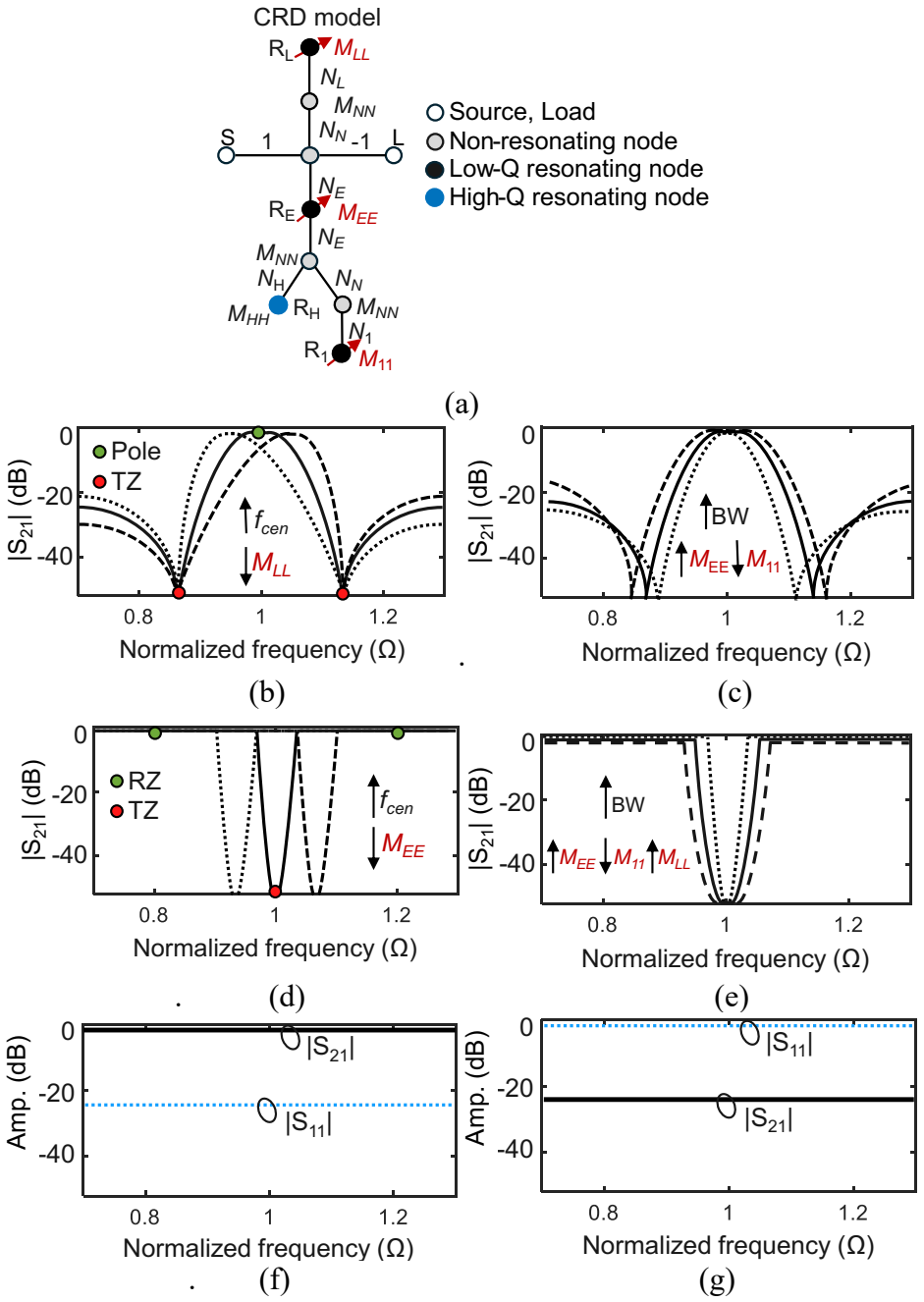


Figure 2.35. BP-to-BS multi-resonant AWLR stage with multi-configurable and continuously-tunable TF characteristics: (a) CRD model; (b) BPF response shaped by one pole and two TZs, showcasing continuous tuning of the f_{cen} achieved by altering M_{LL}; (c) BPF response exhibiting continuous BW control by altering $M_{EE,}$ and M_{11}; (d) BS response shaped by one TZ and two RZs, demonstrating continuous tuning of the f_{cen} achieved by altering M_{EE}; (e) BS response featuring continuous BW control by altering $M_{EE,}$ $M_{11,}$and $M_{LL,}$; (f) AP mode; (g) AS mode [92].

iii) an AP response as shown in Figure 2.35(f); and iv) an AS response as illustrated in Figure 2.35(g). The AP and AS stop modes are obtained by narrowing

the BW of both the BP and BS modes, respectively. Particularly, reducing the BW of the BS mode yields an AP response, while narrowing the BW of the BP mode results in an AS response. In practice these tuning capabilities can be implemented using electronically-reconfigurable varactors in the low-Q resonant nodes as it will be discussed in the Section 2.4.1.2.

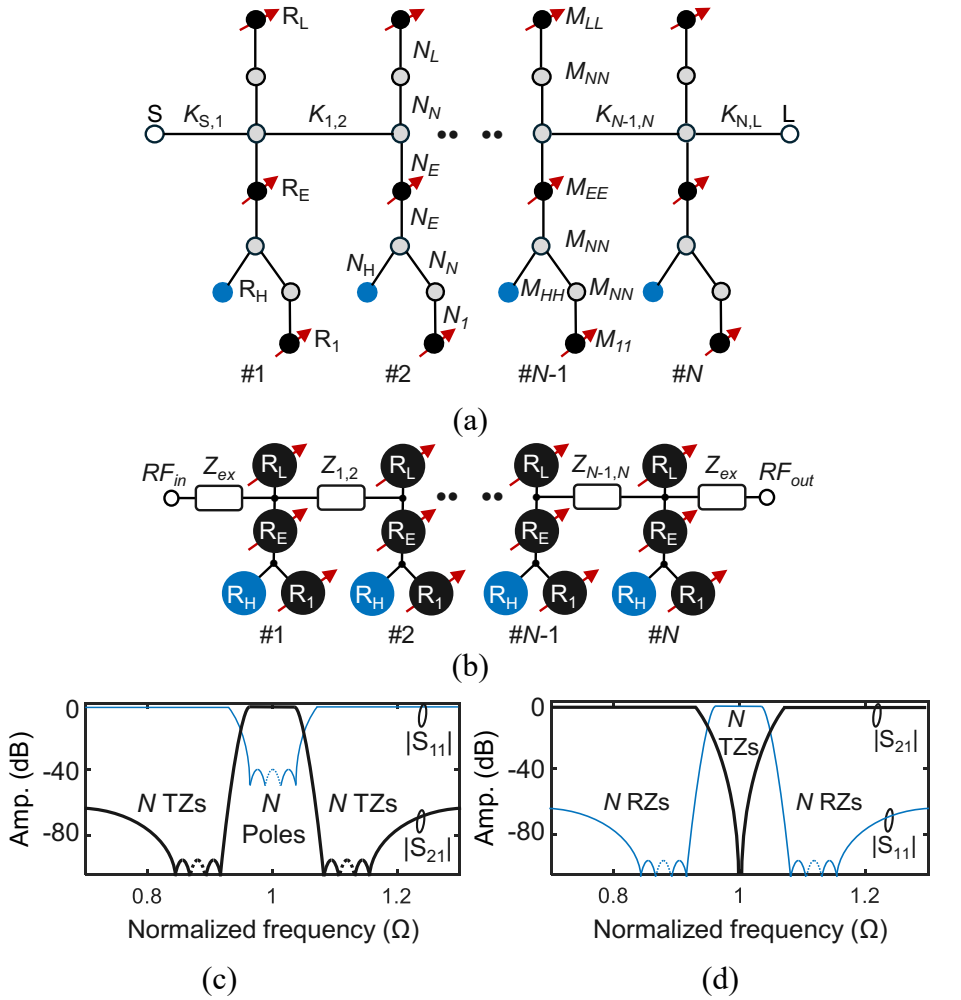


Figure 2.36. Generalized N^{th} order filters using N multi-configurable BP-to-BS AWLR stages with continuously tunable TF: (a) Generalized CRD (R_H: high-Q resonating node; R_E, R_1, and R_L: low-Q resonating nodes; white circles: source and load; grey circles: non-resonating nodes); (b) Generalized circuit block diagram using N AWLR stages and N+1 impedance inverters; (b) Illustration of the generalized BP mode TF exhibiting N poles and 2N TZs close to its passband; (c) Illustration of the generalized BS mode TF exhibiting N TZ and 2N RZs close to the stopband [92].

The multi-configurable AWLR-based concept can be exploited for the realization of higher-order TFs, as shown in the generalized CRD in Figure 2.36(a)

and the generalized circuit block diagram in Figure 2.36(b). It consists of N high-Q AWLR stages cascaded by N-1 inverters ($K_{1,2}$– $K_{N\text{-}1,N}$ in the generalized CRD, realized by $Z_{1,2}$– $Z_{N\text{-}1,N}$ impedance inverters), which are coupled to the RF ports through two additional inverters ($K_{S,1}$ and $K_{N,L}$ in the generalized CRD, realized using Z_{ex} impedance inverters). This configuration enables the realization of high-order quasi-elliptic BP TFs shaped by N poles and 2N TZs as shown in Figure 2.36(c), and high-order BS TFs shaped by N TZs and 2N RZs as can be seen in Figure 2.36(d).

Table 2.1. Normalized coupling coefficients of the synthesized examples in Figure 2.37, Figure 2.38, Figure 2.41, and Figure 2.42, and associated with the CRDs in Figure 2.37, and Figure 2.41.

Example	EX. #1: BP mode	EX. #2: BS mode	EX. #3: AP mode	EX. #4: AS mode
M_{EE}	590	178	-1050	-550
M_{11}	310.3	320	1850	950
M_{LL}	140	-424	-179.4	3300

Table 2.2. Normalized coupling coefficients of the synthesized examples in Figure 2.39, and Figure 2.43, and related to continuous f_{cen} and BW tuning in the BP mode.

Example	EX. #5	EX. #6	EX. #7	EX. #8	EX. #9	EX. #10
M_{EE}	590	590	590	800	590	430
M_{11}	310.3	310.3	310.3	228	310.3	427
M_{LL}	800	140	-500	140	140	140

Table 2.3. Normalized coupling coefficients of the synthesized examples in Figure 2.39, and Figure 2.44, and related to continuous f_{cen} and BW tuning in the BS mode.

Example	EX. #11	EX. #12	EX. #13	EX. #14	EX. #15	EX. #16
M_{EE}	1300	178	-1080	-390	-597	-930
M_{11}	62	320	-55	-250	-80	97
M_{LL}	-72	-424	54	-930	30	-25

2.4.1.2 Multi-configurable AWLR stage

To better explain its operating principles, a detailed qualitive analysis is presented in Figure 2.37 to Figure 2.40, using synthesized CRD-based examples and the normalized CRD coupling coefficients listed in Table 2.1 to Table 2.3. They have

been obtained by fitting the synthesized S-parameters of the CRD to the ones obtained by circuit simulations as detailed in [47]. The high-Q resonator (R_H), based on the commercially available Murata RO3144 SAW resonator, has fixed characteristics. Based on its S-parameters response, the AWLR stage is initially designed using circuit simulation. After determining characteristics of the low-Q resonators (R_1, R_E, and R_L), their coupling coefficients, as well as those of R_H, are extracted by fitting the synthesized Coupling Matrix (CM) response of the CRD model to their circuit-simulated response. Once the fitted coupling coefficients for all resonators are obtained, the CRD model of the AWLR stage is constructed, and the extracted coefficients are used to synthesize the CRD model, as listed in the caption of Figure 2.37.

A comparison between the simulated AWLR circuit model and synthesised CRD model responses is illustrated in Figure 2.37 and Figure 2.38. Specifically, the CRD and circuit models of the proposed multi-configurable AWLR stage, with BP-to-BS, AP and AS reconfigurability, are shown in Figure 2.37(a). The circuit model consists of one high-Q resonant node (R_H)–represented by a two-terminal-one-port type AWR–represented by its BVD model equivalent circuit [106], with motional capacitance (C_M), inductance (L_M), resistance (R_M), and parasitic capacitance (C_0), resonating at $f_s = 1/2\pi(C_M \bullet L_M)^{1/2}$–and three low-$Q$ resonant nodes: R_1 is shaped by a parallel LE LC resonator (C_1 and L_1) resonating at $f_1 = 1/2\pi((C_0+C_1)\bullet L_1))^{1/2}$; R_E is implemented using a series LE LC resonator (C_E and L_E) resonating at $f_E=1/2\pi(C_E \bullet L_E)^{1/2}$; and R_L is implemented by a parallel LE LC resonator (C_L and L_L) resonating at $f_L = 1/2\pi(C_L \bullet L_L)^{1/2}$). R_H is cascaded in parallel with R_1, and this combination is cascaded in series with R_E and then it is loaded by R_L. In the CRD model, additional non-resonating nodes and coupling inverters are employed to independently control the FBW of different low-Q resonators (R_E, R_1, and R_L).

To design the AWLR at a specific f_{cen} and BW, an AWR with $f_s=f_{cen}$ and appropriate k_t^2 is selected. Its BW can then be fitted by adjusting N_H in the CRD model. As can be seen in Figure 2.37(b) and using the coupling element values in Table 2.1, the AWLR can generate a BP response shaped by one pole and two TZs. Moreover, the same circuit can be configured to achieve a BS response shaped by one TZ and two RZs, as depicted in Figure 2.37(c), by altering M_{EE}, M_{11}, and M_{LL}. Additionally, the proposed AWLR stage enables two additional reconfigurable TF states: an AP

mode of operation, as illustrated in Figure 2.38(a), obtained by reducing the BW of the BS mode; and an AS mode of operation, as shown in Figure 2.38(b), achieved by narrowing the BW of the BP mode. These responses are achieved by adjusting M_{EE}, M_{11}, and M_{LL}, as specified in Table 2.1. In the CM synthesized responses, reconfiguration is achieved by altering the self-coupling coefficients of the low-Q resonating nodes (M_{11}, M_{EE}, and M_{LL}) which in practice is achieved by adjusting the resonance frequencies of the low-Q LE resonators (f_1, f_E, and f_L). The resonance frequency of the low-Q LE resonators is determined by: $f= 1/2\pi(C \bullet L)^{1/2}$, where C is the capacitance and L is the inductance.

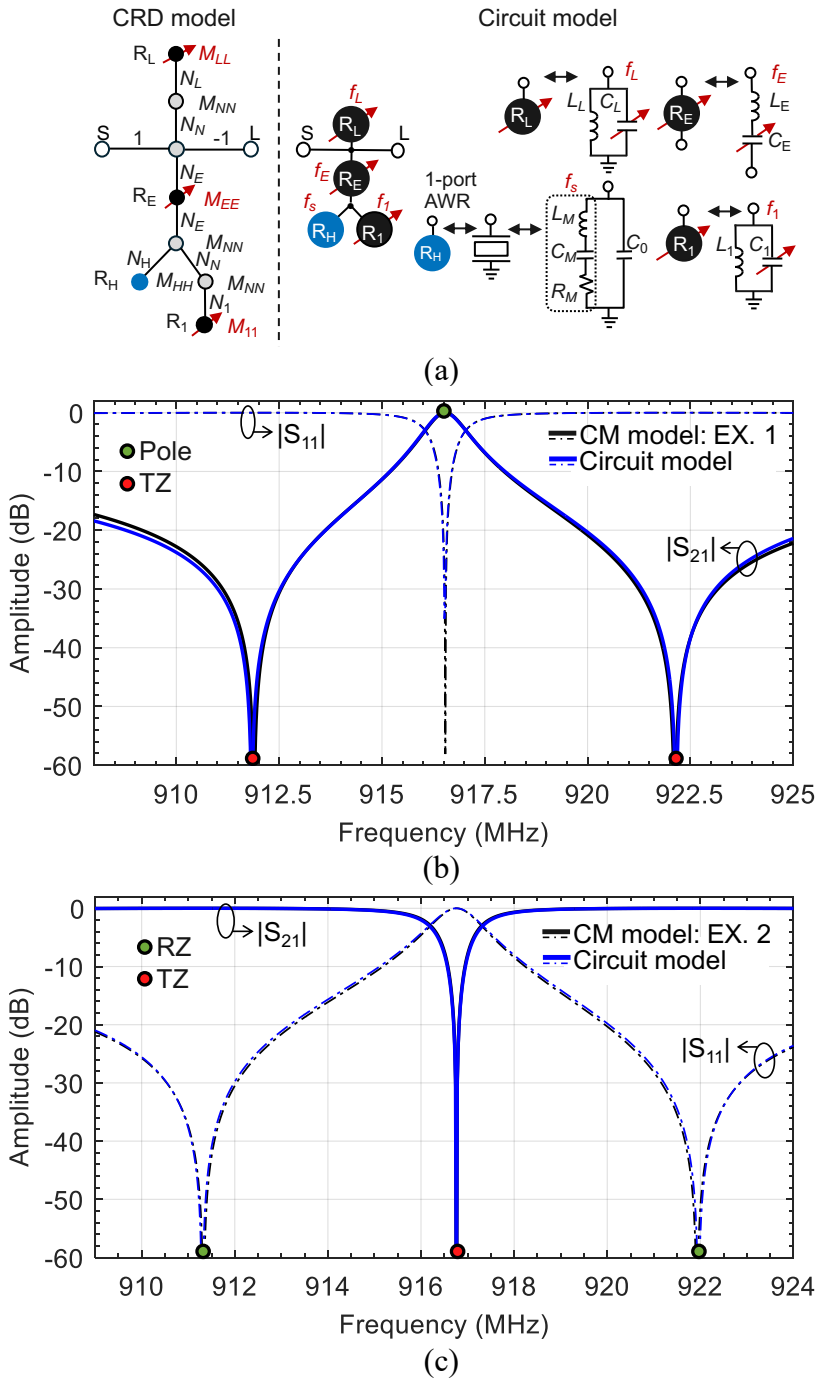


Figure 2.37. Proposed multi-functional AWLR stage CRD and circuit models with corresponding CM-based synthesized and circuit-simulated responses: (a) CRD and detailed circuit models; (b) BP response with one pole and two TZs obtained by setting the resonant frequencies of the low-Q resonant nodes to $f_E = 0.753f_s$, $f_1 = 0.822f_s$, and $f_L = 0.904f_s$; (c) BS response with one TZ and two RZs obtained by setting: $f_E = 1.076f_s$, $f_1 = 1.705f_s$, and $f_L = 0.671f_s$. AWR parameters: $k_t^2 = 0.12\%$, BW= 1 MHz at f_{cen}= 916.4 MHz (i.e., FBW= 0.109%), C_M= 1.895 fF, L_M= 15.92 uH, R_M= 11.3 Ohm, C_0= 2.17 pF. Low-Q resonator parameters: L_E= 20 nH, L_1= 4.2 nH, and L_L= 4 nH. The static coupling coefficients of the CRD model are N_N= 1, N_E= 23.9, N_H= 0.71, N_1= 19, N_L= 17.2, M_{NN}= 0, and M_{HH}= 0, with variable coefficients are listed in Table 2.1 [92].

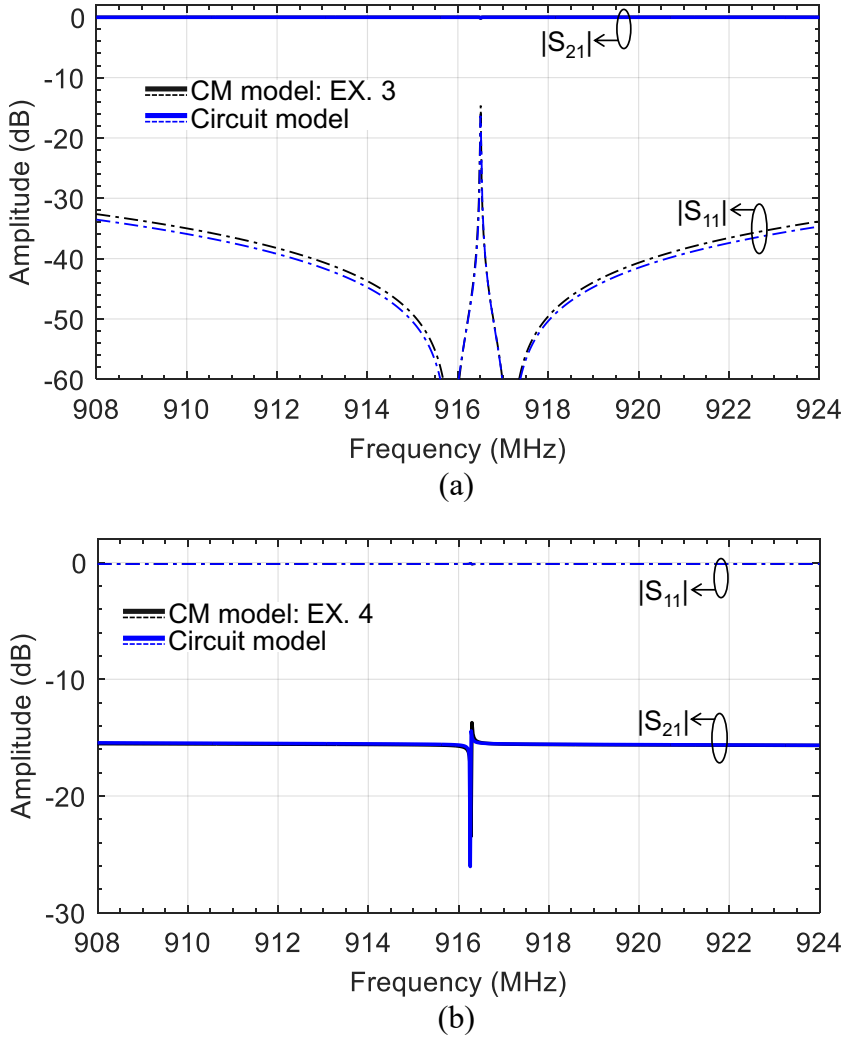


Figure 2.38. CM-based synthesized and circuit-simulated responses of the multi-resonant AWLR stage shown in Figure 2.37(a) showcasing: (a) AP response obtained by setting: f_E= 1.47f_s, f_1= 0.74f_s, f_L = 1.25f_s; (b) AS response obtained by setting: f_E= 0.55f_s, f_1= 1.505f_s, f_L = 0.388f_s. The coupling coefficients are listed in Table 2.1 [92].

In practice, capacitance tuning is achieved using varactor diodes which adjust their capacitance based on the applied reverse voltage at their terminals. This electronic tuning capability allows dynamic modification of the resonance frequency, enabling the filter to reconfigure its response. Figure 2.39 demonstrates the continuous f_{cen} and BW tuning capabilities of the AWLR when configured in the BP mode, by varying, M_{EE}, M_{11}, and M_{LL}, as detailed in Examples 5 to 7 in Table 2.1. In Figure 2.39, the BP response shows a BW= 1.16 MHz at f_{cen}=916.4 MHz (i.e., FBW= 1.05k_t^2, > 0.4– 0.8k_t^2 limit). By altering M_{LL} from -500 to 800, the f_{cen} continuously tunes from 915.95 to 917.12 MHz (TR: 100.128%:1). Figure 2.39(b) demonstrates the BW tuning

which can be varied between 0.56 and 1.94 MHz (i.e., FBW= 0.51– 1.76k_t^2 and TR:3.46:1) by increasing M_{EE} and decreasing M_{11}, as indicated in Examples 8 to 10 in Table 2.2. Figure 2.40 illustrates the continuous f_{cen} and BW tuning capabilities of the AWLR when being reconfigured in its BS mode of operation by varying, M_{EE}, M_{11}, and M_{LL}, as detailed Examples 11 to 13 in Table III. In Figure 2.40(a), the BS response shows a BW= 0.532 MHz (i.e., FBW= 0.484k_t^2). By decreasing M_{EE} and adjusting M_{11} and M_{LL} to maintain a fixed BW, the f_{cen} is continuously tuned from 915.415 to 917.07 MHz (TR: 100.183%:1). Additionally, Figure 2.40(b) depicts BW tuning at f_{cen}= 916.7 MHz, where increasing M_{EE} and M_{LL} and decreasing M_{11}, the BW increases from 0.2 to 1.08 MHz (i.e., FBW= 0.18– 0.98k_t^2), as indicated in Examples 14 to 16 in Table 2.3.

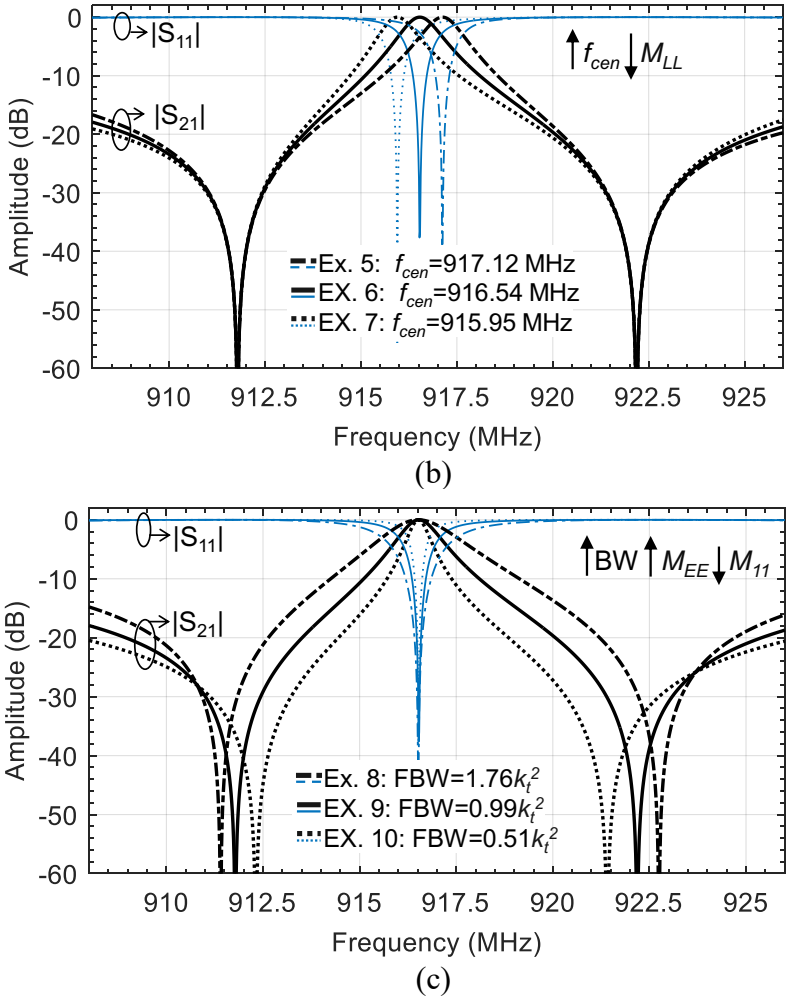
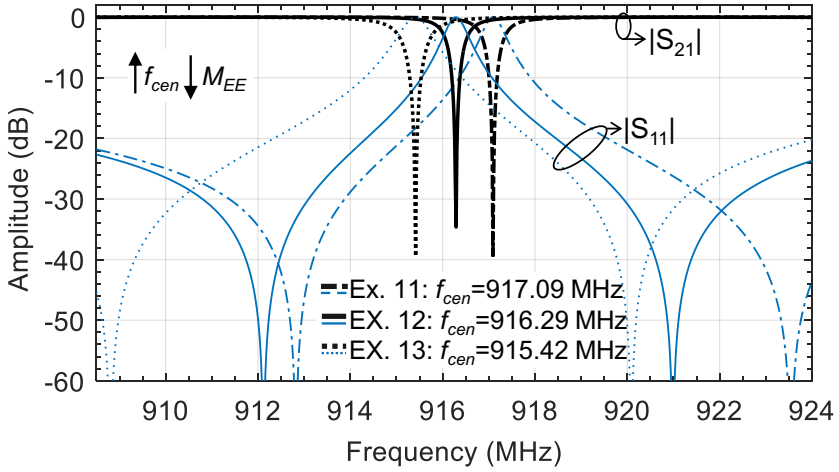
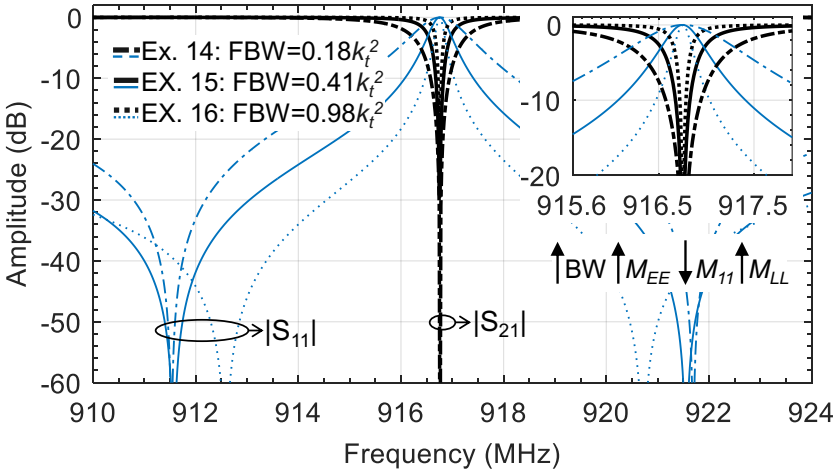


Figure 2.39. Synthesized S-parameters of the multi-resonant AWLR stage when operating in its BP mode showcasing: (a) Continuous f_{cen} tuning by altering the self-coupling coefficient of the low-Q resonant node R_L (M_{LL}); (b) Continuous BW tuning by altering the self-coupling coefficient of the low-Q resonant nodes R_E and R_1 (M_{EE} and M_{11}) [92].



(a)



(b)

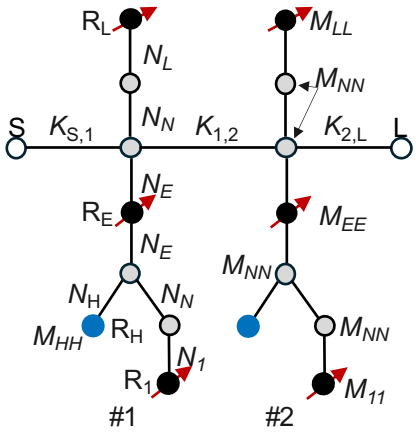
Figure 2.40. Synthesized response of the multi-resonant AWLR stage when operating in its BS mode showcasing: (a) Continuous f_{cen} tuning obtained by altering the self-coupling coefficient of the low-Q resonant node R_E (M_{EE}), and by adjusting the self-coupling coefficient of the low-Q resonant nodes R_L and R_1 (M_{LL} and M_{11}) in order to maintain the BW; (b) Continuous BW tuning obtained by altering the self-coupling coefficient of the low-Q resonant nodes R_E, R_1 and R_L (M_{EE}, M_{11} and M_{LL}) [92].

2.4.1.3 Higher-order multi-configurable filters

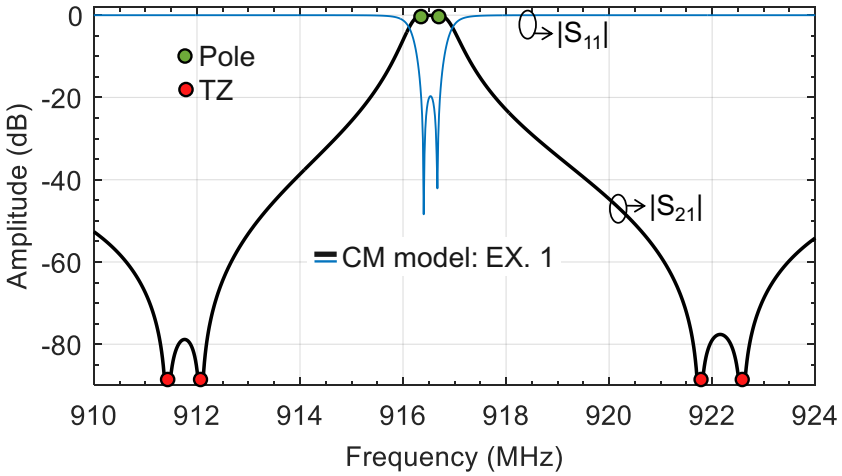
Higher-order (i.e., N^{th} order) TFs can be synthesized by cascading N AWLR stages in series using impedance inverters, as shown in in Figure 2.36. Specifically, a two-stage example is considered using the CRD in Figure 2.41(a) where two AWLR stages are cascaded with impedance inverters $K_{1,2}$ and are coupled to the RF ports

through inverters $K_{S,1}$ and $K_{2,L}$. Using the same coupling coefficients listed in Table 2.1**,** the two-stage filter can operate in the same modes and follow the continuous tuning principles demonstrated for the single AWLR stage in Section 2.4.1.2, by altering M_{EE}, M_{11}, and M_{LL}. The two-stage filter response when configured in the BP mode is shown in Figure 2.41(b), exhibiting two poles and four TZs, with a BW= 1.62 MHz (i.e., FBW= $1.47k_t^2$) at f_{cen}= 916.4 MHz. The response when configured in BS mode is depicted in Figure 2.41(c), exhibiting a BW= 0.7 MHz (i.e., FBW= $0.64k_t^2$) at f_{cen}= 916.76 MHz. The AP and AS modes of operations are illustrated in Figure 2.42(a) and Figure 2.42(b), respectively.

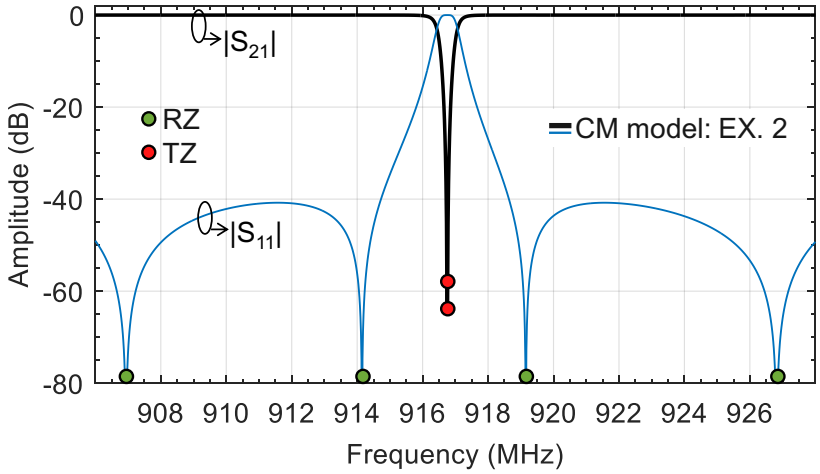
The continuous tuning of f_{cen} and BW of the two-stage filter when configured in BP mode is illustrated in Figure 2.43, achieved by altering M_{EE}, M_{11}, and M_{LL}, as detailed in Table 2.2. The BP response in Figure 2.43(a) exhibits a BW= 0.846 MHz (i.e., FBW= $1.47k_t^2$, > 0.4– $0.8k_t^2$ limit) at f_{cen}= 916.5 MHz. By increasing M_{LL} from -500 to 800, the f_{cen} is tuned between 915.96 to 917.15 MHz (TR: 100.13%:1). In Figure 2.43(b), by Increasing M_{EE} and decreasing M_{11} the BW can be continuously increases from 0.46 to 1.53 MHz (i.e., FBW= 0.42– $1.39k_t^2$ and TR:3.3:1). The continuous tuning principles of f_{cen} and BW of the two-stage filter when configured in BS mode are shown in Figure 2.44, achieved by varying, M_{EE}, M_{11}, and M_{LL}, as detailed in Table 2.3. In Figure 2.44(a), the BS response shows a BW= 0.66 MHz (i.e., FBW= $0.6k_t^2$); by increasing M_{EE} and adjusting M_{11} and M_{LL} to maintain the BW, f_{cen} is continuously tuned from 915.56 to 917 MHz (TR: 100.157%:1). In Figure 2.44(b), by increasing M_{EE} and M_{LL} while decreasing M_{11}, the BW increases from 0.266 to 1.52 MHz (i.e., FBW= 0.24– $1.38k_t^2$ and TR:5.7:1) at f_{cen}= 916.74 MHz.



(a)



(b)



(c)

Figure 2.41. CRD and synthesized S-parameter response of a two-stage AWLR-based filter: (a) CRD model; (b) BP mode showing two transmission poles and four TZs; (c) BS mode exhibiting two TZs and four RZs. The static coupling coefficients are $K_{S,1}$= 1, $K_{2,L}$= -1, $K_{1,2}$= 1.11, N_N= 1, N_E= 23.9, N_H= 0.71, N_I= 19, N_L= 17.2, M_{NN}=M_{HH}= 0 [92].

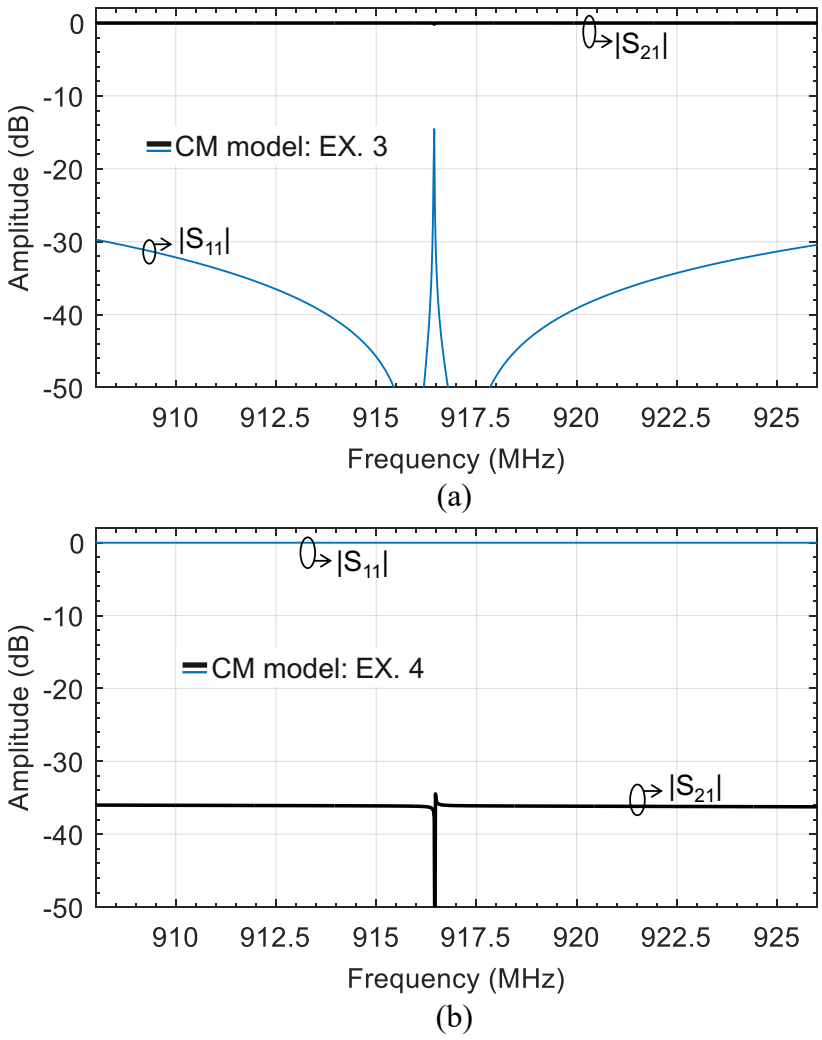


Figure 2.42. Synthesized S-parameter response of the two-stage AWLR-based filter in Figure 2.41(a) showcasing: (a) AP mode; (b) AS mode [92].

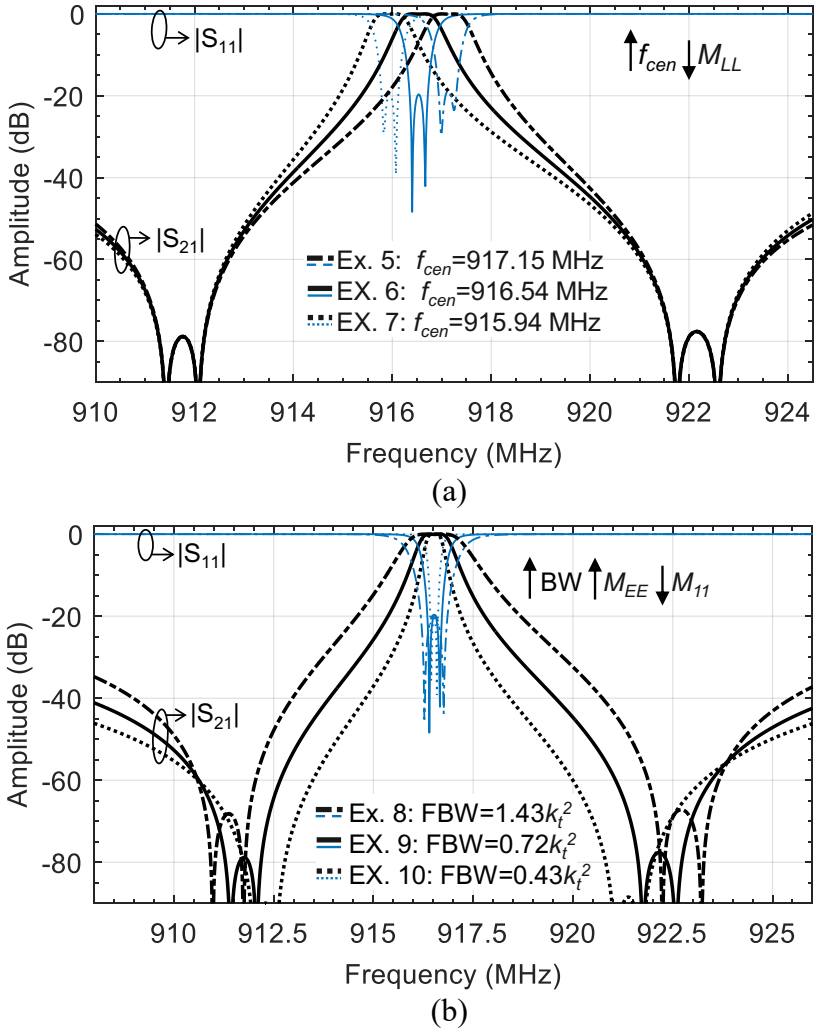
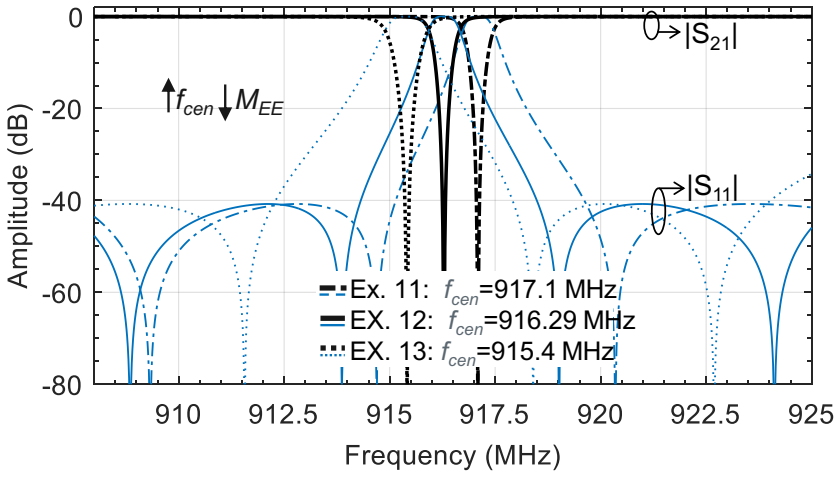
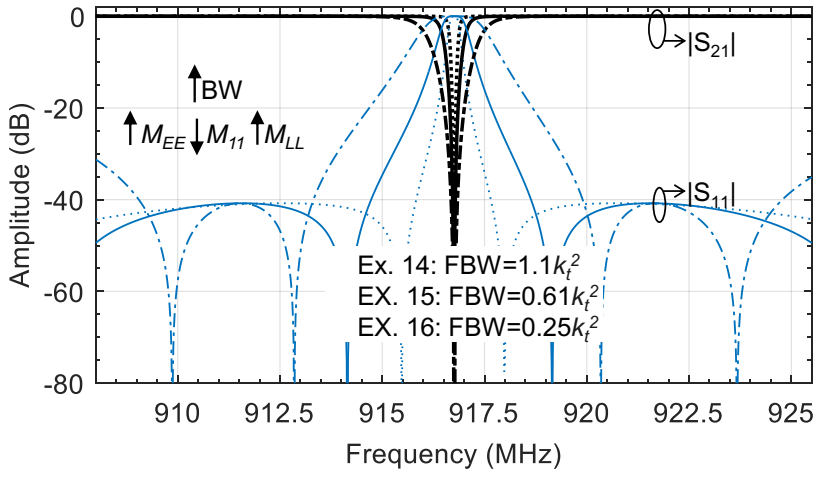


Figure 2.43. Synthesized S-parameter response of the two-stage AWLR-based filter in Figure 2.41(a) when configured in BP mode showcasing: (a) a BP response with continuous f_{cen} tuning obtained by altering the self-coupling coefficient of the low-Q resonant node R_L (M_{LL}); (b) a BP response with BW tuning obtained by altering the self-coupling coefficient of the low-Q resonant nodes R_E and R_1 (M_{EE} and M_{11}) [92].



(a)



(b)

Figure 2.44. Synthesized S-parameter response of the two-stage AWLR-based filter in Figure 2.41 (a) when operating in its BS mode showcasing: (a) Continuous f_{cen} tuning obtained by altering the self-coupling coefficient of the low-Q resonant node R_E (M_{EE}), and by adjusting the self-coupling coefficient of the low-Q resonant nodes R_L and R_1 (M_{LL} and M_{11}) in order to maintain the BW; (b) Continuous BW tuning obtained by altering the self-coupling coefficient of the low-Q resonant nodes R_E, R_1 and R_L (M_{EE}, M_{11} and M_{LL}) [92].

2.4.2 Experimental validation

To experimentally validate the proposed multi-configurable AWLR-based filter concept with continuously tunable f_{cen} and BW and four distinct modes of operation, two prototypes were designed, manufactured and tested at L-band. The prototypes are based on a commercially available, two terminal, one-port-type, SAW resonator from

Murata Inc. (Murata RO3144E1 with series resonant frequency= 916.4 MHz and Q_M= 8500), LE components from Coilcraft Inc. and Johanson, and varactor diodes from MACOM Inc. [102], [99], and [107]. Notably, most commercially available SAW resonators operate at f_{cen} <1 GHz, with a typical BW of approximately 0.3 MHz. However, if SAW resonators with higher k_t^2 become available, the proposed filter TF can be designed to operate at higher frequencies and achieve significantly wider BWs, making it suitable for practical application requirements.

Following the design guidelines in Section 2.4.1, the filters were implemented on a Rogers RO4003C substrate (dielectric thickness H = 0.813 mm, permittivity ε_r= 3.55, dissipation factor tan (δ)= 0.0027, with 1 oz copper cladding), and simulated using the software package Keysight ADS. RF measurements were conducted using a Keysight N5244A network analyser. The prototypes include: i) a two-stage AWLR-based BPF (i.e., N= 2), and ii) a three-stage AWLR-based filter (i.e., N= 3). In the following RF summary of the measured prototypes, some measured prototypes exhibit higher IL than simulations due to narrower FBWs, varactor losses, and PCB-related parasitics. IL variations also result from the varactor Q factor, which changes with applied voltage.

2.4.2.1 Two-stage BP-to-BS filter prototype

The circuit block diagram and photograph of the manufactured two-stage AWLR filter prototype, along with the utilized SMD components are shown in Figure 2.45. Detailed RF-measured performance parameters are summarized in Table 2.4. In BP mode, the continuous f_{cen} tuning characteristics are demonstrated in Figure 2.46(a). For a 3-dB BW of 1 MHz, f_{cen} is continuously tunable from 916.22 to 917.01 MHz. The measured BW tuning capability is illustrated in Figure 2.46(b), showing a continuous 3-dB BW tunable between 0.47 and 1.18 MHz at f_{cen}= 916.56 MHz. The provided EM/circuit co-simulated states in Figure 2.46 agree well with the measured responses, successfully validating the measured results. It should be noted that the spurious response appearing at around 913.5 MHz is due to the inherent spurious mode of the SAW resonator itself and is not related to the proposed filtering TF. This has been demonstrated previously in Section 2.2.2 and is a known characteristic of SAW resonators.

The f_{cen} tuning performance of the BS mode of operation is illustrated in Figure 2.47 for two different BW levels. For a 3-dB BW of 0.96 MHz, shown in Figure 2.47(a), f_{cen} can be continuously tuned from 915.76 to 917.22 MHz. When the 3-dB BW is increased to 1.42 MHz, as depicted in Figure 2.47(b), f_{cen} is continuously tunable from 915.7 to 917.58 MHz. The BW tuning characteristics in the BS mode of operation are presented in Figure 2.48 for three different operating frequencies. At f_{cen} = 916.14 MHz, as shown in Figure 2.48(a), the BW can be tuned from 0.54 to 1.62 MHz. At f_{cen} = 916.5 MHz, Figure 2.48(b) demonstrates BW tuning between 0.33 and 0.96 MHz. Finally, at f_{cen} = 916.9 MHz, as illustrated in Figure 2.48(c), the 3-dB BW is tunable over a wider range, from 0.33 to 1.96 MHz.

The provided EM/circuit co-simulated states show good agreement with the measured results. The measured RF AP mode response is shown in Figure 2.49(a) with an average IL of 1.2 dB. The measured RF AS mode is shown in Figure 2.49(b), demonstrating approximately 50 dB of IS across the measured frequency range. The EM/circuit co-simulated states agree well with measured responses in Figure 2.49 successfully validating the multi-configurable AWLR concept.

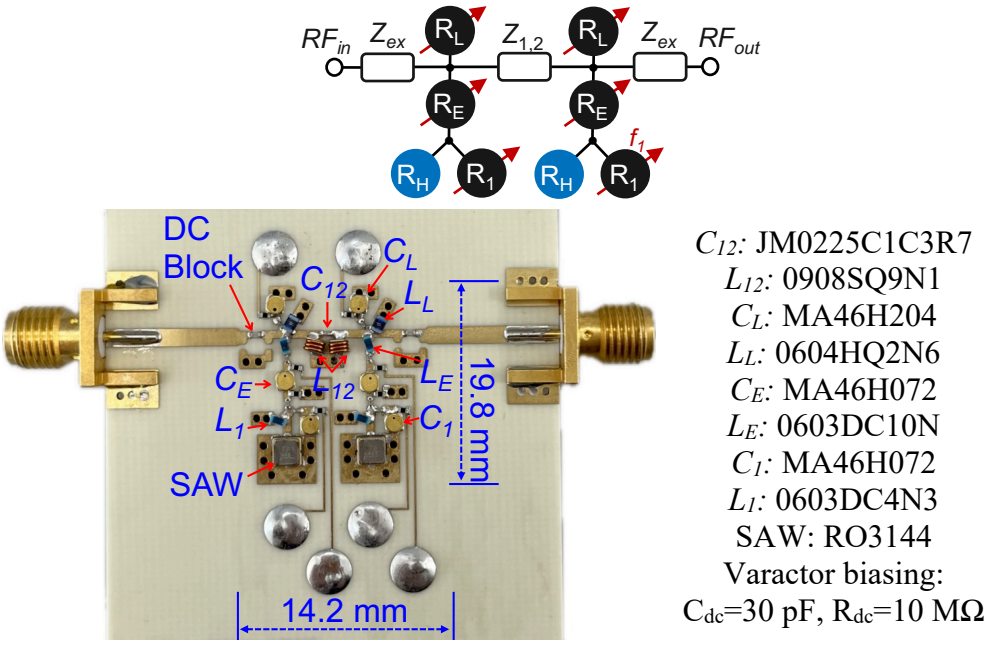
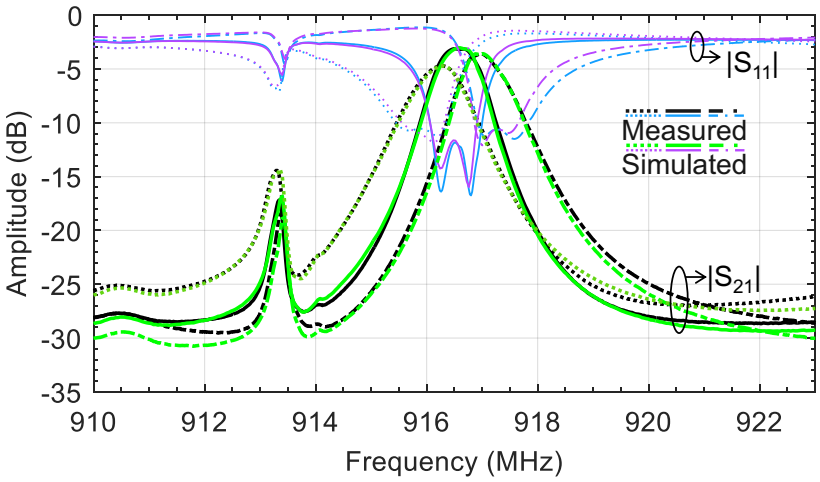
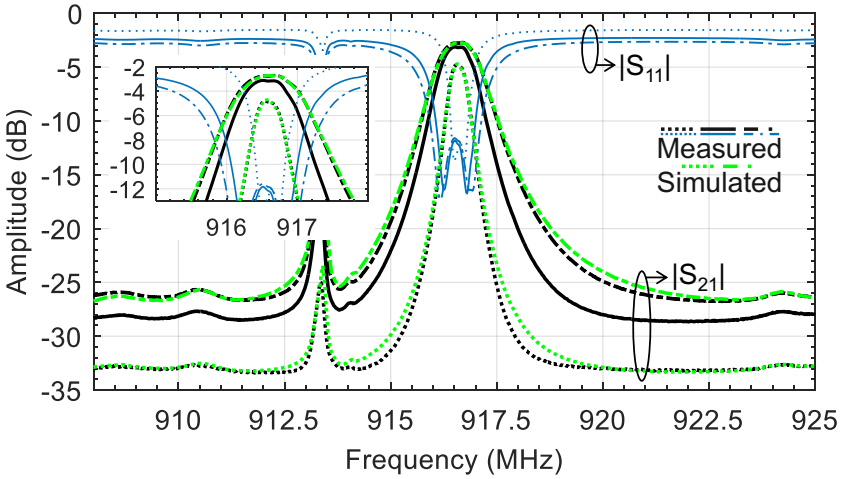


Figure 2.45. Circuit block diagram and photograph of the manufactured two-stage BP-to-BS AWLR filter along with the utilized SMD components [92].

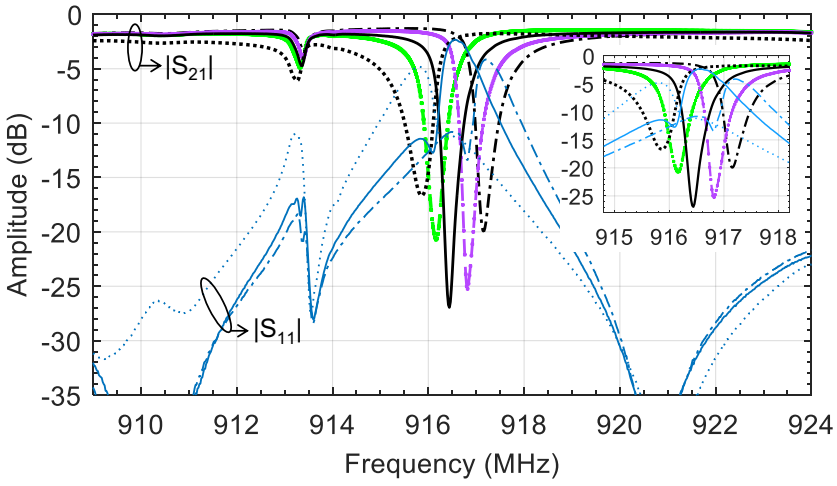


(a)

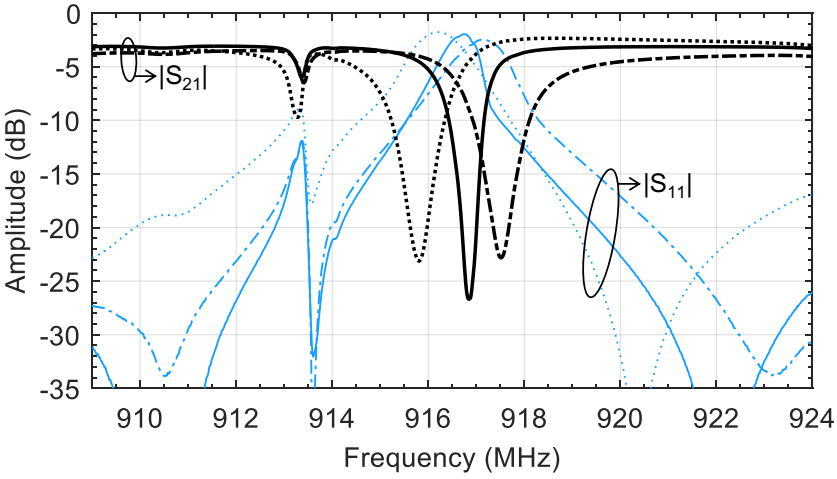


(b)

Figure 2.46. RF-measured S-parameters of the manufactured two-stage AWLR filter prototype in Figure 2.45 demonstrating its: (a) BP response exhibiting continuous f_{cen} tuning; (b) BP response exhibiting continuous BW tuning [92].



(a)



(b)

Figure 2.47. RF-measured S-parameters of the manufactured two-stage filter prototype in Figure 2.45, showcasing its BS response with tunable f_{cen} when: (a) BW= 0.96 MHz (i.e., FBW= $0.87k_t^2$), EM/circuit co-simulated states also included (b) BW= 1.42 MHz (i.e., FBW= $1.3k_t^2$) [92].

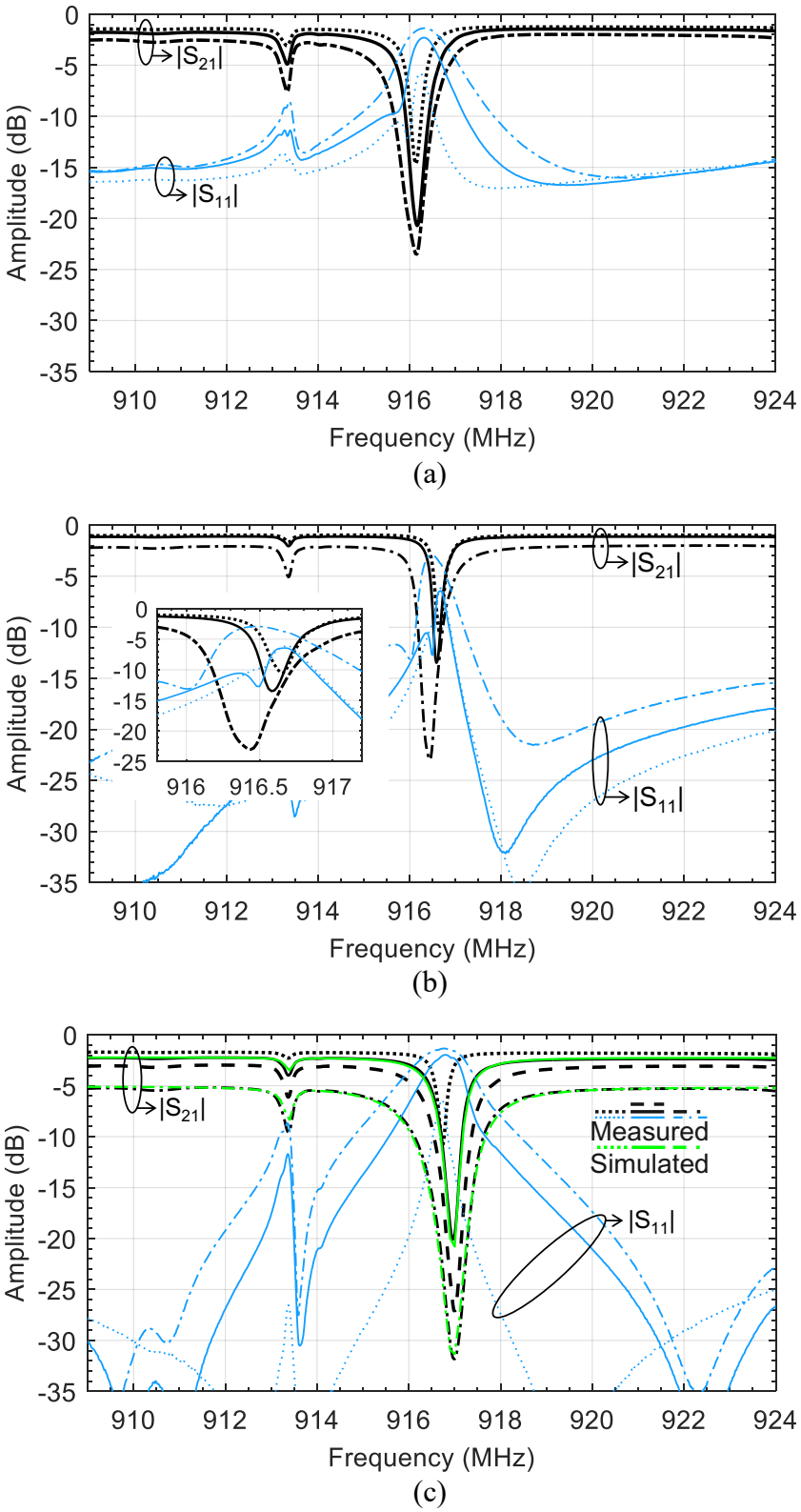


Figure 2.48. RF-measured S-parameters of the manufactured two-stage filter prototype in Figure 2.45, illustrating its BS response with tunable BW when: (a) f_{cen}=916.14 MHz; (b) f_{cen}=916.5 MHz; (c) f_{cen}=916.9 MHz; EM/circuit co-simulated states also included [92].

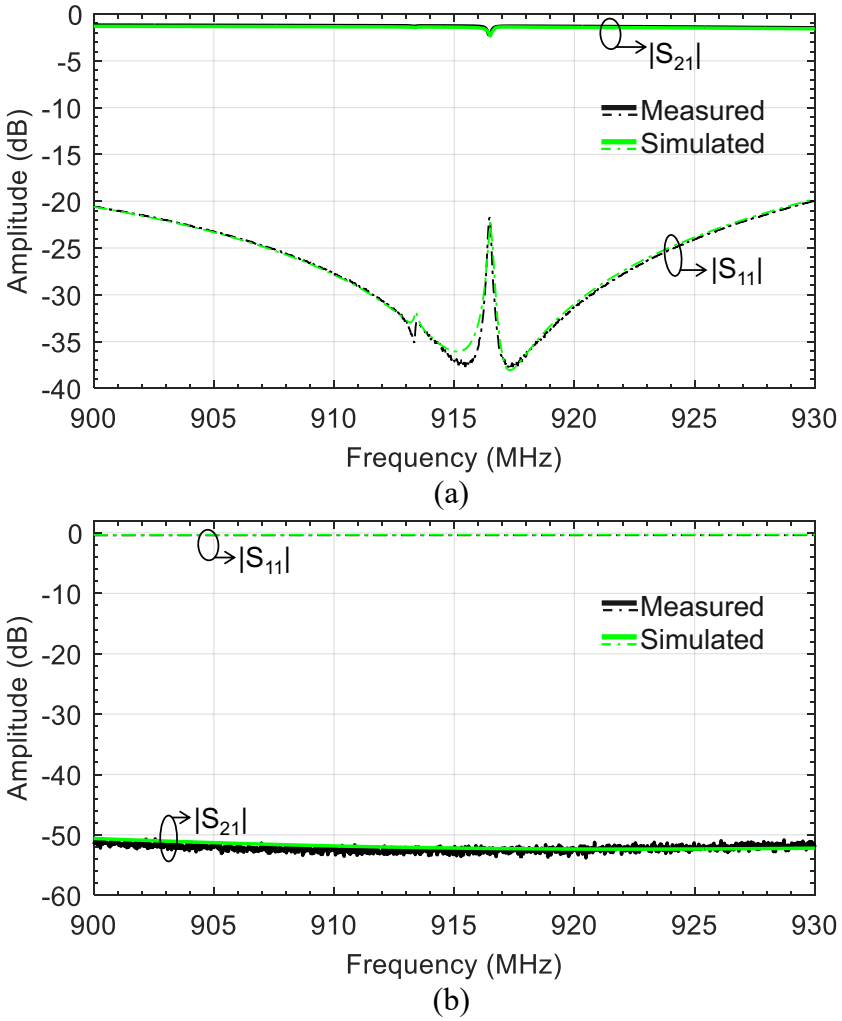
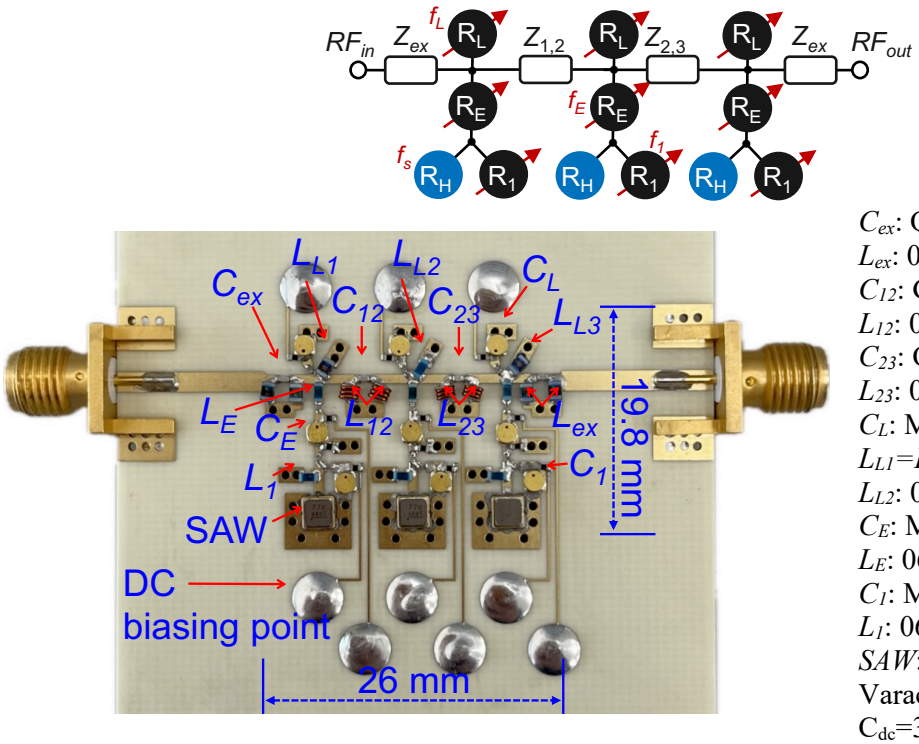


Figure 2.49. RF-measured S-parameters of the manufactured two-stage filter prototype in Figure 2.45 showcasing: (a) AP mode; (b) AS mode. EM/circuit co-simulated results are also included [92].

2.4.2.2 Three-stage BP-to-BS AWLR filter prototype

The circuit block diagram and photograph of the manufactured three-stage AWLR filter prototype, along with the utilized SMD components are provided in Figure 2.50. Detailed measured performance parameters are summarized in Table 2.4. In BP mode, the continuous f_{cen} tuning characteristics are depicted in Figure 2.51(a). For a 3-dB BW of 1.05 MHz, f_{cen} is continuously tunable from 916.38 to 917 MHz. The RF-measured BW tuning capabilities are shown in Figure 2.51(b), indicating a 3-dB BW that is continuously tunable between 0.5 and 1.14 MHz at f_{cen}= 916.6 MHz. In BS mode, the f_{cen} tuning characteristics are depicted in Figure 2.53. RF(a), where f_{cen} is continuously tunable from 915.88 to 917.26 MHz for a 3-dB BW is 1.02 MHz. The

BW tuning capabilities are shown in Figure 2.53. RF(b), where the BW continuously tunable between 0.41 and 1.46 MHz at f_{cen} = 916.76 MHz. The RF-measured AP mode response is shown in Figure 2.53(a) with an average IL of 1.3 dB. The AS mode is shown in Figure 2.53(b) demonstrating approximately 62 dB of IS across the measured frequency range. The f_{cen} TR of the filter is limited by the low Q-factor of the varactor, which degrades passband IL when tuning away from the originally designed f_{cen}, as shown in Figure 2.46(a), and Figure 2.51(a). The TR can be increased by using higher-Q varactors or by adopting a multi-module AWLR stage, as investigated in Section 2.4, which extends f_{cen} tuning while preserving filter performance.



C_{ex}: QM1555C2D3R9
L_{ex}: 0604HQ7N6
C_{12}: GQM1555C2D5R0
L_{12}: 0806SQ5N5
C_{23}: QM1555C2D4R7
L_{23}: 0806SQ6N0
C_L: MA46H204
L_{L1}=L_{L3}: 0604HQ2N6
L_{L2}: 0603DC1N6
C_E: MA46H072
L_E: 0603DC10N
C_1: MA46H072
L_1: 0603DC4N3
SAW: RO3144
Varactor biasing:
C_{dc}=30 pF, R_{dc}=10 MΩ

Figure 2.50. Circuit block diagram and photograph of the manufactured three-stage filter, along with the utilized SMD components [92].

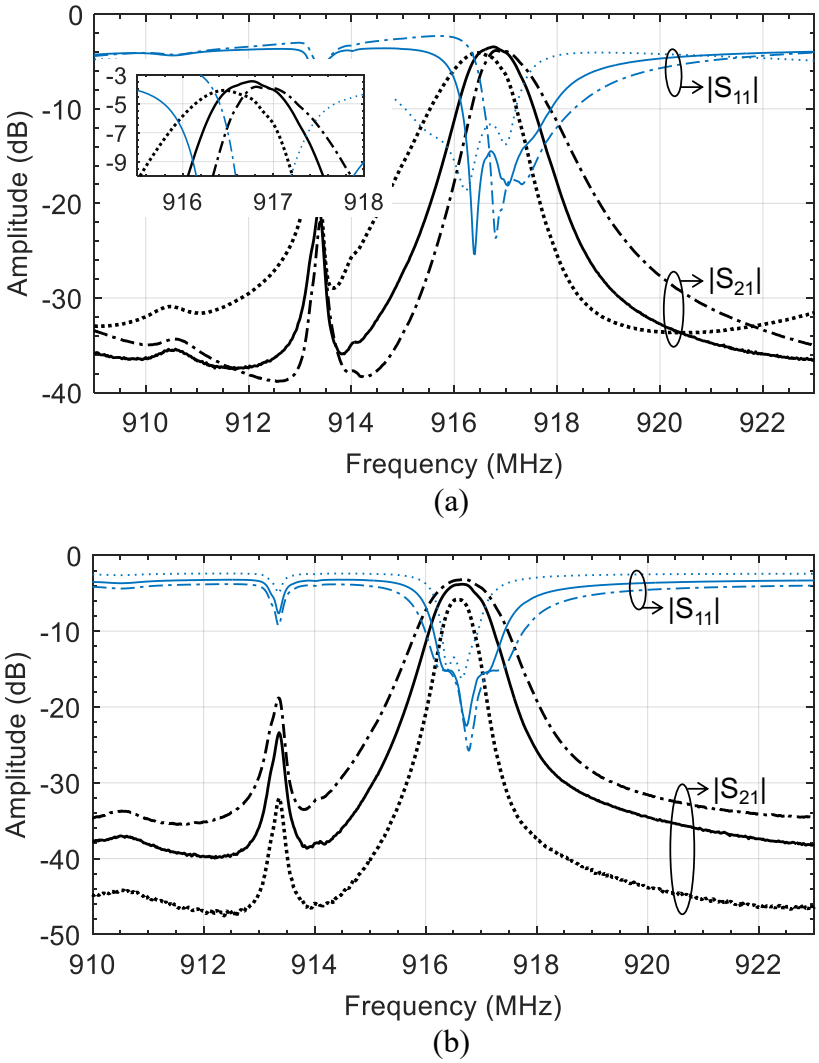


Figure 2.51. RF-measured S-parameters of the manufactured three-stage prototype in Figure 2.50 illustrating its: (a) BP response exhibiting continuous f_{cen} tuning; (b) BP response exhibiting continuous BW tuning. EM/circuit co-simulated states are also included [92].

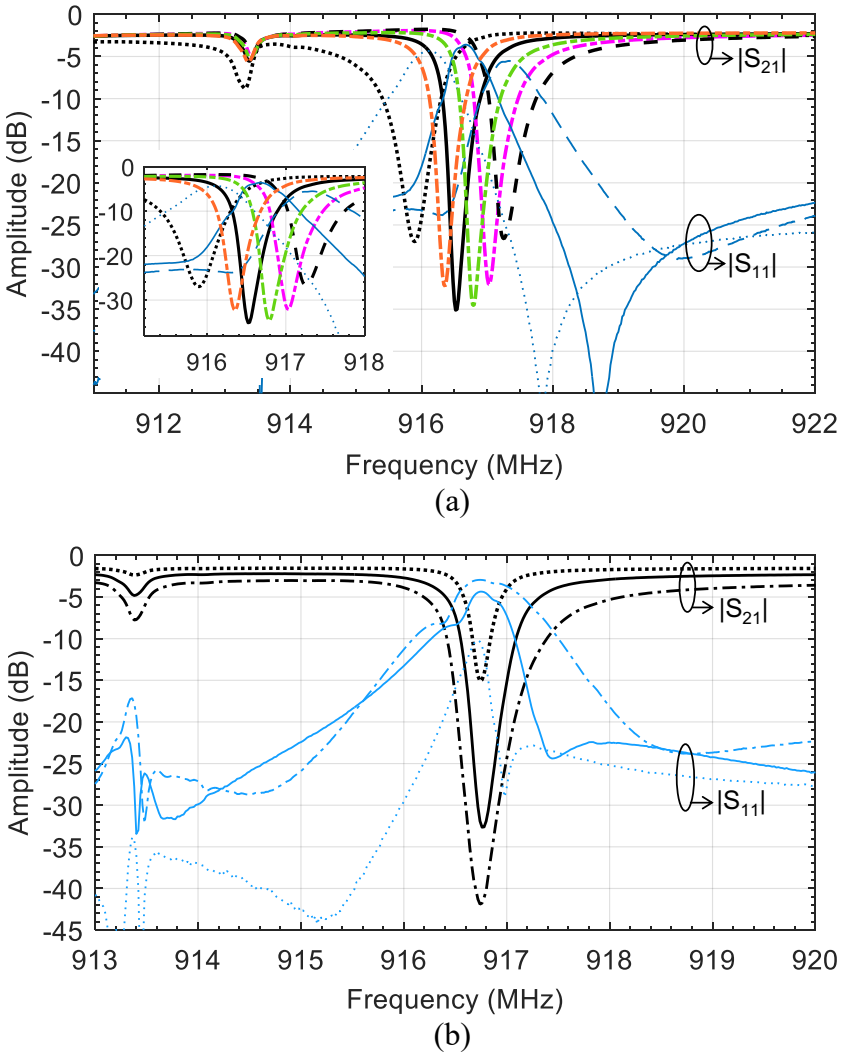


Figure 2.52. RF-measured S-parameters of the manufactured three-stage prototype in Figure 2.50 depicting its: (a) BS response exhibiting continuous f_{cen} tuning; (b) BS response exhibiting continuous BW tuning [92].

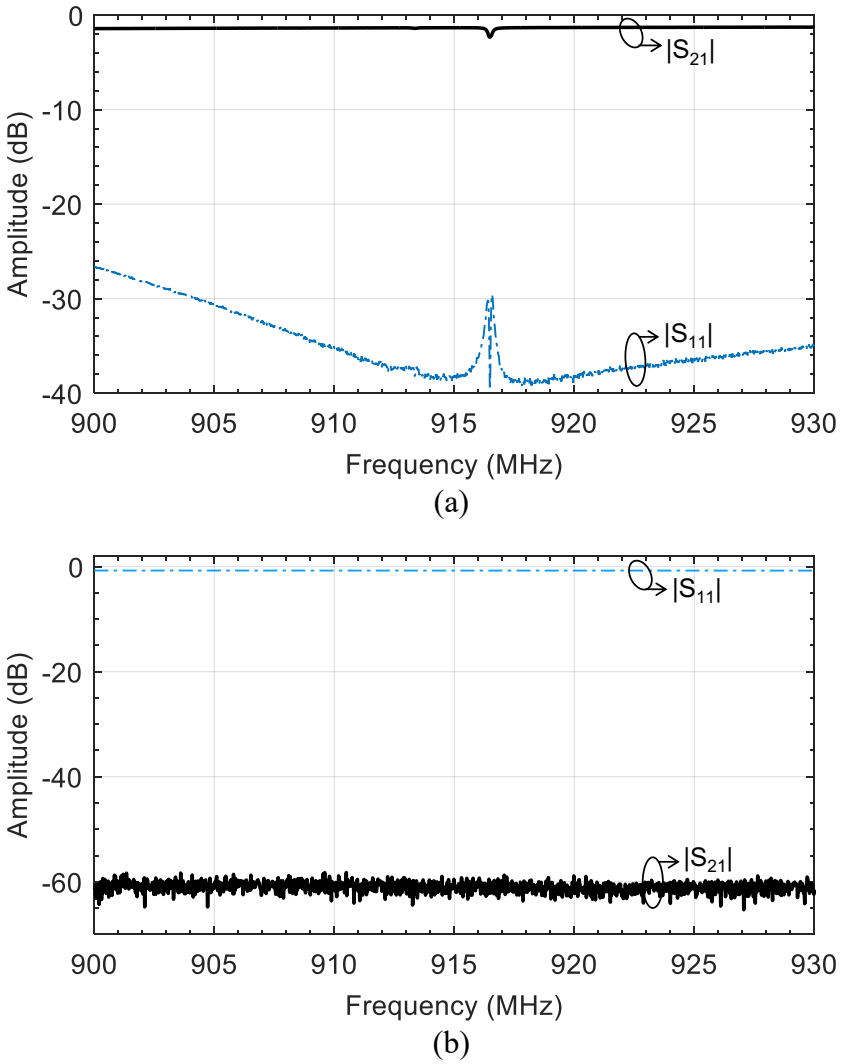


Figure 2.53. RF-measured S-parameters of the manufactured three-stage prototype in Figure 2.50 depicting its: (a) AP mode; (b) AS mode [92].

Table 2.4. Performance summary of the measured two-, and three-stage prototypes

prototype	Bandpass operation mode							Bandpass operation mode							
	f_{cen} tuning			BW tuning				f_{cen} tuning					BW tuning		
	BW (MHz)/ FBW (xk_t^2)	f_{cen} (MHz)/ [TR]	Min-IL (dB)/ [Q_{eff}]	f_{cen} (MHz)	BW (MHz) /FBW (xk_t^2)	Min-IL (dB)/ [Q_{eff}]	IS. (dB)	BW (MHz)	f_{cen} (MHz)/ [TR]	Out-of-band IL (dB)	IS. (dB)/ [Q_{eff}]	f_{cen} (MHz)	BW (MHz)/ FBW (xk_t^2)	Out-of-band IL(dB)	IS. (dB)/ [Q_{eff}]
Two-stage	BW:1 FBW:0.91	916.22– 917.01/ [100.086%:1]	3.1– 4.7/ [2,700– 4,400]	916.56	BW:0.47– 1.18 FBW:0.43– 1.073 TR: 2.5:1	2.7 - 4.8/ [3,900– 5,100]	27– 33	0.96	915.76– 917.22/ [100.159%:1]	1.3– 2.5	16.6–27/ [2,050– 4,600]	916.14	BW:0.54–1.62 FBW:0.49–1.47 TR: 3:1	1.2– 2	14.6– 23.5 [2,200– 3,300]
												916.5	BW: 0.33– 0.96 FBW:0.3– 0.87 TR: 2.9:1	1– 2	10.4– 23 [3,650– 4,250]
								1.42	915.7– 917.58/ [100.205%:1]	3.2– 3.6	20.7–26/ [1,950– 3,350]	916.9	BW: 0.33– 1.96 FBW= 0.3– 1.78 TR: 5.94:1	1.7– 5.2	20– 31.86 [3,350– 4,250]
Three-stage	BW:1.05 FBW:0.95	916.38– 917/ [100.067%:1]	3.4– 4.1/ [3,450– 4,500]	916.6	BW:0.5–1.14 FBW:0.45– 1.036 TR:2.28:1	3.1-5.8/ [5,800- 5,200]	34– 46	1.02	915.88– 917.26/ [100.15%:1]	1.9– 3	27–35/ [2,360– 4,650]	916.76	BW:0.41–1.46 FBW:0.37– 1.33 TR:3.56:1	1.55– 4	15– 42 [2,320– 4,410]

2.5 Comparison With State-of-the-Art AWR Filters

Table 2.5 provides a comprehensive comparison of the proposed adaptive AWLR-based filter concepts introduced in Sections 2.2,2.3, and 2.4 with state-of-the-art AWR-based reconfigurable filters. The proposed AWLR-based BPF with tunable BW (Section 2.4) is the only AWR-based BPF that allows electronically continuous BW tuning with enhanced FBW while exhibiting high Q_{eff}. For instance, the BPF concepts in ([50], [42]) only allow for reconfigurable TF states and the BPF in [34] facilitates discrete BW tuning. Additionally, the AWLR BPF concept in [52] is based on mechanically-tunable capacitors. The proposed AWLR-Based BPFs with multi-configurable and continuously tunable TF capabilities (Section 2.3) stands out as the only one that allows continuous electronic f_{cen} tuning, which is introduced in this work for the first time. Furthermore, this design is the only one that facilitates multiple levels of analog TF tunability and reconfigurability, namely continuous f_{cen} tuning, continuous BW, reconfigurable AP and AS mode of operation to be obtained in the same AWR-based filter while having comparable size with other AWLR-based BPFs, however with added functionality. In comparison, the filters in ([39], [41], [42], [43], [50]) only enable BP-to-AS TF reconfigurability. When compared to the filter architectures in ([47], [52], [90]), they only facilitate continuous BW tuning and ([47], [52]) rely on trimmer capacitors as opposed to electronically tunable TFs presented here. Furthermore, the AWR-based BSFs in ([11], [48], [51], [54]) only allow notch BW tuning and the ones in [50], [54] only enable BP-to-AP TF reconfiguration and are mostly implemented with mechanical trimmer capacitors. The RF-switch-based AWLR BPF concept in [12] only allows RF switched single-to-multi-band reconfiguration, while the AWR-based ladder BPF concept in [45] only switching ON/OFF the operation bands. Lastly, the filter in [44] only allows discrete f_{cen} reconfigured bands.

The proposed AWLR-based filter physical implementations is larger than the all-AWR monolithic acoustic-filter implementations in ([34], [39], [41], [42]) due being based on a low-cost PCBs integration using discrete SMD components, which dictate the size of the filter. However, the filters in ([34], [39], [41], [42]) aren't tunable. Regardless, the size of the proposed multi-configurable concept is comparable to AWLR-based BPFs as for example the ones shown in ([49], [51], [54], [90]) and is smaller than the one provided in [12]. In fact, the proposed implementation can be

considered to be effectively even smaller as it combines multiple functions within the same design volume as opposed to RF switched-based AWR filter implementations. Notably, the proposed concept (Section 2.4) is the only one that allows multiple levels of reconfigurability within the same filter volume and without needing to use any RF switches. These include: i) a BP mode with continuous f_{cen} and BW tuning, ii) a BS mode with continuous f_{cen} and BW tuning, iii) an AP mode and iv) an AS mode. Furthermore, the proposed filter concept demonstrates the potential to realize continuous f_{cen} tuning in an AWR-based BSF for the first time. In comparison to the filters listed in Table 2.5, the configurations in ([34], [39], [41], [43], [50], [42]) only facilitate BP-to-AS reconfiguration, with [34] and [53] also allowing for discrete BW tuning. The filters in [50] and [54] only facilitate BS-to-AP reconfiguration and the architectures in [45] and [12] only allow switching ON or OFF their operating bands. The AWLR-based filters in ([11], [47], [48], [52], [90]) only exhibit continuous BW tuning, and the topology in [47] additionally provides IS tuning alongside BP-to-AP reconfiguration. The filter concept in [51] only supports a BS response with tunable IS whereas the filter in [49] allows BP-to-BS reconfiguration with the aid of RF switches. The filter concept presented in [44] offers only two discrete states of f_{cen} reconfiguration. Finally, the previously introduced work in Section 2.3 supports a BP response with continuous f_{cen} and BW tuning, alongside a BP-to-AP-to-AS reconfiguration, but it doesn't support any BS mode of operation as is the case in this work (Section 2.4).

Table 2.5. Comparison with state-of-the-art reconfigurable AWR-based filters.

Ref.	Resonator Technology	Rec. modes	Order	FBW (xk_t^2)	f_{cen} (MHz)	Area (mm^2)	Min-IL (dB)	Q_{eff}	Rejection levels (dB)
2.2	AWLR/SAW	E. Tun. BW	4	0.573-1.32	916.6	441	2.2-3.9	6,000-7,700	27-55
2.3	AWLR/SAW	BP (C. E. Tun. f_{cen} & BW)/ AP/AS	2	0.34-1 & 0.22-0.47	999.9 & 1000.74	595	4.1-7.3	3,000-5,900	20-38
2.3	〃	〃	3	0.36-1.35 & 0.31 - 1.03	999.9 & 1000.74	882	3.3-6.9	4,000-6,400	25-59
2.4	AWLR/SAW	BP (C. E. Tun. f_{cen} & BW) / BS (C. E. Tun. f_{cen} & BW) / AP / AS	2	0.3-1.78	〃	281	1-5.2	1,950-5,100	10-33
2.4	〃	〃	3	0.37-1.33	〃	514.8	1.55-5.8	2,360-5,200	15-46
[34]	Ladder FBAR	BP (S. BW) / AS	N/A	0.33-0.50	2000	0.046	2.5-3.5	~340	12-25
[50]	AWLR/FBAR	BP / AS	2	0.333	2130	20.46	4	~300	16-19
[50]	AWLR/FBAR	BS / AP	2	0.31	2043	15.08	3.2	~300	27
[41]	BST-FBAR	BP / AS	3	0.43	2080	0.0088	2.25	~300	11.5
[39]	AIN Resonator	BP / AS	N/ A	N/ A	635	0.2	29.5	2,000-2,500	15-25
[43]	AIGaN Resonator	BP / AS	1	N/ A	246	0.0055	57-62	608-910	19
[45]	VO_2 Switched SAW/ Ladder	BP (S. bands)	5	N/ A	765/935	23.76	3.7-4.3	N/A	18-20
[44]	VO_2 Switched SAW/ Ladder	S. f_{cen}	6	N/A	732/755	6.72	1.5-1.8	~121-724	12
[53]	SAW/ ladder (PCM switches)	BP (S. BW)	7	N/A	650	N/A	N/A	~800-1,300	25-60
[52]	AWLR/SAW	BP (M. Tun. BW)	3	0.50-1.50	418	545.1	1.2-3.3	>10,000	23-46
[47]	AWLR/ SAW	BP (M. Tun. BW & IS) / AP	6	0.93-1.68	418/433.9	629.5	0.81-1.75	>10,000	10-40
[11]	AWLR/SAW	BS (M. Tun. BW)	2	0.27-1.9	433.9	765.4	3-6	3,500	22-25
[48]	AWLR/ SAW	BS (Tun. BW)	2	0.55-2.2	418	338.64	0.55-2	~8,000	25-40
[49]	AWLR/ SAW	BP/ BS	2	1.03/ 1.26	418/433	1089	1.5	>10,000	22-35
[54]	AWLR/SAW	BS (M. Tun. IS) / AP	2	2.7-3.3	917.5	792	5	N/A	20-43
[42]	Ladder/ lattice FBAR	BP/AS	N/A	0.50	2000	0.0378	5-6.2	N/A	12-50
[12]	AWLR/SAW	BP (S. bands)	2	0.8 -0.9	1000-1040	3211.5	2.37-4.25	3,500-5,300	>60
[51]	AWLR/SAW	BS (Tun. IS)	6	0.34	418.4	2188.3	0.96-1.14	N/A	15-37

(T.W.: This work, C. E. Tun.: Continuous electronically tunable, M. Tun.: Manual tuning, S.: Switchable, BP: Bandpass, BS: Bandstop, AS: All-stop, AP: All-pass, IS: Isolation)

2.6 Summary

This chapter has presented alternative design techniques and practical implementation concepts for the realization highly versatile AWLR-based RF filters. Several quasi-elliptic-type AWLR-based filter topologies have been introduced, including: i) highly selective BPFs with enhanced and continuously tunable FBW; ii) BPFs with multi-configurable and continuously tunable characteristics, and; iii) multi-configurable BP-to-BS filters with continuously tunable BW and f_{cen} tuning for both of its BP and BS modes of operation. As a unique contribution of this thesis, f_{cen} tuning is demonstrated for first time. Additionally, the proposed designs enable intrinsic switching between their BP, BS, AP, and AS modes within a single filter device, eliminating the need for RF switches. Several prototypes were implemented to experimentally validate the proposed designs, including two-stage, three-stage, and four-stage AWLR-based filters. These prototypes exhibited tunable BW and f_{cen}, along with intrinsic operating mode reconfiguration. They demonstrated enhanced FBW > 0.4-0.8k_t^2, Q_{eff} > 1,900, and out-of-band IS levels up to 55 dB. The multi-configurable filters introduced in this chapter pave the way for significant improvements in spectral efficiency, while reducing size, weight, power, and cost (SWaP-C). These innovations push the capabilities of filtering hardware to meet the evolving demands of next-generation RF systems, including frequency agility, spectrum management, and dynamic signal acquisition. The work introduced in this chapter work was published in [89], [90], [91], and [92]. Together, these innovations advance the development of compact, frequency-agile RF front-end modules, as envisioned in Figure 1.1(b), by introducing novel, ultra-compact, and highly reconfigurable RF filters that enable continuous tunability and multifunctionality through alteration of the operating mode within a single filtering component. These filters can adapt their response to varying spectrum conditions and communication device requirements, thereby facilitating further development toward highly miniaturized, multifunctional RF front-end modules.

Chapter 3: Multi-Band AWLR-Based BPFs With Reflectionless Characteristics

This chapter introduces a new class of AWLR-based multi-band BPFs architectures that uniquely support both reflective and symmetric quasi-reflectionless characteristics. Each passband is formed using multi-resonant AWLR stages composed of in-parallel SAW resonators and a single lumped inductor, reducing circuit complexity while maintaining compactness. Independent FBW control per band is achieved by varying the number of resonators without altering the inter-stage coupling. The proposed design utilizes unique resistively terminated bandstop AWLR stages configuration at the input/output ports, enabling—for the first time—a symmetric quasi-reflectionless multi-band response in AWR-based filters. The concepts introduced in this chapter has been published in [93], and [94].

3.1 Theoretical Foundations

3.1.1 Generalized multiband AWLR-Based filter concept using multi-resonant stages

The generalized concept of the reflective, multi-band, N^{th} order AWLR-based, BPF concept is illustrated in Figure 3.1(a). It is based on N high-Q multi-resonant bandpass-type AWLR stages (R_i) that are cascaded in-series with N-1 impedance inverters. Each multi-resonant stage comprises one lumped-inductor L_{0i} and K distinct one-port type AWRs (represented by their Butterworth-Van-Dyke circuit model [108] where C_{Mj}, L_{Mj}, R_{Mj} are the motional capacitance, inductance and resistance that resonate at the series resonance f_{sj}, and C_{0j} is the parasitic capacitance) whose f_{sj} (j=1, 2, …, K) defines the location of each passband. As such, each multi-resonant stage contributes to the filtering TF with K poles at f_{sj}. By selecting L_{0i} to resonate with the sum of the AWRs' parasitic capacitances $C_0=\Sigma_1^K C_{0j}$ at f_{0i} (i=1, 2, …, N) the series resonances of each AWR are decoupled from their anti-resonances and create (K+1) TZs. The multi-resonant stages R_i are coupled to the RF-ports through impedance inverters Z_{ex} and are cascaded using (N-1) impedance inverters ($Z_{1,2}$- $Z_{N-1,\,N}$) to form an N^{th} order quasi-elliptic filtering TF shaped by K•(N) poles and N•(K+1) TZs, as illustrated by the conceptual response in Figure 3.1(b).

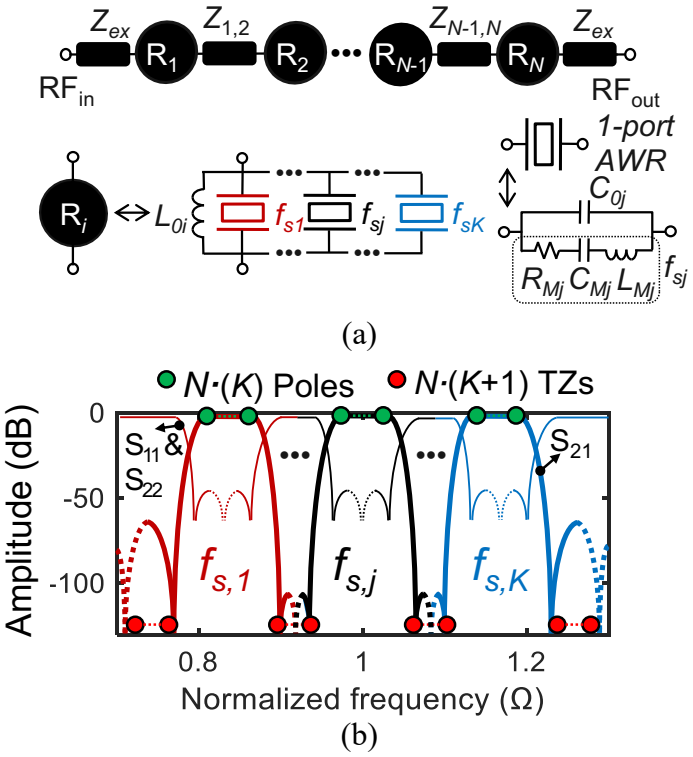


Figure 3.1. Multi-band quasi-elliptic AWLR-based BPFs using multi-resonant AWLR stages with reflective response characteristics: (a) Generalized circuit schematic of the reflective multi-band AWLR-based BPF comprising N in-series cascaded bandpass-type multi-resonant stages (black circles) (R_1, … ,R_N) and N-1 impedance inverters (black rectangles). Each multi-resonant stage comprises one LE inductor and K in-parallel cascaded AWRs, each with a different series resonant frequency, f_{sK},where f_{sK} is the f_{cen} of the K^{th} passband; (b) Conceptual S-parameters of the reflective multi-band AWLR-based BPF that exhibits K bands shaped by K•(N) poles and a total of N•(K+1) TZs [94].

The N^{th} order multi-band AWLR-based BPF can be adapted to achieve symmetric quasi-reflectionless characteristics. This is accomplished by incorporating two resistively terminated BS-type multi-resonant AWLR stages (R_C) at the RF input/output ports of the first (R_1) and last stage (R_N). In this manner a symmetric quasi-reflectionless multi-band TF can be created as a result of the generalized block diagram depicted in Figure 3.2(a). Each R_C multi-resonant stage comprises two lumped-inductors, L_1 and L_L, one lumped-capacitor, C_E, and K distinct one-port type AWRs (each resonating at the series resonance f_{sj}, j=1, 2, …, K). The K AWRs and L_1 are cascaded in parallel and are connected in series to the C_E and loaded by the inductor L_L. The inductor L_1 decouples the series resonances of the AWRs from their anti-resonances, and together with C_E and L_L they create a multi-band bandstop-type

filtering response that is formed by K stopbands. The FBW of the K-stopband is controlled by altering the values of L_1, C_E, and L_L (see Figure 3.8 for K=2 example). The R_C stages are designed to have a complementary response to the R_i stages. When resistively-terminated and connected to the input/output of the R_1 and R_N, the signal reflected at the input of R_1 is transmitted through R_C and dissipated in the resistive termination. Similarly, the signal reflected at the output of R_N is transmitted through R_C and dissipated in the resistive termination. This allows tailoring a symmetric quasi-reflectionless N^{th} order multi-band BPF response as depicted in the conceptual response in Figure 3.2(b) and will be further developed through practical examples in Section 3.1.3.

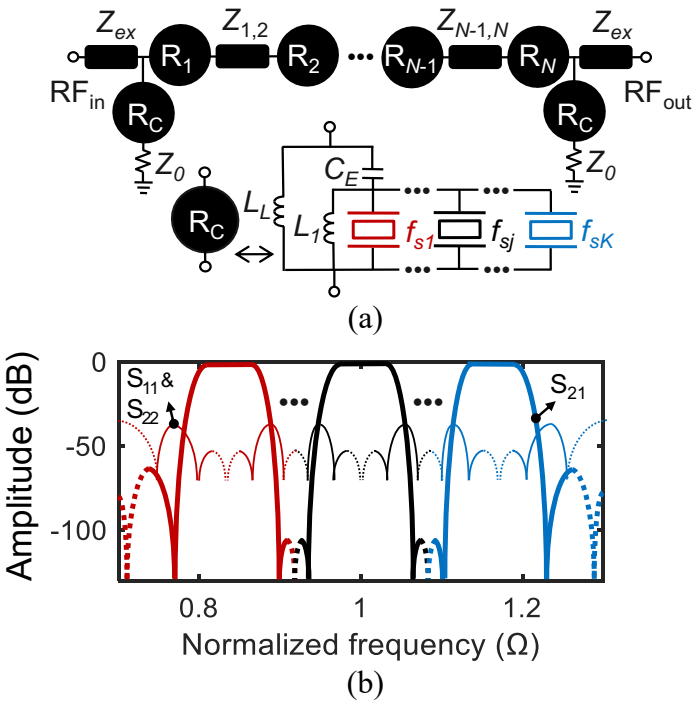


Figure 3.2. Multi-band quasi-elliptic AWLR-based BPFs using multi-resonant AWLR stages with quasi-reflectionless response characteristics: (a) Generalized circuit schematic of the quasi-reflectionless AWLR multi-band BPF. The quasi-reflectionless response is obtained by connecting two resistively-terminated bandstop-type multi-resonant AWLR stages (R_C) at the RF input/output ports of the multi-band AWLR BPF in Figure 3.1(a). Each R_C stage comprises one LE inductor (L_1) that is connected in-parallel to K AWRs. These are connected in series to a LE capacitor, C_E, and are loaded with a LE inductor, L_L; (b) Conceptual S-parameters of the quasi-reflectionless multi-band AWLR-based BPFs [94].

3.1.2 Reflective multi-band AWLR-based BPF

To elucidate the operating principles of the reflective-type multi-band AWLR-based BPF concept, a second-order dual-band BPF (K=2, N=2) example is considered in Figure 3.3(a) using two commercially available SAW resonators from TST SAW with k_t^2= 0.12%, f_{s1}=1033.3 MHz (L_{M1}=22.47 µH, C_{M1}=1.056 fF, and C_{01}=1.142 pF) and f_{s2}=1040 MHz (L_{M2}=19.42 µH, C_{M2}=1.206 fF, and C_{02}=1.272 pF). The filter consists of two in-series, cascaded, dual-band, bandpass-type, AWLR stages (each one is formed by two distinct AWRs resonating at f_{s1} and f_{s2} and one LE inductor, L_{0i}) that are interconnected through the impedance inverters Z_{ex} and $Z_{1,2}$, utilizing a total of four SAW resonators. It exhibits a quasi-elliptic TF that is shaped by two two-pole passbands and six TZs, i.e., four-pole/six-TZ. Unlike traditional AWR-based filter designs, its FBW can be designed to be wider than the 0.4-0.8k_t^2 limit by only adjusting Z_{ex} and $Z_{1,2}$. Notably, wider FBWs are obtained by increasing the values of Z_{ex} and $Z_{1,2}$, as demonstrated in the linear circuit S-parameter simulations in Figure 3.4.. The achievable BW ranges are Band 1: BW_1= 0.47 to 2.5 MHz (i.e., FBW_1= 0.38– 2k_t^2) and Band 2: BW_2= 0.54 – 3.05 MHz (i.e., FBW_2= 0.43– 2.44k_t^2). The out-of-band IS characteristics of the multi-band BPF can be reconfigured to achieve alternative IS profiles by adjusting the location of the TZs around the passbands, as illustrated in Figure 3.5. These TZs can be tuned by changing f_{01} and f_{02}, which are practically controlled by altering the inductance of the LE inductors L_{01} in stage R_1 and L_{02} in stage R_2, of the TF shown in Figure 3.3(a). Additionally, the TZs can be merged by setting f_{01}=f_{02}=1.0013f_s. The resonant frequencies f_{0i} and f_{sj} are defined as ($f_{s1}=1/2\pi\cdot(L_{M1}\cdot C_{M1})^{1/2}$, $f_{s2}=1/2\pi\cdot(L_{M2}\cdot C_{M2})^{1/2}$, $f_s=(f_{s1}\cdot f_{s2})^{1/2}$, $C_0=C_{01}+C_{02}$, $f_{01}=1/2\pi\cdot(L_{01}\cdot C_0)^{1/2}$ and $f_{02}=1/2\pi\cdot(L_{02}\cdot C_0)^{1/2}$).

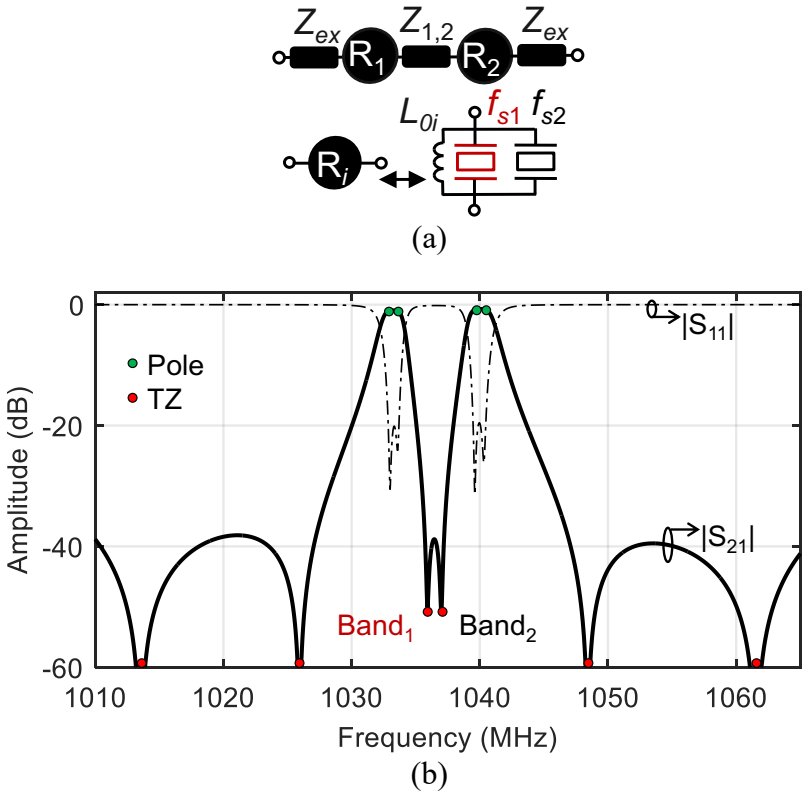


Figure 3.3. Dual-band BPF shaped by two multi-resonant stages and that exhibits a four-pole/six-TZ TF: (a) Circuit schematic; (b) Simulated S-parameters using linear circuit simulations (Z_{ex}=86 Ω, Z_{12}=37 Ω, f_{01}=0.988f_s, f_{02}=1.0138f_s, f_{s1} is the series resonant frequency of the commercially available SAW resonator with L_{M1}=22.47 µH, C_{M1}=1.056 fF, and C_{01}=1.142 pF, f_{s2} is the series resonant frequency of the commercially available SAW resonator with L_{M2}=19.42 µH, C_{M2}=1.206 fF, and C_{02}=1.272 pF, both SAW resonators have a k_t^2=0.12%, and f_s=(f_{s1}·f_{s2})$^{1/2}$) [94].

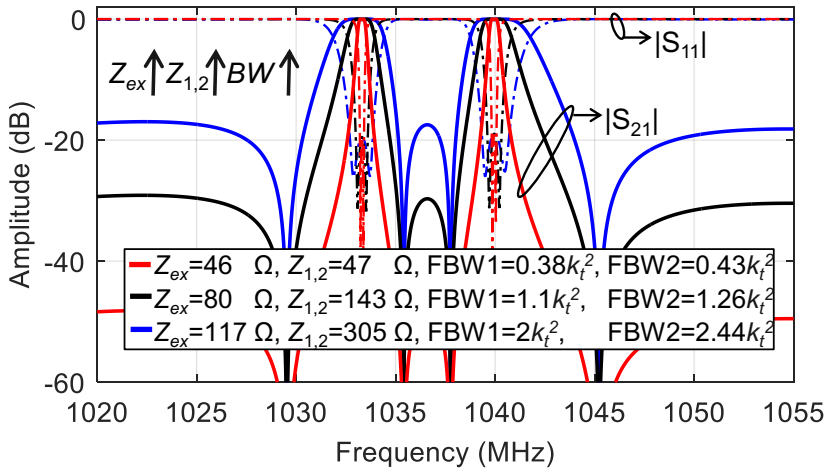


Figure 3.4. Simulated S-parameters of the two-stage dual-band BPF in Figure 3.3(a) for alternative FBWs obtained by altering the Z_{ex} and Z_{12} impedance values. In these examples, f_{01}=0.988f_s and f_{02}=1.0138f_s [94].

The maximum achievable FBW is limited by the maximum realizable impedance inverter values of Z_{ex} and $Z_{1,2}$. For example, in Figure 3.4., the maximum achievable FBW for bands 1 and 2 is 2 and $2.44k_t^2$, respectively, when Z_{ex} = 117 Ω and $Z_{1,2}$=305 Ω . To realize high impedance Z=305 Ω at f= 1 GHz using LE technology, the required LC equivalent of a π-network impedance inverter is $L=Z/(2\pi \cdot f)$ = 47 nH and $C=1/(2\pi \cdot f \cdot Z)$ =0.5 pF. Achieving accurate impedance inverter values higher than 300 Ohm at 1 GHz or higher frequencies on a PCB using off-the-shelf SMD LE components is challenging due to the need for lower capacitances (less than 0.5 pF). These are hard to realize accurately given SMD capacitors typically have tolerances of ±(0.05–0.1) pF [107], and considering that the parasitic capacitance from SMD soldering onto the PCBs is about 0.05 pF. To address this constraint, the FBW of the TF can be expanded by augmenting the total capacitance $C_{Tj}= M \cdot C_M$ (M is the total number of AWRs with f_{sj}) in the corresponding circuit branch of each passband. This is accomplished by increasing the number of AWRs for each passband by cascading several of them in parallel, as depicted in Figure 3.6(a) while utilizing impedance inverters of the same characteristics. In this example, tripling the number of the AWRs (i.e., using three resonators per f_{sj}) widens the FBWs of bands 1 and 2 by a factor of 2.9 times compared to the standard AWLR scenario (where only one AWR is employed per f_{sj}).

The increase in the number of SAW resonators in the AWLR stages also allows for independent control of the FBW of each passband. This is achieved by increasing the number of SAW resonators in the multi-resonant AWLR stage that control the specific band of interest as shown in Figure 3.6(b) and without needing to alter the impedance inverters. In this example, by tripling the number of AWRs corresponding to band 1 (i.e., using three resonators per f_{s1}), the FBW of band 1 widened by a factor of 2.9 compared to the standard AWLR case (where only one AWR is utilized per f_{s1}), while the FBW of band 2 remains the same as in the standard AWLR case. On the contrary, by tripling the AWRs corresponding to band 2, the FBW of band 2 is widened whereas the FBW of band 1 remains the same as in the standard AWLR case. Moreover, the multi-band AWLR concept can be easily extended to accommodate additional operating bands. This is illustrated in Figure 3.7, where a two-stage-based BPF is considered, comprising two bandpass-type multi-resonant AWLR stages shaped by three distinct AWRs cascaded in parallel, with the following characteristics

k_t^2= 0.12%, f_{s1}=1029.9 MHz (L_{M1}=22.04 µH, C_{M1}=1.056 fF, and C_{01}=1.142 pF), f_{s2}=1033.3 MHz (L_{M2}=22.47 µH, C_{M2}=1.084 fF, and C_{02}=1.122 pF) and f_{s3}=1040 MHz (L_{M3}=19.42 µH, C_{M3}=1.206 fF, and C_{03}=1.272 pF). The filter uses a total of six SAW resonators and exhibits three bands centered at 1029.9, 1033.36, 1040 MHz and having FBWs of 1.58, 1.39, and 1.73k_t^2 respectively.

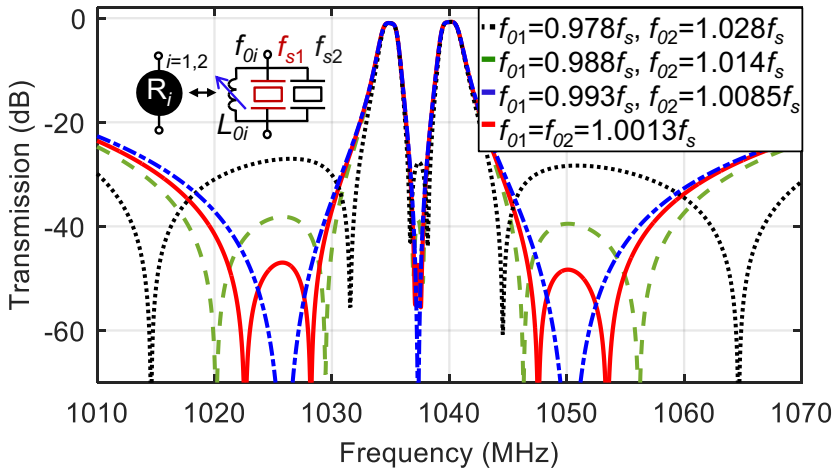
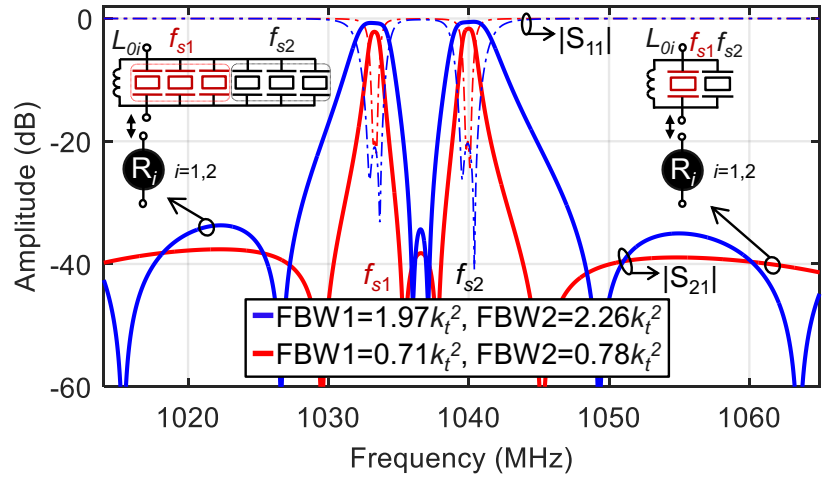
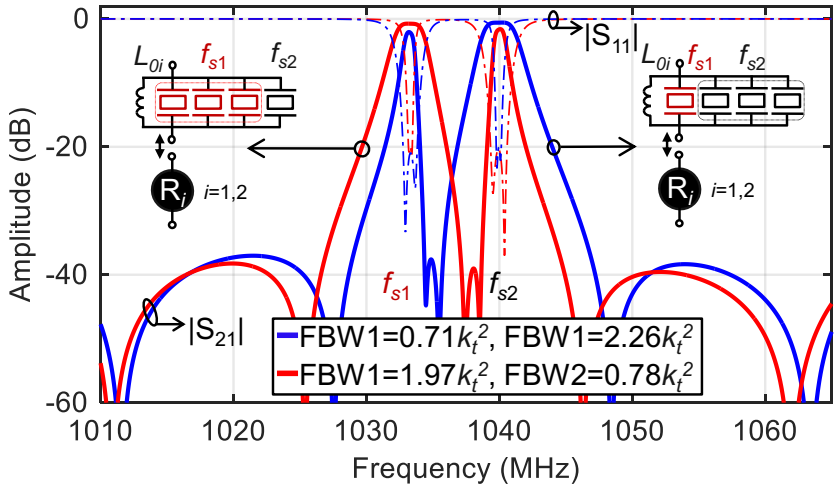


Figure 3.5. Simulated S-parameters of the two-stage dual-band BPF showing TZs tuning.



(a)



(b)

Figure 3.6. Simulated S-parameters of the two-stage dual-band BPF in Figure 3.3(a): (a) FBW enhancement by increasing the number of SAW resonators in the multi-resonant AWLR stage for each f_{sj} without needing to alter the impedance inverters; (b) Independent FBW control by increasing the SAW resonators in the multi-resonant AWLR stage that correspond to a specific f_{sj} without needing to alter the impedance inverters. In these examples, the impedance inverters are set to Z_{ex}=62.7 Ω and Z_{12}=86.25 Ω [94].

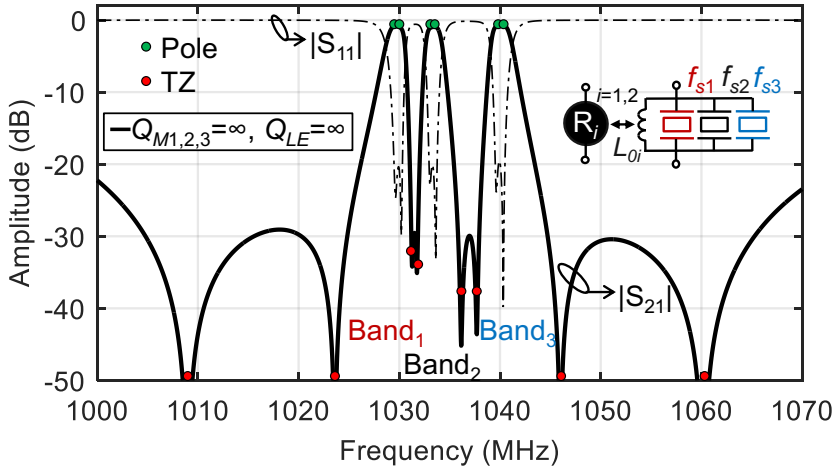


Figure 3.7. Simulated S-parameters for a two-stage, triple-band, BPF by incorporating in the multi-resonant AWLR stages (R_i) three distinct AWRs with series resonant frequencies f_{s1}, f_{s2}, f_{s3} that correspond to the f_{cen}s of band 1, 2, and 3 respectively [94].

3.1.3 Quasi-reflectionless multi-band AWLR-based BPFs

To demonstrate the operating principles of the symmetric quasi-reflectionless multi-band BPF, first the design of the bandstop-type multi-resonant AWLR stage is presented. Specifically, the schematic and linear simulation of a dual-band single stage (K=2) BS-type AWLR (R_C) are shown in Figure 3.8. The R_C is shaped using two distinct AWRs–SAW resonators from TST with k_t^2= 0.12%, f_{s1}=1033.3 MHz (L_{M1}=22.47 µH, C_{M1}=1.056 fF, and C_{01}=1.142 pF) and f_{s2}=1040 MHz (L_{M2}=19.42 µH, C_{M2}=1.206 fF, and C_{02}=1.272 pF)—, two LE inductors L_1 and L_L and one capacitor C_E. The inductor L_1 decouples the series resonances of the AWRs from their anti-resonances, and together with C_E and L_L, they create a dual-band bandstop-type filtering response with two stopbands, as shown by the simulated results in Figure 3.8. The FBW of the two stopbands can be increased by increasing the value of C_E and by decreasing the values of L_1, and L_L. The response is termed symmetric because it can achieve the quasi-reflectionless behaviour at both the input and output ports. It is described as quasi-reflectionless because the reflections are significantly suppressed, although not eliminated completely, resulting in a response that is nearly—but not perfectly—reflectionless.

In Figure 3.9, a symmetric, quasi-reflectionless, single-stage, dual-band BPF (N=1, K=2) is considered using the BSF stage in Figure 3.8. The design process includes: i) adjusting both the BP-type and BS-type stages to complement each other's

responses (see power transmission response in Figure 3.9(a)); ii) connecting the R_1 stage in the main filtering channel and iii) incorporating two resistively terminated R_C stages at the input/output of R_1, as depicted by the block diagram in Figure 3.9(b). In this manner, the R_1 stage determines the overall power transmission response of the symmetric quasi-reflectionless stage, while the reflected power in its stopband regions dissipates in the resistive termination of the R_C stages, achieving quasi-reflectionless behaviour with a maximum reflection level of -10 dB, as demonstrated in the linear simulated example in Figure 3.9(b). In this example, the quasi-reflectionless AWLR stage utilizes a total of six AWRs.

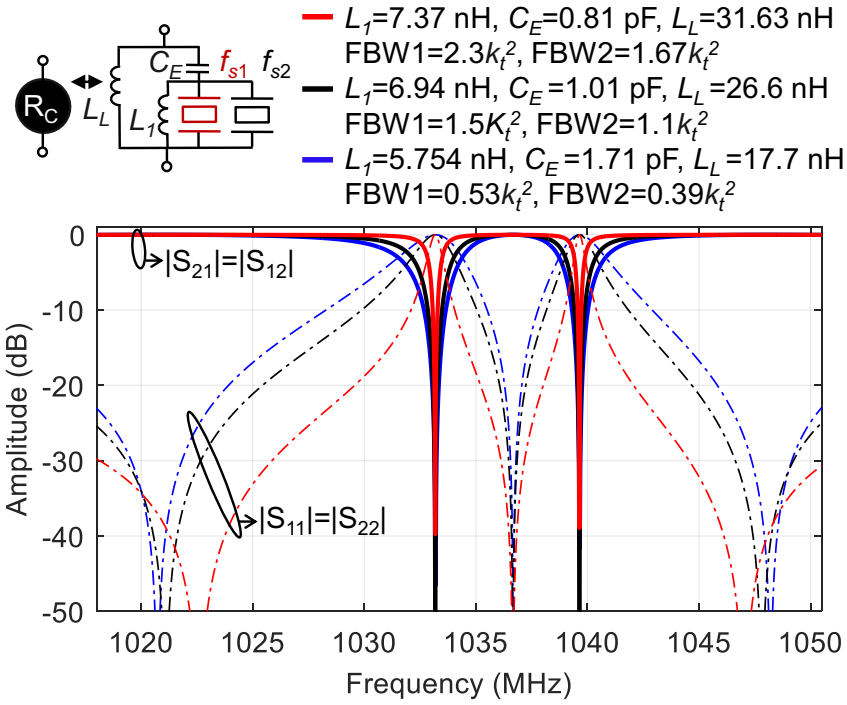


Figure 3.8. Simulated power transmission ($|S_{21}|=|S_{12}|$) and reflection ($|S_{11}|=|S_{22}|$) responses of the BS-type, multi-resonant, AWLR stage illustrating FBW control by altering L_1, C_E, and L_L [94].

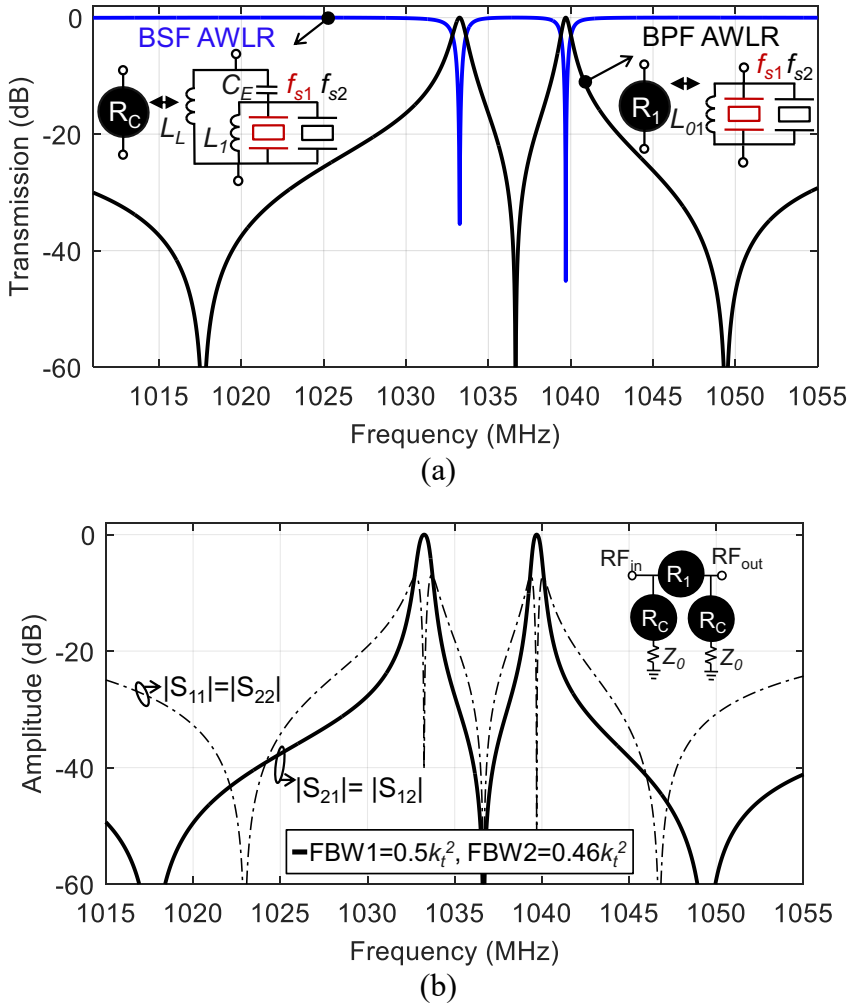


Figure 3.9. Simulated power transmission ($|S_{21}|=|S_{12}|$) and reflection ($|S_{11}|=|S_{22}|$) responses of the: (a) BP-type multi-resonant AWLR stage and its complementary BS-type multi-resonant AWLR stage; (b) and the quasi-reflectionless dual-band stage. Simulated S-parameters using linear circuit simulations (f_{01}=0.988f_s, f_{02}=1.0138f_s, L_1=6.94 nH, C_E= 1.01 pF, L_L=26.6 nH) [94].

The symmetric quasi-reflectionless multi-band BPF concept can be extended to realize higher order TFs. An example of a two-stage, dual-band (N=2, K=2), quasi-reflectionless BPF TF is shown in Figure 3.10. It incorporates two, in-series, cascaded dual-band, bandpass-type, AWLR stages, R_1 and R_2, which are coupled through impedance inverters, Z_{ex} and $Z_{1,2}$, and are connected to two resistive-terminated dual-band BS-type AWLR stages (R_C) exhibiting complementary characteristics to R_1 and R_2. The two resistive-terminated R_C stages are connected at the input/output of R_1 and R_2. The quasi-reflectionless two-stage, dual-band, BPF, utilizes a total of eight AWRs. As shown by the linear simulation in Figure 3.10, the TF exhibits a symmetric quasi-

reflectionless quasi-elliptic response shaped by two two-pole passbands and six-TZ, i.e., a four-pole/six-TZ configuration with passbands centred at 1033.36 and 1040 MHz, with FBWs of 0.5, and $0.4k_t^2$, respectively. The power transmission response is determined by the main filtering channel based on the bandpass-type AWLRs R_1 and R_2, while the reflected power at the stopband regions is dissipated in the resistive termination of the BS-type R_C stages connected at the input/output side of R_1 and R_2, achieving a symmetric quasi-reflectionless behaviour with a maximum reflection level of -10 dB. The AWLR stages used in this example are identical to those shown in Figure 3.9(a). Furthermore, an example of a three-stage, triple-band (N=3, K=3), quasi-reflectionless BPF TF is provided in Figure 3.11, demonstrating the scalability of the concept to higher order and higher number of passbands. The TF consists of three in-series, cascaded, triple-band, bandpass-type, AWLR stages, R_1, R_2, and R_3, which are coupled through impedance inverters Z_{ex}, $Z_{1,2}$, and $Z_{2,3}$, and connected to two resistive-terminated triple-band, BS-type, AWLR stages (R_C) exhibiting complementary characteristics to R_1, R_2, and R_3. The two resistive-terminated R_C stages are connected at the input/output of R_1 and R_3. The quasi-reflectionless three-stage triple-band BPF utilizes a total of 15 AWRs. As shown in the linear simulation in Figure 3.11, the TF exhibits a symmetric quasi-reflectionless quasi-elliptic response shaped by three three-pole passbands and twelve-TZ, i.e., a nine poles/twelve TZs configuration with passbands centered at 1029.9, 1033.36, and 1040 MHz, having FBWs of 0.47, 0.52, and $0.4k_t^2$, respectively. The power transmission response is determined by the main filtering channel based on the bandpass-type AWLRs, R_1, R_2, and R_3, while the reflected power in the stopband regions is dissipated in the resistive termination of the BS-type R_C stages, achieving a symmetric quasi-reflectionless characteristics with a maximum reflection level of -10 dB. The multi-resonant AWLRs are based on three distinct AWRs with the following characteristics: k_t^2= 0.12%, f_{s1}=1029.9 MHz (L_{M1}=22.04 µH, C_{M1}=1.056 fF, and C_{01}=1.142 pF), f_{s2}=1033.3 MHz (L_{M2}=22.47 µH, C_{M2}=1.084 fF, and C_{02}=1.122 pF), and f_{s3}=1040 MHz (L_{M3}=19.42 µH, C_{M3}=1.206 fF, and C_{03}=1.272 pF).

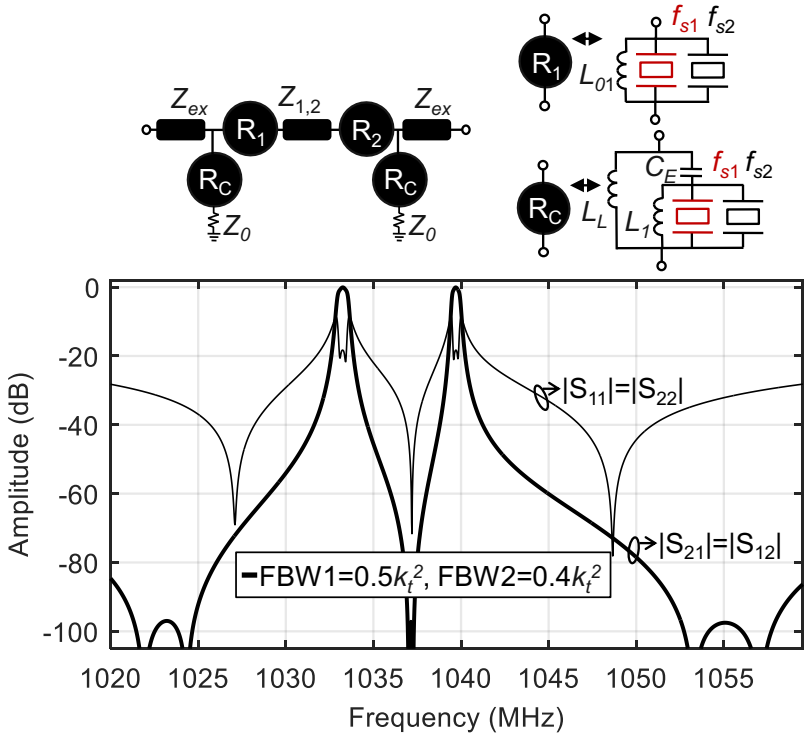


Figure 3.10. Two-stage, dual-band, quasi-reflectionless, AWLR-based BPF shaped by two multi-resonant AWLR stages and two resistively-terminated multi-resonant AWLR stages with complementary TF. It exhibits a four-pole/six-TZ TF: (a) Circuit schematic; (b) Simulated S-parameters using linear circuit simulations (Z_{12}=56.5 Ω, f_{01}=0.988f_s, f_{02}=1.0138f_s, f_1=1.24f_s, C_E= 1.91 pF, L_L=12.14 nH) [94].

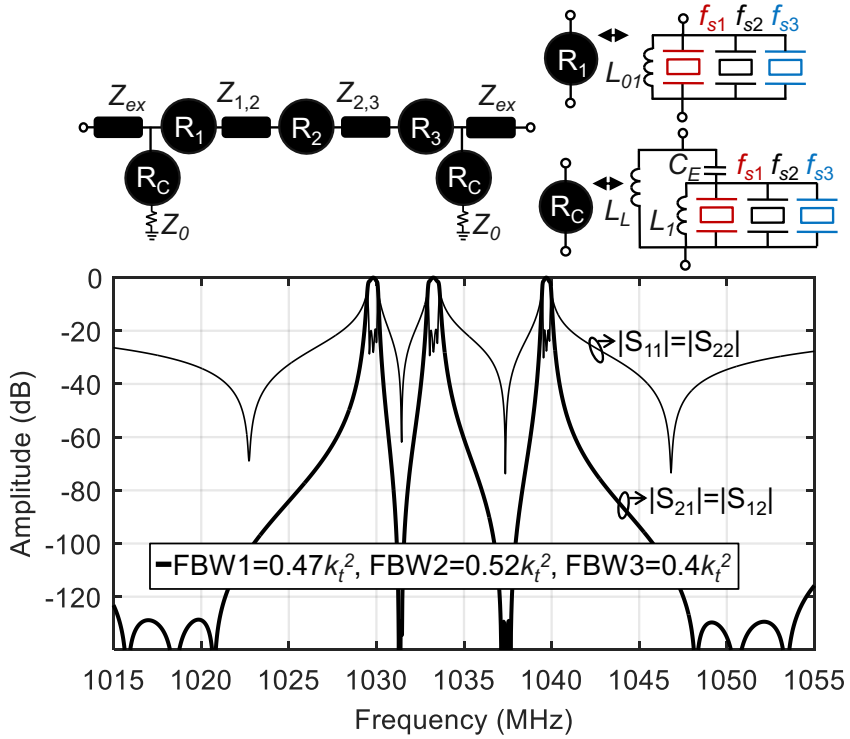


Figure 3.11. Three-stage triple-band, quasi-reflectionless BPF shaped by three multi-resonant AWLR stages and two resistively-terminated BS-type multi-resonant AWLR stages. It exhibits a nine-pole/twelve-TZ TF: (a) Circuit schematic; (b) Simulated S-parameters using linear circuit simulations (Z_{12}=50 Ω, Z_{12}=52 Ω, f_{01}=0.988f_s, f_{02}=1.0138f_s, f_1=1.24f_s, C_E= 1.91 pF, L_L=12.14 nH) [94].

3.2 Experimental Validation

To experimentally validate the quasi-elliptic multi-band BPF concept with reconfigurable reflection characteristics, three filtering prototypes were designed manufactured and tested. Their RF design was performed using the design guidelines in Section 3.1, linear and EM simulations using the software packages ADS from Keysight [109] and high-frequency structure simulator (HFSS) from Ansys [110]. The prototypes were implemented on a 0.813 mm thick Rogers 4003C substrate. Furthermore, commercially available SAW resonators from TST SAW Inc. [105] were used for the implementation of the AWLRs.

3.2.1 Reflective multi-band AWLR-based BPFs

Two second-order, reflective, multi-band, AWLR-based BPF prototypes were designed, manufactured, and experimentally tested. The first prototype is a dual-band (i.e., N=K=2) BPF with passbands centred at 1033.4 and 1039.9 MHz, while the second prototype is a triple-band BPF (i.e., N=2 and K=3) with passbands centred at 1029.9, 1033.4 and 1039.9 MHz. The layout of the dual-band prototype is illustrated in Figure 3.12(a), and a photograph of the manufactured prototype is shown in Figure 3.12(b) along with the utilized SMD components. As shown the dual-band BPF prototype uses a total of four AWRs. Its measured RF response is shown in Figure 3.12(c). Additionally, its corresponding EM simulated responses using the single- and multi-mode BVD models are also provided in Figure 3.12(c). Overall, the EM simulated state shows a good agreement with the RF measured ones. The measured RF performance exhibits the following characteristics: i) low band: f_{cen}=1033.2 MHz, 3-dB BW=0.96MHz that corresponds to FBW=0.78k_t^2, minimum in-band IL of 2.4 dB that corresponds to an extracted Q_{eff} of 6,200; ii) high band: f_{cen}=1039.9 MHz, 3-dB BW=1.25 MHz i.e. FBW=1k_t^2, IL of 1.63 dB that corresponds to an extracted Q_{eff} of 6,700. The out-of-band IS was measured to be better than 24 dB over the entire stopband region.

The layout of the triple-band prototype is illustrated in Figure 3.13(a), and a photograph of the manufactured prototype is shown in Figure 3.13(b) along with the utilized SMD components. As can be seen, the triple-band BPF prototype uses a total of six AWRs. Its measured response is depicted in Figure 3.13(c) alongside its corresponding EM simulated states which are in a good agreement. The RF measured

performance shows the following characteristics: i) low band: f_{cen}=1029.83 MHz, 3-dB BW=0.65 MHz that corresponds to FBW=0.53k_t^2, minimum in-band IL of 3.95 dB that corresponds to an extracted Q_{eff} of 5,400; ii) middle band: f_{cen}=1033.4 MHz, 3-dB BW=0.6 MHz, i.e. FBW=0.48k_t^2, min-IL of 3.88 dB that corresponds to an extracted Q_{eff} of 6,000; iii) high band: f_{cen}=1039.9 MHz, 3-dB BW=0.87 MHz, i.e. FBW=0.7k_t^2, min-IL of 3-dB that corresponds to an extracted Q_{eff} of 6,000. The out-of-band IS was measured to be better than 30 dB across the entire measured stopband region. Overall, the manufactured prototypes validate the proposed multi-band reflective BPF concept.

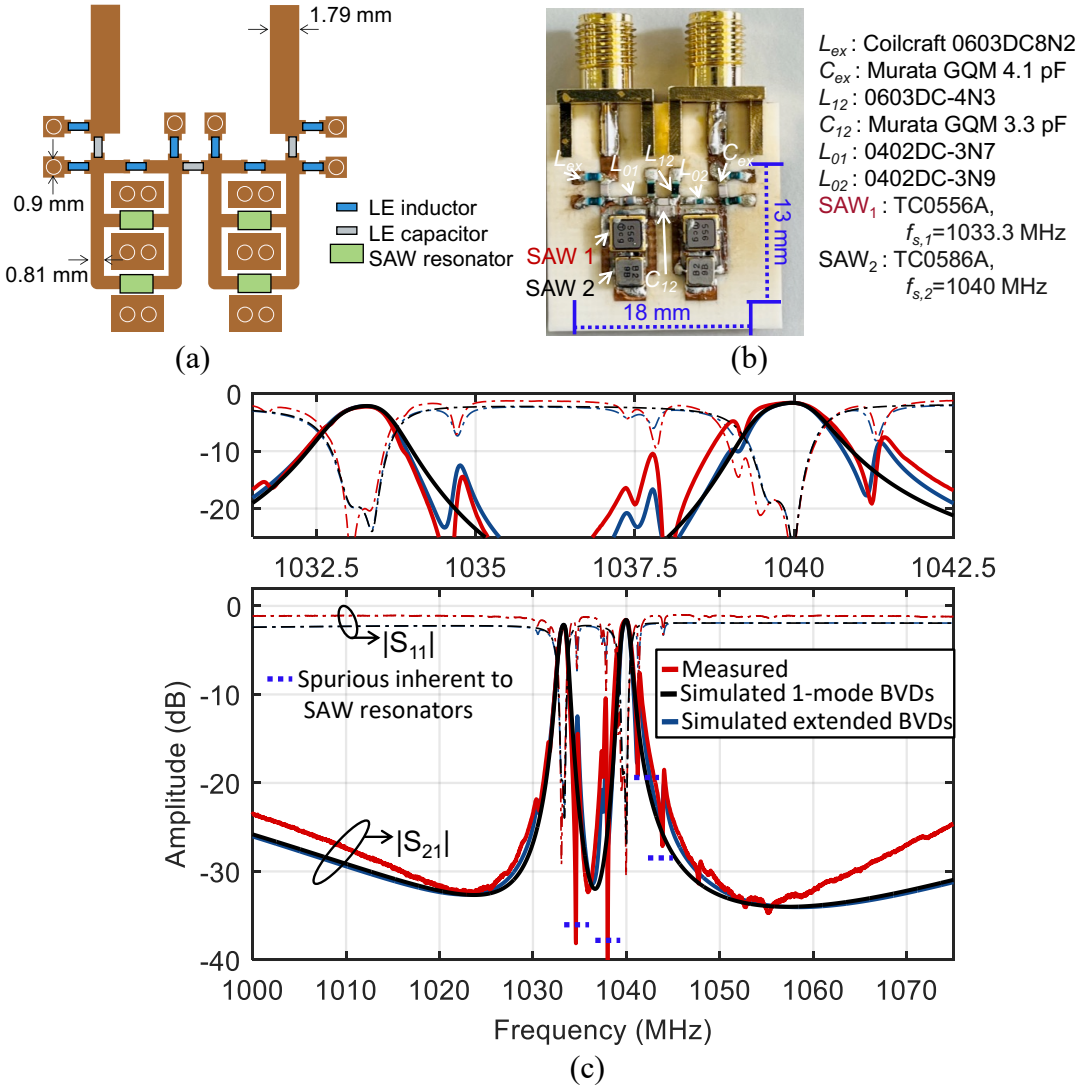


Figure 3.12. Second-order dual-band AWLRs BPF: (a) Filter layout; (b) Photograph of the manufactured prototype; (b) RF-measured power transmission ($|S_{21}|=|S_{12}|$) and reflection ($|S_{11}|=|S_{22}|$) response of the manufactured prototype alongside its corresponding EM-simulated response using: i) single-mode (black trace), ii) multi-mode (blue trace) SAW BVD models [94].

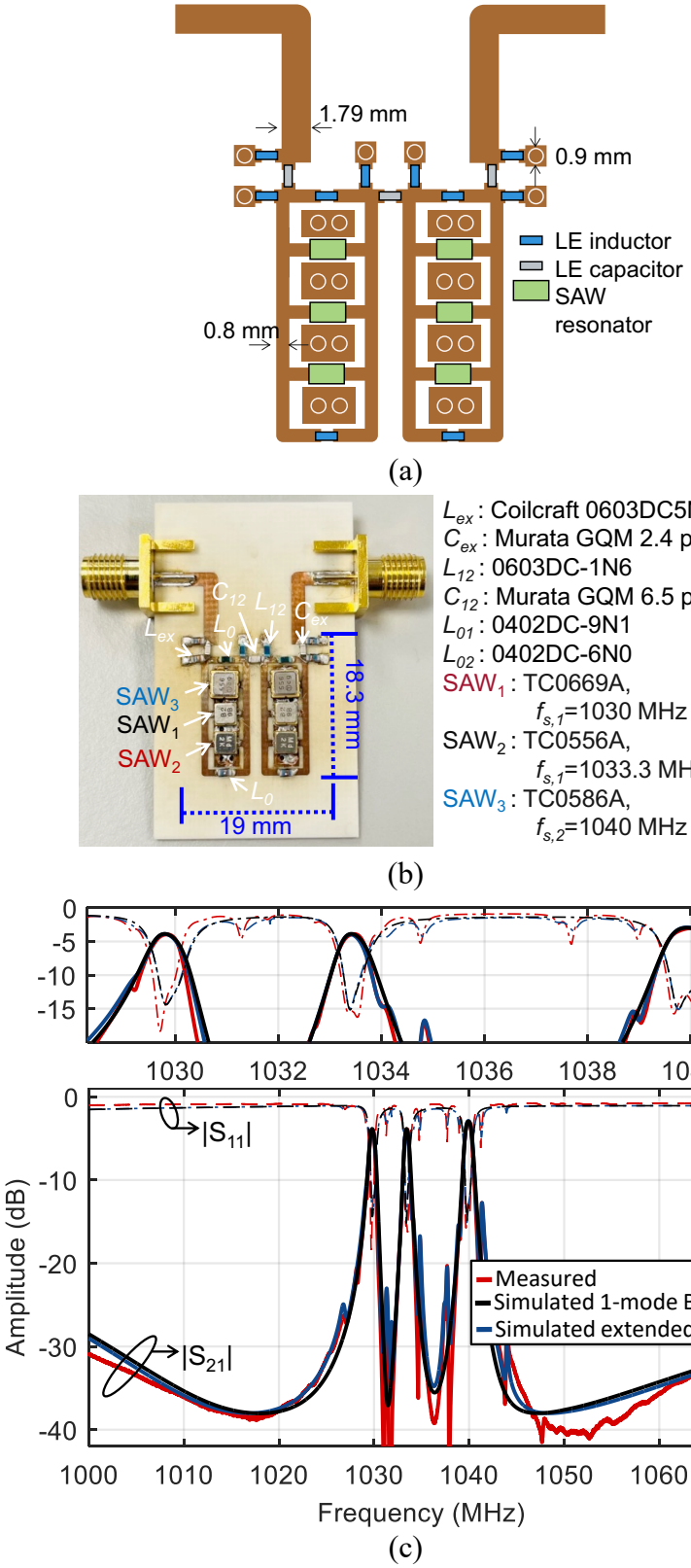
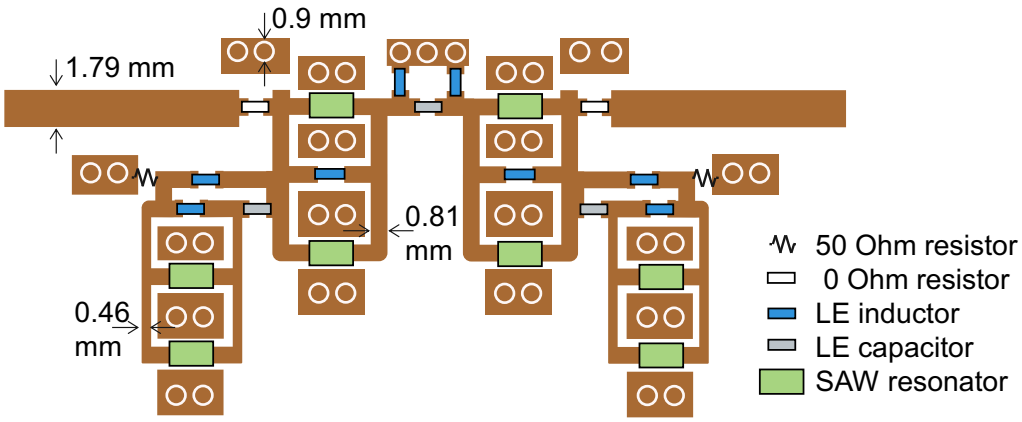


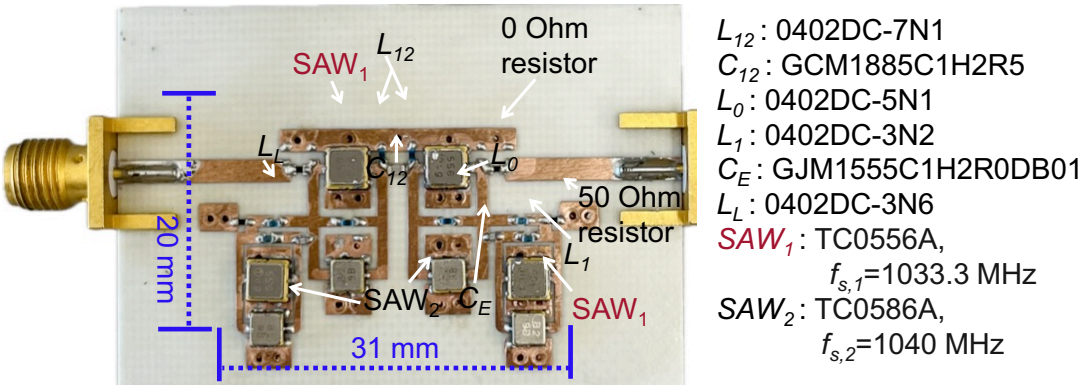
Figure 3.13. Second-order triple-band AWLRs BPF: (a) Filter layout; (b) Photograph of the manufactured prototype; (c) RF-measured power transmission ($|S_{21}|=|S_{12}|$) and reflection ($|S_{11}|=|S_{22}|$) response of the manufactured prototype alongside its corresponding EM-simulated response [94].

3.2.2 Quasi-reflectionless multi-band AWLRs

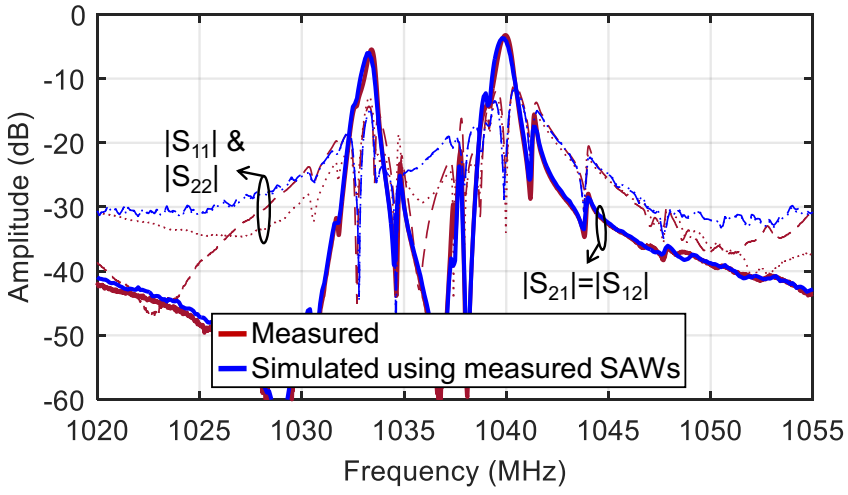
A two-stage, dual-band (i.e., N=K=2), quasi-reflectionless, BPF prototype with passbands centred at 1033.4 and 1039.9 MHz was developed and experimentally tested. The layout and a photograph of the manufactured prototype are depicted in Figure 3.14(a) and (b). Its RF-measured performance is shown in Figure 3.14(c) in addition to the corresponding EM simulated response using measured SAW resonators for comparison purposes, and they are in good agreement. The measured RF response is summarised as follows: i) in band 1: f_{cen}=1033.4 MHz, 3-dB BW=0.46 MHz (i.e., FBW=0.38k_t^2), min-IL of 5.45 dB corresponding to Q_{eff} of 5,500; ii) in band 2: f_{cen}=1039.96 MHz, 3-dB BW=0.65 MHz (i.e. FBW=0.52k_t^2), min-IL of 3.2 dB with Q_{eff} of 6,300. The overall TF is shaped by two two-pole passbands and six TZs, i.e., a four-pole/six TZs, with a quasi-reflectionless behaviour exhibiting a maximum reflection level of -11.5 dB. Additionally, the out-of-band IS was measured to be better than 40 dB throughout the entire stopband region.



(a)



(b)



(c)

Figure 3.14. Symmetric, quasi-reflectionless, second-order, dual-band AWLR BPF: (a) Filter layout; (b) Photograph of the manufactured prototype; (c) RF-measured power transmission and reflection response [94].

3.2.3 Comparison with state-of-the-art multi-band AWR filters

A comparison of the proposed multi-band, AWLR-based, BPF concept with state-of-the-art AWR-based multi-band filters is presented in Table 3.1. When compared with the concepts in [47] and [12], the proposed concept leads to a smaller size, requiring fewer LEs per stage. The reflective type BPF in this work utilizes only one LE inductor per stage, whereas in [47] and [12], five LE components are required. The reduced number of required LEs results in a smaller filter layout. Furthermore, when compared with the filters in [111] and [112], the proposed configuration uses fewer number of distinct AWR resonators to form the passbands. Moreover, this is the only, multi-band, AWLR-based BPF concept that facilitates symmetric quasi-reflectionless characteristics, compared to [47], [12], [111], and [112], which exhibit reflective type, out-of-band responses.

Table 3.1. Comparison with state-of-the-art AWR-based multi-band BPFs.

Ref.	Out-of-band reflection response	Order	# of bands	# of distinct AWRs	# of LEs per AWLR stage	Operating centre freq. (MHz)	IL (dB)	Q_{eff}	Size (λ^2)
3.2.1	Reflective	2	Dual-band	2	1	1030-1040	1.6, 2.4	6,200-6,700	0.00264
3.2.1	Reflective	2	Tripple-band	3	1	1030-1040	3- 3.9	>5,400	0.0041
3.2.2	Quasi-reflectionless	2	Dual-band	2	1 per R_i / 3 per R_C	1033-1040	5.45, 3.2	5,500-6,300	0.0068
[47]	Reflective	3	Dual-band	2	5	418 - 433.9	0.97-0.87	>10,000	0.0075
[12]	Reflective	2	Tripple-band	3	5	1000-1040	4.25-2.37	> 3,500	0.0324
[111]	Reflective	9	Dual-band	18	2 per filter	1284-1316	~2	N/A	N/A
[112]	Reflective	5	Dual-band	8	2 per filter	765-935	3.7-3.9	~427 (resonator)	0.00018

3.3 Summary

This chapter presented a unique class of AWLR-based multi-band BPFs that support both reflective and symmetric quasi-reflectionless responses in a compact form factor. The proposed filters enable multiple high-Q passbands, with Q_{eff} between 5400 and 6700, and enhanced FBW > (0.4- 0.8k_t^2). The FBW of each passband can be independently controlled by varying the number of resonators without modifying the inter-stage coupling. Notably, this architecture is the first to realize a multi-band response in AWR-based filters with symmetric quasi-reflectionless characteristics, contributing to RF front-ends with enhanced SNRs. The multi-band and quasi-reflectionless filtering capabilities demonstrated in this work further advance the development of highly integrated, multifunctional RF front-ends, reducing dependence on large numbers of fixed filter banks. As illustrated in Figure 1.1, although this study does not introduce dircetly frequency-agile filters, it presents multi-band filters capable of significantly decreasing the number of discrete filtering components while enabling multi-standard functionality. This advancement facilitates the design of compact RF front-end models with fewer interconnection/ impedance-matching networks required to integrate components into complete multi-standard modules. Moreover, the proposed filters readily support BW tuning through control of the TZs around the operating bands, enabling highly reconfigurable multi-band BPFs that can adapt their operating channel bandwidth in response to varying spectrum conditions and communication system requirements. The work introduced in this chapter has been published in [93], [94].

Chapter 4: Switchless Multi-Octave Tune-All BPF Manifold

This chapter reports on a novel RF-switchless BPF manifold architecture with multi-octave f_{cen} tuning. The proposed design employs a unique RF-switchless integration scheme based on two low-pass filter (LPF)/ high-pass filter (HPF) diplexer junctions, enabling a compact implementation using only passive components, and eliminating the need for DC biasing required in RF-switch-based manifolds. A unique optimization method for the performance of the varactors is introduced to reduce IL and improves the overall response of the passbands. The resulting manifold exhibits highly versatile TF characteristics and supports three distinct modes of operation, namely a: i) single-band BPF mode with tunable f_{cen} and BW, ii) a dual-band BPF mode with independently tunable passbands, and iii) a AS mode. Unlike conventional RF-switched manifolds that typically support only a single active passband, the proposed switchless architecture enables simultaneous dual-band operation. To the best of the authors' knowledge, it is the first RF-switchless manifold capable of tuning f_{cen} across the majority of the FR1 band—specifically covering 1.9 to 7.3 GHz—while also supporting continuous BW tuning at each operating f_{cen} with TR > 3:1.

4.1 Theoretical Foundations

4.1.1 Concept of the RF switchless manifold

Figure 4.1 depicts the block diagram and the conceptual power transmission response of the switchless tune-all BPF manifold. It consists of: i) two diplexer junctions comprising a LPF and a HPF, whose combined response is shown in Figure 4.2; and ii) two fully-reconfigurable, five-pole/two TZs BPFs ($BPF_{\#1}$ and $BPF_{\#2}$) with tune-all TF characteristics. The tuning capabilities of one of these BPFs is illustrated in Figure 4.3 for the example case of $BPF_{\#1}$. They include f_{cen} tuning, BW tuning and intrinsic switching OFF. In the manifold configuration in Figure 4.1, $BPF_{\#1}$ operates through the LPF channel with a continuously tunable TF between f_1 and f_2, while $BPF_{\#2}$ operates through the HPF channel with a continuously tunable TF between f_3 and f_4. By intrinsically switching ON/OFF the $BPF_{\#1}$ or the $BPF_{\#2}$, continuous f_{cen} and

BW tuning between f_1 and f_4 can be obtained. A crossover region is considered between the LPF and HPF channels to allow for continuous f_{cen} coverage. Furthermore, the manifold facilitates two additional modes of operation. Specifically, by intrinsically switching ON both of the BPFs a dual-band mode can be achieved. Conversely by intrinsically switching OFF both of the BPFs an AS mode is materialized.

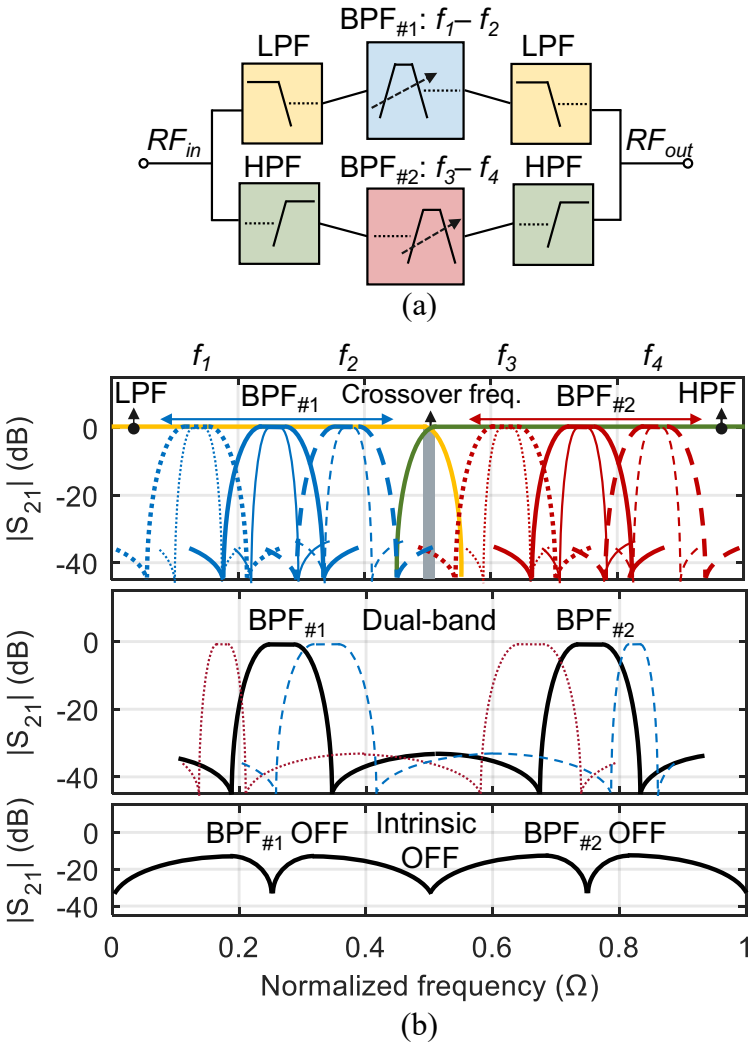


Figure 4.1. RF-switchless two-BPF manifold using a high-pass/low-pass diplexer junction: (a) Block diagram; (b) Conceptual power transmission response exhibiting a tune-all TF with: i) a single-band mode featuring ultra-wide and continuous f_{cen} and BW tuning (either $BPF_{\#1}$ and $BPF_{\#2}$ is ON); ii) a dual-band mode with independently-tuned bands in terms of f_{cen} and BW (both $BPF_{\#1}$ and $BPF_{\#2}$ are ON), and iii) an AS mode (both $BPF_{\#1}$ and $BPF_{\#2}$ are intrinsically-switched OFF) [96].

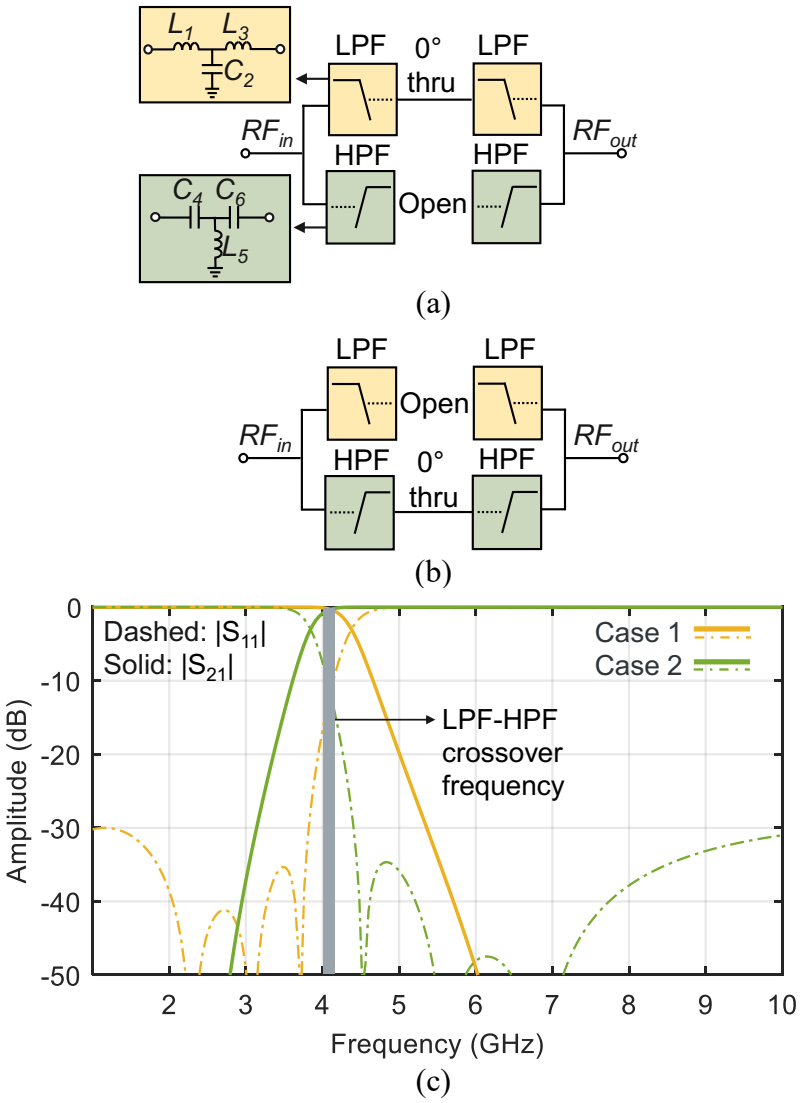


Figure 4.2. Low-pass/high-pass diplexer in back-to-back configuration: (a) Case 1: LPFs: directly connected (via short thru line), HPFs: open. (b) Case 2: HPFs: directly connected, LPFs: open; (c) Circuit simulations: LPF: L_1=3.04 nH, C_2=1.44 pF, L_3=1.79 nH, HPF: C_4=0.52 pF, L_5=1.1 nH, C_6=0.88 pF [96].

4.1.2 BPF manifold implementation

Using the aforementioned concept as a basis, the RF switchless tune-all BPF manifold is designed for f_{cen} tuning between 1.9 GHz and 7.3 GHz, BW tuning > 3:1, FBW > 6%, a dual-band and an AS mode of operation. To meet these design goals, $BPF_{\#1}$ is implemented for f_{cen} tuning between 1.9 and 3.9 GHz, whereas $BPF_{\#2}$ has f_{cen} tuning between 3.8– 7.3 GHz. Both BPFs are realized for a BW TR: 3:1 and wide FBWs > 6%. To accommodate the switchless integration, the LPF/HPF diplexer is designed in a back-to-back configuration using third-order LPF/HPF channels considering two design cases: i) Case 1: LPFs directly connected (via a zero-length thru line), HPFs open-ended, and ii) Case 2: HPFs directly connected and LPFs open-ended. In contrast to conventional RF diplexers designed for 50 Ω terminations [113], alternative zero-length thru and open-circuit interconnection terminations are considered when the diplexer junction is designed in a back-to-back configuration as shown in Figure 4.2(a), (b). In Figure 4.2(a), the two LPFs are cascaded via a zero-length thru line while the other two HPFs are open-circuited, and in Figure 4.2(b), the two HPFs are cascaded via a zero-length thru line while the other two LPFs are open-circuited. The values of the LE components for the diplexer are specified using optimized g-coefficients (g_1=1.527, g_2=1.813, g_3=0.9, g_0=g_4=1) at f_c=4 GHz ($\omega_c=2\pi \cdot f_c$) and the following formulas: $L_1=(Z_0 \cdot g_1)/\omega_c$, $C_2=g_2/(Z_0 \cdot \omega_c)$, $L_3=(Z_0 \cdot g_3)/\omega_c$, *and* $C_4=1/(Z_0 \cdot g_1 \cdot \omega_c)$, $L_5=(Z_0)/(g_2 \cdot \omega_c)$, $C_6=1/(Z_0 \cdot g_3 \cdot \omega_c)$ for a return loss (RL) > 30 dB, where f_c is the centre of the crossover region at which the power transmission is transferred from the LPF channel to the HPF channel when arranged in a back-to-back and terminated to Z_0=50 Ohm. The ideal circuit-simulated S-parameters for Case 1 and Case 2 are provided in Figure 4.2(c). As shown, the LPF channel spans between DC and 4.34 GHz and covers the desired specifications of $BPF_{\#1}$, while the HPF starts from 3.7 GHz and covers the desired specifications of $BPF_{\#2}$. An overlapping cross over frequency range between 3.7 GHz (3 dB cut-off of the HPF) and 4.34 GHz (3 dB cut-off of the LPF) is considered to allow for continuous f_{cen} tuning.

It should be noted that $BPF_{\#1}$ and $BPF_{\#2}$ of the manifold implement the same type of TF (Figure 4.3(a)); however, they are shifted in frequency. Their TF comprises five poles and two TZs as shown in Figure 4.3(c) alongside its CRD (Figure 4.3(b)). In practice each of the BPFs is realized with two varactor-loaded coupled resonators contributing to four poles and a multi-resonant cell contributing to one pole and two

TZs. The simulated S-parameters in Figure 4.3(c), and Figure 4.3(d) illustrate the tuning principles of the BPF TF. Specifically, i) f_{cen} shifts to lower frequencies by increasing all capacitances loading the resonators (C_{p1}, C_{p2}, C_{Z1}, *and* C_{Z2}), as illustrated in Figure 4.3(c) by the black and blue traces; ii) BW decreases by decreasing C_{Z1} and increasing C_{Z2} (tuning TZs to the center of the passband), as demonstrated in Figure 4.3(d), by the black and green trances; and iii) intrinsic-OFF is achieved by decreasing C_{Z1} and increasing C_{Z2} until both of the TZs are set at the center of the passband, and by offsetting the capacitances C_{p1} and C_{p2} in the varactor-loaded coupled line, as depicted in Figure 4.3(d), by the red trace. These principles are also outlined in [95]. However, two additional poles are introduced in this concept by altering the coupling between the varactor-loaded coupled resonators to widen the BPF's FBW, achieving up to 44%, as opposed to 7.3% in [95].

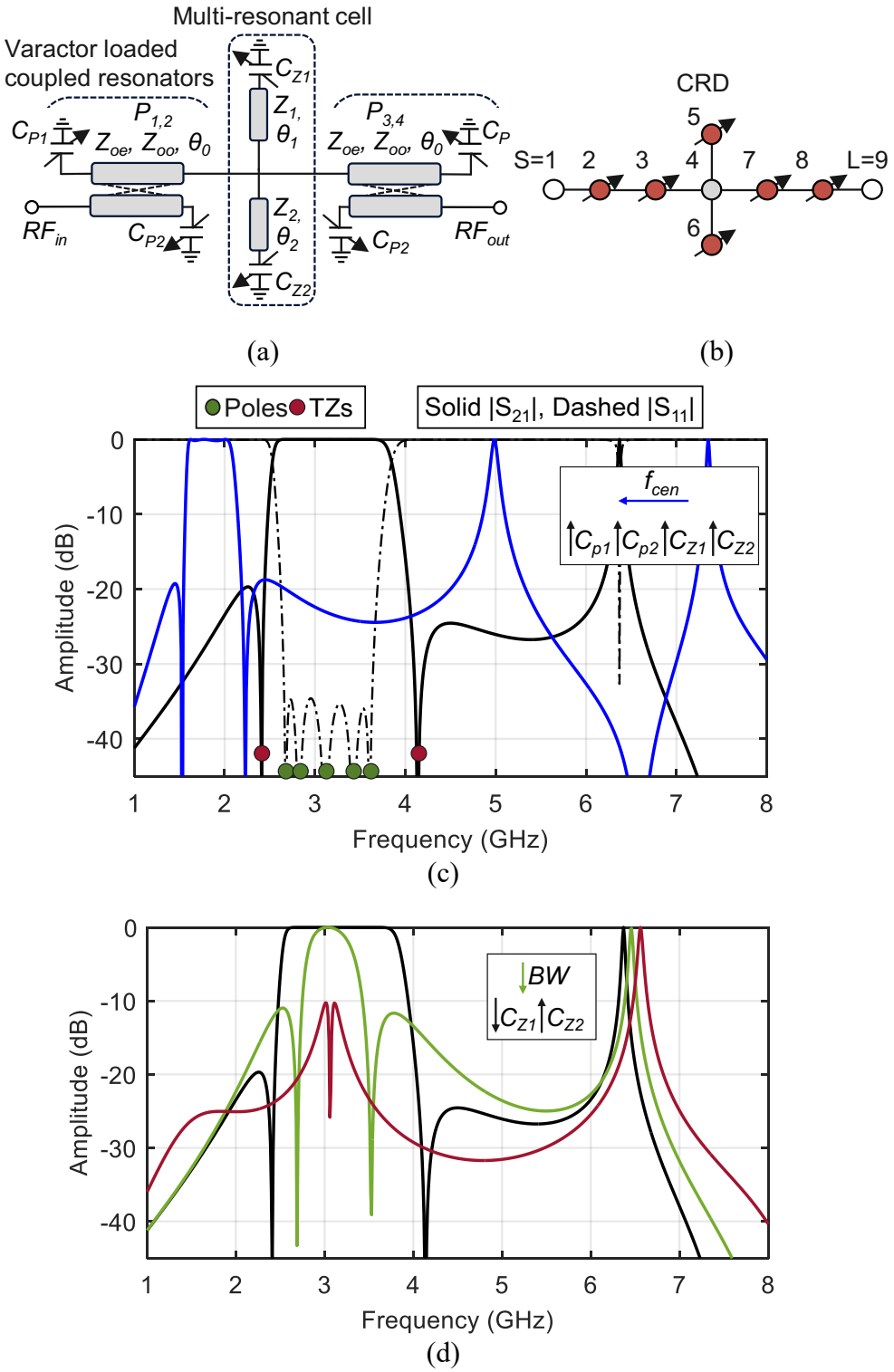


Figure 4.3. (a) Five-pole/two-TZ BPF comprising four varactor-loaded coupled resonators and one multi-resonant cell; (b) CRD; (c) f_{cen} tuning, circuit-simulated response in black with f_{cen}= 3 GHz, FBW= 44% obtained for Z_{oe}= 180 Ω, Z_{oo}= Z_{oe}/2 Ω, θ_0= 62°, Z_1= 117 Ω, θ_1= 87.8°, C_{z1}= 0.2 pF, Z_2= 123 Ω, θ_2= 41.6°, C_{P1}=C_{P2}=C_{Z1}=C_{Z2}= 0.2 pF; (d) BW tuning [96].

The performance of the BPFs is linked to the varactor's loss and TR. For high frequency implementations it is also influenced by the DC block capacitance (C_{block}) in its biasing network. Thus, a study of the C_{block} impact on the total unloaded quality factor (Q_{total}) and total capacitance tuning range (CTR) is illustrated in Figure 4.4. Specifically, Figure 4.4(a) demonstrates the effect of C_{block} while maintaining the varactor diode capacitance ($C_{varactor}$) and Q-factor ($Q_{varactor}$), and the DC block Q-factor (Q_{block}) constant. As observed, when C_{block} is comparable to $C_{varactor}$, Q_{total} rises and is comparable to Q_{block}, indicating that a low C_{block}, comparable to $C_{varactor}$, increases Q_{total}. Furthermore, Figure 4.4(b) demonstrates that lowering C_{block} limits the CTR of the resonator. Thus, the DC block selection is based on a trade-off between Q-factor and capacitance tuning.

To analyse the varactor performance before designing the BPFs, a varactor-loaded resonator was manufactured as shown in Figure 4.5(a) and tested between 2 and 5 GHz. MACOM MAVR-000120-14110G varactor diodes (with total capacitance C_t=0.128 to 1.1 pF and Murata DC block capacitors were used. The resonator's measured performance in terms of applied DC voltage and extracted unloaded Q-factor (Q_U) is shown in Figure 4.5(b); and Figure 4.5(c) illustrates its measured performance in terms of applied DC voltage and f_{cen} tuning. The results show that a lower capacitance DC block enhances the resonator's Q_U (Figure 4.5(b)) but limits the TR of the f_{cen} (Figure 4.5(c)). This agrees well with the theoretical study in Figure 4.4, successfully validating the proposed design method. Having specified the varactor and resonator performance trade-offs, the manifold can be designed as follows. First the BPFs and the diplexers are designed independently. Afterwards, the diplexers are optimized for realistic loads. i.e., the open circuit is replaced by the corresponding BPF in its intrinsically switched-OFF state and the thru load is replaced by a BPF in its ON state to accommodate for finite loading effects. Then the BPFs and diplexers are connected in a manifold configuration and their performance is co-optimized with full EM simulations in Keysight ADS and ANSYS HFSS.

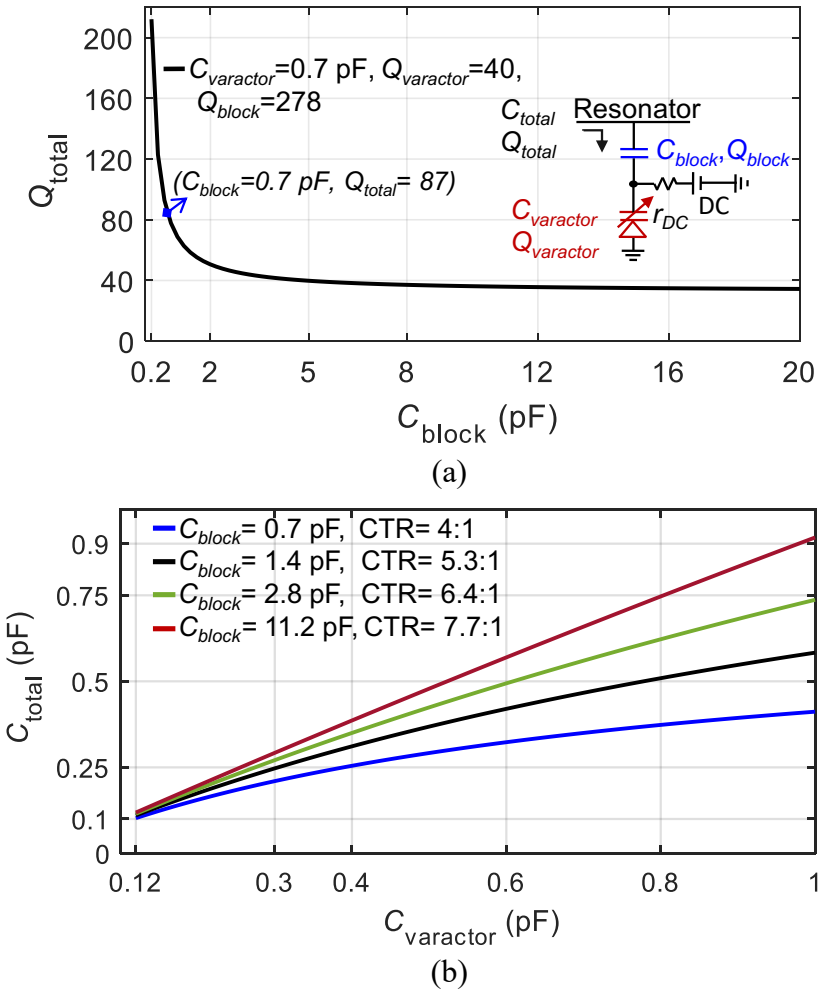
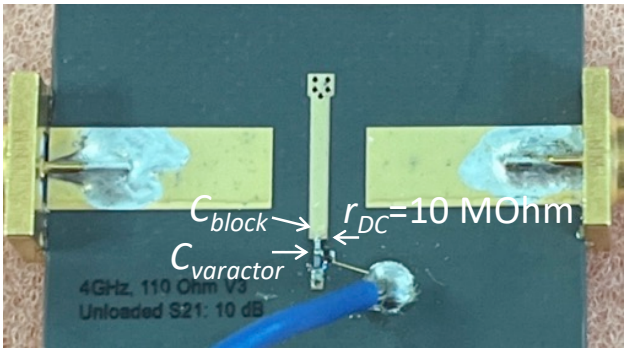
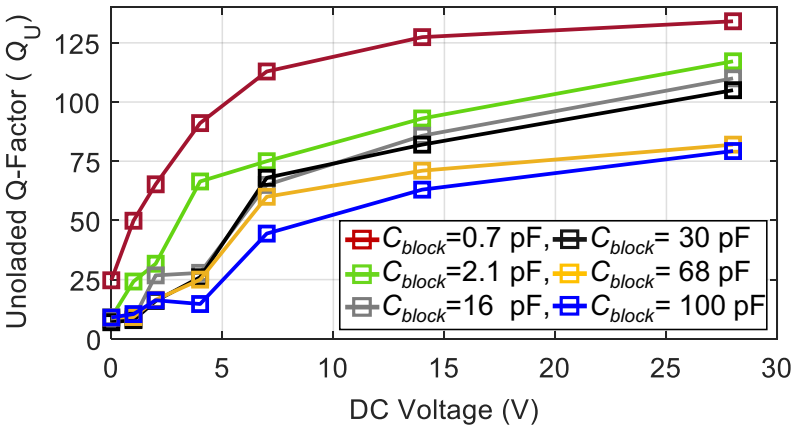


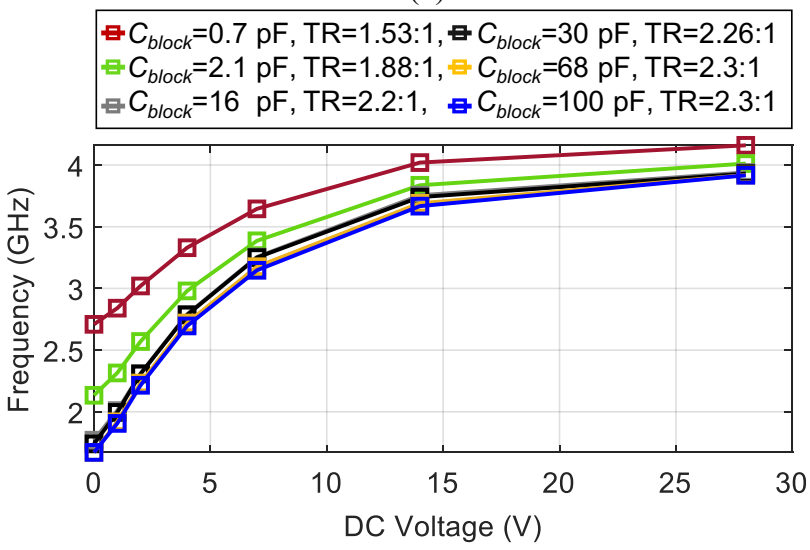
Figure 4.4. DC block effect on: (a) Q_{total}. (b) C_{varactor} and C_{total}.



(a)



(b)



(c)

Figure 4.5. Experimental evaluation of the effect of the DC block on the unloaded *Q*-factor (Q_U) and TR of the varactor-loaded resonator: (a) Photograph of the manufactured resonator. The utilized SMDs and resonator's characteristics are as follows: Varactor: MACOM MAVR-000120-14110G; DC blocks: GJM0335 and GRM0335 Murata series; Resonator characteristic: impedance Z=109 Ω, electrical length: 55°at 4 GHz, substrate: RO5880 with a height of 1.575 mm; (b) Relationship between applied DC voltage and extracted Q_U; (c) Relationship between applied DC voltage and f_{cen} TR [96].

4.2 Experimental Validation

To validate the switchless tune-all BPF manifold concept, a prototype was designed, manufactured and tested for a wide span of frequencies in the extended FR1 band starting from the edge of L-band and up until C-band. The prototypes were built on RT/duroid RO5880 substrate. Test structures of the diplexers for both Case 1 and Case 2 were also manufactured and measured and are shown in Figure 4.6 along with their corresponding co-simulated states. In Case 1, the IL was measured to be less than 0.8 dB for frequencies between 1 and 3.6 GHz, with the LPF channel cutoff at 3.97 GHz, while the out-of-band IS was measured as > 23 dB from 4.2 GHz to higher than 10 GHz. In Case 2, the IL was measured as < 2.4 dB for frequencies between 4.1– 10 GHz, with the HPF channel cutoff at 3.76 GHz, while the out-of-band IS was measured as > 31 dB from 3.14 GHz to frequencies below 1 GHz. As can be seen, the RF-measured states agree well with the EM-simulated ones. The observed small deviations are due to the lack of discrete commercially-available SMD components with the exact optimal inductance and capacitance values as specified in EM simulations. The LE components employed in the simulation are based on their measured responses.

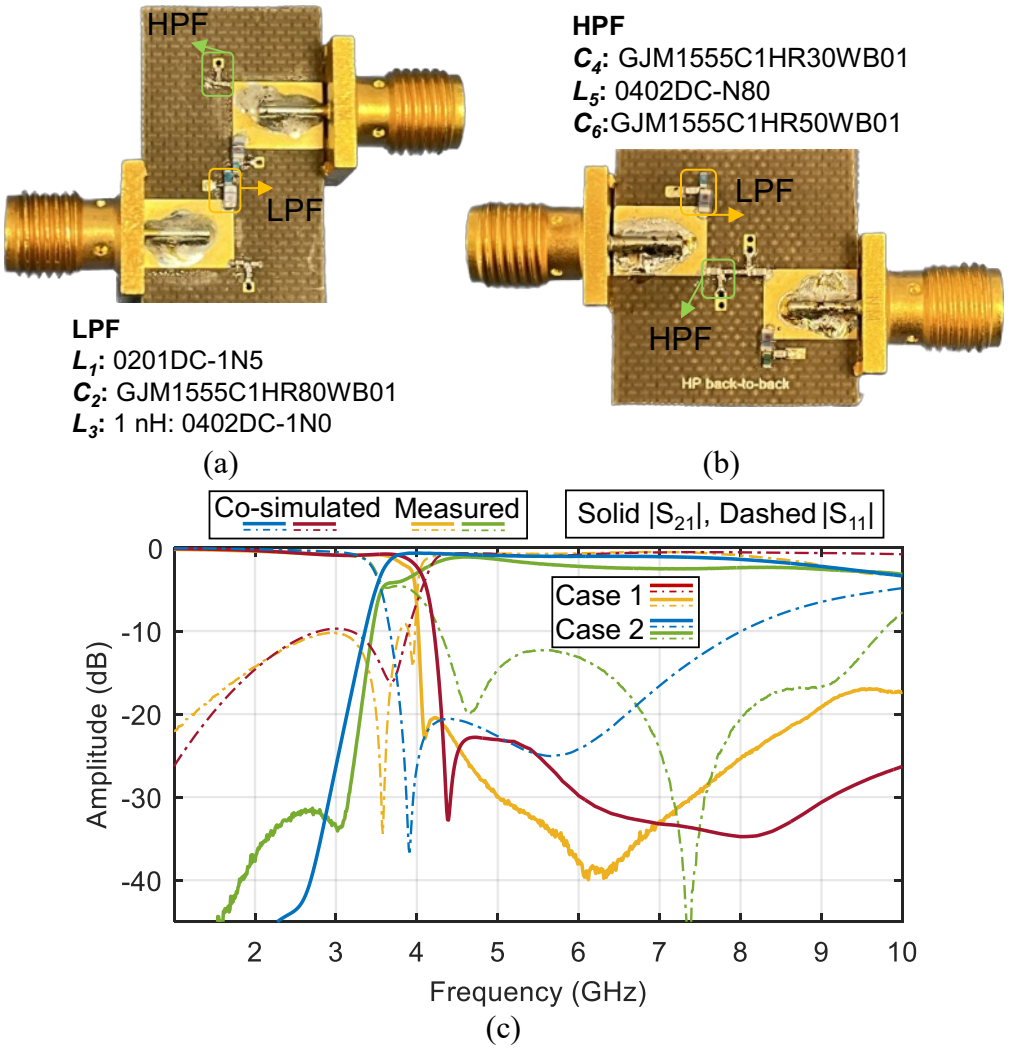
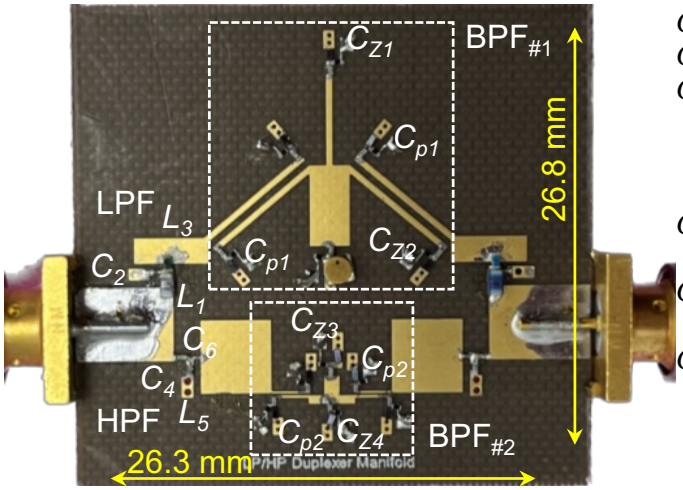


Figure 4.6. Measured and EM simulated back-to-back diplexers: (a) Case 1: LPFs: connected and HPFs: open; (b) Case 2: LPFs: open and HPFs: connected. (c) RF measured response for Case 1 and Case 2 [96].

The manufactured manifold is shown in Figure 4.7(a) alongside its SMD elements. Its RF measured performance in terms of f_{cen} tuning is summarized as follows: i) Figure 4.7(b): $BPF_{\#1}$ is ON and $BPF_{\#2}$ is switched OFF and its f_{cen} is continuously tuned from 1.89 to 3.43 GHz (i.e., TR: 1.81:1). The spurious signals in the upper stopband of $BPF_{\#1}$ are naturally suppressed by the network of the LPF channel, allowing for broadband spur-free out-of-band IS around 20 dB up to 13 GHz. ii) Figure 4.7(c): $BPF_{\#2}$ is ON and $BPF_{\#1}$ is switched OFF and $BPF_{\#2}$ continuously tunes its f_{cen} from 3.8 to 7.28 GHz (i.e., TR: 1.91:1). As such, the manifold demonstrates a combined ultra-wide f_{cen} tuning between 1.89 and 7.28 GHz (i.e., TR: 3.85:1). A detailed performance summary of the measured RF f_{cen} states in terms of

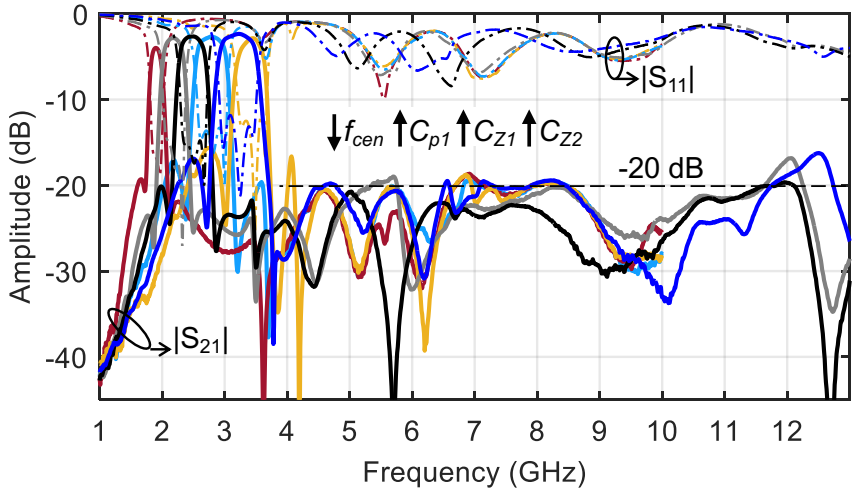
BW and minimum IL is provided in Figure 4.8. The BW tuning capabilities of the manifold alongside its dual-band and AS modes of operation are illustrated in **Error! Reference source not found.**. Namely **Error! Reference source not found.**(a) shows BW tuning of $BPF_{\#1}$ ($BPF_{\#2}$ is switched OFF) at: i) f_{cen}= 2.2 GHz, where its BW tunes between 0.135 and 0.59 GHz (i.e., a TR: 4.37:1) with a minimum IL of 2.44 to 4.6 dB; and at: ii) f_{cen}= 3 GHz, where its BW tunes between 0.24 and 0.725 GHz (i.e., a TR: 3:1) with a minimum IL between 2.3 and 3.6 dB.



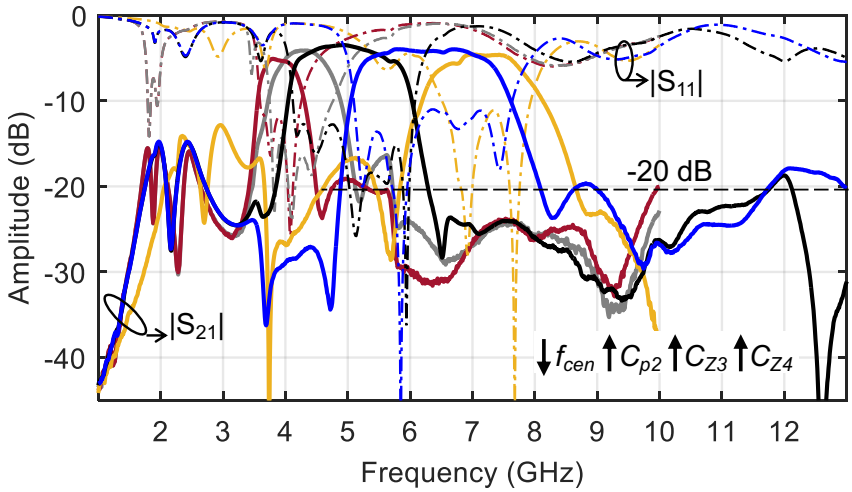
C_{P1}: MAVR-000120-14110G
C_{Z1}: MAVR-000120-14110G
C_{Z2}: MA46H071-1056
C_{block}: GRM0335C1H300JA01
r_{DC}: 10 MOhm

C_{P2}: MAVR-000120-14110G
C_{block}: GJM1555C1HR70WB01
C_{Z1}: MAVR-000120-14110G
C_{block}: GRM0335C1H300JA01
C_{Z2}: MAVR-000120-14110G
C_{block}: GRM0335C1H300JA01
r_{DC}: 10 MOhm

(a)



(b)



(c)

Figure 4.7. Manufactured prototype of the switchless two-BPF manifold and its RF-measured S-parameters: (a) Prototype; (b) BPF$_{\#1}$ ON exhibiting continuous f_{cen} tuning and BPF$_{\#2}$ intrinsically-switched OFF; (c) BPF$_{\#2}$ ON exhibiting continuous f_{cen} tuning with BPF$_{\#1}$ intrinsically-switched OFF [96].

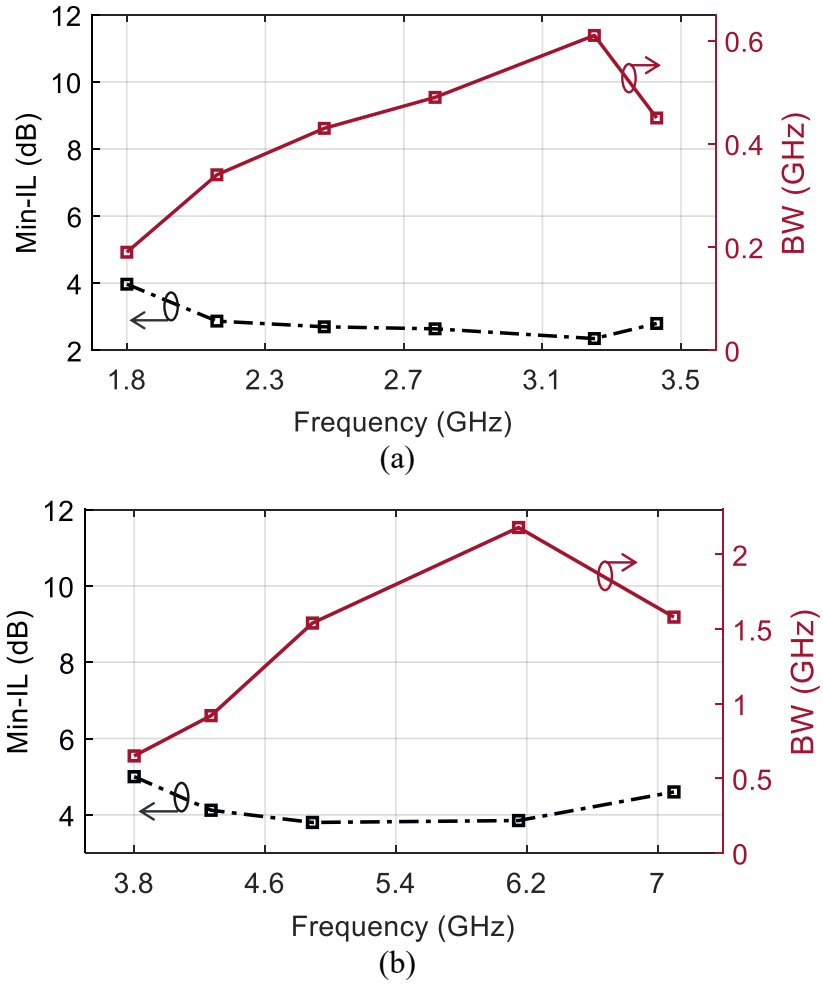


Figure 4.8. RF performance summary of the measured f_{cen} tuning states presented in Figure 4.7 in terms of BW and minimum IL (min-IL): (a) $BPF_{\#1}$ f_{cen} tuning performance when $BPF_{\#2}$ is switched OFF (Figure 4.7(a)); (b) $BPF_{\#2}$ f_{cen} tuning performance when $BPF_{\#1}$ is switched OFF (Figure 4.7(b)) [96].

Error! Reference source not found.(b) illustrates the BW tuning capabilities of $BPF_{\#2}$ (with $BPF_{\#1}$ switched OFF) at: i) f_{cen}= 4.9 GHz, where its BW tunes between 0.52 and1.88 GHz (i.e., a TR: 3.6:1) with a minimum IL of 3.6 to 5.7 dB; and ii) f_{cen}= 6.2 GHz, where its BW tunes between 0.695 and 2.625 GHz (i.e., a TR: 3.77:1) with a minimum IL between 3.6 and 5.1 dB. The RF summary of manifold BW tuning performance is listed in Table 4.1. Furthermore, Figure 4.10(a) demonstrates the manifold's dual-band capabilities when both $BPF_{\#1}$ and $BPF_{\#2}$ are switched ON, alongside independent f_{cen} and BW control for both of its bands. Lastly, Figure 4.10(b) illustrates the measured response of the AS mode of operation with an IS greater than 15 dB between DC and 18 GHz, achieved by intrinsically-switching OFF both $BPF_{\#1}$ and $BPF_{\#2}$.

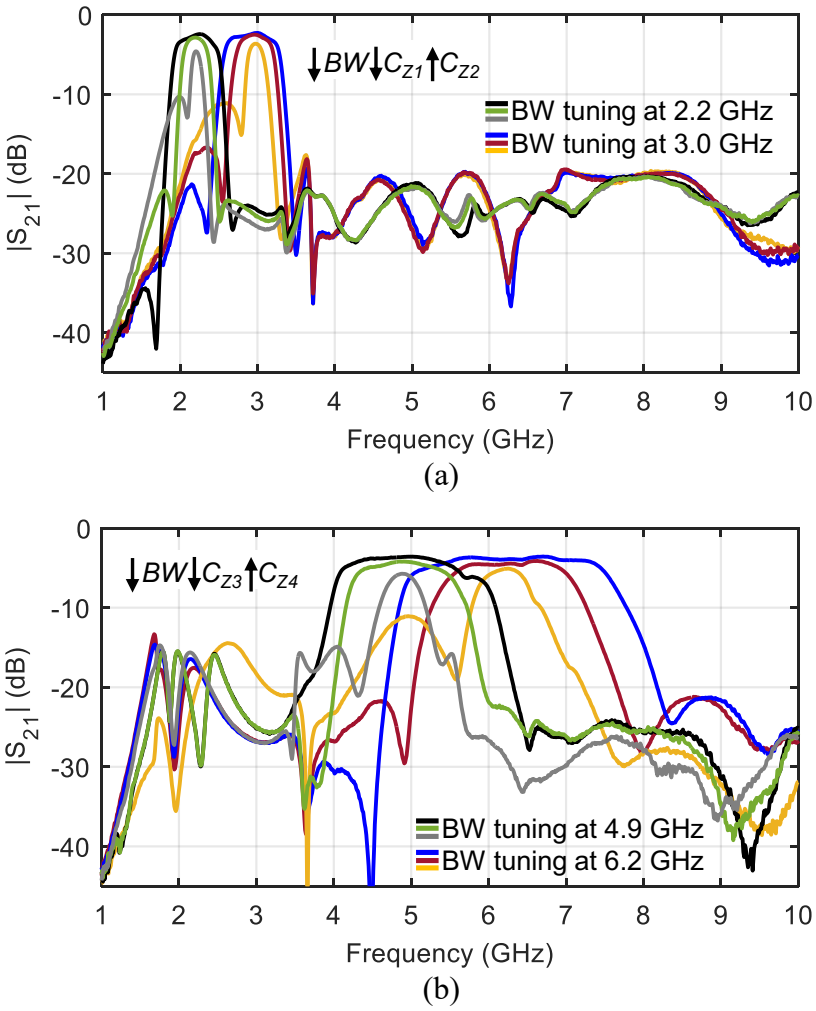


Figure 4.9. RF-measured S-parameters: (a) Continuous BW tuning of $BPF_{\#1}$ at f_{cen}= 2.2 and 3 GHz, when $BPF_{\#2}$ is OFF; (b) Continuous BW tuning of $BPF_{\#2}$ at f_{cen}= 4.9 and 6.2 GHz, when $BPF_{\#1}$ is OFF [96].

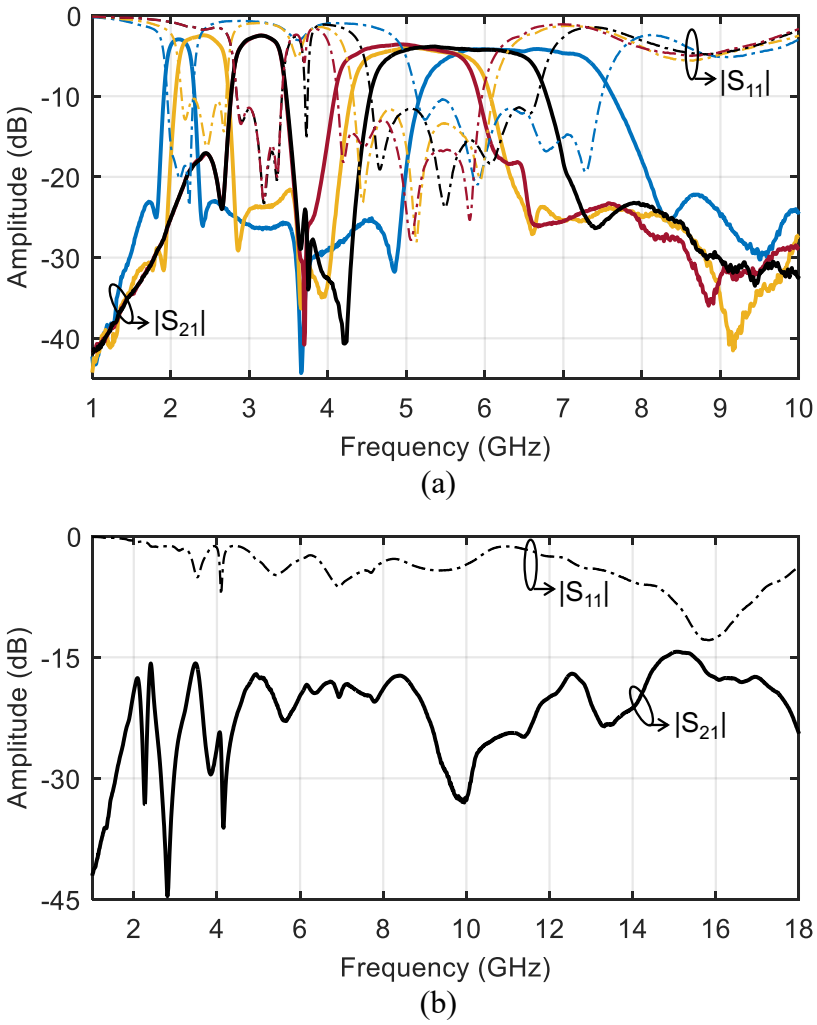


Figure 4.10. RF-measured S-parameters: (c) Dual-band responses when $BPF_{\#1}$ and $BPF_{\#2}$ are ON; (d) AS response: $BPF_{\#1}$ and $BPF_{\#2}$ are OFF [96].

Table 4.1. Performance summary for various tuning states when either $BPF_{\#1}$ or $BPF_{\#2}$ is ON, based on the measured data in Figure 4.7(a), (b).

	f_{cen} (GHz)	Min-BW (GHz)/ Min-IL (dB)	Max-BW (GHz) / Min-IL (dB)
$BPF_{\#1}$	2.2	0.135/ 4.6	0. 590/ 2.44
	3	0.240/ 3.6	0.725/ 2.3
$BPF_{\#2}$	4.9	0. 500/ 5.6	1.880/ 3.6
	6.2	0. 695/ 5.1	2.625/ 3.6

The measured third-order input intercept point (IIP3) performance of the manifold when either $BPF_{\#1}$ and $BPF_{\#2}$ are switched ON is illustrated in Figure 4.11. Specifically, when $BPF_{\#1}$ is ON, an IIP3 between 13.5 and 21.6 dBm is obtained when f_{cen} tunes between 2 and 3.4 GHz. Likewise, when $BPF_{\#2\ in}$ is ON the IIP3 values ranges between 19 and 26.5 dBm when f_{cen} tunes between 4.1 and 7.2 GHz. To illustrate the BPF manifold performance around the cross-over region of the diplexer, Figure 4.12 provides the RF-measured response of: i) the maximum f_{cen} state of $BPF_{\#1}$ when $BPF_{\#2}$ is switched OFF and ii) the minimum f_{cen} state of $BPF_{\#2}$ when $BPF_{\#1}$ is switched OFF. The upper 3-dB frequency of $BPF_{\#1}$ is 3.64 GHz (blue trace), while the lower 3-dB frequency of $BPF_{\#2}$ is 3.59 GHz (red trace). Therefore, the BPF manifold allows complete frequency coverage between 1.89 and 7.28 GHz.

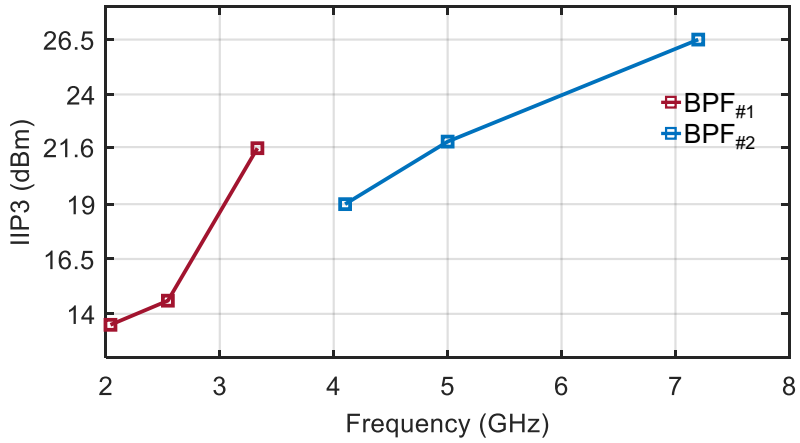


Figure 4.11. RF-measured IIP3 for various tuning states [96].

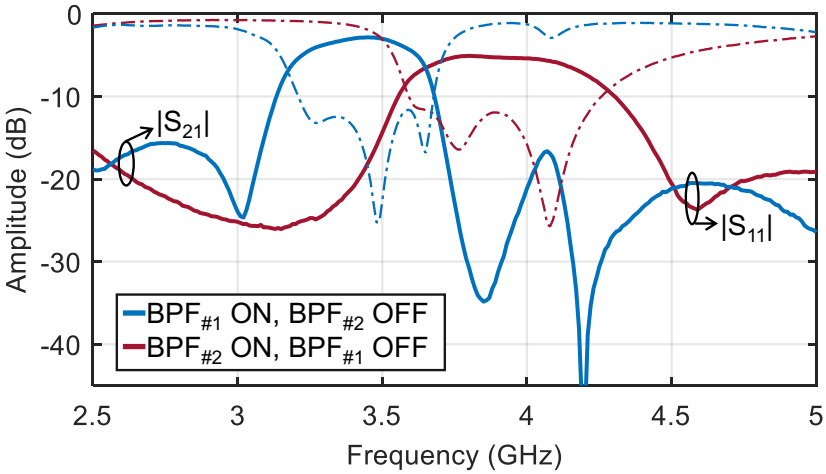


Figure 4.12. RF-measured S-parameters showing the: i) the maximum f_{cen} of $BPF_{\#1}$ when $BPF_{\#2}$ is OFF and ii) the minimum f_{cen} of $BPF_{\#2}$ when $BPF_{\#1}$ is OFF [96].

To demonstrate the potential of the proposed switchless BPF manifold for ultra-wide and tune-all RF tuning in FR1, a comparison with state-of-the-art tunable manifolds is presented in Table 4.2. As shown, the proposed configuration is the only RF-switchless manifold to date covering the highest operational frequency, while exhibiting ultra-wide f_{cen} tuning and BW tuning and supporting the largest number of modes of operation namely; single, dual-band, and AS modes of operation. Furthermore, it exhibits the lowest IL and the widest out-of-band suppression with better than 20 dB of IS up to 6xf_{cen}. The concepts in [85], [87] are only tunable in terms of f_{cen} and the manifold in [95], doesn't facilitate a dual-mode of operation, and has significantly higher IL up to 9 dB and can only operate up to 3.85 GHz.

Table 4.2. Comparison with state-of-the-art tunable manifolds.

Ref.	Integration	# filters	f_{cen} tuning (GHz), [TR]	FBW, TR	IL (dB)	Q_{eff}	#AE	Isolation	Operation modes
4.2	LPF/HPF diplexer	2	1.89-7.28, [3.85:1]	6,%42 - TR:3-4.7:1	2.3-5.7	12-34	12	20 dB up to 6xf_{cen}	Single/ Dual band/AS
[85]	PIN diodes	3	0.54-2.4, [4.44]	3.4-15%, No tuning	1.8-5.4	4.5-18.5	24	20 dB up to 5xf_{cen}	Single band
[87]	PIN diodes	2	1.1-2.1, [1.9:1]	1.9-3.6%, No tuning	4.4-6.1	35-60	9	20 dB up to 2.3xf_{cen}	Single band
[95]	RF switch	2	1.8-3.85, [2.14]	5- 36%, TR: 2.5-3:1	2-9	11-24	14	20 dB up to 2xf_{cen}	Single band/AS

(T.W: This work, #AE: total number of active elements)

4.3 Summary

This chapter introduced, for the first time, a novel switchless, ultra-wideband tune-all two-BPF manifold design with multi-octave f_{cen} and BW tuning capabilities. The switchless integration scheme is based on two LPF/HPF diplexer junctions. The resulting manifold exhibits ultra-wide and highly versatile TF characteristics, supporting three distinct modes of operation: i) a single-band BPF with up to 3.85:1 f_{cen} tuning and 4.4:1 BW tuning, ii) a dual-band BPF with two independently tunable passbands, and iii) an AS mode with greater than15 dB IS from DC to 18 GHz. Unlike conventional RF-switched manifolds that support only a single passband, the proposed switchless design enables simultaneous dual-passband operation. Moreover, it is the first RF-switchless manifold reported to date that achieves f_{cen} tuning across most of the FR1 band (covering from 1.9 to 7.3 GHz), with continuously tunable BW at each f_{cen} and TRs greater than 3:1. Additionally, it supports the highest number of operating modes—single-band, dual-band, and AS modes—compared to state-of-the-art designs. A method for optimizing varactor performance is also introduced, focusing on the use of high-Q static DC block capacitors to minimize IL.

The switchless, ultra-wideband filter manifold developed in this chapter serves as a key enabling element for the compact and reconfigurable RF architectures shown in Figure 1.1(b), providing wide spectral coverage without reliance on RF-switched filter banks. The proposed manifold supports operation over an ultra-wide frequency range with wide channel bandwidth tuning, advancing the future RF front-end vision outlined in Figure 1.1. In addition, it enables simultaneous dual-channel operation, allowing a single filter volume to replace conventional static filter banks and support multiple communication standards across different spectrum bands concurrently. The contributions of this chapter have been published in [95] and [96].

Chapter 5: Conclusion and Future Work

5.1 Conclusion

This thesis has laid the foundations for novel design techniques and architectures for highly-reconfigurable and continuously-tunable RF filters using acoustic-wave and planar-microwave resonators. Its key contributions can be summarized as follows:

Chapter 2 reported on new types of highly versatile quasi-elliptic AWLR-based filters capable of multiple levels of TF reconfigurability and continuously tunable characteristics. Specifically, it introduced: i) a novel class of highly selective quasi-elliptic BPFs with enhanced FBW greater than $0.4k_t^2$–$0.8k_t^2$, supporting continuous FBW tuning by an electronic tuning method based on varactor diodes; ii) a unique class of AWLR-based BPFs with f_{cen} tuning and multi-configurable TF that includes continuous f_{cen} tuning—demonstrated for the first time in this thesis—along with continuous BW tuning and the ability to reconfigure the TF to AP and AS states; iii) an advanced class of AWLR-based BP-to-BS filters, offering multi-configurable and continuously tunable TF characteristics. This includes continuous f_{cen} and BW tuning in both BP and BS operation modes, with f_{cen} tuning in BS mode being uniquely introduced in this thesis for the first time. The filter can reconfigure the TF response to AP and AS states. The proposed architecture achieves all these functionalities within a single RF filtering component. The contributions outlined in this chapter have been published in [89], [90], [91] and [92].

Chapter 3 introduced a novel architecture for quasi-elliptic AWLR-based multi-band BPFs with reflective and symmetric quasi-reflectionless characteristics. This multi-band functionality is essential for supporting multi-standard operations across various frequency bands. The proposed filter design enables the realization of highly selective, high-Q passbands with enhanced FBWs exceeding $0.4k_t^2$–$0.8k_t^2$. Each passband is formed using multi-resonant AWLR stages composed of in-parallel cascaded SAW resonators and a single lumped inductor, effectively reducing circuit complexity while maintaining compactness. Additionally, the design allows for independent FBW control per band by varying the number of SAW resonators corresponding to each band. For the first time, a symmetric quasi-reflectionless multi-band response in AWR-based filters is demonstrated by integrating resistively

terminated bandstop-type AWLR stages at the input and output ports. The innovations presented in this chapter have been published in [93], and [94].

Chapter 4 presented a novel RF-switchless BPF manifold architecture with multi-octave f_{cen} tuning. For the first time, a switchless integration scheme for RF BPF manifolds is demonstrated using an LPF/HPF diplexer junction, eliminating the need for the DC biasing typically required in RF-switch-based designs. A unique optimization method for varactor performance is introduced to improve the performance at the tunable BPFs by reducing IL of operating passbands. Unlike conventional RF-switched manifolds that are generally limited to a single active passband, the proposed manifold supports three distinct modes of operation: i) a single-band BPF mode with tunable f_{cen} and BW; ii) a dual-band BPF mode with two independently tunable passbands, and iii) an AS mode. To the best of the authors' knowledge, this is the first RF-switchless manifold capable of tuning f_{cen} across the majority of the FR1 band, covering frequencies between 1.9 and 7.3 GHz, while supporting continuous BW tuning at each f_{cen} with TR exceeding 3:1. The contributions of this work have been published in [95] and [96].

Overall, the thesis presents a framework for acoustic-wave and planar-microwave filtering technologies that enables the transformation of rigid, conventional RF receiver architectures—typically relying on multiple RF-switched filter banks (Figure 1.1(a))—into compact, reconfigurable, and multifunctional front ends (Figure 1.1(b)). The proposed approach provides continuous frequency and bandwidth agility, multi-band consolidation, and quasi-reflectionless operation. Together, these innovations help reduce hardware complexity and footprint while enabling future wireless systems to dynamically adapt to increasingly crowded and evolving spectrum environments.

5.2 List of Publications

5.2.1 Publications emanated from this thesis

1) M. R. A. Nasser and D. Psychogiou, "Quasi-elliptic SAW Filters Using Multi-Resonant Acoustic-Wave Lumped-Element Resonator Stages," *2022 52nd European Microwave Conference (EuMC)*, Milan, Italy, 2022, pp. 420-423, doi: 10.23919/EuMC54642.2022.9924400.
2) M. R. A. Nasser and D. Psychogiou, "Acoustic Wave Resonator-Based Bandpass Filters with Continuously Tunable Fractional Bandwidth," in *IEEE Transactions on Circuits and Systems II: Express Briefs*, vol. 70, no. 4, pp. 1390-1394, April 2023, doi: 10.1109/TCSII.2022.3225735.
3) M. R. A. Nasser and D. Psychogiou, "Acoustic-Wave-Resonator-Based Bandpass Filters with Multiconfigurable and Continuously Tunable Transfer Function Capabilities," in *IEEE Transactions on Microwave Theory and Techniques*, 2024, doi: 10.1109/TMTT.2024.3408335.
4) M. R. A. Nasser, K. G. McCarthy and D. Psychogiou, "Multiconfigurable Acoustic-Wave-Lumped-Resonator (AWLR)-Based Bandpass-to-Bandstop Filters With Continuously Tunable Characteristics," in *IEEE Transactions on Microwave Theory and Techniques*, 2025, doi:10.1109/TMTT.2025.3564552.
5) M. R. A. Nasser and D. Psychogiou, "Quasi-Elliptic Multi-band BPFs using Multi-Resonant Acoustic-Wave Lumped-Element Resonators," *2023 53rd European Microwave Conference (EuMC)*, Berlin, Germany, 2023, pp. 170-173, doi: 10.23919/EuMC58039.2023.10290545.
6) M. R. A. Nasser and D. Psychogiou, "Reflective and Quasi-reflectionless Multiband Bandpass Filters using Multi-Resonant Acoustic-Wave Lumped-Element Resonators," in *International Journal of Microwave and Wireless Technologies*, 2024, doi:10.1017/S1759078724001211.
7) M. R. A. Nasser and D. Psychogiou, "Switchless Multi-Octave Tune-All BPF Manifold Using Low-Pass/High-Pass Diplexer Junctions," in *IEEE Journal of Microwaves*, 2024, doi: 10.1109/JMW.2024.3421535.

5.2.2 Other publications

1) M. R. A. Nasser, R. K. Jaiswal and D. Psychogiou, "A Compact Bandpass Filter Manifold with Ultrawide Frequency and Bandwidth Tuning," in *IEEE Access*, vol. 11, pp. 41054-41060, 2023, doi:10.1109/ACCESS.2023.3269884. (Mohammed R. A. Nasser and Rahul K. Jaiswal contributed equally to this work.)
2) V. S. Nagaraja, S. Khan, M. R. Nasser, B. McCarthy, M. -H. Li and D. Psychogiou, "AlScN-Based SAW Resonator with Improved RF Performance Using High-Resistivity Silicon Substrate," *2023 Joint Conference of the European Frequency and Time Forum and IEEE International Frequency Control Symposium (EFTF/IFCS)*, Toyama, Japan, 2023, pp. 1-4, doi: 10.1109/EFTF/IFCS57587.2023.10272056.

5.3 Future Work

The findings presented in this thesis highlight significant advancements in reconfigurable filtering technology. However, several limitations and challenges associated with reconfigurable AWLR-based and planar resonator-based RF filtering components remain to be addressed. Future research directions to address these challenges are summarized as follows:

- Although this research introduced advanced reconfigurable AWLR-based filter architectures, the experimental validation was conducted using commercially available off-the-shelf SAW resonators operating at around 1 GHz with a FBW of less than 0.3%. To achieve filtering responses at higher operating frequencies and wider FBWs, the proposed architectures can be realized using customized acoustic wave resonators—such as SAW, BAW, or FBAR devices [28], [114], [115], [116], [117], and [118]—which support broader bandwidths and higher frequencies. Additionally, this enables the realization of specification-driven AWLR-based filter designs that meet standard defined specifications.
- The advanced multi-reconfigurable AWLR-based filter proposed in this research was validated using PCB and LE technologies, achieving optimal size within the limitations of these platforms. However, there exists a class of acoustic filters that can be implemented as compact integrated circuits occupying less than 1 mm² [21]. Therefore, a potential direction for future research could involve the use of hybrid integration techniques—such as flip-chip or wafer bonding—to combine MEMS acoustic resonators (e.g., SAW or BAW) with integrated passive devices (IPDs) [119]. These IPDs can be implemented on substrates such as glass, SOI, or gallium arsenide (GaAs), enabling further miniaturization of the filter topologies developed in this work. These approaches leverage the high-Q performance of acoustic resonators and the compactness of integrated passive components. Conceptual EM simulation-based approaches, such as the one reported in [120] and illustrated in Figure 5.1, have reduced filter sizes to just a few mm². This type of integration is particularly advantageous for implementing chip-

scale, advanced AWLR-based filters in applications that require both miniaturization and high performance, such as 5G+/ 6G communication systems.

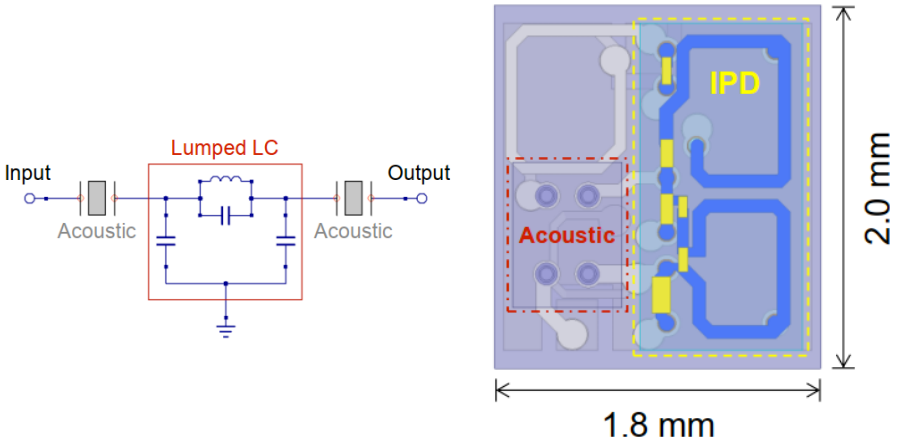


Figure 5.1. Schematic and layout of the hybrid BPF design integrating IPD, acoustic, and substrate technologies [120].

- The switchless multi-octave tune-all BPF manifold demonstrated ultra-wideband f_{cen} tuning from 1.9 to 7.3 GHz, representing the widest frequency coverage achieved by any manifold reported to date in the open literature. However, emerging communication technologies such as 5G+ and 6G are expected to operate across both FR 1: 0.41–7.125 GHz and Frequency Range 2 (FR2: 24.25–52.6 GHz). To address the requirements of higher frequency operation, GaAs-based monolithic microwave integrated circuit (MMIC) technologies offer a promising solution for implementing reconfigurable filters. GaAs processes support high-performance operation across a wide frequency range, typically from 1 GHz to well beyond 100 GHz. Furthermore, in GaAs-based reconfigurable filter designs, varactor diodes can be monolithically integrated within the reconfigurable BPF structure, facilitating a compact and more reliable design and fabrication process.
- A further direction for future work involves advancing the integration of the proposed reconfigurable AWLR- and planar-based filtering concepts into compact, multifunctional RF front-end architectures, aligned with the long-term vision illustrated in Figure 1.1(b). While this thesis has

demonstrated continuous f_{cen} and BW agility, multi-band, and quasi-reflectionless operation at the component level, additional research is required to co-design these filters with low-noise amplifiers, adaptive matching networks, and control circuitry to enable a unified reconfigurable receive chain. Such consolidation would support real-time spectral adaptation while reducing the hardware footprint, thereby moving closer to practical, highly-miniaturized front ends capable of replacing conventional RF-switched filter banks.

Bibliography

[1] W. J. Chappell, E. J. Naglich, C. Maxey, and A. C. Guyette, "Putting the Radio in 'Software-Defined Radio': Hardware Developments for Adaptable RF Systems," *Proc. IEEE*, vol. 102, no. 3, pp. 307–320, 2014, doi: 10.1109/JPROC.2014.2298491.

[2] Resonant Inc., "RF Innovation and the Transition to 5GWirelessTechnology," White Paper, 2016. [Online]. Available: https://content.equisolve.net/_f541645e7e983dea4a40a043703ba8a6/resonant/db/128/585/pdf/5G_Vision_wp_final_hires.pdf [Accessed: May 21, 2025].

[3] D. Kim and D. Im, "A Reconfigurable Balun-LNA and Tunable Filter With Frequency-Optimized Harmonic Rejection for Sub-GHz and 2.4 GHz IoT Receivers," *IEEE Trans. Circuits Syst. I Regul. Pap.*, vol. 69, no. 8, pp. 3164–3176, 2022, doi: 10.1109/TCSI.2022.3169364.

[4] R. Ferrus, O. Sallent, G. Baldini, and L. Goratti, "Public Safety Communications: Enhancement Through Cognitive Radio and Spectrum Sharing Principles," *IEEE Veh. Technol. Mag.*, vol. 7, no. 2, pp. 54–61, 2012, doi: 10.1109/MVT.2012.2190180.

[5] A. Kumbhar, F. Koohifar, İ. Güvenç, and B. Mueller, "A Survey on Legacy and Emerging Technologies for Public Safety Communications," *IEEE Commun. Surv. Tutorials*, vol. 19, no. 1, pp. 97–124, 2017, doi: 10.1109/COMST.2016.2612223.

[6] P. Liu, J. Mendoza, H. Hu, P. G. Burkett, J. V. Urbina, S. Anandakrishnan, and S. G. Bilén, "Software-Defined Radar Systems for Polar Ice-Sheet Research," *IEEE J. Sel. Top. Appl. Earth Obs. Remote Sens.*, vol. 12, no. 3, pp. 803–820, 2019, doi: 10.1109/JSTARS.2019.2895616.

[7] W. Feng, J.-M. Friedt, and P. Wan, "SDR-Implemented Ground-Based Interferometric Radar for Displacement Measurement," *IEEE Trans. Instrum. Meas.*, vol. 70, pp. 1–18, 2021, doi: 10.1109/TIM.2021.3069805.

[8] R. Gómez-García, J. P. Magalhães, J.-M. Muñoz-Ferreras, J. M. N. Vieira, N. B. Carvalho, and J. Pawlan, "Filling the Spectral Holes: Novel Future Wireless Communications and Radar Receiver Architectures," *IEEE Microw. Mag.*, vol. 15, no. 2, pp. 45–56, 2014, doi: 10.1109/MMM.2013.2296214.

[9] M. Rais-Zadeh, J. T. Fox, D. D. Wentzloff, and Y. B. Gianchandani, "Reconfigurable Radios: A Possible Solution to Reduce Entry Costs in Wireless Phones," *Proc. IEEE*, vol. 103, no. 3, pp. 438–451, 2015, doi: 10.1109/JPROC.2015.2396903.

[10] S. A. Hameed, "Controlling computers and electronics waste: Toward solving environmental problems," in *2012 International Conference on Computer and Communication Engineering (ICCCE)*, 2012, pp. 972–977. doi: 10.1109/ICCCE.2012.6271361.

[11] D. Psychogiou and D. J. Simpson, "Multi-Band Acoustic-Wave-Lumped-Element Resonator-Based Bandstop Filters with Continuously Tunable Stopband Bandwidths," in *2018 IEEE/MTT-S International Microwave*

Symposium - IMS, 2018, pp. 860–863. doi: 10.1109/MWSYM.2018.8439844.

[12] K. Zhao and D. Psychogiou, "Single-to-Multi-Band Reconfigurable Acoustic-Wave-Lumped-Resonator Bandpass Filters," *IEEE Trans. Circuits Syst. II Express Briefs*, vol. 69, no. 4, pp. 2066–2070, 2022, doi: 10.1109/TCSII.2021.3139008.

[13] P. Bahramzy, P. Olesen, P. Madsen, J. Bojer, S. Caporal Del Barrio, A. Tatomirescu, P. Bundgaard, A. S. Morris III, and G. F. Pedersen, "A Tunable RF Front-End With Narrowband Antennas for Mobile Devices," *IEEE Trans. Microw. Theory Tech.*, vol. 63, no. 10, pp. 3300–3310, 2015, doi: 10.1109/TMTT.2015.2470237.

[14] Emergen Research, "Surface Acoustic Wave Filters Market Size, Share, Industry Forecast by 2032," 2024. [Online]. Available: https://www.emergenresearch.com/industry-report/surface-acoustic-wave-filters-market [Accessed: May 21, 2025].

[15] C. C. W. Ruppel, "Acoustic Wave Filter Technology–A Review," *IEEE Trans. Ultrason. Ferroelectr. Freq. Control*, vol. 64, no. 9, pp. 1390–1400, 2017, doi: 10.1109/TUFFC.2017.2690905.

[16] A. Hagelauer, G. Fattinger, C. C. W. Ruppel, M. Ueda, K. Hashimoto, and A. Tag, "Microwave Acoustic Wave Devices: Recent Advances on Architectures, Modeling, Materials, and Packaging," *IEEE Trans. Microw. Theory Tech.*, vol. 66, no. 10, pp. 4548–4562, 2018, doi: 10.1109/TMTT.2018.2854160.

[17] A. R. Brown and G. M. Rebeiz, "A varactor-tuned RF filter," *IEEE Trans. Microw. Theory Tech.*, vol. 48, no. 7, pp. 1157–1160, 2000, doi: 10.1109/22.848501.

[18] S.-U. Choi, M.-S. Chung, and S.-W. Yun, "Hairpin Tunable Bandpass Filter with Improved Selectivity and Tunability," in *2007 Asia-Pacific Microwave Conference*, 2007, pp. 1–4. doi: 10.1109/APMC.2007.4555061.

[19] M. A. El-Tanani and G. M. Rebeiz, "Corrugated Microstrip Coupled Lines for Constant Absolute Bandwidth Tunable Filters," *IEEE Trans. Microw. Theory Tech.*, vol. 58, no. 4, pp. 956–963, 2010, doi: 10.1109/TMTT.2010.2042517.

[20] Y.-C. Chiou and G. M. Rebeiz, "A Tunable Three-Pole 1.5–2.2-GHz Bandpass Filter With Bandwidth and Transmission Zero Control," *IEEE Trans. Microw. Theory Tech.*, vol. 59, no. 11, pp. 2872–2878, 2011, doi: 10.1109/TMTT.2011.2164619.

[21] K. Yang, C. He, J. Fang, X. Cui, H. Sun, Y. Yang, and C. Zuo, "Advanced RF filters for wireless communications," *Chip*, vol. 2, no. 4, p. 100058, 2023, doi: 10.1016/j.chip.2023.100058.

[22] F. Z. Bi and B. P. Barber, "Bulk acoustic wave RF technology," *IEEE Microw. Mag.*, vol. 9, no. 5, pp. 65–80, 2008, doi: 10.1109/MMM.2008.927633.

[23] S. Gong and G. Piazza, "Design and Analysis of Lithium–Niobate-Based High Electromechanical Coupling RF-MEMS Resonators for Wideband Filtering," *IEEE Trans. Microw. Theory Tech.*, vol. 61, no. 1, pp. 403–414, 2013, doi: 10.1109/TMTT.2012.2228671.

[24] Y. Xu, Y. Fu, Y. Zhang, and C. Liu, "Large-range spurious mode elimination

for wideband SAW filters on $LiNbO_3/SiO_2/Si$ platform by $LiNbO_3$ cut angle modulation," *IEEE Trans. Ultrason. Ferroelectr. Freq. Control, and Frequency Control*, vol. 69, no. 11, pp. 3117–3125, Nov. 2022, doi: 10.1109/TUFFC.2022.3152010.

[25] H. Wu, Y. Wu, Z. Lai, W. Wang, and Q. Yang, "A Hybrid Film-Bulk-Acoustic-Resonator/Coupled-Line/Transmission-Line High Selectivity Wideband Bandpass FBAR Filter," *IEEE Trans. Microw. Theory Tech.*, vol. 68, no. 8, pp. 3389–3396, 2020, doi: 10.1109/TMTT.2020.2989264.

[26] S. Gong and G. Piazza, "Multi-frequency wideband RF filters using high electromechanical coupling laterally vibrating lithium niobate MEMS resonators," in *2013 IEEE 26th International Conference on Micro Electro Mechanical Systems (MEMS)*, 2013, pp. 785–788. doi: 10.1109/MEMSYS.2013.6474360.

[27] R. Su *et al.*, "Wideband and Low-Loss Surface Acoustic Wave Filter Based on 15° YX-$LiNbO_3/SiO_2$/Si Structure," *IEEE Electron Device Lett.*, vol. 42, no. 3, pp. 438–441, 2021, doi: 10.1109/LED.2021.3051298.

[28] R. Su *et al.*, "Wideband Surface Acoustic Wave Filter at 3.7 GHz With Spurious Mode Mitigation," *IEEE Trans. Microw. Theory Tech.*, vol. 71, no. 2, pp. 480–487, 2023, doi: 10.1109/TMTT.2022.3208213.

[29] Z. Hao *et al.*, "Single Crystalline ScAlN Surface Acoustic Wave Resonators with Large Figure of Merit ($Q \times k_t^2$)," in *2019 IEEE MTT-S International Microwave Symposium (IMS)*, 2019, pp. 786–789. doi: 10.1109/MWSYM.2019.8700824.

[30] Y. Zou *et al.*, "Design, Fabrication, and Characterization of Aluminum Scandium Nitride-Based Thin Film Bulk Acoustic Wave Filter," *J. Microelectromechanical Syst.*, vol. 32, no. 3, pp. 263–270, 2023, doi: 10.1109/JMEMS.2023.3263187.

[31] R. Beaucejour, V. Roebisch, A. Kochhar, C. G. Moe, M. D. Hodge, and R. H. Olsson, "Controlling Residual Stress and Suppression of Anomalous Grains in Aluminum Scandium Nitride Films Grown Directly on Silicon," *J. Microelectromechanical Syst.*, vol. 31, no. 4, pp. 604–611, 2022, doi: 10.1109/JMEMS.2022.3167430.

[32] H. Wu, Y. Wu, Z. Lai, W. Wang, and Q. Yang, "A Hybrid Filter With Extremely Wide Bandwidth and High Selectivity Using FBAR Network," *IEEE Trans. Circuits Syst. II Express Briefs*, vol. 69, no. 7, pp. 3164–3168, 2022, doi: 10.1109/TCSII.2022.3156725.

[33] G. Ariturk, N. R. Almuqati, Y. Yu, E. T.-T. Yen, A. Fruehling, and H. H. Sigmarsson, "Exact Synthesis of Hybrid Acoustic–Electromagnetic Filters With Wideband Chebyshev Responses," *IEEE Trans. Microw. Theory Tech.*, vol. 72, no. 5, pp. 3185–3199, 2024, doi: 10.1109/TMTT.2023.3319987.

[34] M. Z. Koohi, S. Nam, and A. Mortazawi, "Intrinsically Switchable and Bandwidth Reconfigurable Ferroelectric Bulk Acoustic Wave Filters," *IEEE Trans. Ultrason. Ferroelectr. Freq. Control*, vol. 67, no. 5, pp. 1025–1032, 2020, doi: 10.1109/TUFFC.2019.2958675.

[35] X. Lu, K. Mouthaan, and Y. T. Soon, "Wideband bandpass filters with high

passband selectivity using SAW-like resonators," in *2013 Asia-Pacific Microwave Conference Proceedings (APMC)*, 2013, pp. 485–487. doi: 10.1109/APMC.2013.6694839.

[36] X. Lu, K. Mouthaan, and T. S. Yeo, "A Wideband Bandpass Filter With Frequency Selectivity Controlled by SAW Resonators," *IEEE Trans. Components, Packag. Manuf. Technol.*, vol. 6, no. 6, pp. 897–905, 2016, doi: 10.1109/TCPMT.2016.2553105.

[37] M. Zolfagharloo Koohi, S. Lee, and A. Mortazawi, "Compact Intrinsically Switchable FBAR Filters Utilizing Ferroelectric BST," *IEEE Trans. Ultrason. Ferroelectr. Freq. Control*, vol. 65, no. 8, pp. 1468–1474, 2018, doi: 10.1109/TUFFC.2018.2839756.

[38] M. Z. Koohi and A. Mortazawi, "Intrinsically Switchable Filter Bank Employing Ferroelectric Barium Strontium Titanate," *IEEE Trans. Microw. Theory Tech.*, vol. 66, no. 12, pp. 5501–5507, 2018, doi: 10.1109/TMTT.2018.2867196.

[39] C. D. Nordquist *et al.*, "MEMS switching of contour-mode aluminum nitride resonators for switchable and reconfigurable radio frequency filters," *J. Micromechanics Microengineering*, vol. 26, no. 10, p. 104001, Aug. 2016, doi: 10.1088/0960-1317/26/10/104001.

[40] H. Wu, X. Cai, Y. Wu, Z. Lai, Q. Yang, and W. Wang, "An Investigation on Extraction of Material Parameters in Longitudinal Mode of FBAR," *IEEE Trans. Circuits Syst. II Express Briefs*, vol. 67, no. 6, pp. 1024–1028, 2020, doi: 10.1109/TCSII.2019.2928854.

[41] M. Z. Koohi, S. Lee, and A. Mortazawi, "Fabrication of a Low insertion loss intrinsically switchable BAW filter based on BST FBARs," in *2017 IEEE MTT-S International Microwave Symposium (IMS)*, 2017, pp. 1480–1483. doi: 10.1109/MWSYM.2017.8058900.

[42] M. Z. Koohi, W. Peng, and A. Mortazawi, "An Intrinsically Switchable Balanced Ferroelectric FBAR Filter at 2 GHz," in *2020 IEEE/MTT-S International Microwave Symposium (IMS)*, 2020, pp. 131–134. doi: 10.1109/IMS30576.2020.9223799.

[43] L. C. Popa and D. Weinstein, "Switchable piezoelectric transduction in AlGaN/GaN MEMS resonators," in *2013 Transducers & Eurosensors XXVII: The 17th International Conference on Solid-State Sensors, Actuators and Microsystems (TRANSDUCERS & EUROSENSORS XXVII)*, 2013, pp. 2461–2464. doi: 10.1109/Transducers.2013.6627304.

[44] A. Fouladi Azarnaminy and R. R. Mansour, "Reconfigurable SAW Resonators and Tunable Filters Using Monolithically Integrated VO_2 Switches," *IEEE Trans. Microw. Theory Tech.*, vol. 71, no. 1, pp. 181–192, 2023, doi: 10.1109/TMTT.2022.3222303.

[45] A. F. Azarnaminy, J. Jiang, and R. R. Mansour, "Switched Dual-Band SAW Filter Using Vanadium Oxide Switches," in *2021 IEEE MTT-S International Microwave Symposium (IMS)*, 2021, pp. 677–680. doi: 10.1109/IMS19712.2021.9574799.

[46] M. Ou and R. R. Mansour, "PCM-Based Bandwidth-Reconfigurable Acoustic-

Wave Filter," *IEEE Trans. Microw. Theory Tech.*, pp. 1–11, 2025, doi: 10.1109/TMTT.2025.3542357.

[47] D. Psychogiou, R. Gómez-García, and D. Peroulis, "Single and Multiband Acoustic-Wave-Lumped- Element-Resonator (AWLR) Bandpass Filters With Reconfigurable Transfer Function," *IEEE Trans. Microw. Theory Tech.*, vol. 64, no. 12, pp. 4394–4404, 2016, doi: 10.1109/TMTT.2016.2617884.

[48] D. Psychogiou, R. Gómez-García, and D. Peroulis, "Continuously-tunable-bandwidth acoustic-wave resonator-based bandstop filters and their multi-mode modeling," in *2016 46th European Microwave Conference (EuMC)*, 2016, pp. 894–897. doi: 10.1109/EuMC.2016.7824488.

[49] N. S. Luhrs, D. J. Simpson, and D. Psychogiou, "Multiband Acoustic-Wave-Lumped-Element Resonator-Based Bandpass-to-Bandstop Filters," *IEEE Microw. Wirel. Components Lett.*, vol. 29, no. 4, pp. 261–263, 2019, doi: 10.1109/LMWC.2019.2901199.

[50] S. Nam, D. Psychogiou, and A. Mortazawi, "Reconfigurable Transfer Function BST Acoustic Wave Lumped Element Resonator Filters," in *2021 51st European Microwave Conference (EuMC)*, 2022, pp. 301–304. doi: 10.23919/EuMC50147.2022.9784219.

[51] D. Psychogiou, R. Gómez-García, and D. Peroulis, "Acoustic-Wave-Lumped-Element-Resonator Filters With Equi-Ripple Absorptive Stopbands," *IEEE Microw. Wirel. Components Lett.*, vol. 26, no. 3, pp. 177–179, 2016, doi: 10.1109/LMWC.2016.2524997.

[52] D. Psychogiou, R. Gómez-García, and D. Peroulis, "Tunable acoustic-wave-lumped-element resonator (awlr)-based bandpass filters," in *2016 IEEE MTT-S International Microwave Symposium (IMS)*, 2016, pp. 1–4. doi: 10.1109/MWSYM.2016.7540356.

[53] M. Ou, A. F. Azarnaminy, and R. R. Mansour, "Bandwidth-Reconfigurable Acoustic Wave Filter with a Large Tuning Range," in *2024 IEEE International Microwave Filter Workshop (IMFW)*, 2024, pp. 95–98. doi: 10.1109/IMFW59690.2024.10477160.

[54] D. Psychogiou, "Reconfigurable All-Pass-to-Bandstop Acoustic-Wave-Lumped-Element Resonator Filters," *IEEE Microw. Wirel. Components Lett.*, vol. 30, no. 8, pp. 745–748, 2020, doi: 10.1109/LMWC.2020.3004028.

[55] G. Hueber and R. B. Staszewski, Eds., *Multi-Mode/Multi-Band RF Transceivers for Wireless Communications: Advanced Techniques, Architectures, and Trends*. John Wiley & Sons, 2010. doi: 10.1002/9780470634455.

[56] R. Gómez-Garcia, J.-M. Muñoz-Ferreras, and D. Psychogiou, "High-Order Input-Reflectionless Bandpass/Bandstop Filters and Multiplexers," *IEEE Trans. Microw. Theory Tech.*, vol. 67, no. 9, pp. 3683–3695, 2019, doi: 10.1109/TMTT.2019.2924975.

[57] A. C. Guyette, I. C. Hunter, and R. D. Pollard, "Design of absorptive microwave filters using allpass networks in a parallel-cascade configuration," in *2009 IEEE MTT-S International Microwave Symposium Digest*, 2009, pp. 733–736. doi: 10.1109/MWSYM.2009.5165801.

[58] R. Gómez-García, J.-M. Muñoz-Ferreras, and D. Psychogiou, “Symmetrical Quasi-Absorptive RF Bandpass Filters,” *IEEE Trans. Microw. Theory Tech.*, vol. 67, no. 4, pp. 1472–1482, 2019, doi: 10.1109/TMTT.2019.2895531.

[59] N. S. Padmavathi and M. N. Sujatha, “Analysis and Design of Reflectionless Filters for C Band Applications,” in *2018 International Conference on Communication and Signal Processing (ICCSP)*, 2018, pp. 527–531. doi: 10.1109/ICCSP.2018.8524214.

[60] D. Psychogiou and R. Gómez-García, “Tunable reflectionless microstrip bandpass filters,” in *2018 IEEE Radio and Wireless Symposium (RWS)*, 2018, pp. 49–51. doi: 10.1109/RWS.2018.8304943.

[61] R. Gómez-García, L. Yang, and J.-M. Munoz-Ferreras, “Low-Reflection Signal-Interference Single- and Multipassband Filters With Shunted Lossy Stubs,” *IEEE Microw. Wirel. Components Lett.*, vol. 30, no. 4, pp. 355–358, 2020, doi: 10.1109/LMWC.2020.2977864.

[62] X. Wu, Y. Li, and X. Liu, “High-Order Dual-Port Quasi-Absorptive Microstrip Coupled-Line Bandpass Filters,” *IEEE Trans. Microw. Theory Tech.*, vol. 68, no. 4, pp. 1462–1475, 2020, doi: 10.1109/TMTT.2019.2955692.

[63] P. Ma, B. Wei, Y. Heng, C. Luo, X. Guo, and B. Cao, “Design of absorptive superconducting filter,” *Electron. Lett.*, vol. 53, no. 11, pp. 728–730, 2017, doi: https://doi.org/10.1049/el.2017.0768.

[64] J. Lee, B. Lee, S. Nam, and J. Lee, “Rigorous Design Method for Symmetric Reflectionless Filters With Arbitrary Prescribed Transmission Response,” *IEEE Trans. Microw. Theory Tech.*, vol. 68, no. 6, pp. 2300–2307, 2020, doi: 10.1109/TMTT.2020.2976967.

[65] J. Verdu, P. de Paco, and Ó. Menendez, “Double-Ladder Filter Topology for a Dual-Band Transmission Response Based on Bulk Acoustic Wave Resonators,” *IEEE Microw. Wirel. Components Lett.*, vol. 20, no. 3, pp. 151–153, 2010, doi: 10.1109/LMWC.2010.2040215.

[66] D. Psychogiou and R. Gómez-García, “Symmetrical Quasi-Reflectionless SAW-Based Bandpass Filters With Tunable Bandwidth,” *IEEE Microw. Wirel. Components Lett.*, vol. 29, no. 7, pp. 447–449, 2019, doi: 10.1109/LMWC.2019.2918413.

[67] S.-Y. Tseng, M.-Y. Yang, C.-C. Hsiao, Y.-Y. Chen, and R.-B. Wu, “Design for Acoustic Wave Multiplexers With Single Inductor Matching Network Using Frequency Response Fitting Method,” *IEEE Open J. Ultrason. Ferroelectr. Freq. Control*, vol. 2, pp. 140–151, 2022, doi: 10.1109/OJUFFC.2022.3182321.

[68] D. Psychogiou, R. Gómez-García, and D. Peroulis, “Multi-resonant acoustic-wave-lumped-element resonators (AWLRs) for multi-band bandpass filters with enhanced fractional bandwidth,” in *2017 IEEE International Conference on Microwaves, Antennas, Communications and Electronic Systems (COMCAS)*, 2017, pp. 1–4. doi: 10.1109/COMCAS.2017.8244708.

[69] D. Psychogiou, D. J. Simpson, and R. Gómez-García, “Input- Reflectionless Acoustic-Wave-Lumped- Element Resonator-Based Bandpass Filters,” in *2018 IEEE/MTT-S International Microwave Symposium - IMS*, 2018, pp. 852–855.

doi: 10.1109/MWSYM.2018.8439676.

[70] R. Gómez-García, J.-M. Muñoz-Ferreras, and D. Psychogiou, “Fully-reconfigurable bandpass filter with static couplings and intrinsic-switching capabilities,” in *2017 IEEE MTT-S International Microwave Symposium (IMS)*, 2017, pp. 914–917. doi: 10.1109/MWSYM.2017.8058734.

[71] S.-J. Park and G. M. Rebeiz, “Low-Loss Two-Pole Tunable Filters With Three Different Predefined Bandwidth Characteristics,” *IEEE Trans. Microw. Theory Tech.*, vol. 56, no. 5, pp. 1137–1148, 2008, doi: 10.1109/TMTT.2008.921638.

[72] M. Jung and B.-W. Min, “A Widely Tunable Compact Bandpass Filter Based on a Switched Varactor-Tuned Resonator,” *IEEE Access*, vol. 7, pp. 95178–95185, 2019, doi: 10.1109/ACCESS.2019.2929746.

[73] K. Kawai, H. Okazaki, and S. Narahashi, “Center Frequency and Bandwidth Tunable Filter Employing Tunable Comb-Shaped Transmission Line Resonators and J-inverters,” in *2006 European Microwave Conference*, 2006, pp. 649–652. doi: 10.1109/EUMC.2006.281494.

[74] B. E. Carey-Smith, P. A. Warr, M. A. Beach, and T. Nesimoglu, “Wide tuning-range planar filters using lumped-distributed coupled resonators,” *IEEE Trans. Microw. Theory Tech.*, vol. 53, no. 2, pp. 777–785, 2005, doi: 10.1109/TMTT.2004.841221.

[75] P.-L. Chi, T. Yang, and T.-Y. Tsai, “A Fully Tunable Two-Pole Bandpass Filter,” *IEEE Microw. Wirel. Components Lett.*, vol. 25, no. 5, pp. 292–294, 2015, doi: 10.1109/LMWC.2015.2409794.

[76] J.-R. Mao, W.-W. Choi, K.-W. Tam, W. Q. Che, and Q. Xue, “Tunable Bandpass Filter Design Based on External Quality Factor Tuning and Multiple Mode Resonators for Wideband Applications,” *IEEE Trans. Microw. Theory Tech.*, vol. 61, no. 7, pp. 2574–2584, 2013, doi: 10.1109/TMTT.2013.2264684.

[77] G. Zhang, Y. Xu, and X. Wang, “Compact Tunable Bandpass Filter With Wide Tuning Range of Centre Frequency and Bandwidth Using Short Coupled Lines,” *IEEE Access*, vol. 6, pp. 2962–2969, 2018, doi: 10.1109/ACCESS.2017.2786296.

[78] D. J. Simpson, R. Gómez-García, and D. Psychogiou, “Single-/Multi-Band Bandpass Filters and Duplexers With Fully Reconfigurable Transfer-Function Characteristics,” *IEEE Trans. Microw. Theory Tech.*, vol. 67, no. 5, pp. 1854–1869, 2019, doi: 10.1109/TMTT.2019.2899849.

[79] T. Lim, A. Anand, J. Chen, X. Liu, and Y. Lee, “Design Method for Tunable Planar Bandpass Filters With Single-Bias Control and Wide Tunable Frequency Range,” *IEEE Trans. Circuits Syst. II Express Briefs*, vol. 68, no. 1, pp. 221–225, 2021, doi: 10.1109/TCSII.2020.3004614.

[80] M. Fan, K. Song, L. Yang, and R. Gómez-García, “Frequency-Tunable Constant-Absolute-Bandwidth Single-/Dual-Passband Filters and Diplexers With All-Port-Reflectionless Behavior,” *IEEE Trans. Microw. Theory Tech.*, vol. 69, no. 2, pp. 1365–1377, 2021, doi: 10.1109/TMTT.2020.3040481.

[81] J.-X. Xu, L. Yang, Y. Yang, and X. Y. Zhang, “High- Q -Factor Tunable Bandpass Filter With Constant Absolute Bandwidth and Wide Tuning Range Based on Coaxial Resonators,” *IEEE Trans. Microw. Theory Tech.*, vol. 67, no.

10, pp. 4186–4195, 2019, doi: 10.1109/TMTT.2019.2926251.

[82] D. Lu, M. Yu, N. S. Barker, Z. Li, W. Li, and X. Tang, "Advanced Synthesis of Wide-Tuning-Range Frequency-Adaptive Bandpass Filter With Constant Absolute Bandwidth," *IEEE Trans. Microw. Theory Tech.*, vol. 67, no. 11, pp. 4362–4375, 2019, doi: 10.1109/TMTT.2019.2941852.

[83] Q. Xiang, H. Sun, M. Fu, Q. Jin, and Q. Feng, "A 5th-Order Constant Bandwidth Tunable Bandpass Filter With Two Cascaded Trisection Structures," *IEEE Trans. Circuits Syst. II Express Briefs*, vol. 70, no. 1, pp. 126–130, 2023, doi: 10.1109/TCSII.2022.3208601.

[84] Z. Li, X. Tang, D. Lu, Z. Cai, Y. Liu, and J. Luo, "Low-Loss Wide-Tuning-Range Three-Pole Frequency-Agile Bandpass Diplexer With Identical Constant Absolute Bandwidth," *IEEE Access*, vol. 7, pp. 149833–149845, 2019, doi: 10.1109/ACCESS.2019.2946859.

[85] C.-F. Chen, "Design of a Microstrip Three-State Switchable and Fully Tunable Bandpass Filter With an Extra-Wide Frequency Tuning Range," *IEEE Access*, vol. 8, pp. 66438–66447, 2020, doi: 10.1109/ACCESS.2020.2985415.

[86] J. S. Sun, N. Kaneda, Y. Baeyens, T. Itoh, and Y.-K. Chen, "Multilayer Planar Tunable Filter With Very Wide Tuning Bandwidth," *IEEE Trans. Microw. Theory Tech.*, vol. 59, no. 11, pp. 2864–2871, 2011, doi: 10.1109/TMTT.2011.2163201.

[87] C.-F. Chen, G.-Y. Wang, and J.-J. Li, "Microstrip Switchable and Fully Tunable Bandpass Filter With Continuous Frequency Tuning Range," *IEEE Microw. Wirel. Components Lett.*, vol. 28, no. 6, pp. 500–502, 2018, doi: 10.1109/LMWC.2018.2831440.

[88] Skyworks Solutions, Inc., *SKYA21003: 0.4–3.8 GHz SP4T Antenna Tuning Switch*, Datasheet, Rev. 202938K, 2023. [Online]. Available: https://www.skyworksinc.com/-/media/SkyWorks/Documents/Products/2201-2300/SKYA21003_202938K.pdf [Accessed: May 21, 2025].

[89] M. R. A. Nasser and D. Psychogiou, "Quasi-elliptic SAW Filters Using Multi-Resonant Acoustic-Wave Lumped-Element Resonator Stages," in *2022 52nd European Microwave Conference (EuMC)*, 2022, pp. 420–423. doi: 10.23919/EuMC54642.2022.9924400.

[90] M. R. A. Nasser and D. Psychogiou, "Acoustic Wave Resonator-Based Bandpass Filters With Continuously Tunable Fractional Bandwidth," *IEEE Trans. Circuits Syst. II Express Briefs*, vol. 70, no. 4, pp. 1390–1394, 2023, doi: 10.1109/TCSII.2022.3225735.

[91] M. R. A. Nasser and D. Psychogiou, "Acoustic-Wave-Resonator-Based Bandpass Filters With Multiconfigurable and Continuously Tunable Transfer Function Capabilities," *IEEE Trans. Microw. Theory Tech.*, vol. 72, no. 12, pp. 6968-6982, 2024, doi: 10.1109/TMTT.2024.3408335.

[92] M. R. A. Nasser, K. G. McCarthy, and D. Psychogiou, "Multiconfigurable Acoustic-Wave-Lumped-Resonator (AWLR)-Based Bandpass-to-Bandstop Filters With Continuously Tunable Characteristics," *IEEE Trans. Microw. Theory Tech.*, vol. 73, no. 10, pp. 7869-7883, Oct. 2025, doi: 10.1109/TMTT.2025.3564552.

[93] M. R. A. Nasser and D. Psychogiou, “Quasi-Elliptic Multi-band BPFs using Multi-Resonant Acoustic-Wave Lumped-Element Resonators,” in *2023 53rd European Microwave Conference (EuMC)*, 2023, pp. 170–173. doi: 10.23919/EuMC58039.2023.10290545.

[94] M. R. A. Nasser and D. Psychogiou, “Reflective and Quasi-reflectionless Multiband Bandpass Filters using Multi-Resonant Acoustic-Wave Lumped-Element Resonators,” in *International Journal of Microwave and Wireless Technologies*, vol. 17, no. 2, pp. 318-330, Oct. 2025, doi:10.1017/S1759078724001211.

[95] M. R. A. Nasser, R. K. Jaiswal, and D. Psychogiou, “A Compact Bandpass Filter Manifold With Ultrawide Frequency and Bandwidth Tuning,” *IEEE Access*, vol. 11, pp. 41054–41060, 2023, doi: 10.1109/ACCESS.2023.3269884.

[96] M. R. A. Nasser and D. Psychogiou, “Switchless Multi-Octave Tune-All BPF Manifold Using Low-Pass/High-Pass Diplexer Junctions,” *IEEE J. Microwaves*, vol. 4, no. 4, pp. 759-766, Oct. 2024, doi: 10.1109/JMW.2024.3421535.

[97] T.-H. Lee, J.-J. Laurin, and K. Wu, “Reconfigurable Filter for Bandpass-to-Absorptive Bandstop Responses,” *IEEE Access*, vol. 8, pp. 6484–6495, 2020, doi: 10.1109/ACCESS.2019.2963710.

[98] T. Yang and G. M. Rebeiz, “Bandpass-to-Bandstop Reconfigurable Tunable Filters with Frequency and Bandwidth Controls,” *IEEE Trans. Microw. Theory Tech.*, vol. 65, no. 7, pp. 2288–2297, 2017, doi: 10.1109/TMTT.2017.2679182.

[99] Coilcraft Inc., “Chip Inductors - 0603DC Series (1608),” 2022. [Online]. Available: https://www.coilcraft.com/en-us/products/rf/ceramic-core-chip-inductors/0603-(1608)/0603dc

[100] Johanson Technology Inc., High-Q Multilayer Ceramic Capacitors, Datasheet, 2023.[Online]. Available:https://www.johansontechnology.com/docs/4387/johanson-high-q-capacitors_kBKEohj.pdf [Accessed: May 21, 2025].

[101] Skyworks Solutions, Inc., SMV1405–1430 Series: Hyperabrupt Junction Tuning Varactors, Datasheet, Rev. 200068W, 2023. [Online]. Available: https://www.skyworksinc.com/-/media/SkyWorks/Documents/Products/101-200/SMV1405_1430_Series_200068W.pdf [Accessed: May 21, 2025].

[102] MACOM Technology Solutions, MA46 Series: Silicon Abrupt Tuning Varactors, Datasheet, 2021. [Online]. Available: https://cdn.macom.com/datasheets/MA46%20Series.pdf [Accessed: May 21, 2025].

[103] A. Ding *et al.*, “Non-Polar a-plane AlScN(1120) Thin Film Based SAW Resonators with Significantly Improved Electromechanical Coupling,” in *2020 IEEE International Ultrasonics Symposium (IUS)*, 2020, pp. 1–4. doi: 10.1109/IUS46767.2020.9251391.

[104] S. Gong and G. Piazza, “Figure-of-Merit Enhancement for Laterally Vibrating Lithium Niobate MEMS Resonators,” *IEEE Trans. Electron Devices*, vol. 60, no. 11, pp. 3888–3894, 2013, doi: 10.1109/TED.2013.2281734.

[105] R. O. . TST TAI-SAW Technology CO. LTD. Taiwan, “SAW Resonator 1030

MHz: TC0669A," 2019. [Online]. Available: https://www.taisaw.com/products/searchA?param=SAW_Resonators.

[106] J. D. Larson, P. D. Bradley, S. Wartenberg, and R. C. Ruby, "Modified Butterworth-Van Dyke circuit for FBAR resonators and automated measurement system," in *2000 IEEE Ultrasonics Symposium. Proceedings. An International Symposium (Cat. No.00CH37121)*, 2000, pp. 863–868 vol.1. doi: 10.1109/ULTSYM.2000.922679.

[107] Murata Manufacturing Co., Ltd., GJM Series: High-Q Multilayer Ceramic Capacitors (SMD), Product Overview, 2024. [Online]. Available: https://www.murata.com/en-us/products/capacitor/ceramiccapacitor/overview/lineup/smd/gjm [Accessed: May 21, 2025].

[108] D. Psychogiou, R. Gómez-García, and D. Peroulis, "Constant In-Band Group-Delay Acoustic-Wave-Lumped-Element-Resonator-Based Bandpass Filters and Diplexers," *IEEE Trans. Microw. Theory Tech.*, vol. 66, no. 5, pp. 2199–2209, 2018, doi: 10.1109/TMTT.2018.2801824.

[109] Keysight Technologies, "PathWave Advanced Design System (ADS)," 2025.

[110] Ansys, Inc., "Ansys HFSS: 3D High Frequency Electromagnetic Simulation Software," 2025.

[111] Y. Sun, Q. Yang, H. Zhang, D. Zhang, and W. Pang, "A compact dual-passband filter based on bulk acoustic wave technology," in *2015 IEEE MTT-S International Microwave Symposium*, 2015, pp. 1–4. doi: 10.1109/MWSYM.2015.7166848.

[112] A. Fouladi Azarnaminy and R. R. Mansour, "Switched Dual-Band SAW Filters Using Hybrid and Monolithically Integrated Vanadium Oxide Switches," *IEEE Trans. Microw. Theory Tech.*, vol. 70, no. 1, pp. 876–885, 2022, doi: 10.1109/TMTT.2021.3130597.

[113] S. Shin, E. Naglich, and L. Boglione, "Back-to-Back Connected Multiplexers for a Broadband Channel Splitter and Channel Combiner," in *2019 49th European Microwave Conference (EuMC)*, 2019, pp. 188–191. doi: 10.23919/EuMC.2019.8910821.

[114] P. Zheng *et al.*, "Near 5-GHz Longitudinal Leaky Surface Acoustic Wave Devices on LiNbO3/SiC Substrates," *IEEE Trans. Microw. Theory Tech.*, vol. 72, no. 3, pp. 1480–1488, 2024, doi: 10.1109/TMTT.2023.3305078.

[115] X. Cao, C. Wang, W. Li, and Q. Cai, "An On-Chip Fractally Chipped FBAR Filter With Ba-Zn-Fe-Sc-O Thin Film in 5G-FR2 Millimeter-Wave Band," *IEEE Electron Device Lett.*, vol. 44, no. 4, pp. 682–685, 2023, doi: 10.1109/LED.2023.3250423.

[116] S. Nam, W. Peng, P. Wang, D. Wang, Z. Mi, and A. Mortazawi, "A mm-Wave Trilayer AlN/ScAlN/AlN Higher Order Mode FBAR," *IEEE Microw. Wirel. Technol. Lett.*, vol. 33, no. 6, pp. 803–806, 2023, doi: 10.1109/LMWT.2023.3271865.

[117] S. Rassay, D. Mo, C. Li, N. Choudhary, C. Forgey, and R. Tabrizian, "Intrinsically Switchable Ferroelectric Scandium Aluminum Nitride Lamb-Mode Resonators," *IEEE Electron Device Lett.*, vol. 42, no. 7, pp. 1065–1068,

2021, doi: 10.1109/LED.2021.3078444.

[118] H. Zhou *et al.*, “Surface Wave and Lamb Wave Acoustic Devices on Heterogenous Substrate for 5G Front-Ends,” in *2020 IEEE International Electron Devices Meeting (IEDM)*, 2020, pp. 17.6.1-17.6.4. doi: 10.1109/IEDM13553.2020.9372128.

[119] Y. Xu, Y. Wu, H. Wu, Y. Yang, and W. Wang, “Wideband High Selectivity Filter Chips With Adjustable Bandwidth Based on IPD Technology,” *IEEE Trans. Circuits Syst. II Express Briefs*, vol. 69, no. 11, pp. 4273–4277, 2022, doi: 10.1109/TCSII.2022.3186182.

[120] C. Zuo, C. He, W. Cheng, and Z. Wang, “Hybrid Filter Design for 5G using IPD and Acoustic Technologies,” in *2019 IEEE International Ultrasonics Symposium (IUS)*, 2019, pp. 269–272. doi: 10.1109/ULTSYM.2019.8925918.